Design, Modeling, and Testing of High Performance RF Bistable Magnetic Actuators

A Dissertation
Presented to
The Academic Faculty

by

Gary D. Gray, Jr.

In Partial Fulfillment
Of the Requirements for the Degree
Doctor of Philosophy in Chemical Engineering

Georgia Institute of Technology
December, 2004

Design, Modeling, and Testing of High Performance RF Bistable Magnetic Actuators

Approved by:

Dr. Paul A. Kohl, Advisor
School of Chemical & Biomolecular Engineering
Georgia Institute of Technology

Dr. Dennis Hess
School of Chemical & Biomolecular Engineering
Georgia Institute of Technology

Dr. Peter Hesketh
School of Mechanical Engineering
Georgia Institute of Technology

Dr. Pete Ludovice
School of Chemical & Biomolecular Engineering
Georgia Institute of Technology

Dr. Ronald Rousseau
School of Chemical & Biomolecular Engineering
Georgia Institute of Technology

Dr. Joseph Schork
School of Chemical & Biomolecular Engineering
Georgia Institute of Technology

Date Approved: December 2004

ACKNOWLEDGEMENT

There are many who have contributed to my success in graduate school, and first among them is my Ph.D. advisor, Dr. Paul Kohl, who led me to a project well suited for my interests, gave me the freedom to direct my progress, and challenged me throughout this process. I am also very appreciative of the trust and confidence he showed in permitting me to pursue coursework outside of chemical engineering. I also thank my project sponsor, Superconductor Technologies, Inc. located in Santa Barbara, California. In particular I am grateful to Eric Prophet, with whom I worked in design of devices and who shared many valuable discussions into this research topic.

I also wish to acknowledge the entire Kohl research group at Georgia Tech and the Microelectronics Research Center cleanroom facilities in which the device fabrication was performed. In particular, I wish to recognize the extraordinary contributions from the following individuals: Lingbo Zhu, of the Kohl research group, who worked with me to develop the processing steps for the devices presented in this thesis and who worked fabricating many of the magnetic actuators presented in Chapter 5; Matthew Morgan, of the Kohl research group, who performed much of the testing of the electrostatic actuators discussed in Chapter 3; Eric Prophet, of STI, who provided RF performance data of completed devices; Joel Pikarsky, of the MIRC, who helped assemble devices by means of a flip chip bonding device; and Charlie Suh, of the MIRC, who expertly diced completed wafers.

In addition, I wish to thank my father, who encouraged me to pursue this graduate work, my mother, whose pride in me is always felt, and my entire family, always impressed with what I have accomplished. Thanks especially to my wife, Diane, whose patience has endured my countless evenings reading, stressing over coursework, and my repeated need to find pen and paper to scribble some calculation. Finally, I value the friendships I have made during my days at Georgia Tech, as they have often eased the difficult times. Thanks to David Vener, friend and best man, whose success has always motivated me to achieve more. Thanks to Stephen Lewis, a friend who shared hobbies, lunch, and many physics text; Hollie Kelleher, who always was willing to listen, as well as answer detailed thesis questions; and thanks to Kevin Doyle, who lightened the atmosphere with his humor and friendship.

TABLE OF CONTENTS

LIST OF TABLES

LIST OF FIGURES

LIST OF SYMBOLS

MOSFET	Metal Oxide Semiconductor Field Effect Transistor
MESFET	Metal Semiconductor Field Effect Transistor
HEMT	High Electron Mobility Transistors
CVC	Continuously Variable Capacitor
SPS	Short Pulse Switching
MEMS	Microelectromechanical Systems
SPDT	Single Pole Double Throw
RF	Radio Frequency
IC	Integrated Circuit
BCB	Benzocyclobutene
BOE	Buffered Oxide Etch
HTS	High Temperature Superconductor

Chapter 1

R_s	resistance of I region under forward bias
Q	quantity of stored charge in I region
I_f	forward bias current
f_{cutoff}	cutoff frequency
R_{on}	on state resistance
C_{off}	off state capacitance

Chapter 3

E	elastic modulus
I	moment of inertia
M(x)	bending moment as a function of position x
z	deflection of cantilever beam
L	beam length
w	beam width
b	beam thickness
σ_i	compressive or tensile stress in layer i
x	position measured along the length of cantilever beam
dM	differential moment
dF	differential force
y	position along thickness of beam from midplane
dy	differential in position y
b_o	thickness of nonstressed beam layer
b(x)	average thickness of composite beam along position x
b_s	thickness of stressed beam layer
d(x)	deflection of beam along coordinate x
a	dimensionless quantity dependent on beam geometry
$d_{patterned}$	deflection of beam with patterned hard gold
$d_{uniform}$	deflection of beam with uniform hard gold
E_{sub}	elastic modulus of the substrate material
v_{sub}	poisson ratio of the substrate material

t_{film}	thickness of the thin film material
R	radius of curvature of the bimetallic structure
h_{sub}	thickness of substrate material

Chapter 4

V	magnetic material volume
M	magnetic material magnetization
B	magnetic flux density
$B_{external}$	external magnetic field
γ	angle between magnetization vector and external magnetic field
N_L	length demagnetization factor
θ	angle the magnetization vector bends out of plane of the magnetic material
$\Gamma_{elastic}$	elastic torque due to stiffness of the hinge material
H_c	coercivity of magnetic material
B_{coil}	magnetic flux density supplied by integrated coil
x	target deflection for required isolation
x_o	deflection observed with permalloy thickness t_o
T	total initial thickness of gold/permalloy beam
t_o	initial permalloy thickness
M_{new}	magnetic moment with permalloy thickness $t_o + \Delta t_o$
M_{old}	magnetic moment with permalloy thickness t_o
Δt_o	increment in permalloy thickness
I_{new}	moment of inertia with permalloy thickness $t_o + \Delta t_o$

I_{old}	moment of inertia with permalloy thickness t_o
r_{old}	old radius of curvature
r_{new}	new radius of curvature
M	magnetization of the magnetic material
N_D	total demagnetization factor in the direction of M
N_T	thickness shape demagnetization factor
M_{sat}	saturation magnetization
$\Gamma_{magnetic}$	magnetic torque
$\Gamma_{anistropy}$	anisotropy torque
H_{total}	total magnetic field generated from integrated coil
$H_{i,j}$	magnetic field generated from turn i, side j of coil
$\varepsilon_{i,j}$	angle the line connecting the field point to the nearest point of segment i, j makes with line segment connecting the coil center to coil segment i, j.
z	unit vector in direction of z
r	unit vector in direction of r
$L_{i,j}$	length of segment i, j in the integrated coil
$r_{i,j}$	distance on the midline from segment i, j to the field point
$\Gamma_{elastic}$	elastic torque acting to pull cantilever back to its initial position
k_φ	angular spring constant of cantilever hinges
φ	angle the ferromagnetic material makes with the external magnetic field
φ_o	initial angle the ferromagnetic material makes with the external magnetic field, primarily due to intrinsic stresses in the cantilever
φ_{top}	angle corresponding to top latched position
φ_{max}	the maximum positive angle achievable for a given actuator, determined by the volume of ferromagnetic material and external magnetic field

	strength
φ_{min}	the most negative angle achievable for a given actuator, determined by the volume of ferromagnetic material and external magnetic field strength
φ_{bottom}	angle corresponding to bottom latched position
$F_{contact}$	contact force between actuator tip and substrate
X	length of actuator beam
J	angular moment of inertia of MEMS cantilever about fixed hinge anchor
C	angular damping coefficient for dynamic operation of MEMS switch
m	mass of actuator beam and hinges
x	length of actuator hinges

Chapter 5

$M_{critical}$	reverse magnetization necessary for switching
ΔB_{coil}	extra magnetic field necessary for SPS
ΔI	extra coil current necessary for SPS
B_{min}	minimum external magnetic field required for latching

Chapter 6

L	Lagrangian
T	kinetic energy of system
U	potential energy of system
yi	positional coordinates
y_i`	momentum coordinates

$\lambda_j(t)$	time varying forces of constraint
g_i	constraining relations
T_{beam}	kinetic energy of beam
T_{hinge}	kinetic energy of hinge
$T_{translational}$	translational kinetic energy
$T_{rotational}$	rotational kinetic energy
H_o	external magnetic field
m	system mass
I	moment of inertia
$U_{magnetostatic}$	magnetostatic potential energy
$U_{hinge\text{-}potential}$	mechanical potential energy stored in hinge
I_{hinge}	moment of inertia of hinge
Δz	change in height of non-anchored hinge end
K	deflection spring constant for hinge
dM	differential in magnetization, M
e_z	unit vector in direction of external magnetic field, z
e_m	unit vector in direction of internal magnetization, M
I_{beam}	moment of inertia of beam
x	projection of hinge length x on the axis along the substrate
x_1	change in x due to buckling of hinge
x_2	change in x due to frictional effects
g_1	constraint relationship 1
g_2	constraint relationship 2

g_3	constraint relationship 3
λ_1	force of constraint for equation of constraint 1
λ_2	force of constraint for equation of constraint 2
λ_3	force of constraint for equation of constraint 3
x_o	initial hinge length before wiping
$F_{contact}$	contact force present between cantilever tip and bottom substrate
$U_{hinge-2}$	potential energy in hinge due to friction between actuator and substrate
$F_{hinge-2}$	force acting on hinge due to friction between actuator and substrate
$F_{friction}$	force of friction between cantilever tip and bottom substrate

Chapter 7

g	gap distance
V	voltage applied across electrode and cantilever
ε	permittivity of gap separation

Appendix A

$F_{magnetic}$	force on magnetic material in inhomogeneous magnetic field
U	potential energy of magnetic material in external magnetic field
V	volume of magnetic material
M	magnetization
B	magnetic flux density
M_{mag}	magnetic moment
μ_o	permittivity of free space

χ	magnetic susceptibility
H	magnetic field
N	number density of spins
M_b	magnetic moment of spinning electron
θ	angle between magnetic moment M_b and external field H
n	number of electrons
$L(\gamma)$	Langevin function with argument γ
γ	argument of Langevin function
α	dimensionless quantity relating magnetic field to thermal energy
k	Boltzman's constant
T	absolute temperature
M	technical magnetization
w	molecular field constant
μ_r	relative permeability

Appendix B

$H_{internal}$	internal field
$H_{external}$	external applied field
H_{demag}	demagnetization field
N_{beam}	shape demagnetization factor directed along beam length
a	length of major axis of ellipsoid
b	length of semi-major axis of ellipsoid
c	length of minor axis of ellipsoid

α	parameter used in determination of demagnetization factors
φ	parameter used in determination of demagnetization factors
ν	elliptical integral amplitude
E	elliptical integral of the second kind
F	elliptical integral of the first kind
k	elliptical integral modulus
F_{spring}	elastic restoring force due to spring
k	spring constant
x	distance spring element extended
V	applied voltage difference between the two electrostatic electrodes
$F_{electrostatic}$	electrostatic force between two electrodes with potential difference
ε	permittivity of material
A	electrode area
d	initial separation distance between the two electrodes
F_{total}	sum of spring and electrostatic forces
V_{pullin}	pull-in voltage
t_D	thickness of dielectric at pull-in
$V_{release}$	release voltage for electrostatic actuator
y(x)	deflection of cantilever on coordinate x
x	coordinate along beam length
p(x)	pressure distribution on cantilever as a function of distance x
C_1, C_2, C_3	integration constants
L	length of cantilever

SUMMARY

In this work, electrostatic and magnetic actuation mechanisms were investigated for providing continuous and discrete control of MEMS components. The project goal was to design and fabricate high performance RF compatible switch and tuning elements for use in a cryogenic filter system.

Electrostatic actuation was used to fabricate MEMS variable capacitors with extended tuning ranges. To enable this extended tunability, a stress gradient was induced in two directions (through the plane of the beam and along its length) to produce a beam with variable curvature upon release. The stress gradient in the through-plane direction was produced by altering the conditions during electroplating and in the in-plane direction through lithographic patterning. The pull-in characteristics of four electrostatic actuator designs were analyzed. The in-plane stress gradient, along the length of the beam, significantly improved the tuning range compared with devices containing a spatially uniform stress profile. This advance has greatly eased the instability problem of electrostatically actuated beams. The tuning range of a device with two hinges and a square front improved from less that 33% to 70%. Devices with two hinges and elliptical front improved to 45% tuning range and those with rectangular shape improved to 65% stability. This advance has been applied to actuators for RF tuners.

Due to the limitations of electrostatic RF actuators, magnetic actuation was also

investigated, and the optimal design space for a bistable magnetic actuator with ultra-low actuation energy and large actuation distance (100 μm) has been modeled. Attention was paid to minimizing the energy expended to minimize heat dissipation and power consumption so that the device could be used over a wide temperature range, including cryogenic environments. A more desirable switching regime existing for low magnetic fields (10 mT) was found that requires shorter pulses (μs vs ms) and lower actuation energy (< 5 μJ vs 100 μJ) than designs outside of this space. The device was modeled to latch in two states, based on the interaction of the magnetic actuator with an external magnetic field.

Based on this model, a bistable magnetic MEMS actuator was fabricated using microelectronic processes, including a two-substrate flip-chip assembly, multilevel metallization, and sublimation release to avoid stiction. The actuator was found to have excellent correspondence between observed and modeled behavior. The benefits of shape anisotropy are quantified. Lithographic patterning of the magnetic material into long narrow strips along the actuator's length resulted in greater magnetic torques developed at reduced external field levels. Low levels of anisotropy led to designs with low levels of magnetization and required higher external magnetic fields, whereas high levels of anisotropy led to designs latching at 10 mT levels with contact forces greater than 15 μN, switching energies less than 100 μJ, and a switching speed faster than 5 ms. More moderate levels of anisotropy resulted in a design space where < 1 μJ switching energies could be realized. Electrical performance has been demonstrated over 2 million cycles, and mechanical performance to 150 million cycles. Applications include

electronics, microfluidics, and cryogenic devices.

The magnetic actuator, in addition to the primary cantilever bending, exhibits a secondary wiping motion during overdrive. The wiping action occurs as lower the total energy of the actuator system decreases with increasing external magnetic field. The total wiping distance for a 1000 μm long switch was 50 μm with magnetic fields of 10 to 100 mT. A first-principles physical model has been derived for the equilibrium and dynamic behavior of the device, as well as discrete changes in position due to frictional effects.

CHAPTER 1

INTRODUCTION

Conventional Radio Frequency (RF) switch technology is based on solid state devices, such as field-effect-transistor (FET)-based devices and p-type/intrinsic/n-type (PIN) diodes, which provide a high degree of ruggedness, relatively simple fabrication, and very short switching times [1].

FET-based devices, such as metal-semiconductor-field-effect-transistors (MESFETs), and high electron mobility transistors (HEMTs) are each based on CMOS transistor fabrication [1-4]. They each differ from metal oxide semiconductor (MOS) FETs, most notably in the use of a reverse biased Schottky diode. The Shottky diode has a short reverse recovery time, allowing rectifying of high frequency alternating current into direct current. In MOSFETs, the wavefunction of the electrons in the conducting channel extends into the gate oxide, reducing the mobility of the charge carriers. Free charge carriers diffuse across the metal / silicon junction, creating a depletion region that acts to separate the conducting channel from the gate (shown in Figure 1.1). The resulting depletion layer enhances the isolation between the gate and the channel [1-2], and the increase in the mobility of the charge carriers greatly increases the transit frequency, making this device ideal for microwave and RF applications up to frequencies of 100 GHz [1]. Use of GaAs as the substrate material is common, as the room temperature

mobility in this material is 5 times that of silicon [1].

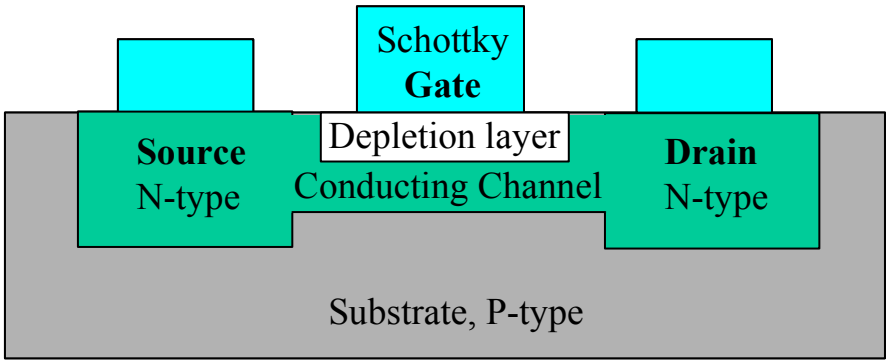

Figure 1.1. Schematic of MESFET. The reverse biased Shottky diode acts to isolate the conducting channel, increasing the mobility of the charge carriers.

Another RF solid state technology is the PIN diode, a semiconductor device which operates as a variable resistor capable of 1 – 10,000 Ω range over RF frequencies. The forward biased DC current determines the resistance value of the PIN diode. In switch and attenuator applications, the PIN diode should ideally control the RF signal level without introducing distortion, which might change the shape of the RF signal.

A PIN diode is fabricated beginning with a high resistivity, almost intrinsically pure silicon, germanium or InGaAs substrate. P-type and n-type regions are then formed by diffusion of dopants into opposite sides of the diode surface. During forward bias, the charge carryiers, holes and electrons, are moved from the p-type and n-type regions, respectively, into the intrinsic region. These charge carriers have a nonzero lifetime, and the finite quantity of charge lowers the resistance of the intrinsic region [1]. The quantity of stored charge, Q, is linearly dependant on the product of the carrier lifetime and the

forward bias current, I_f. This results in the resistance of the I-region under forward bias, R_s, being inversely proportional to Q. Over a forward bias current of 10 μA to 1 A, typical resistance values from 10,000 to 0.1 Ω are typically achieved [1]. When the control current is switched on and off or in discrete steps, the device is useful in switching, pulse modulating, and phase shifting an RF signal. Isolation better than 50 dB can be obtained with PIN diode technology, but insertion loss in the 1-3 dB range limits use in high performance applications. In addition, the variable resistance of the PIN diode is not observed for all frequencies. For frequencies less than about 10-100 MHz, electrons do not suitably accumulate in the intrinsic region, and the variable resistivity of the PIN diode is not observed. Furthermore, the high frequency limit of the PIN diode is determined by the shunt capacitance of the PN junction, but are typically above 30 GHz [1].

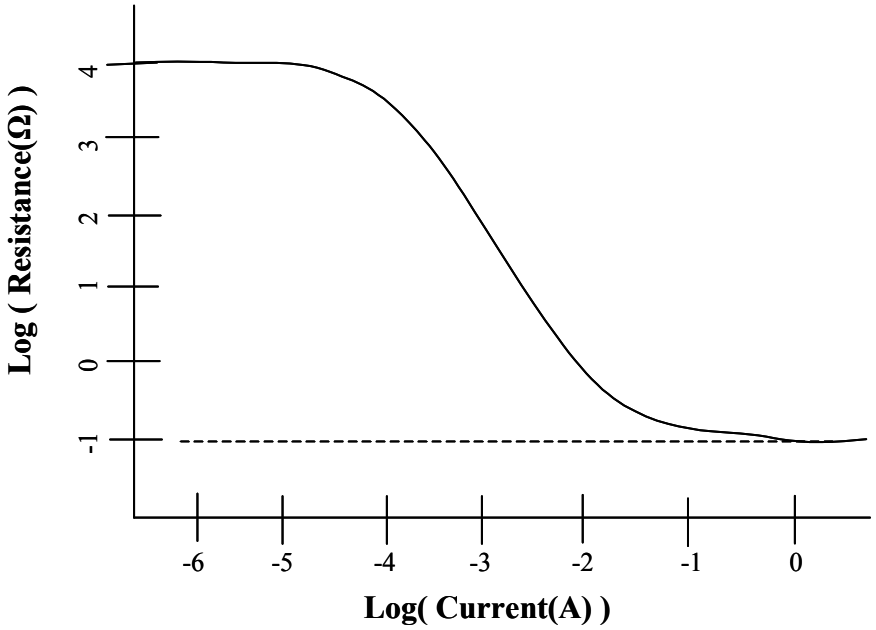

Figure 1.2. Dependence of PIN diode resistance on current applied.

These solid state devices, however, are characterized by significant losses and limited isolation. Microelectromechanical system (MEMS) technology enables the batch fabrication of miniature mechanical structures, devices, and systems. The first MEMS switch was reported in 1971, in which an electrostatically actuated cantilever was used to switch low-frequency electrical signals [5]. Today, additional actuation mechanisms for MEMS designs include electromagnetic, thermal, and piezoelectric actuation to move micro-machined parts [6]. The first RF MEMS switch was presented in 1991, fabricated on a GaAs substrate [7]. MEMS devices are fabricated through use of various technologies, including silicon-micromaching, surface micromaching, LIGA, and thin film technology [8]. MEMS devices may be fabricated simultaneously with the RF circuitry, or they can be fabricated on separate substrates and later incorporated into the finished RF device using batch transfer integration [9]. This allows complete decoupling of the processing and independent optimization of the MEMS components and RF circuits and transmission lines [9].

MEMS devices may be used in place of traditional solid state components that require high power consumption and a high manufacturing cost. In addition, there are many applications where MEMS devices offer improved performance over existing technologies. This is especially evident in RF applications, where the characteristic small "on" resistance and small "off" capacitance are well suited for high frequency applications [6]. Compared to semiconductor devices, RF MEMS offer a drastic reduction in insertion loss, as well as increased linearity and reduced signal distortion [10-11]; however, disadvantages include increased actuation voltages, slower switching

speeds, and limited power handling. Table 1.1 summarizes characteristic RF performance of electrostatically actuated RF MEMS devices in addition to existing PIN-diode and FET based technologies [1].

Table 1.1. Comparison of performance of RF MEMS, PIN-Diode, and FET technologies for RF applications.

	RF MEMS	PIN Diode	FET
Control Voltage (V)	20-80	~5	~5
Control Current (mA)	0	~20	0
Control Power (mW)	~0.1	10-100	~0.1
Cutoff Frequency (THz)	80	4	2
Isolation (1-40 GHz)	Very High	High/Medium	Medium/Low
Insertion Loss (dB)	~0.2	~1.2	~2.5
Switching Time	~200 μs	~100 ns	~100 ns

From this table, RF MEMS are seen to require the low control power of FET technology, while offering much improved insertion loss and isolation.

When used in a RF system, a single MEMS component replaces and outperforms an entire solid-state circuit [6], as they offer lower power consumption and increased functionality in applications where a high degree of frequency agility and sharp filtering is critical. However, hysteresis and stiction must be considered [12-13]. In comparison to macroswitches, MEMS devices offer decreased size and reduced operating power, yet

have the disadvantages of limited contact force.

There are two common divisions of RF MEMS switches, i.e., series and shunt switches, which differ depending on the mechanism of signal routing. In a series switch, such as in the Rockwell Science Center MEM relay, a movable element acts to short or complete continuity in a transmission line, as shown in Figure 1.3 [14]. In a typical MEMS RF series switch, a movable conductive element such as a cantilever is actuated by electrostatic forces, typically by a pull-in electrode which acts to overcome the elastic restoring forces of the cantilever hinge [12-13]. In another approach a push-pull electrode system is utilized in which the pull electrode attracts the conductive cantilever to close the transmission line, and the push electrode acts to repel the cantilever in the open state for improved isolation [4]. Series switches make direct metal contact, so this design can be used in low frequency applications without compromising performance.

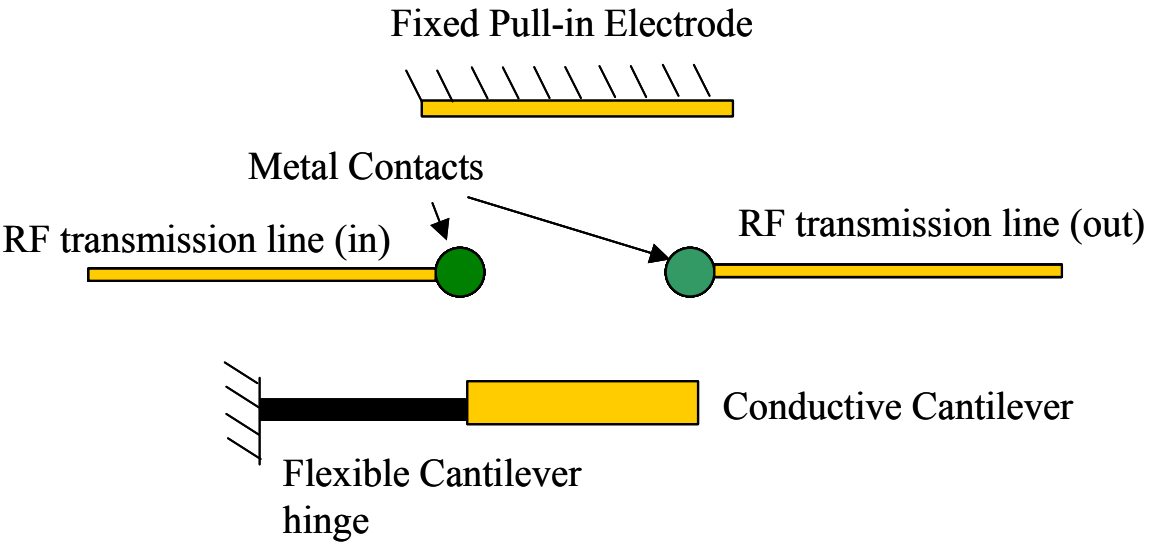

Figure 1.3. Simple schematic of RF MEMS series switch.

In a RF MEMS shunt switch, such as the Raytheon switch [15], the RF signal is routed through the transmission line without activating an electrode. A grounded conductive element is offset from the transmission line by a dielectric layer and some gap distance of air, as shown in Figure 1.4. This air gap results in a relatively small off-state capacitance, which corresponds to a high impedance path for the RF signal to ground. However, application of an electrostatic force on the grounded conductive element causes the cantilever to act as a variable capacitor, resulting in potentially orders of magnitude increase in capacitance between the conductive element and transmission line. This increased capacitance greatly reduces the impedance for the RF signal through the beam and effectively shorts the RF signal to ground [1]. Another figure of merit for shunt switches is the cutoff frequency, which is the frequency at which the impedance in the on state, i.e., the resistance of the transmission line, is equal to the impedance of the RF signal to ground, i.e., the capacitive reactance, in the off state [16]. This is given by Equation 1.1.

$$f_{cutoff} = \frac{1}{2\pi R_{on} C_{off}} \tag{1.1}$$

As shown in Table 1.1, MEMS become more attractive at even higher frequencies as the cutoff frequency of RF devices is over an order of magnitude greater than existing solid state technologies [1].

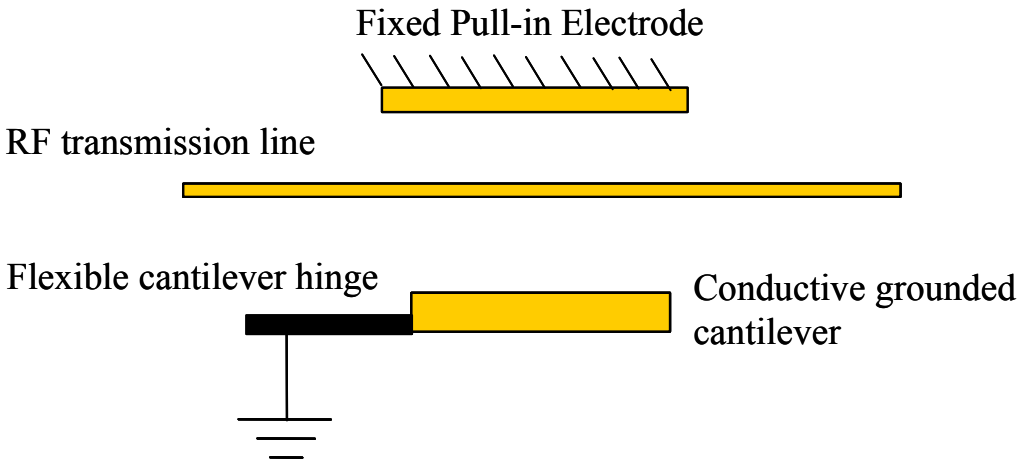

Figure 1.4.Schematic of a RF MEMS shunt switch.

RF MEMS shunt switches offer better hot-switching performance and lower insertion loss than series switches; however, the frequency dependence of the impedance through the beam limits high performance for high frequency RF signals. In fact, for low frequency RF signals (< 5 GHz), series switches which utilize metal / metal contact offer superior performance [1].

Electrostatically activated cantilever beams have been used as variable capacitors [10, 12-13,15,17], relays [18-19], and microfluidic valves [20-21]. In particular, MEMS variable capacitors have recently become an attractive alternative technology for phase shifters and tunable filters, owing to advances in tuning range and high quality-factor Q [10].

In a variable capacitor, a movable top electrode acts as one plate of the capacitor, and the fixed-position bottom electrode acts as the other plate. A potential difference between the bottom electrode and the movable beam (top electrode) is applied, resulting in a charge distribution between the two electrodes. The balance between an attractive, electrostatic force and a mechanical, restoring force controls the position of the top electrode. A problem occurs when the nonlinear electrostatic force overcomes the mechanically elastic, upward force and causes the beam to become unstable and snap-down [12-13].

This snap-down instability problem generally occurs early in the movement of such a device from its initial position and therefore severely limits the tunable range of the actuator. A one-dimensional spring model can illustrate this action, and further details of this analysis can be found in Appendix B.

A large tunable range between the electrodes translates into a larger capacitance range when the device is used as a variable capacitor. Therefore, an extended tuning range is highly desired. Methods have been introduced to extend the tuning range of electrostatic actuators. Hung and Senturia present two techniques of extending the tuning range [22]. In one method, leveraged bending, an electrostatic force was applied to a portion of the beam, and the rest of the beam was used as a lever to position specific parts of the beam through a large range of motion [22]. A small electrode was placed near the anchors and did not cover the entire area of the beam. While the portion of the beam that experienced the electrostatic force moved less than 1/3 (point of instability) of the initial gap distance

downward, the tip of the beam moved the full distance. The leveraged bending technique is very sensitive to the residual tensile stress in the beam [22]. When a beam has a high tensile stress, the portion of the beam that acts as a lever remains flat and decreases the motion of the entire beam. In the strain stiffening method [22], the tensile stress in the beam increases upon application of an applied voltage because of increasing strain. This makes the beam become stiffer with deflection and enhances the tuning range. Another attempt to extend the actuator tuning range makes use of multiple electrodes, each either involved in an attractive or repulsive interaction with the movable element. A change in capacitance of 87% has been reported using this approach [23].

Chinthakindi demonstrated fabrication of cantilevers composed of a single metal with a stress gradient in the through-plane direction. By varying the grain size of the gold, different stressed states of stress were used in a stack to generate out of plane curvature [12,13]. However, the stress profile was independent of position along the beam length, and the observedtuning range was less than 20%. In chapter 3, a significant increase in tuning range is demonstrated through formation of a stress gradient in two directions: along the length of the beam (in-plane), along with the more traditional through-plane gradient. This lithographically patterned hard gold shape changes the pull-in characteristics of the beam. The effect of temperature on the operation of these devices was also investigated. Since the devices are made from all gold, little effect of temperature was anticipated. In addition, a general approach to improved electrostatic beam performance is demonstrated. One target application is RF MEMS actuators. It should be noted that the low-stress, soft gold and the high-stress, hard gold are widely

used in the electronics industry. The mechanical properties are controlled by grain size of the gold. The grain size is highly stable with time and has been in wide-scale use for decades [24].

Electrostatic actuators have the advantage over most magnetically actuated devices in that they require no current and low continuous power in supplying a constant voltage to hold the desired state of the switch. However, electrostatic forces fall off as the gap distance squared, and consequently, actuation over large gap distances requires high voltage. Magnetically actuated MEMS are able to function over larger gap distances since an increase in the magnetic torque or force generated can be achieved by increasing the magnetic volume. There are two common actuation mechanisms used by a majority of magnetic MEMS devices. The first approach is to create a magnetic torque acting on a magnetic element that aligns the magnetic material with some applied external field. Judy and Muller developed magnetically actuated cantilevers that were individually addressable by in-plane coils [25]. The shape of the ferromagnet had a significant influence over the magnetization direction, confining the magnetization vector to the plane of the ferromagnet. The in-plane coil produced a magnetic field, and the cantilever beam rotated towards alignment with the external field, minimizing the energy of the system. In addition, Judy and Muller developed a comprehensive static actuation model [25]. Ahn and Allen developed an early magnetic actuator with a multilevel meander magnetic core [18], and Taylor and Allen later improved the design to achieve < 50 mΩ contact resistance with > 100 μN contact force [19]; however, the "dead legs" and small actuation distances, limit its use for many applications, including high-performance RF

switch applications where greater isolation and reduced insertion loss are valued. The second approach makes use of a low reluctance path, creating a force on the device to close this low reluctance path. The device remains held in a given state until another external force acts to the device. Wright et al. [26] developed a high force actuator using this method. Also, Companu et al. [21] developed a bistable microvalve that latches in order to close one of two low reluctance paths, using a patterned coil to switch the device. However, many of these designs do not lend themselves to large actuation distances. Additionally, the very nature of a low reluctance core requires a large volume of ferromagnetic material be placed in the electrical path, potentially degrading electrical performance and increasing thermal stresses at elevated or cryogenic temperatures. One benefit of the Companu design is the reduced power consumption of the device, owing to its bistability. Devices exhibiting latching, bistable behavior require power during switching of the device state. This is a desirable behavior for devices to be used in cryogenic environments, where power dissipated to the surroundings as heat is undesirable.

Ruan et al. have successfully developed and demonstrated a mechanism for magnetic latching that requires an external magnetic field and a patterned in-plane coil to control the dynamics of a magnetic cantilever [27]. Bistable behavior is achieved using a permanent magnet to provide the latch, without the need for a low reluctance path. The clear benefit of this approach is that since it is the permanent magnet that provides the latching force, power is only required while changing the latched state of the device. In Ruan's design, a magnetic torque is exerted on a beam having a soft magnetic material

(permalloy) electroplated on a gold seed layer and is held latched by an external magnetic field [27].

Chapter 4 presents the application of these concepts of magnetic bistability to the design of large-throw, energy-efficient MEMS actuators. A current is required to operate the bistable magnetic devices, and while this current supplied during device switching may require a higher peak power, overall energy consumption is reduced. In addition, improvements in the design leading to more energy-efficient short pulse switching (SPS) device are provided. Specifically, this is done through: 1) minimization of the power consumption by identifying a regime where shorter switching pulses can be used, and 2) analysis of the design space for such devices [28].

In chapter 5, different switching mechanisms are demonstrated, including the SPS presented in chapter 4. In addition, the method of fabrication and the electrical and mechanical performance are investigated. The test vehicle used to evaluate this type of actuator was a single pole double throw (SPDT) RF switch since many of the design features we have optimized and would like to examine are inherent in this type of device. The device was constructed between two low-loss alumina substrates, flip-chip bonded together. The magnetic actuator forms a cantilever, which is doubly hinged to a post attached to the lower substrate. The post extends 30 μm above the lower substrate. The actuator provides a transmission path to switch between the two microstrip transmission lines on either substrate [29]. With the exception of the thin layer of Sn/Pb solder bonding the connection posts between the two substrates, the entire electrical signal path,

including the posts, hinges, and contact pads are gold. The ferromagnetic element of the beam is clad on both sides with 3 μm of gold to reduce thermal-induced bending and improve electrical performance. Finally, potential applications of the devices, aside from the high-isolation low-loss RF SPDT switch described in this paper, will be presented.

Chapters 4 and 5 focus on minimizing the switching energy required for magnetically bistable switches using the dual-magnetic field source method introduced by Ruan et al. The reduction in energy has been realized through a combination of lower external magnetic field (~10 mT), increased shape anisotropy in the lithographic patterning of the ferromagnetic material, and reduction in hinge stiffness. The longer devices with the highest degree of shape anisotropy (greatest overall susceptibility) also showed an additional mode of movement after making contact with the substrate.

The presence of beam wiping along the substrate is of value for electrical contacts in MEMS relays and other devices. The act of wiping maintains a cleaner contact, preventing buildup of debris [30]. This movement is designed into the operation of the magnetic switches, and is modeled in chapter 6 [31]. Finally, the successes of this work are summarized in chapter 7, and suggestions for improved designs and new applications are offered in chapter 8. Appendix A is provided as a reference to some of the recurring concepts of magnetic materials involved in this thesis, and Appendix B provides relevant and detailed calculations and derivations.

CHAPTER 2

EXPERIMENTAL

2.1 Microelectronic Processing

Microelectronic processing was used to fabricate both the electrostatic and magnetic actuators presented in this document. The fabrication was performed in the Microelectronics Research Center clean room on the campus of the Georgia Institute of Technology in Atlanta, Georgia. The electrostatic actuators were processed on 4-inch silicon wafers, and the magnetic actuators were fabricated on 3-inch alumina squares 5 mils in thickness from CoorsTek.

2.1.1 Metallization

Thin film deposition of Cu, Ti, and Au was achieved using a CVC DC Sputterer. This unit was pumped down to 5 (10^{-6}) torr, and then pressurized to 6 (10^{-3}) torr with argon prior to deposition. This technique deposits metal films on all sides of the sample, including sides not directly aligned to the source. This instrument has the advantage that multiple wafers could be processed simultaneously by use of a rotating sample platform. A CVC Electron Beam Evaporator was also used for metal deposition of Ti, Cu, and Au. This tool operates at 5 (10^{-7}) torr, and due to the enhanced mean free path of the metal,

deposition occurs predominantly on the sample side facing the source. Using this instrument, substrates had to be processed individually; however, the evaporator often proved to be more reliable and was used more often with high-value samples.

2.1.2 Lithography

AZ P4620 positive tone photoresist was purchased from AZ electronic materials and was used for all lithography required for fabrication of the magnetic actuators. The photoresist was spin coated on the alumina substrates using a CEE model 100CB Spinner, and the attached hotplate was used for photoresist curing. The exposure tool used was a Karl Suss MA-6 Mask Aligner. This equipment provided both the front and backside alignment. The 350 W mercury lamp exposed across 220-400 nm wavelengths. A 5-inch mask set from Superconductor Technologies, Inc. was used to pattern the P4620 photoresist. AZ 400K developer was used to clear the exposed regions. An Ultratech Plate Cleaner model 603 was used to perform routine cleaning of the masks.

2.1.3 Etch

An acetic acid (5%) / hydrogen peroxide (2%) aqueous solution was used for etching copper. Buffered Oxide Etch (BOE) was used to etch titanium. A potassium iodide (%) / Iodide (%) aqueous solution was used to etch gold. Acetone was used to dissolve AZ P4620 photoresist. A dicing saw was used to section the completed wafer into individual dies for testing and assembly. Occasionally, wafers were cleaved with a diamond scribe

into manageable pieces for analysis and testing.

2.1.4 Electroplating

Thicker films, such as the gold used in the posts, beams, and transmission lines and permalloy were deposited electrochemically in plating baths. Each electroplating solution was kept in a 4 liter pyrex dish and used on a Corning model PC-620 1000 W laboratory stirrer / hot plate. A 2-inch magnetic stir bar provided agitation for each solution. Current was provided by a Hewlett Packard model E3611 DC power supply, and the bath temperature was measured with a mercury thermometer.

The bath composition for the soft gold plating solution was 40 g/L $KAu(CN)_2$ and 100 g/L KH_2PO_4, as described in [24]. The bath was kept at a pH of 6.5, and agitation was set at 600 RPM. A platinum coated titanium electrode was used as the anode, and the silicon or alumina substrate acted as the cathode where the electrodeposit formed. Electroplating was initiatied once the bath temperature reached 50 ^oC. At a typical current density of 5 mA/cm^2, 30 μm were observed to plate in approximately 100 minutes.

The hard gold electroplating bath was prepared in the same manner as the soft gold bath, with the exceptions of lower pH (pH ~4.0) and the addition of 0.1 g/L of cobalt, as described in [24]. Acidic pH is necessary for appreciable codeposition of cobalt in addition to gold [24]. It is this impurity that changes the grain size of the electrodeposited gold film, as evidenced by a 1-2 μm grain size for soft gold and 225-275 Å grain size for

the hardened gold [32]. This grain size mismatch creates a gradient in the residual stress of a bimetallic soft gold/hard gold layer, and this stress was utilized for inducing curvature in gold cantilevers, as described in chapter 3. Hard gold was deposited at room temperature and at a current density of 5 mA/cm^2. Typical plating rates were 0.2 μm in approximately 45 seconds. In both gold solutions, the quantity of gold electroplated mustbe calculated so that it can be replenished in solution by addition of $KAu(CN)_2$.

Permalloy, an alloy of approximate composition 80% Ni and 20% Fe, was codeposited from an aqueous solution of nickel and iron ions. The permalloy bath composition is as follows: 200 g/L of $NiSO_4 \cdot 6H_2O$, 5 g/L of $NiCl_2 \cdot 6H_2O$, 25 g/l of H_3BO_3, 8 g/L of $FeSO_4 \cdot 7\ H_2O$, and 3 g/L of $C_7H_4NO_3SNa \cdot 2H_2O$. The bath was kept at a pH of 4.0, and agitation was set at 600 RPM. A Nickel anode regenerates the nickel lost during electroplating, but iron must be added back to replenish the electroplating bath, as the concentration of iron in solution greatly influences the rate of deposition. A magnetic field was not applied during electrodeposition, as is often reported. Electroplating proceeded once the bath temperature was 40 ^oC, and typical plating rates were 12 μm in approximately 20 minutes. Energy Dispersive Spectrometry (EDS) confirmed the desired alloy composition was deposited.

2.2 Analysis

A Tencor Alphastep-500 profilometer was used to measure the surface profile of photoresist and metal thin films. This instrument was used to confirm the thickness of electroplated films and to determine when open areas in thick photoresist had been sufficiently filled.

High resolution, high magnification digital images of the fabricated electrostatic and magnetic actuators were obtained using a Hitachi 3500H Scanning Electron Microscope (SEM). Diced samples were attached to an angled sample mount using carbon tape.

A Hysitron TriboIndenter was used to apply small forces to various actuator designs for investigation of buckling and for determination of cantilever stiffness. The nanoindenter consists of a small movable tip that measures the magnitude of the small forces necessary to move such a device over small deflections. Samples were mounted on a magnetic stage. The indenter can be operated in one of two modes. In displacement mode the user defines a displacement ramp, where the indenter tip makes contact with the sample and moves it over the input range. The software measures the force applied to the tip at each position, and produces a graph of force versus displacement. In load control, the user inputs a range of force to apply, and the software plots the corresponding change in sample position.

2.3 Modeling

Simulations of the electrostatic actuators were performed using MEMCAD CoventorWare modeling package version 2002.3 from Coventor, Inc. This finite element solver permitted the user to obtain solutions to systems where both the electrostatic and mechanical solutions were coupled. This was required for simulation of the electrostatic actuators fabricated in this work, as the mechanical solution, i.e. position profile of the cantilever, determines the boundary conditions for the electrostatic solution. The element type used for the modeling of the electrostatic actuators were Manhattan bricks, parallelepipeds each measuring 5 μm by 5 μm in the plane of the cantilever and 1 μm in thickness. This element size was chosen after performing a mesh refinement study on a sample electrostatic actuator. The element size was chosen initially to be larger and then was reduced until variations in the solution with decreased node size were no longer observed. This allowed accurate solutions to be obtained using the fewest number of elements, since computation time increases greatly with the number of elements. Each brick element contained 27 nodes, at endpoints and midpoints of each element edge. During simulation, the edges of the Manhattan brick were allowed to bend so that a smooth solution to the cantilever surface was possible. Larger elements were used for the pull-in electrode and the dielectric layer, since these layers were static.

2.4 Electrostatic Actuator Testing

The electrostatic actuators were measured and tested in a low-temperature microprobe station (MMR Technologies), shown in Figure 2.1. This apparatus is configured with four probe assemblies capable of x, y, and z movement. The probing station allows testing of the CVC sample at temperatures as low as 77 K and as high as 400 K. The heating and cooling functions are provided by an MMR refrigerator, which is housed in the main vacuum chamber. The refrigerator operates on 1800 psig nitrogen. A printed resistor on the end serves as the heater, and a silicon diode monitors the temperature. The cold-end is mounted to the surface of the glass and electrically connected to a software based K-20A temperature controller supplied by MMR. The refrigerators operate on the Joule-Thomson effect. When the nitrogen expands through a capillary tube at high pressure, the gas cools. At room temperature, the magnitude of the effect is small (0.1 K/atm for nitrogen). Allowing the expanded, cooled gas to pass through a countercurrent heat exchanger, precooling the high-pressure gas coming in, can increase this cooling effect. Cooling continues until the heat load to the cooled end of the heat exchanger limits the temperature drop. As the nitrogen gas passes through the capillary tube, the pressure drop results in cooling of the device, and the nitrogen liquefies. The liquid nitrogen absorbs heat from the examined device, and the nitrogen vaporizes. The vapor flows back through the heat exchanger and cools the incoming gas. Before flowing into the heat exchanger, the nitrogen flows through an ultra high purity reversible filter, which filters out any condensate or impurities in the gas. The probe station, shown in Figure 2.1, was evacuated with a Pfeiffer Vacuum TCP 015 turbo pump.

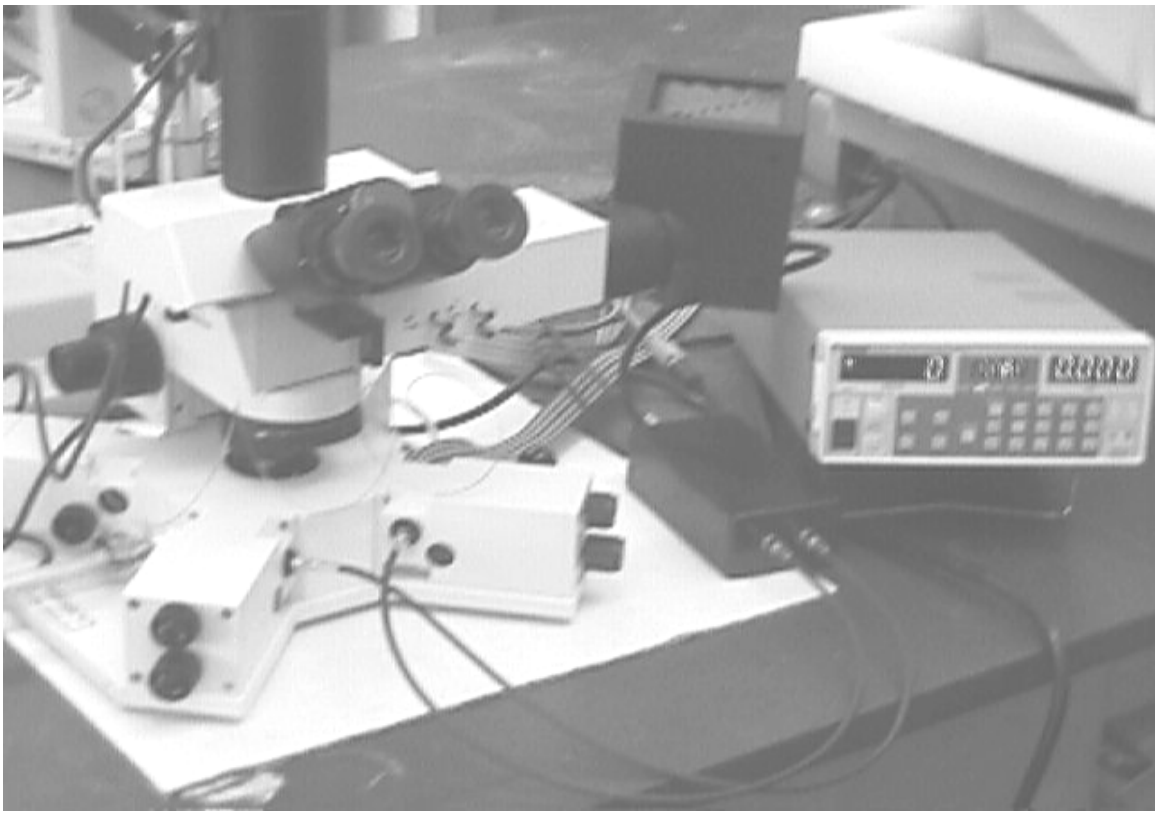

Figure 2.1. Experimental setup for testing of electrostatic actuators. A high voltage is delivered to the vacuum probe station, and the sample is observed with a microscope through a viewing window.

A high voltage power supply was available to deliver large potentials across the CVC devices for testing. The position of the cantilever beam was measured and viewed with an optical microscope through a quartz window on the top of the probe station. Figure 2.2a,b show sample images of the electrostatically actuated devices as seen by the experimenter. In Figure 2.2a, a double-hinged elliptical-end device is shown. In addition, two sets of electrodes are observed. The electrode close to the beam hinges is the DC pull down electrode, while the electrodes under the beam tip were designed for RF testing. Two probes are observed in both 2.2a and 2.2b, through which a potential is applied across the device. The applied voltage creates an electrostatic attraction between the cantilever and the aluminum DC electrode. In Figure 2.2a, no voltage is applied, and the beam shape is observed to extend out of plane of the substrate, with greatest curvature occurring near the elliptical end of the device. In this state, a low capacitance is present between the device and the RF electrodes. With application of a larger voltage, the beam is brought into intimate contact with the BCB dielectric film covering the electrode (as shown in Figure 2.2b), and the largest device capacitance is achieved.

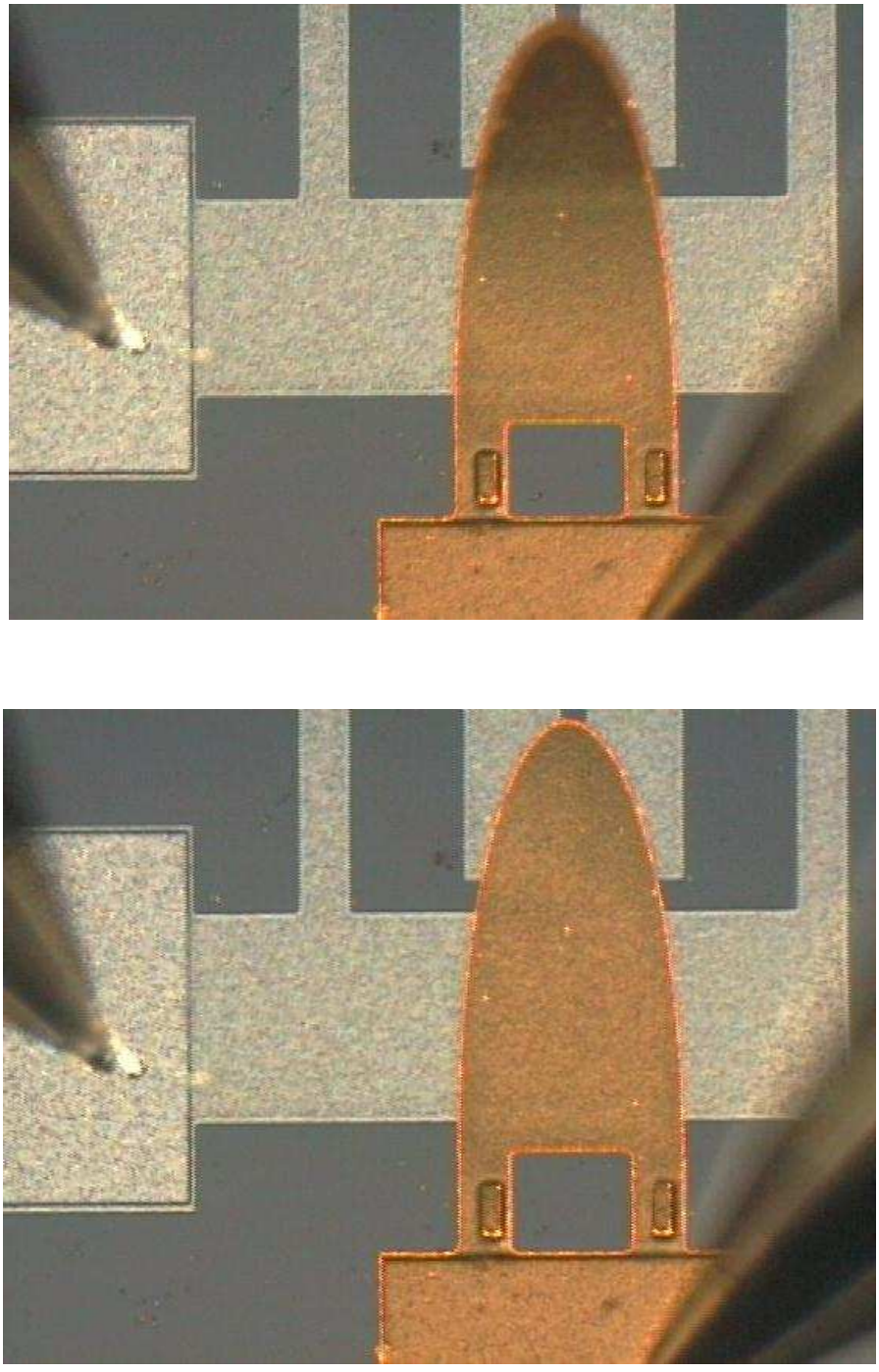

Figure 2.2. CVC device during testing. A potential is applied across the device by means of the two probe tips in contact with electrodes on the left and bottom of the two images. A) shows an elliptical double hinged device in the upstate (note curved tip), while b) shows the device pulled down flat into contact with the dielectric.

2.5 Magnetic Actuator Testing

The magnetic actuators were tested individually on a SUSS Microtec PM5 probe station shown in Figure 2.3. An E-16-260 Tubular electromagnet (2 5/8 inch diameter) from Magnetic Sensor Systems was utilized to provide the variable external field required to move the actuators over their range of motion. The 30 Ω electromagnet was powered by a Topward DC model 33010D power supply, and the electromagnet provided magnetic fields from 0 to 100 mT. Calibration of the magnetic field as a function of input current and position was achieved using a 3-axis Hall Teslameter from GMW Associates. Both vertical hinge movement and lateral motion of the beam tip were measured using an Mitutoyo optical microscope. Digital imaging was provided using a Moticam 480 color camera. The probe tips were each capable of motion in the x, y, and z directions. The probes were each held to the platform by vacuum provided by a Welch model 2522B-01 3.1 Amp vacuum pump.

Testing was performed on many samples using an optically clear thin glass substrate in place of the top alumina substrate. The gold microfabricated actuation coils were printed on these glass substrates. The desired 100 μm offset between the alumina and glass substrates was achieved by applying an aqueous solution of 100 μm diameter polymethacrylate spheres from Fluka at several points on the bottom substrate. Once the solvent evaporated, a single-level matrix of polymethacrylate spheres remained in the applied areas. These spheres provided structural support between the two substrates without bonding to the substrate surface. This permitted relative movements of the two

substrates, useful in aligning the various features on the substrates. The use of a glass top substrate permitted visual observation of the position of the magnetic actuator in response to variable magnetic stimuli from both the external electromagnet and the integrated coils on the glass substrate. Current pulses were supplied to the integrated microfabricated coil through the probe tips. Using two additional probes, a potential was also applied across the switch itself and was monitored by a computer. While the switch was in the upstate, the circuit was open and no current passed across the switch; however, once a sufficient current pulse was provided to the integrated coil, switching speed could be determined by the time difference between the initialization of current pulse to the coil and onset of current flow across the switch in the downstate. Using this method, several operational parameters of the switch were investigated, including: the critical current required to switch the state of the switch as a function of the external magnetic field, the length of the current pulse necessary to switch the device using different switching mechanisms, the time required for the switch to move from its initial state to a new state with acceptable electrical contact, the dependence of the contact resistance between the contact pad and the switch on the external background magnetic field, and the minimum latching external field required to hold the magnetized beam in both stable configurations.

Device reliability and lifetime were investigated by cycling the switch for extended durations. An EG&G PARC model 175 universal programmer was used to apply a square wave potential at frequencies up to 25 Hz across the integrated coil. Contact resistance across the device in both states was monitored for changes in the quality of contact.

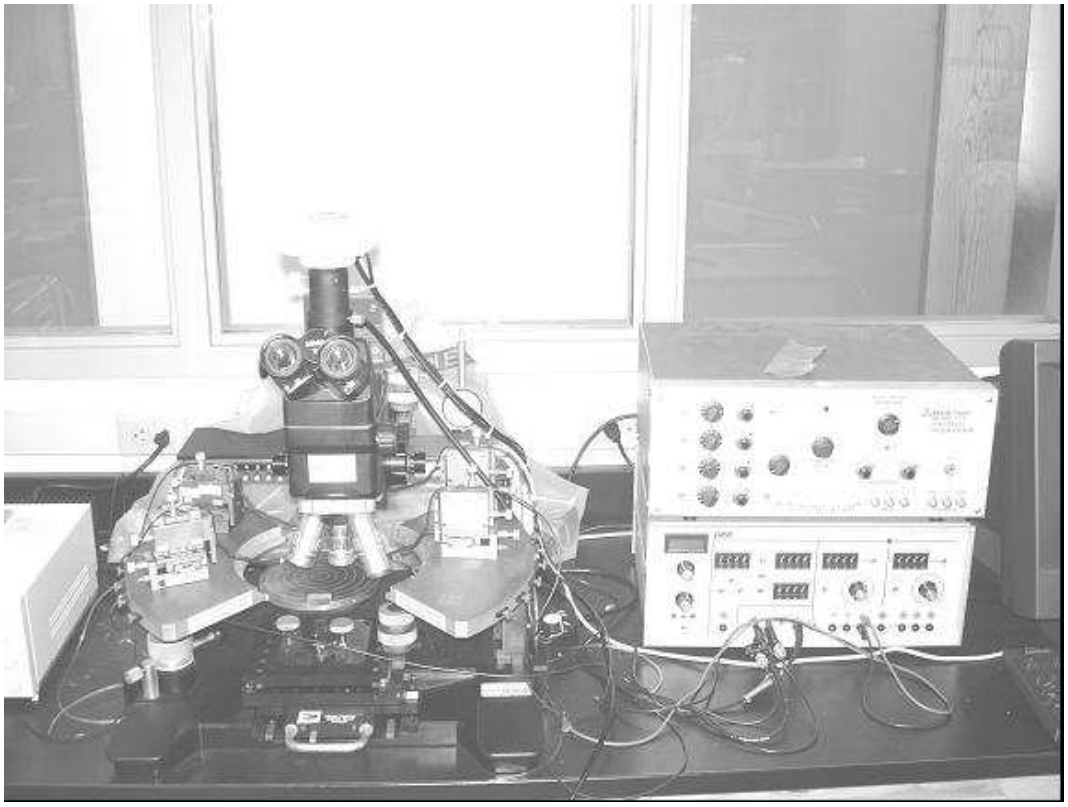

Figure 2.3. Experimental setup for magnetic actuators. A potential is applied across a sample actuator using the waveform generators shown on the right. The potential is delivered to the device on the PM 5 probe station using microprobes while being monitored through the microscope.

CHAPTER 3

IMPROVEMENTS TO CVC TUNING RANGE

The use of MEMS cantilevers as tunable capacitor elements is restricted by the pull-in instability introduced in Chapter 1. Due to the limitations of a pull-in based on a parallel plate configuration, a more complex electrostatic pull-in mechanism is required for extension of the actuator tuning range. The goal of this work was to extend the tuning range of an electrostatically actuated MEMS cantilever. A biaxial stress gradient was demonstrated to be suitable for enabling an unrolling behavior of the cantilever, blending pull-in instabilities into a larger continuous tuning range. A summary of the implementation of the stress gradients and improved performance follows.

A stress gradient was induced in two directions (through the plane of the beam and along its length) to produce a beam deflection of varying curvature. The stress gradient in the through-plane direction was produced by altering the conditions during electroplating and in the in-plane direction through lithographic patterning. The pull-in characteristics of four electrostatic actuator designs were analyzed. The in-plane stress gradient, along the length of the beam, significantly improved the tuning range compared with devices containing spatially uniform stress. This advance has greatly eased the instability problem of electrostatically actuated beams. For example, the stable deflection range of a device with two hinges and a square front improved from less that 33% to 70%, and consequently the capacitance tuning range increased to approximately 100% of the

capacitance in the released state. This advance has been applied to actuators used in RF tuner systems. Voltage cycling impacted the initial cycling of the actuator.

3.1 Theory

A schematic of an electrostatic actuator is shown in Figure 3.1. In this device, a movable top electrode composed of gold acts as one plate of the capacitor, and the fixed-

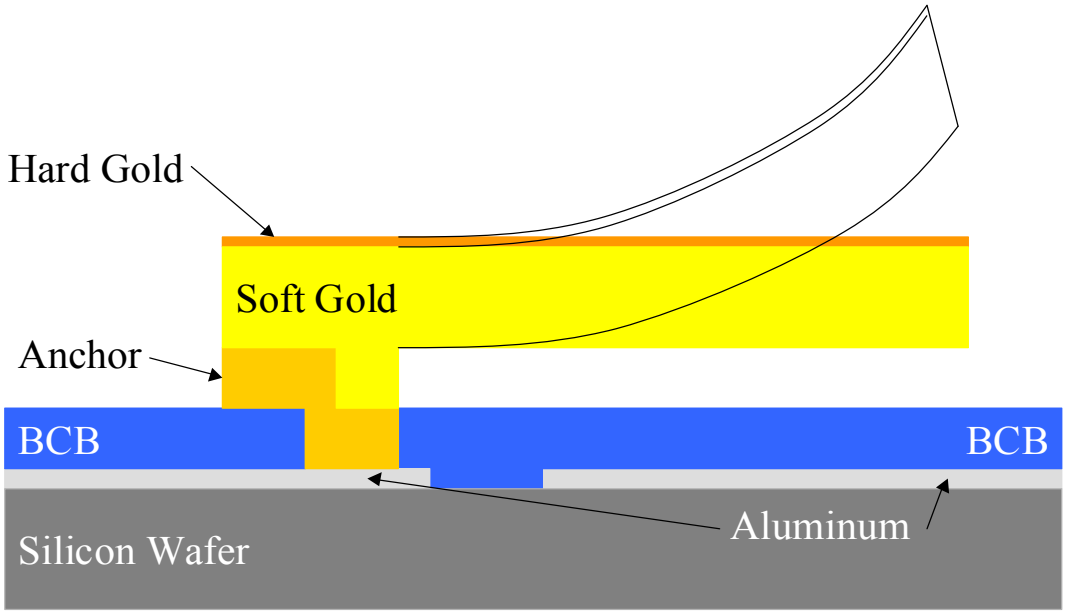

Figure 3.1. Schematic of electrostatically actuated variable capacitor depicting the aluminum bottom electrode and bilayer gold cantilever, separated by a thin dielectric layer of BCB.

position bottom aluminum electrode acts as the other plate. The top electrode is a bimetallic structure that has some positive vertical (y-direction) initial deflection due to internal stresses present in the beam during fabrication. When the top layer of the

bimetallic is at a higher stress state (in tension), release of the structure results in a constriction of the stressed layer and vertical bending of the device. A potential difference between the bottom electrode and the movable beam (top electrode) is applied, resulting in a charge distribution between the two electrodes. The balance between an attractive, electrostatic force and a mechanical, restoring force controls the position of the top electrode. A problem occurs when the nonlinear electrostatic force overcomes the mechanically elastic, upward force and causes the beam to become unstable and snap-down [12-13].

The mechanism of pull-in of the electrostatic actuator is related to the potential for instability, and the details of the pull-in may be greatly influenced by the shape of the released cantilever. In order to determine the expected shape of a cantilever beam, it is necessary to consider the mechanics of the structure. Details of beam theory may also assist in the design of beams with different profiles. For the problem of an out-of-plane displacement due to the internal stress of a thin film (beam), there is no conventional load applied to the beam; however, the internal stresses do produce a moment on the beam. Therefore, the Euler-Bernoulli beam equation is more useful in the form given in Equation 3.1.

$$EI\frac{d^2z}{dx^2} = M(x) \tag{3.1}$$

Where E is the elastic modulus of the beam, I is the moment of inertia, M(x) is the

moment acting on the beam as a function of the x-position, and z is the deflection of the beam as a function of x. This form is applicable to this beam, since there is no y-directed external load from which to calculate bending moments; however, it is possible to obtain a form for the moment acting on the beam through analysis of the beam stresses.

The beams of interest in this study are fabricated with two layers of gold with different internal stresses, creating a stress gradient through the thickness of the beam. The initial curvature of the beam can be established by modeling it as a bimetallic structure, where both layers have elastic properties of gold, but different initial stress states. Consider a bimetallic structure of length L, width w, and thickness b, composed of a highly stressed layer of stress σ_1 and a bottom substrate of stress σ_2. A rectangular coordinate system is set up with the x-direction along the length of the beam, the y-direction along the in-plane thickness of the beam, and the z-direction along the through-plane width of the beam.

Assuming a linear stress gradient vertically throughout the entire beam, and uniform top layer, Equation 3.2 represents the stress at any point in the pre-released beam, shown in Figure 3.2a.

$$\sigma\,(\mathrm{y}) = \frac{\sigma_1 + \sigma_2}{2} + \frac{\sigma_1 - \sigma_2}{\mathrm{b}}\,y \tag{3.2}$$

The vertical distance from the centerline of the structure is y. Since the first term in this

expression is constant for all beam positions, it may be dropped from our analysis. This is due to the fact that it is not the magnitude of the stresses but the difference between their values that gives rise to the deflection of the cantilever.

In the case where the upper, more highly stressed layer is not spatially uniform, the analysis changes, as shown in Fig. 3.2b. The vertex of the triangle begins at the hinges and extends out to the end of the beam. In this way, a larger y-axis stress gradient exists at the tip of the beam than at the hinge. In particular, the slope of the stress profile at the tip is identical to that of the uniformly stressed beam, but vanishes at the hinge, resulting in a curvature of the beam that increases along the beam length. This triangular hard-gold pattern is one example, a demonstration, of the two-axis stress gradient approach. Many other patterns could be used, depending on the particular application. In the fabrication of the newly developed structures, the stressed layer was patterned so as to create a linear variation in the through-plane stress (y-direction), along the length of the beam (x-direction). As mentioned in the introduction, a lithographic patterning method was used to demonstrate this desired stress gradient in the x-direction; however, many alternate approaches can be considered. The upper, stressed gold layer was deposited in the shape of a triangle (Figure 3.1b). The beams depicted in Figure 3.1 are flat, but the stress profiles drawn are for the equilibrium condition with the cantilevers released. The equation for stress was modified to represent this new geometry where the stress difference linearly increases from zero at $x = 0$ and attains a maximum value at $x = L$.

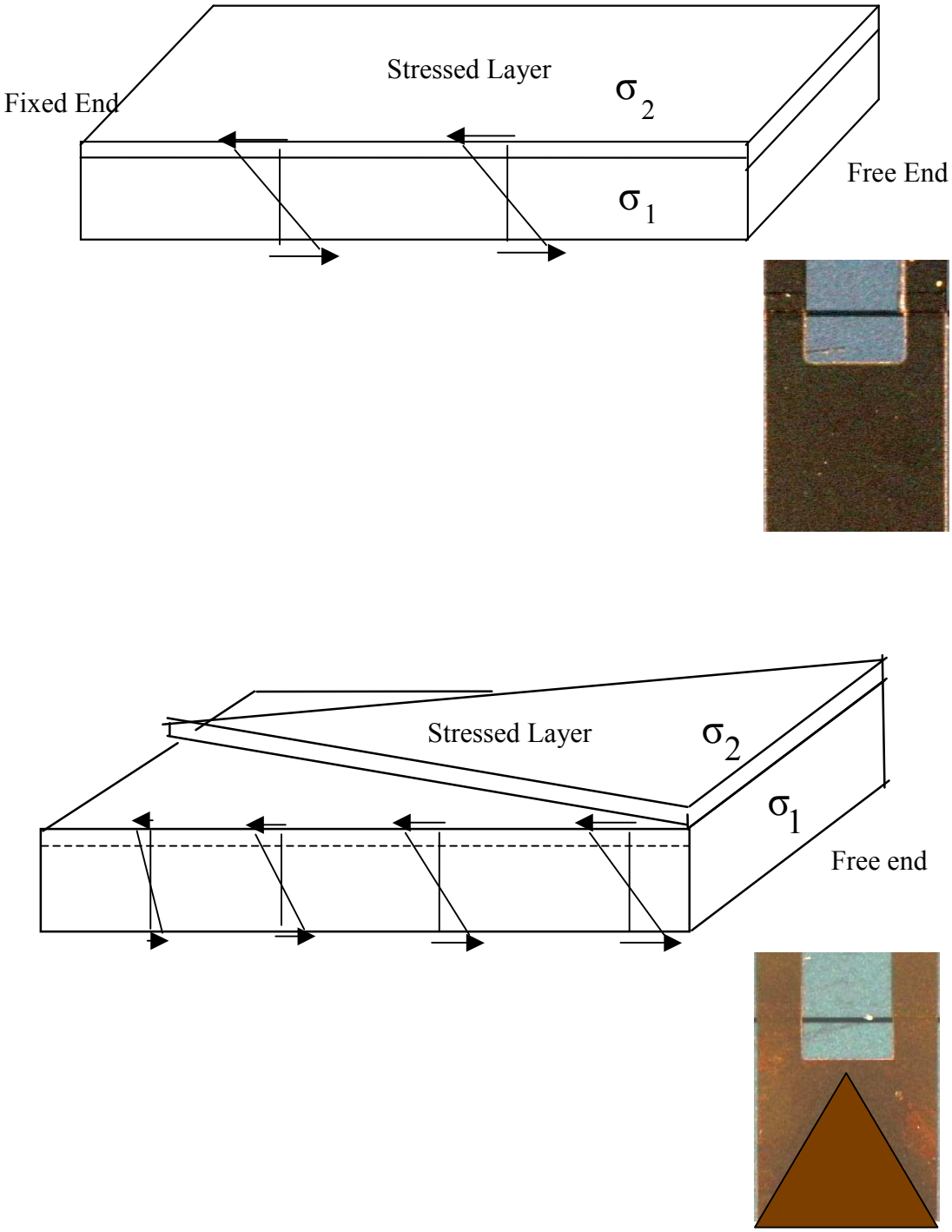

Figure 3.2. Diagram of stress profile for both a) uniform hard gold and b) patterned hard gold.

Equation 3.3 shows the representation of stress.

$$\sigma(y,x) = (\sigma_1 - \sigma_2) \cdot \left(\frac{y}{\mathrm{b}}\right) \cdot \left(\frac{x}{\mathrm{L}}\right) \tag{3.3}$$

Integrating to find the total moment results in Equation 3.4.

$$M(x) = \int_{-b/2}^{b/2} dM = \int_{-b/2}^{b/2} y \cdot dF = \int_{-b/2}^{b/2} y \cdot \sigma(y,x) \cdot w \cdot dy \tag{3.4}$$

$$= \int_{-b/2}^{b/2} (\sigma_1 - \sigma_2) \cdot \left(\frac{y}{\mathrm{b}}\right) \cdot \left(\frac{x}{\mathrm{L}}\right) \cdot \mathrm{w} \cdot y \cdot dy = (\sigma_1 - \sigma_2) \cdot \frac{\mathrm{b}^2 \mathrm{w}}{12 \cdot \mathrm{L}} \cdot x \tag{3.5}$$

Note, the stresses are in plane with the beam, and the moment calculated is due to integrating the value of this in-plane stress through the y-direction [17]. For the analysis of the beam with the patterned stressed layer, the moment varies linearly with the x-position of the beam, as shown in Equation 3.5. It should also be noted that the thickness of the beam, b, varies linearly along the beam length as $b(x) = b_0 + \frac{x}{L} b_s$, where b_0 is the thickness of the soft gold layer and b_s the thickness of the stressed gold layer. Therefore the moment of inertia of the beam, I, also varies along the beam length, $I(x) = \frac{1}{12} w[b(x)]^3$. From this analysis, Equation 3.1 takes the following form.

$$\frac{d^2 z}{dx^2} = \frac{(\sigma_1 - \sigma_2)}{E} \frac{x}{b_0 L + x b_s} \tag{3.6}$$

Solving Equation 3.6 subject to the boundary conditions of zero slope and zero deflection at the fixed end, the following expression for deflection, d(x), of the cantilever beam is obtained.

$$d(x) = \frac{\sigma_1 - \sigma_2}{Eb_0 L}\left(\frac{x}{a^2} + \frac{x^2}{2a} - \frac{\ln(1+ax)}{a^3} - \frac{x\ln(1+ax)}{a^2}\right) \qquad (3.7)$$

$$\text{where} \quad a = \frac{1}{L}\frac{b_s}{b_0}$$

When the above results are compared to the results of the analysis performed for a structure with a uniformly stressed hard gold layer, a relationship is developed to describe the differences in beam shape due to the different stressed layer geometry. Equation 3.8 shows the quantitative difference in beam shape for the patterned stress-layered (Figure 3.1) devices and the uniform stress-layered devices [17],

$$\frac{d_{\text{patterned}}(x)}{d_{\text{uniform}}(x)} = \frac{2}{aL}\left(\frac{1}{ax} + \frac{1}{2} - \ln(1+ax)\left(\frac{1}{a^2x^2} + \frac{1}{ax}\right)\right) \qquad (3.8)$$

where $d_{\text{patterned}}(x)$ is the calculated deflection of the patterned hard gold beam as a function of distance x along the length of the beam. For a ratio of hard gold thickness to soft gold thickness equal to 0.1, Equation 3.8 yields an end beam deflection ratio (x = L) of approximately 0.32, about 1/3. This same approach can be used to construct beams of different deflections by proper design of the hard gold pattern.

Equation 3.9, Stoney's Equation, relates the intrinsic stress of the beam to the elastic modulus and beam geometry.

$$\sigma = \frac{E_{sub}}{6(1-\nu_{sub})} \frac{h_{sub}^{\ 2}}{t_{film} R} \tag{3.9}$$

where E_{sub} is the elastic modulus of the substrate, υ_{sub} is Poisson's ratio for the substrate material, σ is the intrinsic stress of the hard gold, t_{film} is the hard gold thickness, h_{sub} is the soft gold substrate thickness, and R is the radius of curvature of the beam. Therefore, if the stress state of the film is known along with the relevant geometrical and mechanical properties, then the curvature of the beam can be calculated. The agreement is good for film to substrate thickness ratios less than 0.1 [33].

3.2 Electrostatic Actuator Fabrication

The processing sequence used to create the electrostatically actuated cantilever beam devices is provided. The process sequence began with the deposition of 1.0 μm of aluminum onto a bare silicon wafer by DC sputtering (3.3A). The aluminum is patterned into electrodes with the first photolithography step (3.3B). BCB polymer (Cyclotene 4022, 25 wt%) was chosen for the dielectric material needed to insulate the bottom electrode. A 1.5 μm layer of BCB was deposited onto the bottom electrodes (3.3C), and the BCB was subsequently patterned. To form the anchor base, a 300 Å layer of titanium

was deposited to aid in the adhesion of 1 μm of gold. An electron-beam evaporator was used to deposit the titanium and gold layers (3.3D).

Shipley 1813 photoresist was spun onto the wafer (over the anchors) to form the 2.5 μm thick release layer. The wafer was then patterned (3.3E), and the seed layer for electroplating was deposited. The seed layer consisted of 300 Å of titanium (adhesion) and 2000 Å of gold. A 2 μm layer of soft gold was electroplated onto the seed layer at a bath temperature of 60 ^{o}C and at a current density of 3 mA/cm^2 (3.3F).

The triangular-shaped hard gold pattern was formed after the soft gold electroplating. Shipley 1813 photoresist was used to protect the hinges and other parts of the device where hard gold was not desired. A 0.2 μm layer of hard stressed gold was electroplated selectively in these opened regions at a current density of 5 mA/cm^2 and at room temperature. The resist selectively covering the plane of soft gold was then stripped in acetone (3.3G). After using Shipley 1813 photoresist again in order to pattern the beam and hinge shapes, the unwanted gold was etched with I_2/KI etchant, and the titanium was etched with an EDTA solution (3.3H). Finally, the beams were released by dissolving the resist with acetone (3.3I). A side view is also shown (3.3J).

After the top electrodes were released, they were treated with two low surface tension solvents, methanol and ethanol, ensuring the removal of water from the surface of the gold. The top electrodes were then exposed to an alkane thiol solution that forms a

hydrophobic, self-assembled monolayer over the gold surface. This prevented stiction of the top electrodes to the bottom surface.

The effects of shape and dimensions of the cantilever beam on its electrostatic movement were investigated. Figure 3.4 shows the layout of four devices that were fabricated, tested, and measured. In this figure, the shape and size of the top electrode, shape of the bottom electrode, and shape of the stressed gold are shown. The hinge configuration, and beam length, width and tip slope were varied to investigate advantages inherent to different geometries. Included are: a double-hinged square device measuring 700 μm on each side (Figure 3.4a), a double-hinged elliptical device 800 μm long and with an initial width of 450 μm (Figure 3.4b), a double-hinged rectangular device 1000 μm long and 500 μm in width (Figure 3.4c), and a fully-hinged rectangular device 1000 μm long and 500 μm in width (Figure 3.4d).

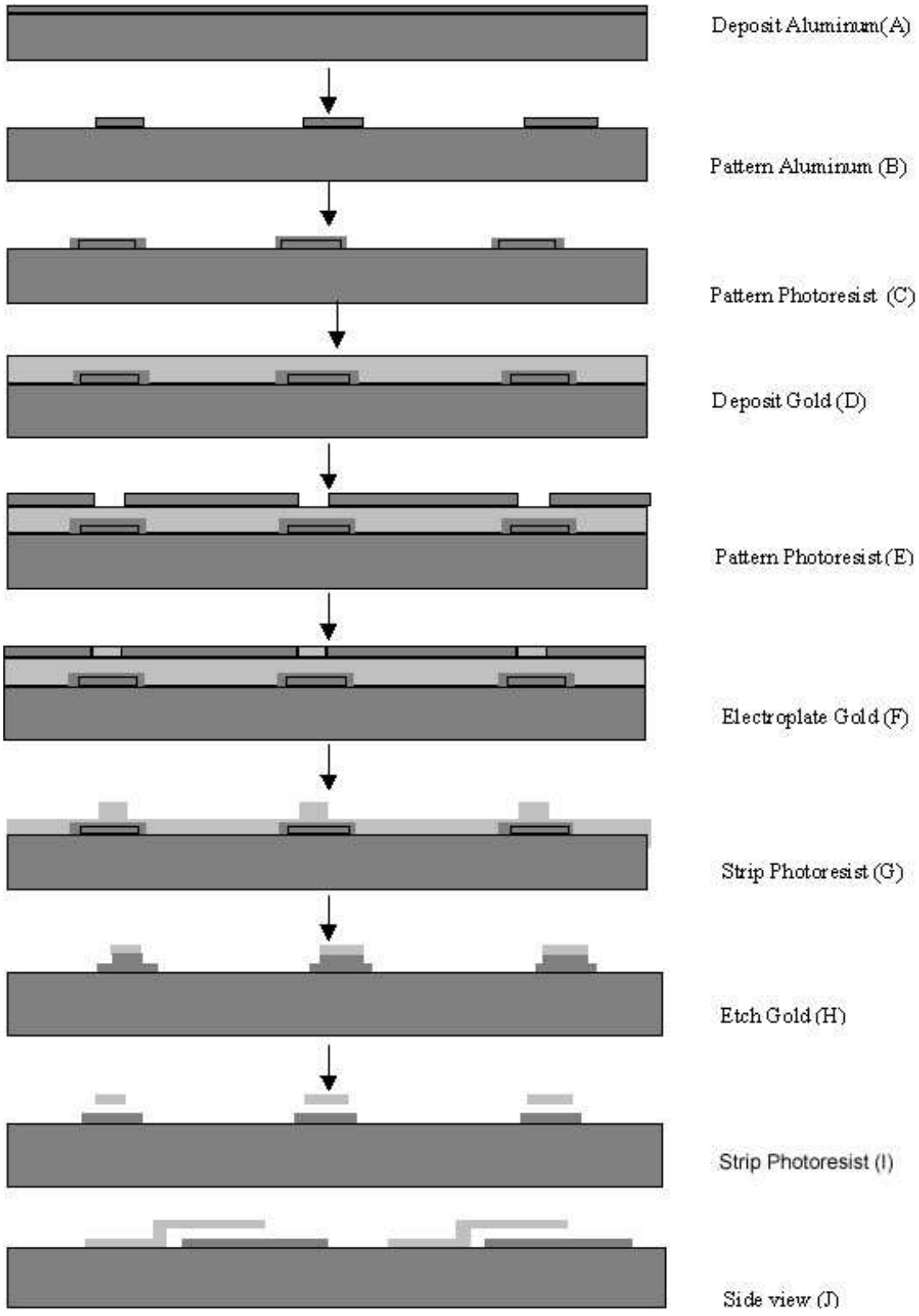

Figure 3.3. Processing steps for CVC device.

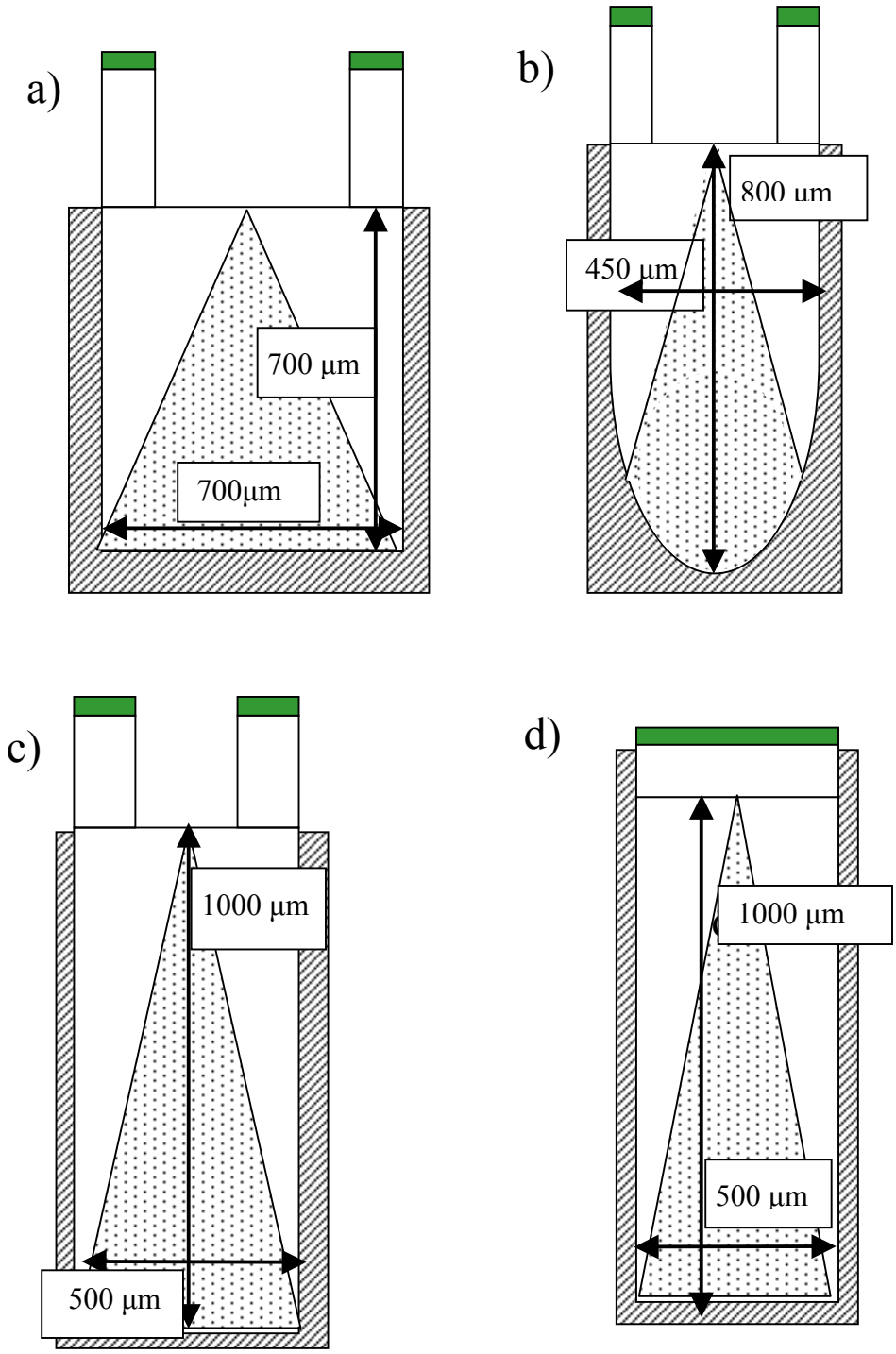

Figure 3.4. The four CVC designs examined in detail, a) double-hinged square, b) double-hinged elliptical, c) double-hinged rectangle, and d) fully-hinged rectangle.

3.3 Results

Figure 3.5 shows a CVC with patterned hard gold coverage. There is a slight coloration difference due to the patterning of the hard gold; however, this distinction is difficult to observe in a grayscale image.

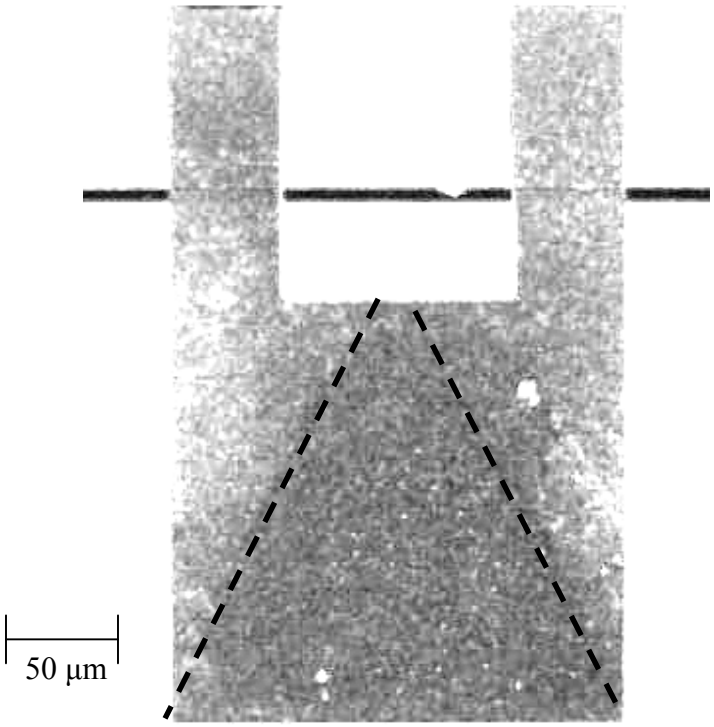

Figure 3.5. Cantilever design with patterned hard gold coverage. The dashed lines indicate the triangular region electroplated with the hard gold.

3.3.1 Device Testing and Measurements: Hinge and Tip Variations

3.3.1.1 Double-Hinged Ellipse

A variety of beam shapes and hinge types were fabricated and measured. The distance between the tip of the cantilever and the bottom electrode (tip deflection) versus applied voltage for a double-hinged, elliptical device (Figure 3.4b) is shown in Figure 3.6. This design was studied to mitigate the problems associated with the sharp corners on the square and rectangular devices. For the uniformly stressed double-hinged elliptical device the initial tip deflection was 250 +/- 5 μm, as shown in Figure 3.6a. As the voltage increased from 0 to 70 V, the tip deflection showed little change. The distance was measured between the midpoint of the end of the beam (x = L and z = w/2) and the substrate. The beam became unstable at 70 V and snapped-down onto the bottom electrode, as shown in Figure 3.6a. Like the double-hinged, square device, the tuning range for the elliptical device with a uniform layer of hard gold was less than $1/3^{rd}$ of the initial displacement. Upon varying the stress gradient along the length of the same shaped structure, the tuning range improved to about 45 percent of the initial deflection. The initial deflection for the double-hinged, elliptical device containing a varying stress gradient was 105 +/- 5 μm, as shown in Figure 3.6c. Upon the application of higher applied voltages between 60 and 160 V in Figure 3.6c, the electrode smoothly pulled down. The beam tip finally uncurled, making contact with the bottom electrode at approximately 170 V. Figures 3.6b and 3.6c show the voltage deflection behavior before

and after cycling of the double-hinged, elliptical device for 500 cycles, respectively. At cycle 500, the beam had a slightly higher initial deflection, resulting in a higher final

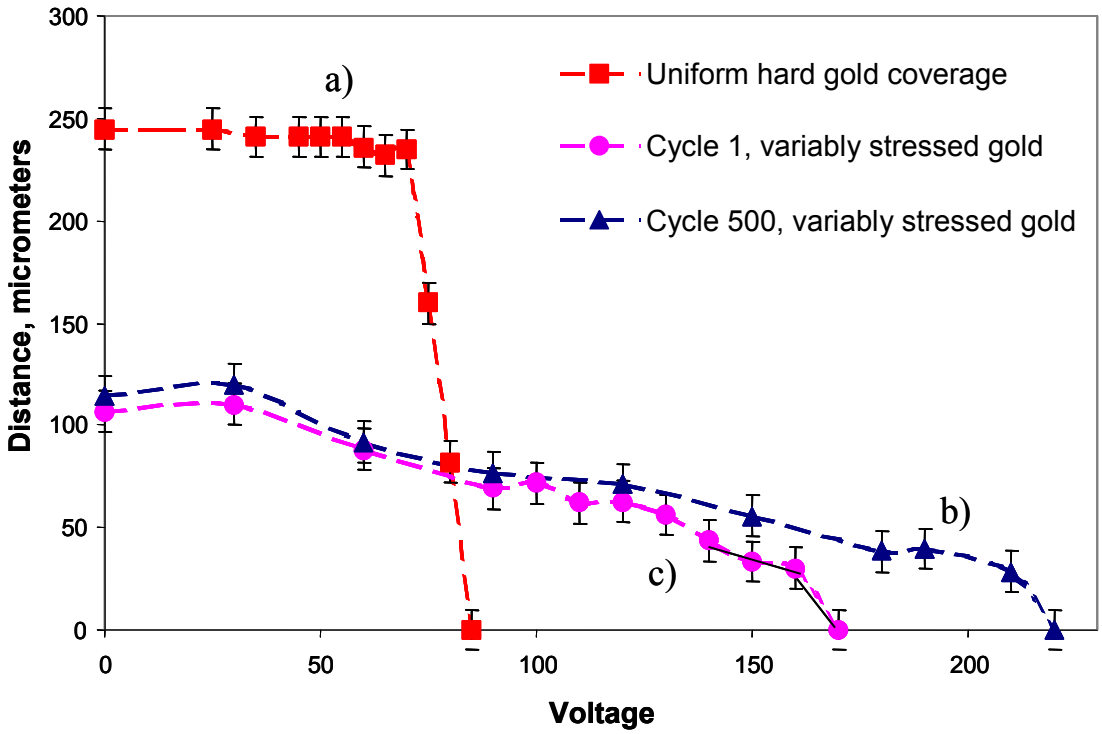

Figure 3.6. Pull-in data for uniform (a) and patterned (b) hard gold elliptical devices, (c) cycling data for elliptical device.

pull-in voltage. This behavior was typical for the metal beams where there was an initial 'break-in' period (first few cycles), followed by a very reproducible deflection versus voltage curve. This is expected because there is no chemical reaction between the layers since they are both gold. Further, the grain structure of the gold layers is known to be stable over long periods of time (30 year reliability of hard gold in electronic uses) [24]. Testing continued up to 10,000 cycles with no observed drift in performance; however, extensive cycling was not investigated.

3.3.1.2 Double-Hinged Rectangle

The next double-hinged beam to be measured was the double-hinged, rectangular device (Figure 3.4c). Figure 3.7 shows the distance between the tip and the bottom electrode (tip deflection) versus voltage for a double-hinged, rectangular device. For the rectangular device with a uniform layer of hard gold (Figure 3.7, curve a), the initial tip deflection was 230 +/- 5 μm. As the voltage increased from 0 to 50 V, the beam moved monotonically to a deflection of 150 +/- 5 μm (approximately x = d/3), after which it snapped down 70 V. Upon varying the stress gradient along the length of the same structure (variably stressed gold), the tuning range improved from 35% to 65% of the possible range (Figure 3.7b). Other devices with the same shape and stress gradient were measured and showed the same tuning range.

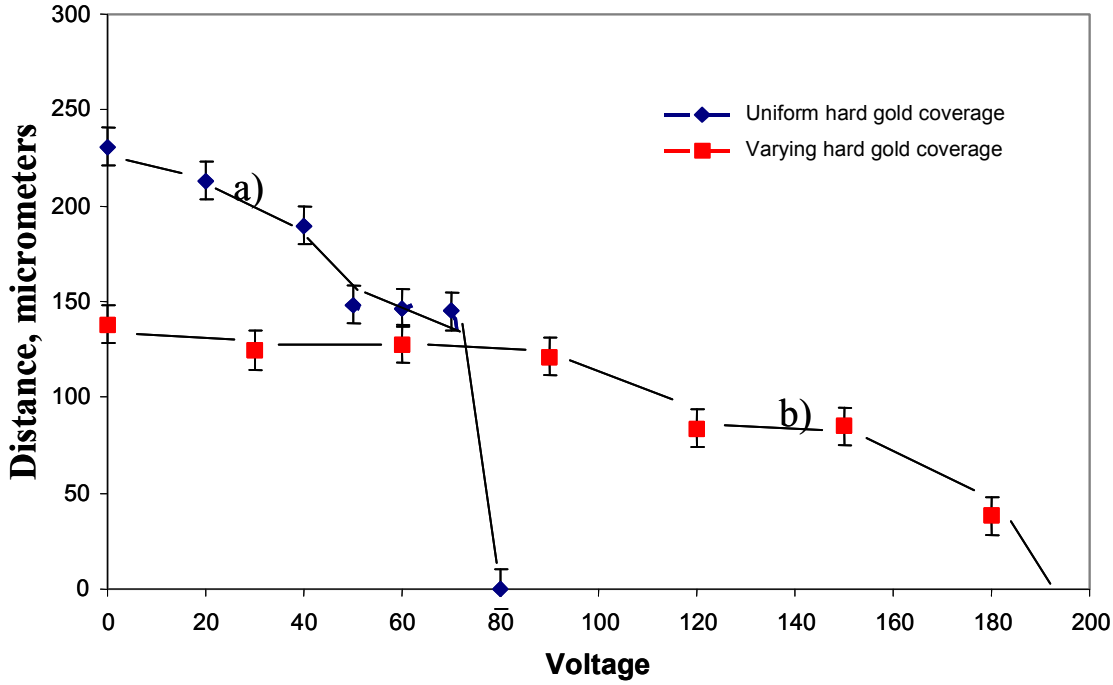

Figure 3.7. Voltage vs. deflection data for double-hinged rectangular device for (a) uniform hard gold and (b) patterned hard gold.

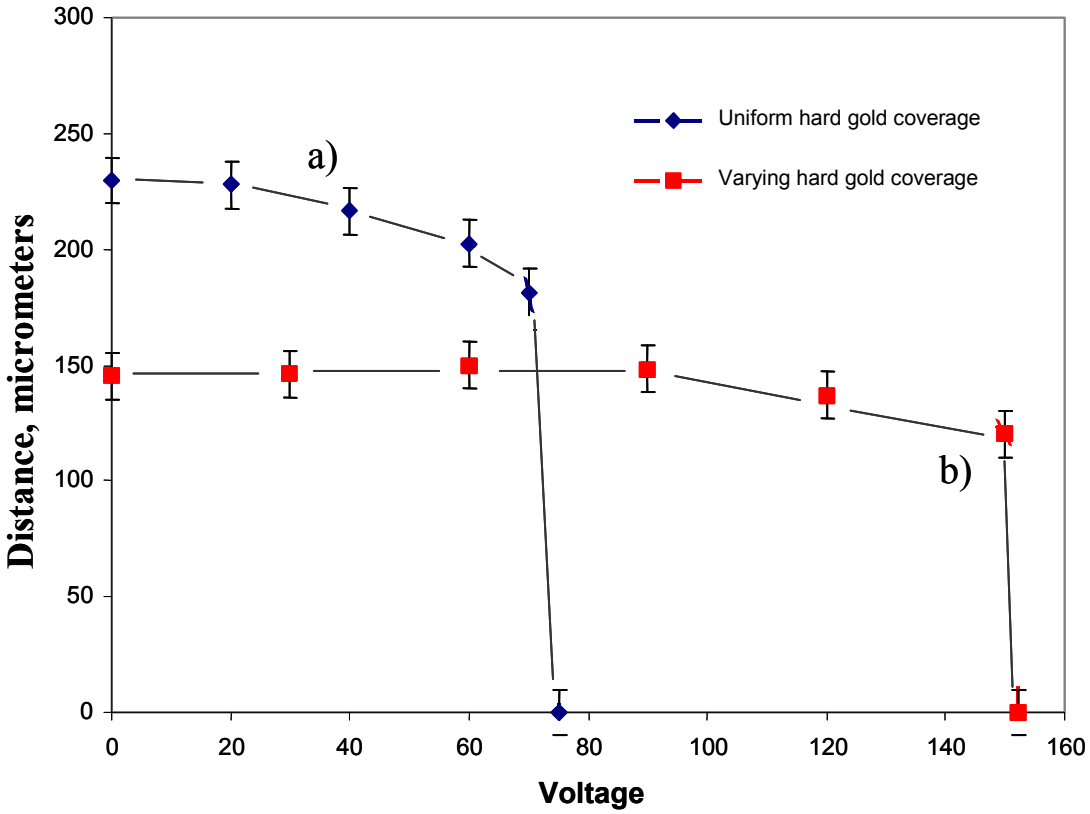

Figure 3.8. Voltage vs. deflection data for fully-hinged rectangular device for (a) uniform hard gold and (b) patterned hard gold.

3.3.1.3 Fully-Hinged Rectangle

The next beam measured was the full-hinged, rectangular device (Figure 3.4). Figure 3.8 shows the distance between the tip and the bottom electrode (tip deflection) versus voltage for a full-hinged rectangle. For the rectangular device with a uniform layer of hard gold, the initial tip deflection was 230 +/- 5 μm (Figure 3.8a). As the voltage increased from 0 to 60 V, the beam moved monotonically to a deflection of 200 +/- 5 μm. The beam became unstable between at 70 V. Upon varying the stress gradient along the length of the full-hinged, rectangular device, the initial tip deflection decreased by about 35 percent to 150 +/- 5 μm (Figure 3.8b). The tip deflection changed slightly with voltage up to 140 V for the variably stressed, full-hinged, rectangle. The beam became unstable at 150 V. The full-hinged, rectangular device with a two-axis stress gradient shows a different deflection behavior than the partial-hinged cantilevers. The difference in behavior can be attributed to the effect of the anchor. The full-hinged, rectangular device has higher rigidity than the double-hinged structures since deflection of the double-hinged structures required bending about an arm of smaller width. In addition, whereas the patterning of the stressed layer introduces curvature along the beam width, this effect is not observed for the fully-hinged devices. Therefore, it is supposed that this 2-D beam curvature greatly increases the impact of the uncurling pull-in, resulting in greater tuning ranges for the double-hinged devices.

3.3.1.4 Double-Hinged Square

The last device studied was the double-hinged square shown in Figure 3.4a. Figure 3.9 shows the distance between the tip and the bottom electrode (tip deflection) versus voltage for a double-hinged, square device. The distance (height) was measured between the midpoint of the end of the beam (the tip) and the substrate. For the uniformly stressed, double-hinged, square device, the initial tip deflection was 205 +/- 5 μm (curve 3.9a). The beam became unstable between 65 and 70 V and snapped-down onto the

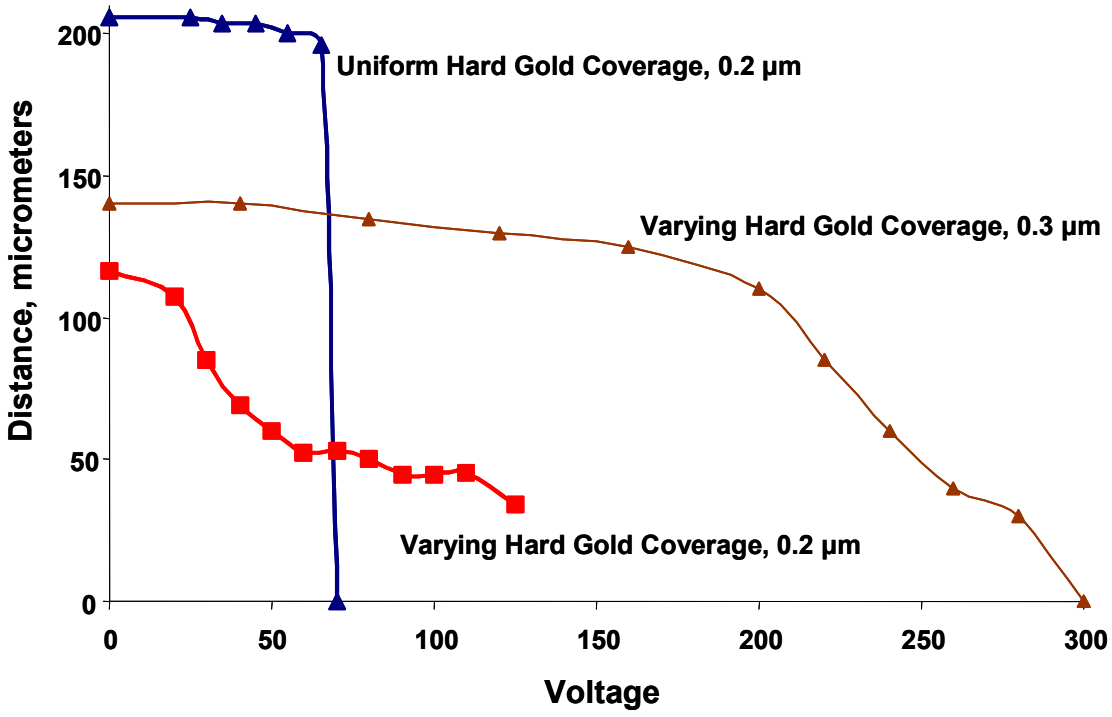

Figure 3.9. Voltage vs. deflection data for double-hinged square device with 2.0 μm soft gold and 0.2 μm (a) uniform hard gold, (b) patterned hard gold. For double-hinged square device with 4.0 μm soft gold and 0.4 μm patterned hard gold.

bottom electrode. In Figure 3.9b, the initial deflection for the double-hinged, square device containing a variable stress gradient was 120 +/- 5 μm. This initial deflection of the variably stressed device is approximately 60 percent of the deflection of the uniformly stressed square device. This is because the average intrinsic stress for the patterned devices is less than the constant stress for the uniformly patterned devices; therefore, since there is less stress acting to deform the cantilever, the initial deflection for the variably stressed devices was reduced. Upon the new variable stress gradient, the double-hinged square device could now be tuned across 70 percent of the initial vertical deflection with a voltage of 100 V. This is a very significant improvement over the uniform layer in Figure 3.9a. Approximately 25 of each beam type depicted in Figure 3.4 were energized and examined. The voltage vs. deflection and tuning range results shown in Figure 3.9 were found to be repeatable between multiple cycles and across several tested devices.

The devices depicted in Figure 3.9a,b are composed of 2.0 μm of soft gold and 0.2 μm of uniform/patterned hard gold, respectively. An additional variation was tested with twice the gold thickness (4.0 μm of soft gold covered with 0.4 μm of patterned hard gold), and is shown in Figure 3.9c. Upon application of an applied voltage across the variably stressed double-hinged square device, the top electrode smoothly pulled down between 150 and 250 V, demonstrating a stiffer pull-in due to the greater spring constant of the hinges. Finally, the tip contacted the bottom electrode at 280 V. This thicker device was controlled over 70% of its initial deflection range, supporting the conclusion

that the voltage range of the pull-in profile can designed by change of the beam stiffness and initial deflection.

Initial deflection, pull-in voltage, and deflection at pull-in were measured and compared to other devices, as well as between corresponding patterned and uniform hard gold structures. Both the initial deflection and pull-in voltage were found to be systematically different between uniform and patterned hard gold structures of comparable geometry. The results for devices composed of 2.0 μm of soft gold and 0.2 μm of hard gold are summarized in Table 3.1. Pull-in voltage, tuning range, and initial deflection are given for the patterned and uniform stressed-gold versions of each of the four devices discussed. All data is after devices have been through 500 cycles. The patterned hard gold devices had increased tuning range at the cost of higher pull-in voltage for each of the double-hinged devices. The fully hinged rectangular structure saw no improvement with the addition of the stressed gold.

Table 3.1. Comparison of pull-in voltage, initial deflection and tuning range for 4 different devices, depending on the coverage of the stressed hard gold.

	Stressed Gold Coverage	Pull-in Voltage, V	Initial Deflection, μm	Tuning Range, %
Double-Hinged Square	Patterned-Triangle	280	143	70
	Uniform	70	205	10
Double-Hinged Ellipse	Patterned-Triangle	170	105	45
	Uniform	80	250	10
Double-Hinged Rectangle	Patterned-Triangle	185	135	65
	Uniform	80	230	35
Full-Hinged Rectangle	Patterned-Triangle	160	150	15
	Uniform	80	230	20

3.3.2 Hysteresis

The reversibility of the device behavior was also investigated. Instability in electrostatic actuators leads to an abrupt pull-in in the voltage vs. deflection curve, during which the cantilever is brought into close contact with the dielectric layer. This movement is accompanied by a large increase in the electrostatic force attracting the cantilever and the aluminum electrode. In order to release the cantilever from the dielectric, a significant reduction in the applied voltage is necessary to regain stability. This leads to a hysteresis in the pull-in profile. This hysteresis is shown in Figure 3.10 for a 4.0 μm soft gold beam with 0.2 μm uniform hard gold coverage. When testing was performed in a rough vacuum, a large reduction in voltage applied to the device was required. Specifically, for a pull-in at 160 V, the device would typically release at 50 V, a difference of 110 V. It was determined that stiction due to the presence of moisture in the testing environment was responsible in part for the magnitude of this hysteresis. Testing was then performed in an enclosed probe station, with high vacuum provided by a turbo pump. In addition, the test chamber was initially heated during evacuation in order to remove surface moisture. This led to a drastic reduction in the hysteresis, as the cantilever now released at 90 V.

This testing was also performed on the patterned hard gold devices in order to determine if any reduction in hysteresis was achieved through this new design. Figure 3.11 shows the behavior of a 2.0 μm soft gold device with 0.1 μm of patterned hard gold.

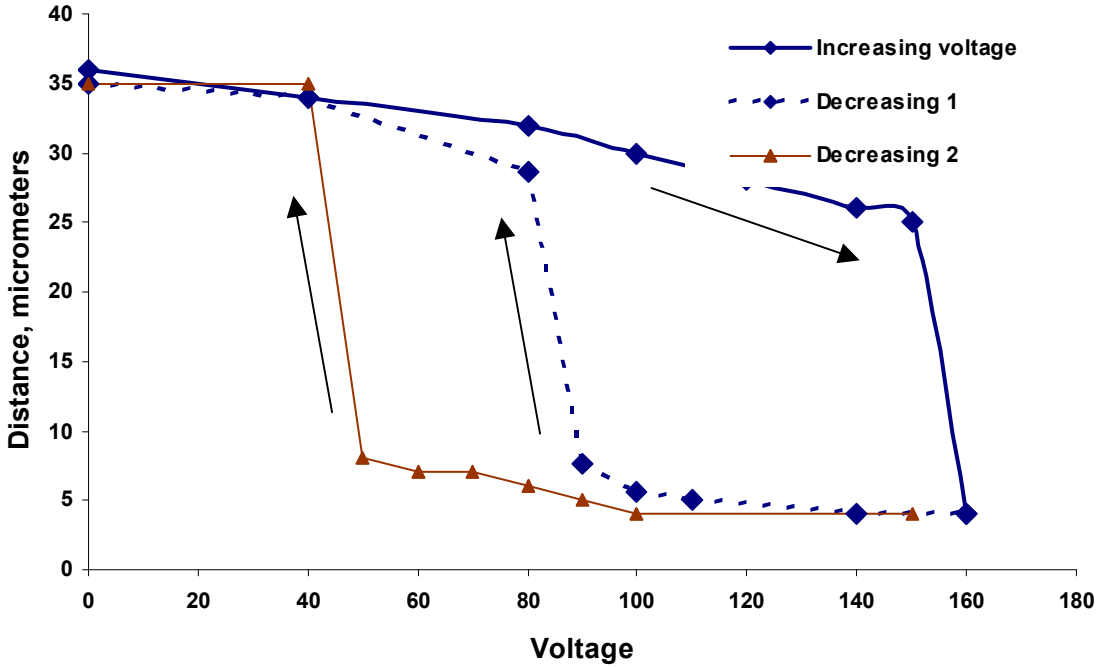

Figure 3.10. 4.0 μm soft gold beam with 0.2 μm uniform layer of hard gold (a) pull-in, (b) release during testing in rough vacuum, (c) release during testing in high vacuum with bakeout.

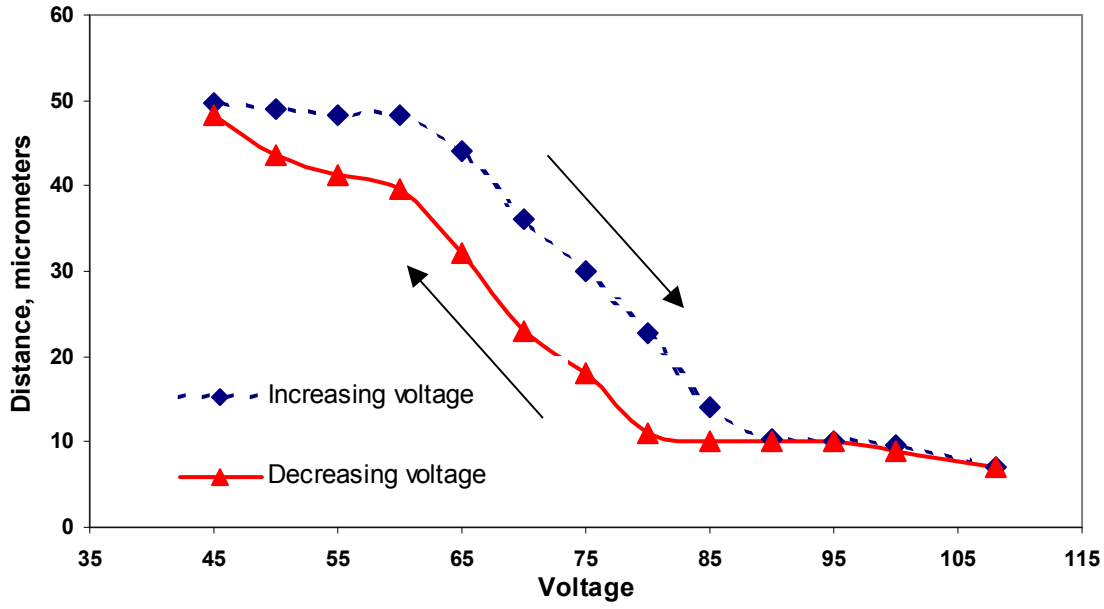

Figure 3.11. Hysteresis behavior of 2.0 μm soft gold device with 0.1 μm of hard gold.

This device demonstrates a maximum hysteresis of 10 V, much lower than the 70 V hysteresis achieved with the uniform hard gold design. The hysteresis behavior of this device is representative of all devices with a patterned stressed hard gold layer. It will be shown in the modeling sections to follow that this reduction in hysteresis is due to a drastic reduction in the instabilities associated with the pull-in movement. Evidence will be presented for a gradual pull-in behavior.

3.4 Modeling

3.4.1 Finite Element Modeling

In addition to device testing, modeling was performed using the Coventorware simulation package from Coventor, Inc. to compare device characteristics between laboratory measurements and simulation through finite element methods. For the model of the patterned hard gold device, a single square layer was constructed with built-in variable stresses both along the beam length (x-direction) and through the depth of the structure (y-direction).

The cantilever, composed of a thin film of electroplated stressed gold deposited above a lower stressed gold, had previously been treated as a single metal layer [13]. The reason for this treatment was that the incorporation of the bilayer structure into the modeling package MEMCAD had previously resulted in difficulty solving the structure.

Instead, a single layer was used in where the stress in the plane of the cantilever varied with the depth of the layer. The magnitude of this stress gradient was set to match the initial deflection of the fabricated device. For earlier work, this treatment was satisfactory. However, for more advanced modeling tests, such as gradients that varied in more than one direction and evaluation of reasonable deflections, treatment of this structure as a bimetallic device would be necessary. This allowed the incorporation of the actual stress of the hard gold layer to be directly input into that particular layer. MEMCAD would then calculate the equilibrium stress/strain profile through the composite, instead of reacting to an applied stress gradient supplied by the user.

The first tests were among the larger structures. For a 1000 μm length structure with 2.0 μm of soft gold and 0.2 μm of hard gold, a stress of 200 MPa was applied to the thin hard gold layer, resulting in an initial deflection of 0.214 mm. The actual radius of curvature of this device can then be shown to be 2.43 mm. This compares favorably with Stoney's Equation, which suggests a radius of curvature of 2.40 mm. Overall, the initial deflections calculated by MEMCAD are less than those fabricated structures measured earlier in the program. However, Stoney's Equation, when given the correct elastic constants for soft gold and the hard gold stress value determined previously, agreed with the MEMCAD results. This justifies our confidence in MEMCAD to treat bimetallic structures. The difference in the actual deflections of the fabricated large structures and those predicted by the modeling is reasonable, on the order of 20-30%. However, the difference for the smaller structures is much greater. This suggests some variation in the

fabrication between the large and small structures, or more likely, a larger error in the actual deposited thickness of the hard and soft gold layers.

The first modeling development was the treatment of both the hard and soft gold layers as separate materials. This has importance in allowing adjacent layers to be analyzed, whereas this ability was not previously available in earlier modeling treatments. Before, an average stress value across the device width had to assumed, given the functional form required by the geometry shown in Figure 3.2. The test structure for this work was a double-hinged long rectangle, measuring 560 μm long and 360 μm wide. The overall device thickness was 2.0 μm of soft gold and 0.2 μm of hard gold. The stressed gold layer was given a stress of 200 MPa, in line with previous measurements of the stress from the hard gold electroplating bath. This magnitude of stress resulted in an initial deflection of 105 μm, which when compared to the value of 97 μm predicted by Stoney's equation, shows a high level of agreement between the simple model and the simulation results. Thus, there is a high degree of confidence in the MEMCAD results. Representative Coventorware models for uniform and patterned hard gold structures are depicted in Figure 3.12.

Another recent modeling development was the ability to add a fictional boundary over the bottom electrode. Previously, once sufficient voltage was applied to the electrode, the electrostatic force would eventually become great enough to pull the cantilever beam down towards the bottom electrode. However, once these two electrodes made contact,

there was no longer a circuit, and the system failed to solve at any higher voltage. In the fabricated devices, there exists a thin dielectric BCB layer covering the bottom electrode. However, as all of the necessary properties of this material were not readily available, and since the addition of this layer would result in much greater computation time (due to the increased number of nodes), an air gap of appropriate thickness (as determined by its dielectric constant) was used in place. Now, a fictional layer was put into the MEMCAD solver that would act as a boundary for the cantilever beam during pull down. The beam would be able to contact this constant thickness layer, but would not be permitted to penetrate further. This addition allowed the modeling to continue at higher voltages, demonstrating the uncurling behavior suggested earlier. Additionally, this analysis now predicted hysteresis present upon decreasing the voltage after pull down.

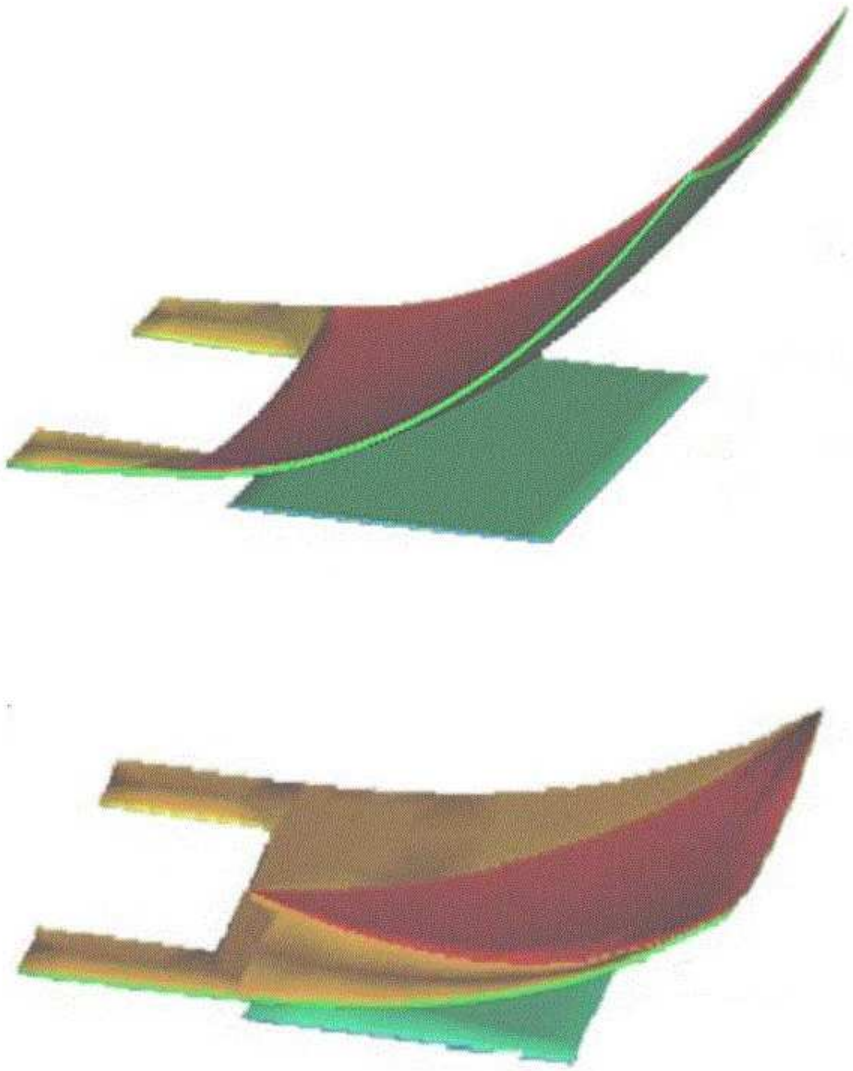

Figure 3.12. Modeling space schematic of rectangle device with a) uniform hard gold, and b) with patterned hard gold. Solved device deflection and curvature due to stressed layers are shown for 0.2 μm hard gold coverage on 2.0 μm thick soft gold cantilever.

3.4.2 Comparison to Experimental Results

The double-hinged square uniform hard gold device was modeled to help understand the deflection and movement with applied voltage. The model was obtained by performing an iterative sequence of simulations at regular voltage intervals between 0 V and 100 V. Figure 3.13 shows the modeled voltage vs. deflection curves for both the patterned and uniform gold versions of the double-hinged square device. There is a sharp pull down at approximately 70 V, and this result agrees well with the experimental result shown in Figure 3.13a. Both the pull-in value and the shape of the deflection curve for the uniformly stressed structures are in agreement with experimental results previously documented [13]. This example clearly shows the nature of the instability problem. Only a small deflection was possible under controlled conditions. Although a simple spring model predicts $1/3^{rd}$ of the displacement can be carried out under controlled conditions, often (as in Figure 3.13a), the value is less.

The voltage pull-in of the variably stressed hard gold device was modeled. The simulation of the variably stressed gold device yielded an initial deflection of 110 μm and a more gradual pull-in compared to the uniformly stressed gold structure. One difference between the finite element MEMCAD model and the analytical solution in the Theory section is that z-direction (width) variations were not considered. Figure 3.9 shows this improved pull-in behavior predicted by the modeling. The calculations showed a lower initial deflection (110 μm) than were observed experimentally (Figure 3.13b). The model

predicted a gradual curve towards the point of instability. The curve in Figure 3.13 shows the model for the patterned device began to deflect between 20 V and 30 V. In spite of this difference in scaling, the absence of a limited tuning range immediately followed by a sudden pull-in instability in the voltage-deflection profile for the patterned hard gold device indicates that a different mechanism of pull-in is at work. Instead, it appears that the beam with patterned hard gold uncurls gradually onto the dielectric layer with the application of increasing voltage. Modeling supports to this observation and is discussed in the following sections.

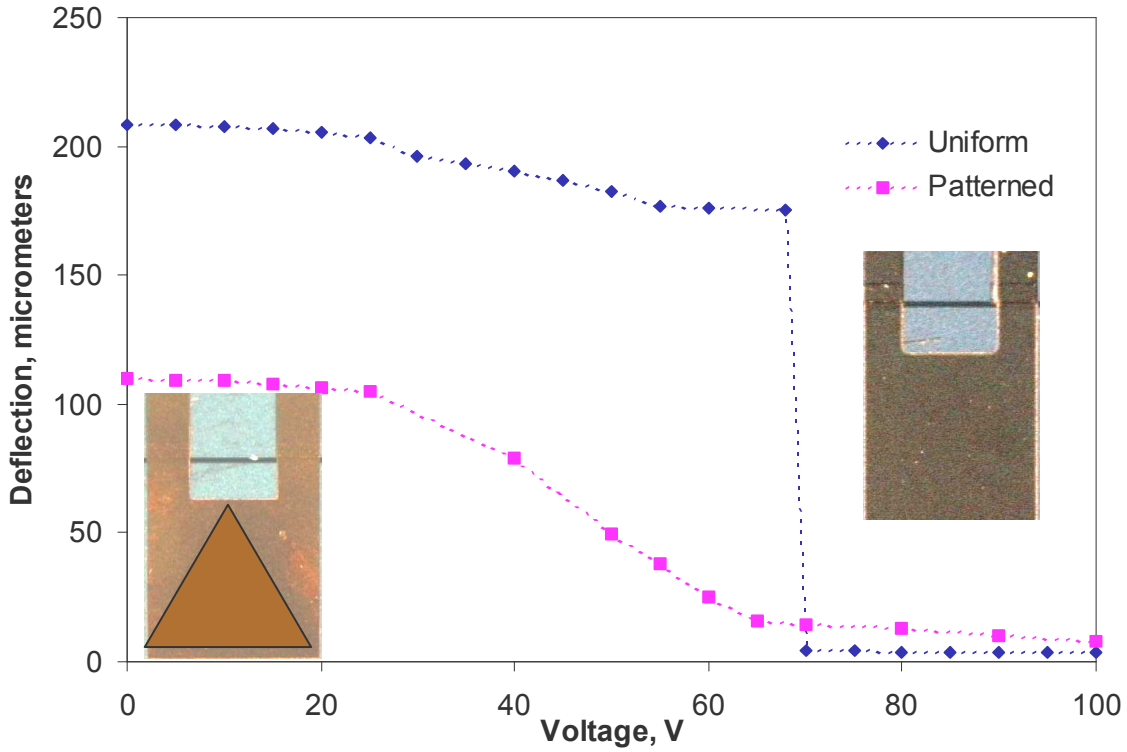

Figure 3.13. Modeled voltage vs. deflection behavior for pull-in of a double-hinged square device.

3.4.3 Pull-in Analysis

The gradual uncurling pull down can be further supported by modeling the area of the beam in contact with the underlying dielectric as a function of voltage. Figure 3.14 (uniformly stressed gold layer) shows the percent area in contact between the cantilever beam and the lower electrode. As can be seen, the contact area increases from zero just below the pull-in voltage to approximately 75 percent at pull-in. Note, that the entire bottom area of the cantilever cannot easily be pulled into contact with the dielectric. Here, the area close to the hinge does not make contact, since one end is constrained above the plane of the BCB.

The model does not predict the same pull-in for the variably stressed gold device. Since the hard gold width increases along the length of the beam, the radius of curvature of the cantilever is not constant with length. Instead, the curvature radius begins at an infinite value at the hinge and decreases along the beam length to the constant value found in the case of the uniform devices. This results in the variably stressed gold device having a large portion of the cantilever positioned in closer proximity to the lower electrode. The separation is such that a much smaller voltage applied to the DC electrode will result in a movement of the actuator. However, instead of this voltage being sufficient to pull down the entire beam, it is only pulls down the part of the beam closest to the electrode. Since the beam experiences increasing curvature along its length, a further increase in voltage is necessary to further deflect the device. At each point along

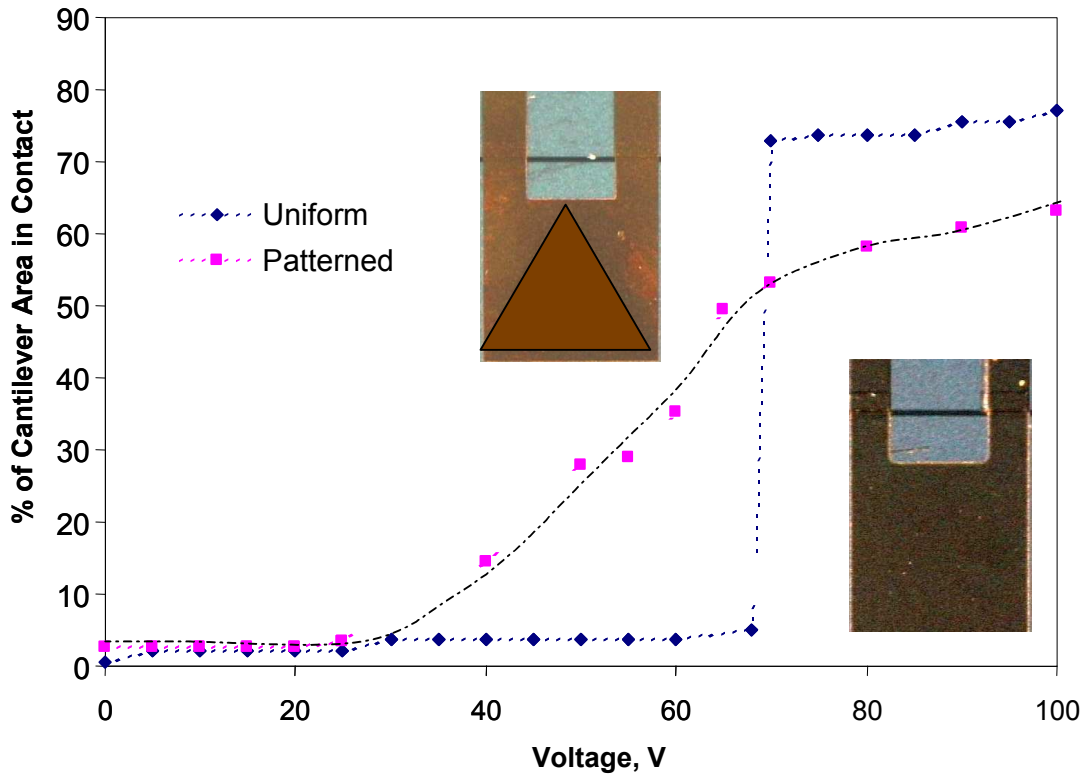

Figure 3.14. Percentage of the cantilever modeled to be in contact with the dielectric during pull-in.

the pull-in, the device's average radius of curvature is smaller than at lower deflections. This results in the shape of the top electrode that is increasingly difficult to pull down. In addition, the length of the moment arm of the device decreases as more of the beam is brought into contact with the dielectric (Figure 3.14). The combination of these two effects counteracts the instability encountered with previous devices, and allows the pull-in to proceed gradually over a range of applied voltage. This theory of pull-in is consistent with the observations from device testing. In order to limit excessive computation time for the electromechanical simulations, a rough mesh was used for the fictional contact layer so as to not greatly increase the number of nodes in the simulated

device. This rough mesh, however, accounts for the non-smooth increasing contact area with voltage shown in Figure 3.14.

Further improvements in this beam could be made. For example, the method of inducing a linear stress gradient along the length of the beam (x-direction) could be improved by replacing the triangular hard gold layer with one where the thickness of gold varies alone the length in a known fashion. This would eliminate the unaccounted for stress gradient along beam width (z-direction). Also, the thickness and shape of the stress gold could be further investigated in order to yield a device that pulls down in accordance with a desired voltage versus deflection profile.

3.4.4 Beam and Tip Geometry

Analysis of these devices shows the advantages of the elliptical structures versus rectangular structure. The elliptical geometry showed a ratio of 2/5 for the initial deflection of the patterned device to the uniform device, and the rectangular geometry has a value of close to 2/3 for this ratio (both in excess of the 1/3 value). This serves as evidence that the nature of the beam tip may be significantly enhanced at low deflections by curvature along the width of the beam. That is, the presence of the hard gold appears to contribute substantially to the deflection of rectangular devices by elevating the beam tip at the corners. Thus, the width of the device plays an important role in determining the overall cantilever shape.

The deflections reported for the modeling correspond to the largest deflection at any point along the beam. With the exception of the double-hinged, square device, the actual devices did not exhibit a large observable variation in deflection along the width of the tip. Modeling predicted the difference was greatest for wide devices with relatively low end-beam slope. In simulations of the double-hinged square device, modeling found the out-of-plane curvature along the beam width accounted for up to a 40 μm variation in deflection from the center of the tip to either corner. Subtracting the difference in deflection from the beam corner to the center of the beam tip, the ratio of the center-tip deflection of the variably stressed device to the uniformly stressed device was found to be approximately 2/5.

3.4.5 Capacitance Modeling

The results have been focused on improvements in beam design. To simulate the action of a variable capacitor, a second small electrode was added to the model under the beam tip, electrically isolated from the DC pull-in electrode. The placement of this second electrode is chosen so that a large range in capacitance is possible. If the capacitance electrode were placed closer to the hinges, the relative movement of the cantilever from release to pull-in is much smaller, resulting in less change in capacitance. A voltage was applied across the beam and the DC electrode in order to change the beam position. The resultant change in capacitance between the beam and the second electrode was evaluated. Figure 3.15 shows the modeling results for the capacitor. There is a significant benefit in capacitance range observed with the patterned hard gold devices.

The uniformly stressed gold structure experiences a tunable capacitance range on the order of 10% before snapping down (Figure 3.15, uniform stressed gold), whereas the patterned hard gold device exhibits a continuous capacitance increase of approximately 100% of its initial value before the slight snap-down to the lower layer near 60 V (Figure 3.15, variably stressed gold). This improvement represents an order of magnitude improvement in the potential tuning range of the variable capacitor

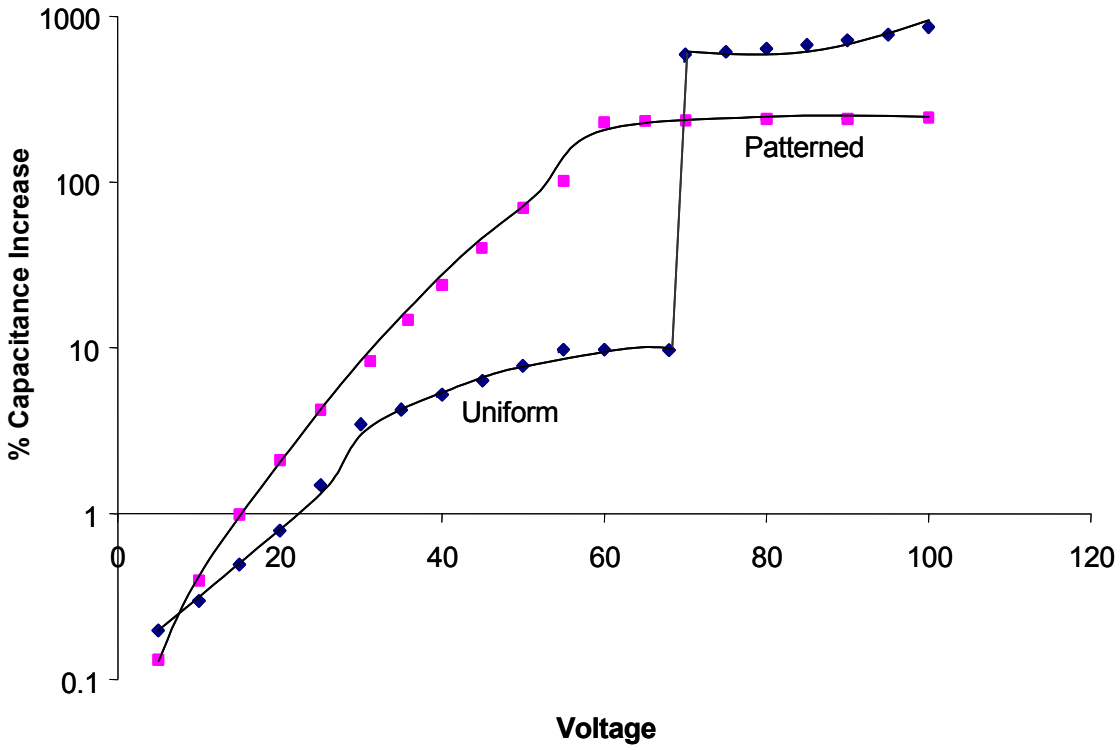

Figure 3.15. Modeled capacitance between aluminum electrode and cantilever during pull-in of double hinged square device with (a) patterned hard gold coverage (b) uniform hard gold coverage.

devices. Capacitance data was not taken with the actual fabricated devices; however, since similar geometrical tuning ranges were observed between the fabricated and simulated devices, it is expected that other geometry-electrostatic based properties would have excellent agreement. Note that a greater percentage increase in capacitance is observed with the uniform hard gold patterning. This is due to the higher initial deflection (smaller initial capacitance) of the device with uniform stress. In addition, the devices with the patterned hard gold layer also had a thicker BCB dielectric layer, resulting in lower capacitances at pull-in.

3.5 Temperature Effects

The effects of temperature on two of the devices discussed above were investigated. Temperature cycling experiments were performed on the double-hinged square and the double-hinged, elliptical devices. Both devices were fabricated with the variably stressed gold layer. A decrease in elastic modulus at lower temperatures has been previously reported [34]. At room temperature, the elastic modulus for bulk gold is 78 +/- 1.5 GPa. At 200 K, close to the low temperature used here, the elastic modulus increased to 81 +/- 1.5 GPa. Temperature also affects the thermal expansion coefficient. As temperature increases, the length of the beam expands, which causes the stress in the beam to change. Figure 3.16 shows the temperature effects on a double-hinged, square device with a variably stressed layer. The curve at room temperature is the same curve shown in Figure 3.9c, displaying an initial deflection of 143 +/- 5 μm. When the temperature is lowered from room temperature to 225 K, the voltage vs. displacement curve shifts slightly above

the curve obtained at room temperature. In Figure 3.16, the initial tip deflection increased to 155 +/- 5 μm, 8% higher than the value at room temperature. At low temperature, the beam follows the same path as the room temperature curve, and snaps-down at the same voltage. The voltage vs. deflection curve for the structure at 395 K shows that the device comes into contact with the bottom electrode at approximately 220 V. While there is significant variation in the pull-in voltage with increasing temperature, this is a direct result of the closer proximity between the cantilever and bottom electrode as evidenced by the reduced initial deflection. However, the variation observed in the initial deflections observed in Figure 3.16 contrasts to typical behavior of bimetallic beams where the difference in coefficient of thermal expansion results in very significant changes in the stress state of the beam with temperature; therefore, a typical bimetallic beam would experience much greater variation in initial deflection over the 170 K temperature range presented in Figure 3.16. The absence of a significant stress variation with temperature is ideal for applications in which the dynamics of the device need to be known over a range in operating temperatures.

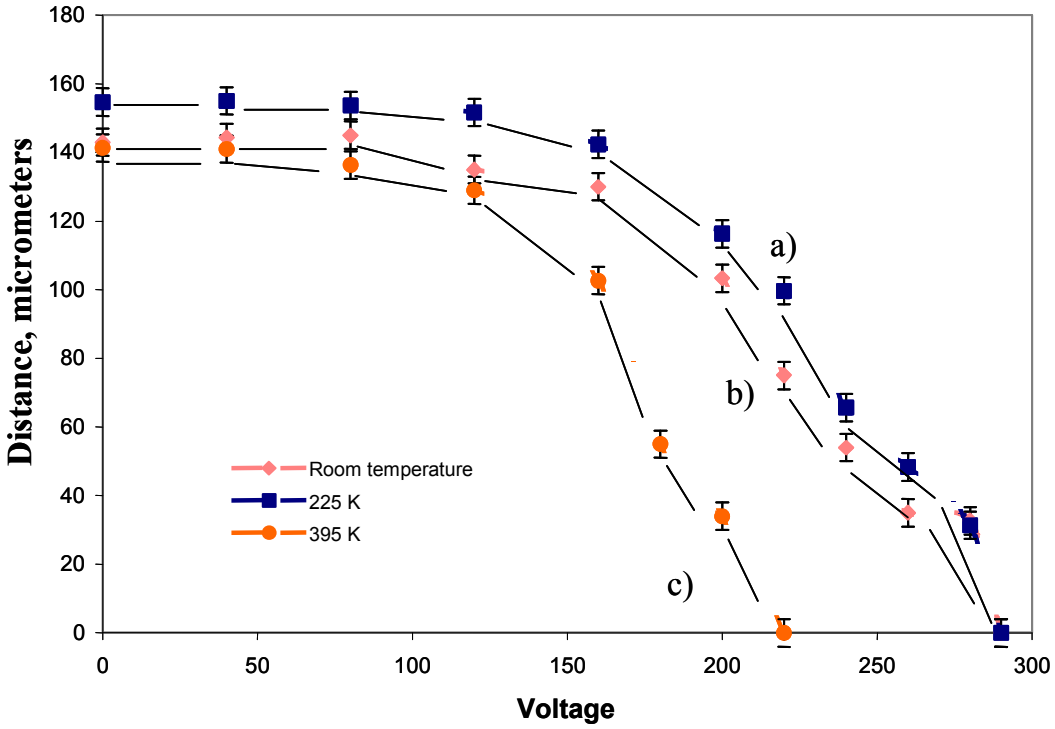

Figure 3.16. Voltage vs. deflection behavior of a double-hinged square device at (a) 225K, (b) room temperature, (c) 395 K.

3.6 Summary

The pull-in characteristics of four electrostatic actuators were measured. Stressed, hard gold was patterned in a triangular shape on top of stress-free soft gold. This induced a variable stress gradient in the cantilever beams that varied with beam thickness and length. This stress gradient along the length of the beams significantly improved the tuning range compared with devices containing spatially uniform stress. The tuning range of the variably stressed gold devices improved to 70 percent for the double-hinged square devices, to 45 percent for the double-hinged elliptical devices, and to 65 percent for the double-hinged rectangular device. The anchor arrangement affects the pull-in behavior of the top electrode, as shown by the full-hinged, rectangular device. The double-hinged arrangement provides more freedom of motion. Voltage cycling had an initial impact on the pull-in characteristics of the actuator, but no observed drift after 500 cycles. Modeling predicted a gradual pull-in curve for the variably stressed devices, which was confirmed by experimental results.

Progress was made in extending the tuning range of the electrostatic actuator by incorporating a stress gradient within the cantilever that varied both with the depth and the length of the beam. Calculations were performed to predict and understand the beam shape and movement, and modeling was completed to verify the extended tuning range of device capacitance and movement. However, there were still many drawbacks associated with electrostatic actuation. Among these were: 1) the capacitor exhibited a significant degree of hysteresis, a characteristic that complicated tuning by making it a path-

dependent process, 2) high voltages were necessary to uncurl the beam in order to take advantage of larger tuning range, 3) the devices had limited reproducibility, 4) the device required continuous power to maintain a change in state, and 5) a wider capacitance range is required.

CHAPTER 4

ULTRA-LOW SWITCHING ENERGY AND MODELING

Due to the drawbacks of the CVC, the addition of the CVC device to the series of discretely valued capacitors provides little benefit for tuning. In a discrete network, small increments of capacitance are added to the circuit in a digital fashion. In order to construct a discrete network, a MEMS microrelay must be designed that could switch on and off the individual capacitative elements in order to produce the total desired capacitance. This concept is illustrated in Figure 4.1. A RF signal is input to the relay network. If the first relay (shown as the dashed line element labeled 'Relay #1') is in the 'up' configuration, the signal will be routed to 'out #1.' If, however, relay #1 is actuated to the 'down' state, then the signal will proceed to the next relay, relay #2. This type of switch is referred to as a single pole double throw (SPDT) switch. In order to avoid unwanted reflections, it is necessary to design a relay with no 'dead-legs' in the RF network. The RF signal must have only a straight path from input to the designated output. Any dead-end paths will result is a signal reflection that will interfere with the desired input signal. The entire network forms a 1xn switch by stringing together a series of n-1 1x2 relays. Since this relay need only have discrete 'on' and 'off' states, this element should be designed to experience bistable behavior. The switch would have two states of stable equilibrium. That is, it would require power only during the switching from one equilibrium position to the other.

Therefore, new designs were undertaken to address many of the above-mentioned concerns. Magnetic actuation has been successfully incorporated into MEMS devices [18-19, 21, 25-27, 35-36]. Magnetic forces provide the ability to enable bistable operation [21,27]. By making use of a ferromagnetic material, such as permalloy, and a combination of an external magnetic field and a current-driven coil, a MEMS device may be constructed so that it experiences two stable equilibria. Such a device would only consume power during device movement, thus greatly increasing the economy of the device. Using magnetic actuation, two different classes of devices were explored. One set made use of magnetic actuation to exhibit magnetically bistable behavior, while in the other set use magnetic actuation to exhibit mechanically bistable behavior was investigated. In chapters 4-5, design advances, fabrication, and performance are presented. In addition, chapter 6 investigates a phenomenon of beam wiping and potential applications. Use of magnetic actuation to exhibit mechanical bistability was found to be unsuitable for our target application, and evidence is provided in chapter 8.

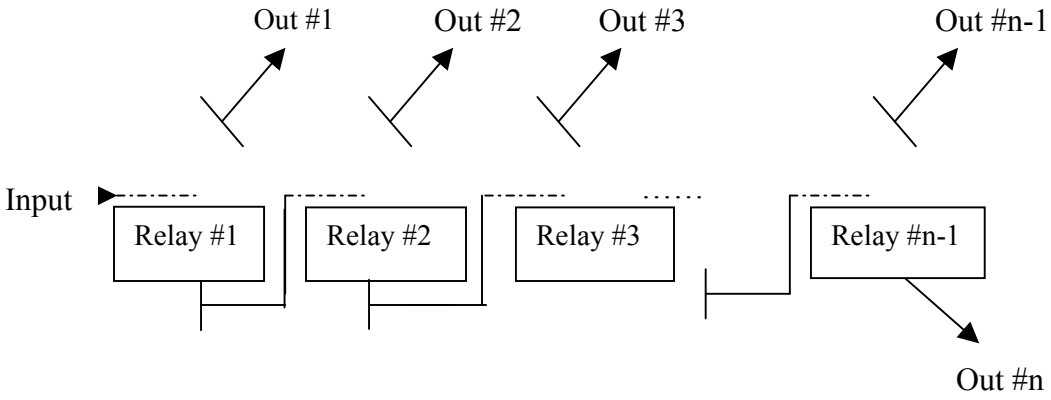

Figure 4.1. Schematic of a 1 x n switch made of n -1 1 x 2 relays.

The optimal design space for a bistable magnetic actuator with ultra-low actuation energy and large actuation distance (100 μm) has been modeled. Attention was paid to minimizing the energy expended to minimize heat dissipation and power consumption so that the device could be used over a wide temperature range, including cryogenic environments. A more desirable switching regime existing for low magnetic fields (10 mT) was found that requires shorter pulses (μs vs ms) and lower actuation energy (< 5 μJ vs 100 μJ) than designs outside of this space [27]. The device was modeled to latch in two states, based on the interaction of the magnetic actuator with an external magnetic field [27].

The Ruan device is switched by momentarily activating a magnetic field drive coil patterned in the plane of the substrate. The torque created by the interaction of the permalloy on the cantilever and the field generated by the external magnet causes latching in one of two possible configurations: upstate and downstate, as shown in Figure 4.2. The beam is anchored at one end, and the permalloy is patterned in such a way that its length is the dominant geometrical dimension. This causes the beam to occupy one of two magnetic states under the influence of an external magnetic field. The two preferred magnetization directions are antiparallel, both lying along the beam's length. The magnetic torque is represented by $V\,\vec{M}\times\vec{B}$, where $\vec{M}$ is the magnetization vector of the beam, V is the volume of the magnetic material deposited on the beam, and $\vec{B}$ is the external magnetic field. Thus, the magnetic torque tends to move the beam such that it is more aligned with the external field. In Figure 4.2(a), $B_{external}$ would move the beam to a

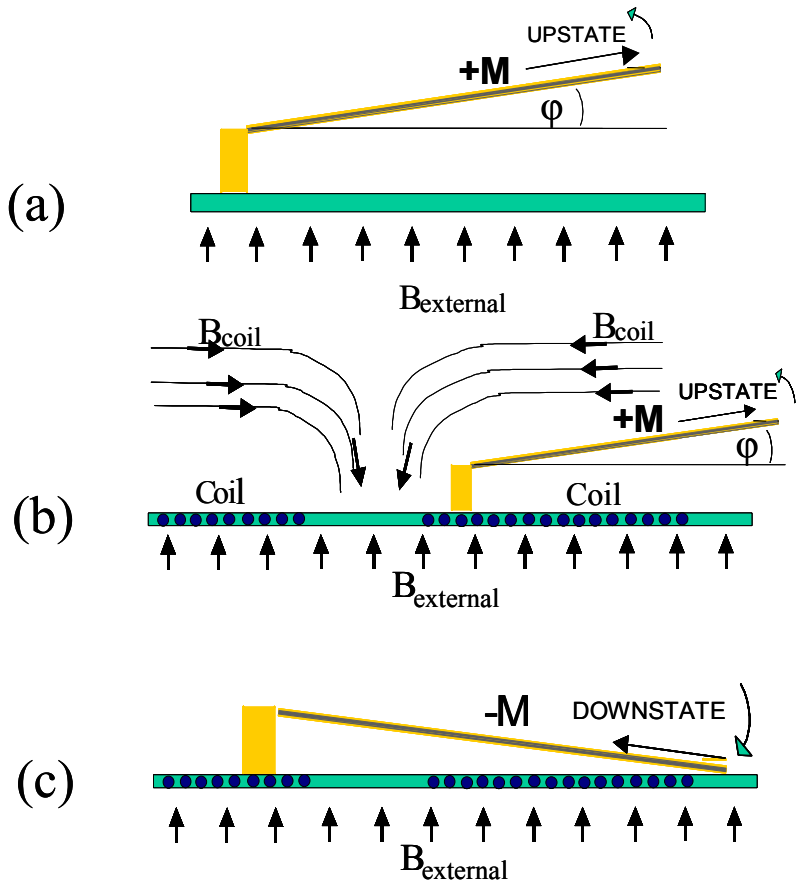

Figure 4.2 a) Magnetic beam device with two stable states, b) Switching mechanism between states, c) New equilibrium position.

more vertical position. The beam remains magnetized by the magnetic field provided from the permanent magnetic source attached to the substrate [27].

The magnetic torque is represented by $V\,\vec{M}\times\vec{B}$, where $\vec{M}$ is the magnetization vector of the beam, V is the volume of the magnetic material deposited on the beam, and $\vec{B}$ is the external magnetic field. Thus, the magnetic torque tends to move the beam such that it is more aligned with the external field. In Figure 4.2a, $B_{external}$ would move the beam to a more vertical position. The beam remains magnetized by the magnetic field provided from the permanent magnetic source attached to the substrate [27]. In order to move the device from the upstate to the downstate, it is necessary to reverse the direction of the magnetization vector along the permalloy. To accomplish this, the local magnetic field in the vicinity of the beam must have a positive component directed towards the opposite side of the beam in Figure 4.2. Since the local magnetic field supplied by the permanent magnet cannot be changed, an alternative magnetic source must be used. One method to overcome the component of the external magnetic field holding the beam in the upstate (i.e. $B_{external}\sin\varphi$, where φ is the angle the beam makes with the horizontal) is to create a second magnetic field opposing $B_{external}$, such as through the use of a current carrying coil. If the coil were placed as shown in Figure 4.2b, the coil's magnetic field would have a large horizontal component in the vicinity of the beam. In order for the direction of the magnetization to reverse, the coil must be powered for a length of time sufficient for the following inequality to be satisfied (assuming B_{coil} is orthogonal to $B_{external}$):

$$B_{coil}\cos\varphi > B_{external}\sin\gamma + H_c - \frac{N_D}{VB_{external}}\Gamma_{elastic} \quad (4.1)$$

Here, γ is the angle between the beam and the direction of the permanent external magnetic field, H_c is the coercivity of the permalloy, N_L is the demagnetization factor of the beam along the length, θ is the angle the magnetization vector is pulled away from the plane of the ferromagnetic material due to the anisotropy torque, and $\Gamma_{elastic}$ is the elastic torque acting on the beam in the current position. Equation 4.1 establishes a lower bound on the externally applied B_{coil} field, which in turn establishes the minimum current that is needed for switching the device as a function of the device position (φ) and external field strength $B_{external}$. This inequality will be developed in the body of this chapter and will be shown to have a higher value compared to the $B_{coil} > B_{external}\sin\varphi$ criterion used previously [27]. When the inequality in Equation 1 is satisfied, the net magnetization switches to the opposite side, and the magnetic torque changes to counterclockwise in Figure 4.2. The beam then begins a downward movement and eventually occupies the downstate (Figure 4.2(c)). Power must be supplied to the coil for a time such that when the coil is terminated the beam will not magnetize in the original direction. For the 30 kA/m magnetic fields reported in Ruan's work, this requires the coil remain powered during a significant fraction of the total time (~50%) for the beam to travel the actuation distance [27]. Once the current through the coil is terminated, the external magnetic field provided by the permanent magnet holds the device in the downward state. When the beam is in the downstate, the counterclockwise motion tends to partially align the beam magnetization vector with the external magnetic field [27].

4.1 Design Criterion

4.1.1 Mechanical Design

In previous work, the static out-of-plane bending of electrostatic cantilever beams was determined by the thickness of a hard gold, stressed layer electroplated onto the beam surface [12-13]. Then, when the beam was to be displaced by force, the entire structure and hinges would bend, yielding to the electrostatic attraction. Partial hinges (narrow segments of metal) connecting the cantilever to the anchor, would bend more easily. The required force was reduced by a factor equal to the relative width of the hinge to the width of the beam. If the beam shape from the previous work were to be used in the fabrication of the magnetically actuated devices, a uniform thickness of permalloy on the beam and hinges would render the device exceedingly stiff. For example, suppose that such a beam/hinge device needed to be deflected a distance x for a given isolation to be achieved. Next suppose that the permalloy thickness, t_0, present on the gold beam/hinge (total thickness T) surface results in a deflection x_0. Assuming that x_0 is less than x, the application of Δt_0 more permalloy would result in a new magnetic moment, M_{new}, given by Equation 4.2, where M_{old} is the magnetic moment from permalloy thickness t_o.

$$\frac{M_{new}}{M_{old}} = \frac{t_0 + \Delta t_0}{t_0} = 1 + \frac{\Delta t_0}{t_0} \tag{4.2}$$

This is due to the fact that the volume of permalloy is linearly related to the magnetic moment at saturation. However, the new moment of inertia, I_{new}, of the beam has now

increased by the factor shown in Equation 4.3, as compared to the old moment of inertia, I_{old}.

$$\frac{I_{new}}{I_{old}} = \left[\frac{T + t_0 + \Delta t_0}{T + t_0}\right]^3 = \left[1 + \frac{\Delta t_0}{t_o + T}\right]^3 \tag{4.3}$$

The ratio M/(EI) gives the inverse of the radius of curvature of the beam, where E is the elastic modulus of the beam material [36]. In this manner, the ratio of the new curvature, r_{new}, to the old curvature, r_{old}, may be written as:

$$\frac{r_{old}}{r_{new}} = \frac{1 + \frac{\Delta t_0}{t_0}}{\left(1 + \frac{\Delta t_0}{t_o + T}\right)^3} \tag{4.4}$$

When the value of the RHS of Equation 4.4 is greater than 1, the ratio of the magnetic moment to the moment of inertia increases with the application of additional permalloy. This translates into a net increase in the deflection of the beam. However, there exists a maximum deflection possible for a device of a given geometry in a uniform magnetic field. This critical condition is found when the RHS of Equation 4.4 is set equal to unity. Neglecting higher order terms in Δt_o, it is found that the criterion for further beam deflection by application of more permalloy is $t_o \leq T/2$. Thus, the beam will only deflect further under the addition of more permalloy if the previous permalloy thickness were less than half the non-permalloy beam thickness. While this geometry may result in

significant deflections for very thin beam designs (<1 μm), hinges of this thickness are very fragile and difficult to use. Since there may only be a lower bound on T, it would be senseless to utilize a design that would penalize the resultant deflection by generating larger magnetic moments.

This necessitates a beam design with reduced stiffness in some areas, allowing a greater degree of bending in the hinge region while maintaining adequate rigidity along the actuator itself. This could be achieved by the use of thinner hinges near the beam anchor. Instead of plating permalloy on the entire device, permalloy can be selectively deposited on a portion of the beam. With this type of design, the stiffness of the hinge region does not depend on the amount of permalloy present, and Equation 4.4 reduces to:

$$r_{new} = \frac{r_{old}}{1 + \frac{\Delta t_0}{t_0}} \tag{4.5}$$

This results in a lower radius of curvature (and therefore greater beam deflection) with further application of permalloy thickness. This holds true under the assumptions that the hinge bending remains elastic and the permalloy is magnetically saturated. The permalloy-plated areas may be considered as a rigid plate, and the deflection of the beam predominantly results from bending the non-permalloy areas. The magnetic material may be clad in gold to cancel out any mechanical bending that would otherwise occur upon cooling due to the thermal mismatches between the gold and the permalloy. Based on these considerations, a double-hinged magnetic actuator was built in modeling space

using Coventorware to evaluate the forces necessary to achieve desired deflections. In addition, the model provided confidence in the rigid plate assumption of the non-hinge region and ensured only elastic bending during normal operation. The structure built is depicted in Figure 4.3a in an unstressed state and in Figure 4.3b with sufficient torque generated inside the magnetic material region to produce enough deflection in the hinges for contact with the substrate.

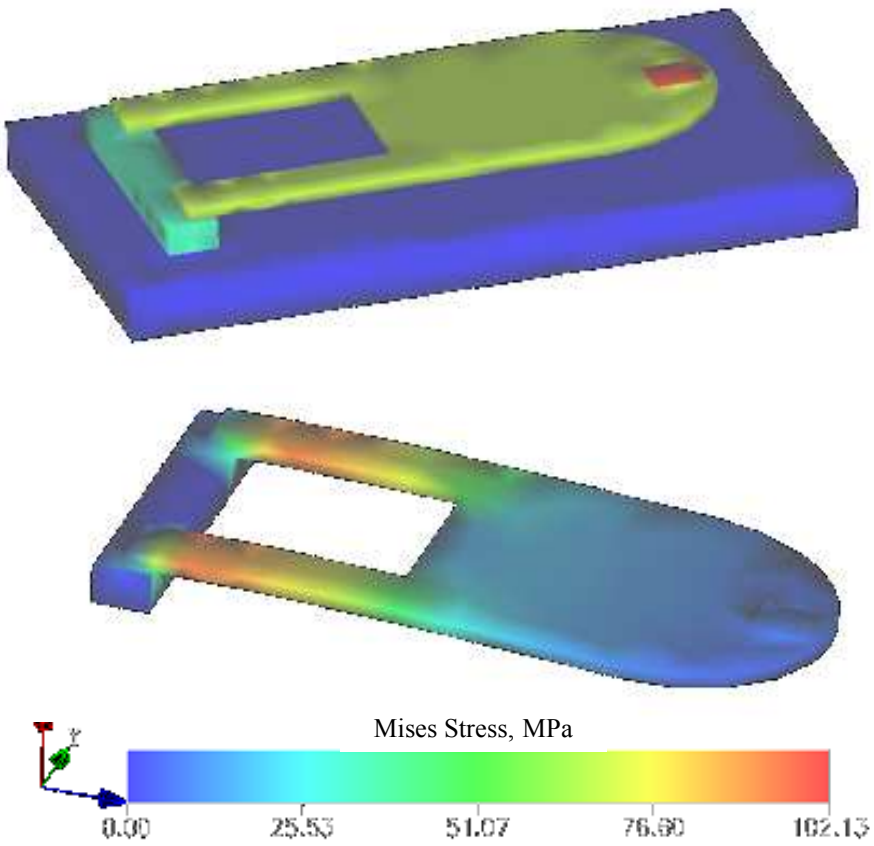

Figure 4.3. Finite element model built using Coventorware to analyze forces and deflections for the magnetic actuator. Shown in an unstressed state (a) and with a set deflection (b).

4.1.2 Magnetic Element Design

An expression for the magnetization for soft magnetic materials has been previously given by Judy and Muller [25].

$$M = \mathrm{Min}\left\{\frac{B\sin\gamma \pm H_c}{N_D}, M_{sat}\right\}, \quad \text{with} \quad \gamma = \varphi + \theta - \alpha$$
$$\text{where } N_D = N_L\cos^2\theta + N_T\sin^2\theta \tag{4.6}$$

Where B is the external magnetic field, α is the angle the external field makes with the vertical; H_c is the coercivity of the ferromagnetic material; N_L and N_T are the demagnetization factors due to the shape of the ferromagnetic element along the length and thickness, respectively; M_{sat} is the saturation value of the ferromagnetic material; θ is an angle the magnetization vector is pulled away from the plane of the ferromagnet, and N_D is the demagnetization factor in the direction of M. The magnetic torque for small deflection angles (valid because of the angular limits imposed by the two substrates) is given by Equation 4.7.

$$\Gamma_{magnetic} = \mathrm{sgn}\gamma \cdot \mathrm{Min}\left\{\frac{B\sin|\gamma| \pm H_c}{N_D}, M_{sat}\right\} VB\cos\gamma$$
$$N_D = N_L + \theta^2 \tag{4.7}$$

Where sgn(γ) returns the sign of the argument, allowing for positive and negative values of M, depending on the direction of magnetization; sin(θ) has been replaced by θ, V is the

ferromagnetic volume, and N_t has been approximated by unity for the high aspect ratio (length/thickness) Ni/Fe shapes of interest. The sign of the coercivity is positive if the ferromagnetic material was last magnetized in the upper latched state and negative if last magnetized in the lower latched state. A balance on the magnetization vector, M, requires that the magnetic torque that acts to bend M out-of-plane of the permalloy is balanced by the anisotropy torque which acts to pull M back in-plane. For polycrystalline Ni/Fe alloys under normal stress, the dominant form of anisotropy in the ferromagnetic material is due to shape anisotropy [25]. Under this condition, Equation 4.8 gives the anisotropy torque. In this case the angle which the saturated magnetization vector is rotated out-of-plane, θ, is the solution to Equation 4.8:

$$\Gamma_{magnetic} = \Gamma_{anisotropy}$$
$$\text{with } \Gamma_{anisotropy} = \frac{N_L - N_T}{2} V M_{sat}^2 \sin 2\theta \tag{4.8}$$

By equating the magnetic torque to the anisotropy torque, Equation 4.8, it can be shown that the magnitude of θ is bounded by 0.01 radians for saturated systems with a 10 mT external magnetic field. Therefore, θ^2 may become significant relative to N_L and have a large influence on the value of the magnetization (Equation 4.6) due to the impact on the denominator.

It should be noted that $\Gamma_{magnetic}$ scales quadratically with the external field at values of φ less than that at which the magnetic material becomes saturated. For values of φ greater than this, $\Gamma_{magnetic}$ scales linearly with the external field. At equilibrium, the

magnetic torque will exceed the anisotropy torque; however, if a contact force is present between the contact pad and the beam tip, then the magnetic and anisotropic torques will not equal the elastic bending torque of the hinges.

For a given design and value of φ, the above system can be solved for θ and the torques. Judy and Muller [25] showed the importance of accurate determination of both the coercivity and the demagnetization of the ferromagnetic material in modeling magnetic actuator responses at low applied magnetic field levels; however, we contend that accurate determination of the angle θ is also critical in predicting the sensitivity of the degree of magnetization with rising magnetic field.

It can be seen from Equation 4.5 that the rate of approach to saturation of the ferromagnetic material is strongly influenced by both the demagnetization value and the angle the magnetization vector makes with the plane of the magnetic material, θ. Increased levels of magnetization at a given field level are desirable since this results in a greater magnetic torque, potentially increasing the potential angular range of motion of the beam and improving the contact force between the beam and the substrate. Therefore, patterning the magnetic actuators to provide a greater anisotropy could greatly enhance the magnetization characteristics. However, in the limit of high anisotropy, the influence of θ becomes more significant, and further reduction of N_L no longer results in the reduction of the external field needed to produce a given magnetization. Since θ is tied to the magnetic torque through Equation 8, decreasing θ is now most readily accomplished by reduction in the background external magnetic field.

4.1.3 Coil Design

A conductor carrying a current, I, produces a magnetic field, H, as given by the Biot and Savart law [37]. For a square planar coil, Equation 4.9 gives the calculated magnetic field produced.

$$H_{total} = \sum_{i=1}^{N}\sum_{j=1}^{4}\left|H_{i,j}\right|(\vec{z}\cos\varepsilon_{i,j} + \vec{r}\sin\varepsilon_{i,j}) \tag{4.9}$$

Where $H_{i,j}$ is the field due the j^{th} side of the i^{th} turn of the coil, ε is the angle the line connecting the field point to the nearest point of segment i,j makes with the line segment connecting the coil center to coil segment i,j, $\vec{r}$ is the unit vector in the radial direction, and $\vec{z}$ is the unit vector orthogonal to the plane of the coil. The contributions due to each of the current segments $H_{i,j}$ may be calculated by the following:

$$\left|H_{i,j}\right| = \frac{I}{2\pi r_{i,j}}\left[\frac{L_{i,j}}{\left(L_{i,j}^{\ 2} + r_{i,j}^{\ 2}\right)^{1/2}}\right] \tag{4.10}$$

Here, L is half the length of the segment i,j, I is the current supplied through the coil, and r_{ij} is the distance on the midline from segment i,j to the field point. This analysis holds provided the field point lies in the midplane of one of the coil segments. This is acceptable as placement of the magnetic material of the MEMS device orthogonal to the coil segments and at the midpoint of one of the coil sides results in only components along the beam length to be developed in the plane of the magnetic material. The designs

were evaluated based on the relative magnitude of the in-plane and out-of-plane field components at a distance equal to the placement of the coil relative to the ferromagnetic material.

Both circular and square coils were evaluated. Each coil type was evaluated with 24 turns with an average spacing of 50 μm. The coil with circular turns yields a broader range of high radial magnetic field, but also generates a significant out-of-plane field component that, along with low external field levels, provides a significant degree of disturbance, and thus affects the background field levels. Figure 4.4 shows the field produced by the rectangular coil, as calculated from Equation 4.9. The square coil has a higher maximum field generation, but is over a narrower range. Also, the out-of-plane component is significantly less than the out-of-plane component for the circular design, and experiences a sign change midway along the range of large radial field levels, as shown in Figure 4.4. This results in an averaging effect of the out-of-plane component over a certain range, meaning that proper design could eliminate consideration of this component as a perturbation to the background external magnetic field. For these reasons the square coil design was chosen. The radial component, used in performing the switching, falls off rapidly with increasing r. At the edge of the coil, 1550 μm, the radial component is only 10% of its maximum value. A 700 μm magnetic beam would see an average field of 50% of the maximum radial field if properly placed. This is still 5 times greater than the field that would be generated just off the coil edge. This means that devices could be placed as close together as adjacent coils with no concern of switching interference between neighboring devices. In addition, coil size could be significantly

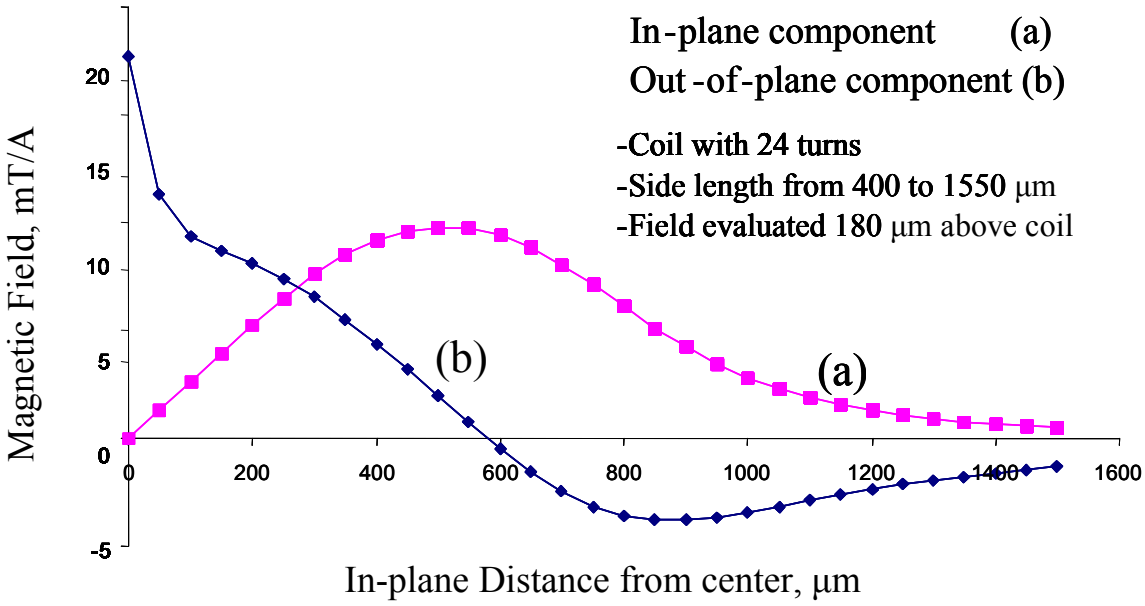

Figure 4.4. In-plane and out-of-plane components of field generated from a 24-turn rectangular coil.

reduced without concern for coil-to-coil interference. Multilevel coils have been utilized by others [38], and could be considered here for added field strength. Since the coil is designed to power the device operating at 77 K, the use of high temperature superconducting (HTS) materials for coil fabrication is possible; however, the cost associated with this step would greatly outweigh any benefit of reduced power consumption of the device itself.

4.2 Establishing The Design Space

A schematic diagram showing the interplay of the various geometrical and magnetic parameters is presented in Figure 4.5. Both the magnetic torque due to the magnetic field acting on the ferromagnetic volume of the cantilever and the elastic torque required to flex the hinges are graphed as a function of the angle, φ, that the beam tip makes with the horizontal. Regions corresponding to latching behavior are detailed with Roman numerals. The model includes the initial angular displacement of the cantilever, as well as the angle the external magnetic field makes with the vertical. Figure 4.5 also shows the angular placements of the upper and lower substrates. Such a graphical representation provides for a more complete understanding of the working device. The bending torque is a linear function of this angle (provided the hinge strain remains in the elastic regime) as shown by the dashed line in Figure 4.5. The slope of the elastic torque is equal to the stiffness, k_φ, of the hinge configuration. The intercept is nonzero if the beam has an initial deflection. Equation 4.11 gives the form of the elastic torque.

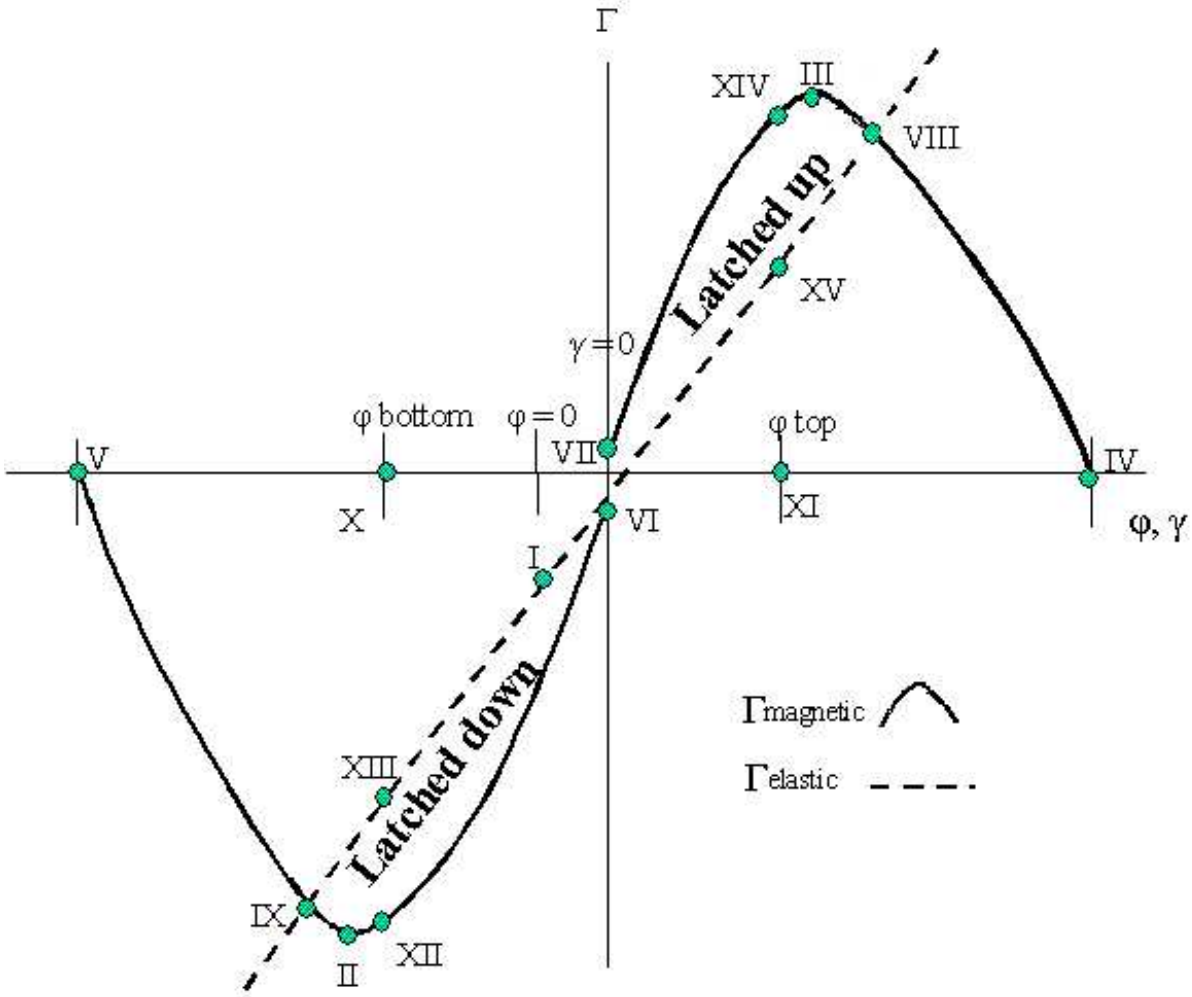

Figure 4.5. Design space for high isolation bistable magnetic actuator, depicting stable 'latched up' and 'latched down' regions where the magnetic torque exceeds the elastic restoring torque of the cantilever hinges.

$$\Gamma_{elastic} = k_{\varphi}\left(\varphi - \varphi^{o}\right) \tag{4.11}$$

For an initial deflection of the beam, φ^o, the intercept of the elastic torque versus φ line will be $-k_{\varphi}\varphi^o$ (point I). The angular stiffness of the hinge configuration depends on its geometry through the third power of the hinge thickness, the first power of beam width, and inversely with the length, as shown in Appendix B.

Incorporation of a nonzero initial deflection angle gives the model an additional level of robustness, since this allows stresses developed in the hinges due to sputtering and/or electroplating of gold to be considered, as well as any other fabrication inconsistencies which can affect the hinge curvature. The initial deflection removes the system symmetry, causing a greater difference between $\Gamma_{magnetic}$ and $\Gamma_{elastic}$ in one state versus the other. This initial deflection tends to decrease the stability of one latched state in favor of increasing the stability of the other state. This effect can be mitigated by control of the angle of the permanent external magnetic field, α. Decreasing the angle between the initial state of the beam and the external magnetic field reduces the stability of the upper latched state, while restoring stability to the lower latched state.

The magnetic torque (Figure 4.4 solid line) is a function of the geometry of the ferromagnetic material and the external magnetic field. Equation 4.6 gave the form of the magnetic torque. The form of Equation 4.7 generates two branches for $\Gamma_{magnetic}$, one for $\gamma > 0$ corresponding to a potential upper-latched state, and one for $\gamma < 0$ corresponding to a potential lower-latched state. Each branch increases with an increase in the magnitude of

φ, and reaches a maximum at which point the ferromagnetic material is saturated, M = M_{sat} (points II and III of Figure 4.5), and then decreases as cos(γ). The magnetic torque is gradually reduced to zero at angles of φ such that γ = ± π/2 (points IV and V). The value of $\Gamma_{magnetic}$ when γ equals zero is determined by Equation 4.7 and depends on the previously magnetized state of the ferromagnetic material. The intercept values are given by Equation 4.12,

$$\Gamma_{magnetic}(\gamma = 0) = \pm VB \cdot \mathrm{Min}\left(1, \frac{H_c}{N_D}\right) \tag{4.12}$$

The positive sign should be used for a beam most recently magnetized to yield a positive φ. The intercept value for the γ < 0 branch will be negative (point VI), and the intercept value for the γ > 0 (point VII) branch will be positive. The value of N_D in Equation 4.12 can be calculated by equating the magnetic torque and the anisotropy torque. The distance between the two intercepts is obtained by subtraction, and is shown in Equation 4.13.

$$\Delta\Gamma_{magnetic}(\gamma = 0) = 2VB \cdot \mathrm{Min}\left(1, \frac{H_c}{N_D}\right) \tag{4.13}$$

This value gives a measure of the separation between the two branches of the magnetic torque in the region of small γ. Equation 4.13 decreases with increasing softness (lower H_c) of the magnetic material, shape anisotropy, and external field. Larger ΔΓ corresponds to a higher degree of minimum magnetization and larger contact forces, but also may result in larger switching energy.

In order for a stable solution to exist and latching to occur, there must exist a value of φ such that the following expression holds:

$$| \Gamma_{magnetic} | > | \Gamma_{elastic} | \tag{4.14}$$

Thus, the magnetic torque generated must exceed the elastic torque resisting the angular movement. In Figure 4.5, these stable regions where the magnitude of the magnetic torque exceeds the magnitude of the elastic torque, are shown and labeled as "latched up" and "latched down." If unimpeded, such as by the presence of a substrate, the actuator will move to an equilibrium position where the magnetic torque and elastic torque are balanced when magnetized. These positions are given as points VIII and IX. These points correspond to the widest span of φ that can be obtained with a given device design and magnetic field. In order for the beam to make contact with either the top or bottom substrates the values φ_{top} and φ_{bottom} must satisfy the following condition, Equation 4.15.

$$| \varphi_{top} | < | \varphi_{max} |, \text{ or } | \varphi_{bottom} | < | \varphi_{min} | \tag{4.15}$$

This is equivalent to stating that the range of φ over which stable solutions exist must bound the values of φ corresponding to the latched up and latched down states. At such values of φ_{top} and φ_{bottom}, the magnetic torque exceeds the elastic torque. Graphically, this excess is the distance between points XII and XIII for the latched up state and points XIV and XV for the latched down state. The magnitude of this excess is related to the contact force between the top/bottom contact and the tip of the cantilever. Therefore, it is

also some measure of the quality of contact between the two surfaces.

4.3 Optimized Designs

Once a design is in hand that exhibits stable latched up and latched down states, the following parameters determine the attractiveness of the design: large gap distance, low cost, good contact force, and moderate magnetic field levels. In the case of an RF switch for example, the electrical isolation between transmission lines is a strong function of the geometrical arrangement of the transmission lines, improved by increase in their separation. Therefore, this is a case where large gap distances are desirable. However, once φ_{top} and φ_{bottom} begin to approach the values φ_{max} and φ_{min}, higher isolation comes at the cost of reduced contact force. Furthermore, once φ_{top} and φ_{bottom} surpass given values of φ_{max} and φ_{min}, changes must be made that either reduce the slope of $\Gamma_{elastic}$ (reduction in hinge stiffness) or increase in $\Gamma_{magnetic}$ (through further anisotropy, increased magnetic field). Reduction in hinge stiffness is achieved by reducing the hinge thickness. Increased contact force provides for a more stable latched position, and lower contact resistance [39-42], which is significant for potential electrical applications. Higher contact force can be achieved by increasing the magnetic field required to switch the device from one latched position to another, however at the expense of large coil currents (and switching energy).

4.4 Contact Force Modeling

For the beam to have a low resistance electrical contact, it is necessary to analyze the moments acting on the actuator, Equation 4.16.

$$\Gamma_{\text{magnetic}} - \Gamma_{\text{elastic}} - \Gamma_{\text{contact}} = 0 \tag{4.16}$$

Where Γ_{contact} is the torque due to the contact force. The magnetic and elastic torques have been given previously (Equation 4.7 and Equation 4.11). The torque due to the point of contact is given by Equation 4.17.

$$\Gamma_{\text{contact}} = F_{\text{contact}} \; X \cos\varphi \tag{4.17}$$

Where X is the length of the permalloy section of the beam. Substitution of the above equations yields an expression for F_{contact} in terms of the previously defined variables as follows, Equation 4.18.

$$F_{\text{contact}} = \frac{VB \cdot \text{Min}\left\{\frac{B\sin|\gamma| + \text{sgn}(\gamma)H_c}{N_D}, M_{\text{sat}}\right\} \cdot \text{sgn}(\gamma)\cos\gamma - k_\varphi(\varphi - \varphi^o)}{X\cos(\varphi)} \tag{4.18}$$

Here it can be seen that for a given design, the contact force at a given position is proportional to the difference between the magnetic and elastic torques evaluated at that position. Furthermore, both the volume of the magnetic element and the angular hinge stiffness scale as s^3, while the denominator scales as s (where s is the scaling factor of the

system size). Therefore the contact force decreases as the system scale is decreased. For a permalloy volume 1000x100x10 μm in a 10 mT external magnetic field and a permalloy length, X, of 1000 μm, the maximal contact force is 25/π μN, assuming complete saturation and negligible elastic torque. Hosaka [39] has shown that contact forces greater than 50 μN are necessary to achieve contact resistances below 100 mΩ, but smaller forces in the tens of μN may yield contact resistances in the 200 mΩ range. Therefore a magnetic volume greater than 10^6 μm^3 was anticipated for acceptable contact.

4.5 Results

To investigate the switching energies needed to actuate this type of device, three candidate designs were chosen to illustrate the variations in switching speed and switching energy. These variations are summarized in Table 4.1. Each design was generated to yield two stable equilibria in a magnetic field no greater than 25 mT. Each of the three designs was given a different degree of shape anisotropy, ranging from a single permalloy slab (N_L = 0.010) to long, narrow strips (N_L = 0.0010). These calculations are provided in Appendix B. This was done so that the effect of anisotropy on switching characteristics, in particularly those used in justifying a low-energy switching regime could be investigated. Additionally, shape anisotropy was varied in order to generate greater magnetic element movement at low magnetic fields. The beam length was varied in order to investigate switching speed on device size, as well as to quantify the additional power requirement anticipated for smaller devices. In its simplest form Equation 4.1 requires that the magnetic field produced by the integrated coil be of

the same size as the component of the external field in-plane with the cantilever beam. Smaller devices require a greater angular distance between the upstate and downstate, requiring the coil overcomes a larger component of the external magnetic field. Required values of the upper and lower substrate angles to achieve 100 μm actuation distance, φ_{top} and φ_{bottom}, are shown in Table 4.2 for each device. The hinge thickness was 2 μm for each design.

Table 4.1. Geometries of three candidate devices.

Design	Ni/Fe Design	Shape Demag. Factor	Hinge Design	Angular Range for 100 μm separation
1	8 strips; each 940 μm long, 30 μm wide, and 12 μm thick. Volume = 2.7 E6 μm^3	N_L=1.0 E-3 N_T= 0.95	2 hinges; 260 μm long, 40 μm wide, 2 μm thick	φ_{down}: -0.027 rad φ_{up} : 0.063 rad
2	1 section; 500 μm long, 200 μm wide, and 10 μm thick. Volume = 1.0 E6 μm^3	N_L =1.0 E-2 N_T= 0.95	2 hinges; 270 μm long, 50 μm wide, 2 μm thick	φ_{down}: -0.050 rad φ_{up} : 0.112 rad
3	4 strips; each 800 μm long, 30 μm wide, and 10 μm thick. Volume = 9.6 E5μm^3	N_L =1.0 E-3 N_T= 0.95	2 hinges; 290 μm long, 30 μm wide, 2 μm thick	φ_{down}: -0.027 rad φ_{up} : 0.063 rad

Graphical analysis of designs 1, 2, and 3 were performed and are shown in figures 4.6, 4.7, and 4.8, respectively. Designs 1 and 3 are shown with an external field of 10 mT and design 2 with 25 mT, since the lower magnetization values in this design required a minimum magnetic field strength for latching greater than 10 mT. For each latched state the magnetic torque line must exceed the elastic torque (curve a). The upper latched position for each device (point I) is located at the intersection of the upper magnetic torque line (curve b) with the $\varphi = \varphi_{up}$ line. Similarly, the lower latched position for each device (point II) is located at the intersection of the lower magnetic torque line (curve c) with the $\varphi = \varphi_{down}$ line. The angle corresponding to $\gamma = 0$ is shown (point V). This angle is different than $\varphi = 0$, due to the effect of the application angle of the magnetic field, α. This is done to regain symmetry of the latched states that is lost due to initial inclination angle of the beam (nonzero y-intercept). Device 3 displays a different relationship between the elastic torque and magnetic torque lines in Figure 4.8 when compared to the graphical analysis in Figures 4.6 and 4.7. The difference is that the upper magnetic torque line corresponding to the latched up state is readily stable at the lower stable position. That is, if the magnetization direction of the device could be instantly switched with a short current pulse through the coil, the pulse could be terminated and the magnetic torque line of the device would be switched from the bottom curve (c) to the upper curve (d). Then, without continued power to the integrated coil, the device would begin travel to the upstate. This behavior defines the short-pulse switching (SPS) regime.

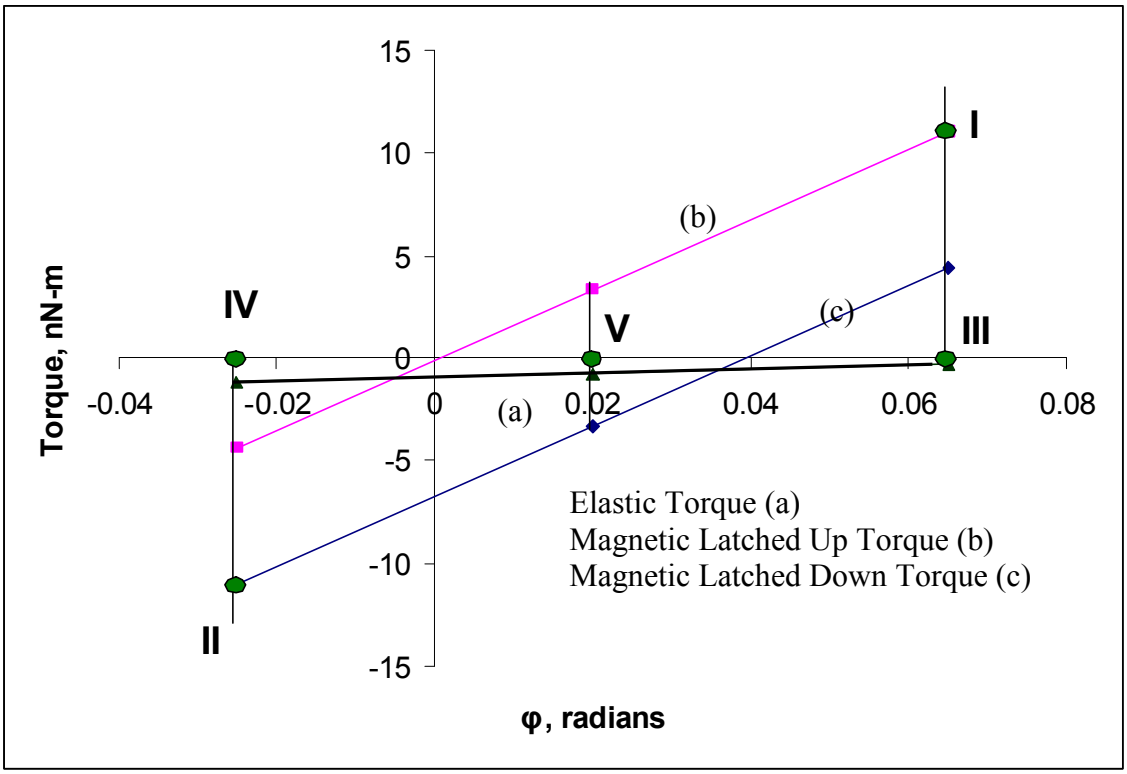

Figure 4.6. Stability schematic for a type-1 magnetic actuator in a 10-mT external magnetic field. The initial upward angular deflection is approximately 0.1 rad.

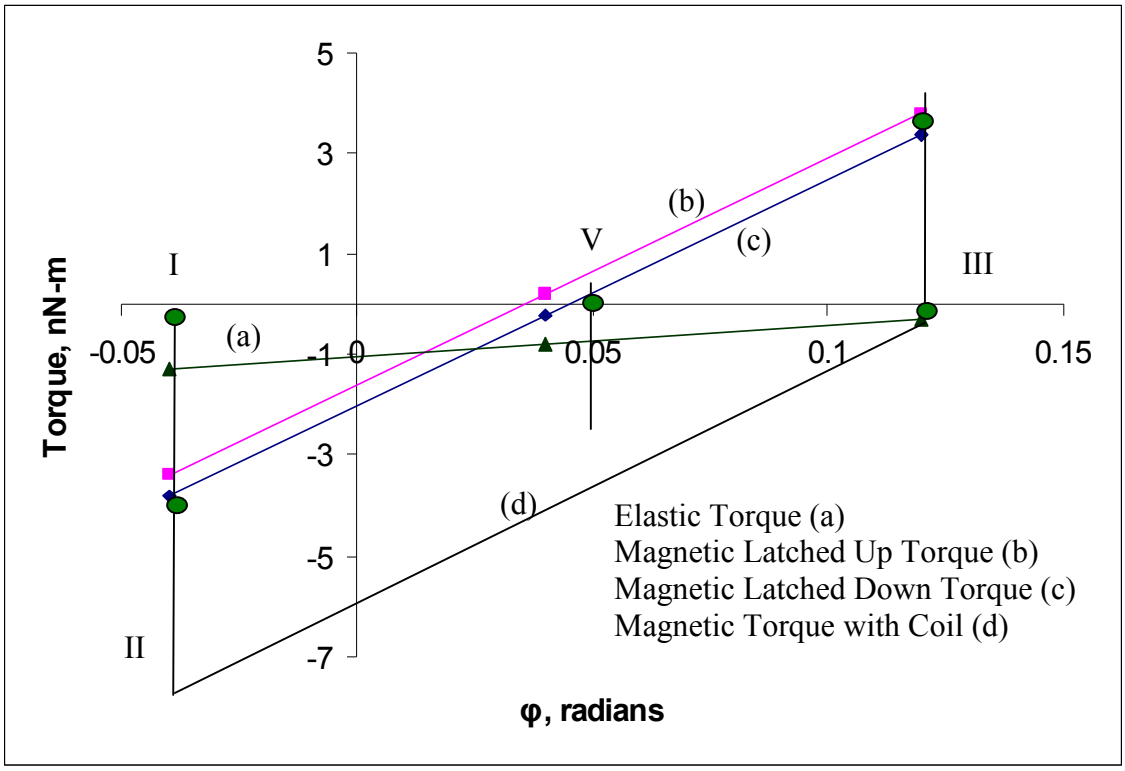

Figure 4.7. Stability schematic for a type-2 magnetic actuator in a 25-mT external magnetic field. The initial upward angular deflection is approximately 0.12 rad.

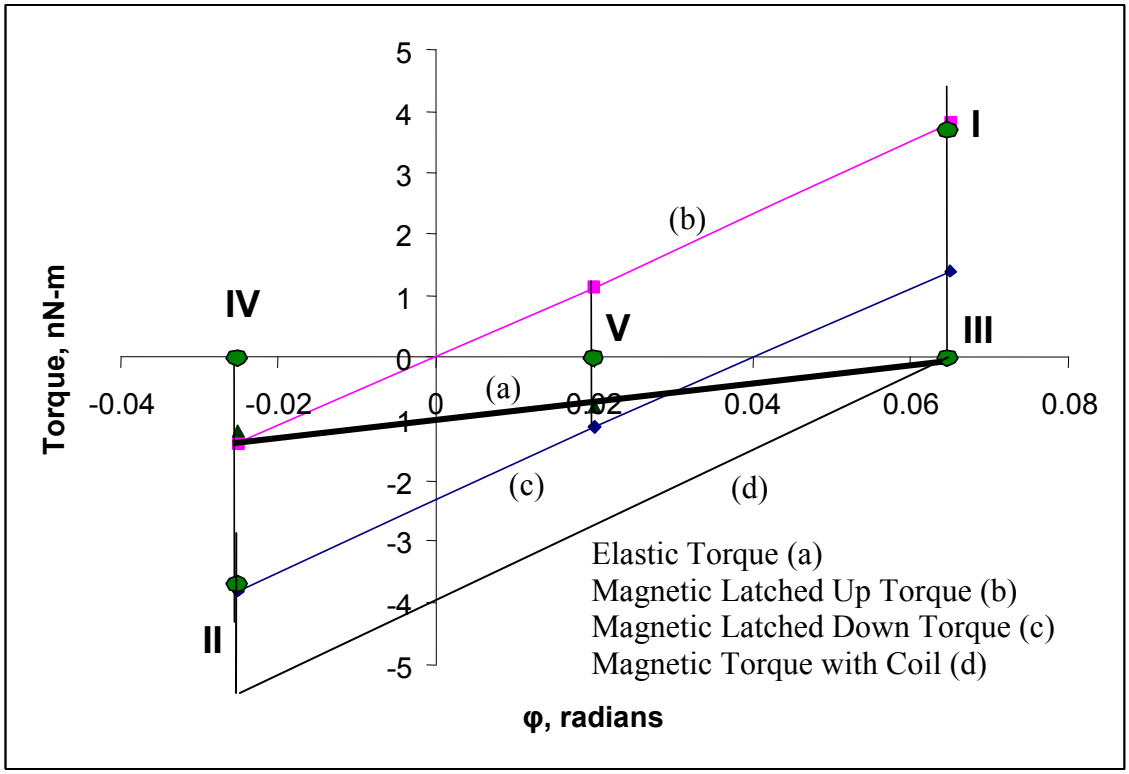

Figure 4.8. Stability schematic for a type-3 magnetic actuator in a 10-mT external magnetic field. The initial upward angular deflection is approximately 0.06 rad.

Shape anisotropy is significant in providing for SPS. Device 2, with the lowest degree of shape anisotropy, has the lowest relative separation of the two magnetic torque branches (explained by Equation 4.13), and shows that the previous direction of magnetization is not significantly influential in determining a stable equilibrium. Furthermore, the relatively low degree of shape anisotropy in design 2 requires a significant magnetic field to saturate the magnetic material in the reverse direction. This combination of small magnetic torque curve separation and low anisotropy prevents the existence of the short-pulse switching regime for design 2. However, devices 1 and 3, with much higher shape anisotropy, have much greater separation of magnetic torque branches; however, the relative placement of the magnetic and elastic torque lines at the substrate positions still depends on the background magnetic field level and hinge stiffness. Figure 4.6 demonstrates that design 1 does not satisfy the conditions for short-pulse switching, but could with a reduction in the background magnetic field and/or with an increase in the spring constant of the hinge. The vertical offset at $\gamma = 0$ is proportional to B (Equation 4.12), but the slope of the magnetic torque curve is proportional to B^2 (Equation 4.7). Therefore reduction in the external magnetic field would keep the upper magnetic torque line in excess of the elastic torque over a wider angular range, eventually reaching the bottom stable position. The dependence of the slope and offset of the magnetic torque curves on the magnetic field can be used to show the angular range over which the required relationship exists between the elastic and magnetic torques scales as B^{-1} for low stiffness hinges. It is for this reason that, regardless of shape anisotropy, short-pulse switching will not be observed for large actuation distances with background magnetic fields significantly larger than the 10 mT fields considered here. Continued

reduction in the background magnetic field, however, reduces the available contact force holding the device in the latched state. Only design 3 exhibits the short-pulse switching regime in at least one direction.

4.6 Discussion

The purpose of this work was to explore the performance limits of the design space of a magnetic MEMS actuator and, in particular, to determine the region corresponding to the lowest switching energy necessary to move the device from one stable state to another. Since static models demonstrating the magnetic behavior of each of the designs have been generated, additional information related to the operation of the device may be determined.

4.6.1 Minimum Latching Field

The strength of the latching magnetic field can be reduced in each of these designs to find the minimum external field that satisfies the latching criterion (Equation 4.14) in each of the stable states. At equality of this minimum condition, the magnetic torque equals the elastic torque. The minimum switching field values can be obtained for each of the designs by reducing the external field until no solutions for latching exist at the substrates.

4.6.2 Minimum Switching Field/Current

The minimum current supplied to the coil that produces a switching event can be determined by including the field produced by the coil in Equation 4.7, giving

$$\Gamma_{magnetic} = VB\left(sgn\gamma \cdot Min\left\{ \frac{B_{coil,x} + Bsin|\gamma| \pm H_c}{N_D}, M_{sat} \right\} \right) \cdot cos\gamma \qquad (4.19)$$

Where the +/- refers to the most recent magnetization state of the Ni/Fe. Furthermore, the component of the field in-plane with the beam acts to produce a magnetization opposite to the previous state. Equating Equation 4.19 with the elastic torque yields the criterion for device switching presented in the Introduction (Equation 4.1). That is, if this coil field is great enough to overcome the coercivity and the in-plane component of the external field, less the elastic torque, the device will begin movement to the other latched region, producing a switching event. This is seen graphically by requiring the magnetic torque line to be depressed below the elastic torque line by application of B_{coil}. Using 0.3 mT as the value of the coercivity, the minimum coil field necessary to create a switching event is found to be 0.3 mT for design 1 and 0.4 mT for design 3 (both operating at 10 mT) and 1.2 mT for design 2 operating at 25 mT. These minimum switching field values are summarized in Table 4.2 and form the lower bound asymptotes in Figures 7 and 8, which describe the influence of the coil field on switching speed and switching energy, respectively. The minimum coil field values increase with the background magnetic field, and for devices with low anisotropy (design 2) the elastic torque may not be

negligible. For example, switching from down to up for device 2 requires consideration of the elastic torque as shown in Figure 4.5. Furthermore, these calculated minimum magnetic field values are translated into minimum currents supplied to the coil via Figure 4.3.

For SPS, a larger current is needed since the applied magnetic field is now required to switch the magnetization of the magnetic material instead of just reducing it for the long-pulse method. The amount of extra current depends on the demagnetization factors, the elastic torque at the latched positions, the anisotropy torque, and the minor hysteresis loops of the ferromagnet, as will be shown in chapter 5.

4.6.3 Switching Dynamics

Once the magnetic torque is no longer dominant, additional information can be obtained from these models by considering the dynamic behavior of the device during a switching event, Equation 4.19.

$$J\frac{d^2\varphi}{dt^2} + C\frac{d\varphi}{dt} + k_\varphi\left(\varphi - \varphi^o\right) = \Gamma_{magnetic}$$
$$\text{where : } J = \frac{1}{2}m\left(x + X\right)^2 \qquad k_\varphi = \frac{Ewt^3}{6x} \tag{4.20}$$

Where C is the angular damping parameter, J is the angular moment of inertia of the cantilever beam, x is the hinge length, X is the length of the permalloy portion of the beam, w is the hinge width, t is the hinge thickness, E is the elastic modulus of the hinge

material, and $\Gamma_{magnetic}$ is given by Equation 4.18. Damping parameter values similar to that measured by Judy and Muller [25] have a negligible impact on the calculated switching speeds at the reduced angular velocities characteristic of the designs and external magnetic fields of interest here; hence, damping is neglected in calculations of switching speed. The magnetic actuators presented here are larger than those presented in [12], due to design constraints resulting from necessities of RF performance. In fact, the values of J of magnetic actuators described in Table 4.1 are 3 to 25 times are large as those in [12], diminishing the impact of the angular damping term. From this analysis, estimates of the minimum switching energy and time were obtained.

Figure 4.7 shows a model of device 2 with an initial inclination angle of 0.1 radians in a background external magnetic field of 25 mT. The elastic torque (a) is shown as a function of the inclination angle of the cantilever and is labeled 'elastic.' Since the cantilever has a certain amount of residual stress, the elastic torque is negative at a neutral beam angle. The slope of the elastic torque line is the angular spring constant of the hinges, k_{φ}. The magnetic torque curves (b, c) are also graphed on the figure, with the difference between them being the effect of the coercivity; i.e., once the device has been magnetized in the up state, the coercivity acts to increase the magnetic torque (b), whereas when the device is magnetized in the down state the coercivity acts to further decrease the magnetic torque (c). The vertical lines mark the angular range of motion of the device, allowed by the presence of the lower (point IV) and upper (point III) mechanical stops (substrates). An upper (point I) / lower (point II) latched state exists provided that the magnetic torque is more positive / negative than the elastic torque at the

upper / lower positions.

In order to switch the state of the device from latched up to latched down, an additional component of the magnetic field is added by supplying a current to the integrated coil. The field generated by this coil acts to reduce the magnitude of the magnetic torque created by the presence of the permanent magnet field thereby reducing the magnetization of the beam. The magnetic field generated by the coil must be great enough to bring the magnetic torque below the elastic torque line. This critical shift is shown in Figure 4.6 as the curve d. At this point, the net torque on the beam acts to reduce the inclination angle of the beam, φ, and the beam begins to accelerate toward the bottom substrate. For beams with low anisotropy, such as the beams described by Ruan et al. [27], the current pulse provided to the coil must remain powered until the unperturbed magnetic torque line is below the elastic torque line. Otherwise, once the coil is turned off, the beam will once again accelerate toward the upper substrate and switching will not occur. An instantaneous high current pulse is not sufficient since the lower magnetic torque line is below the elastic torque line while the beam is at the upper substrate. The beam must move the prescribed angular distance before the coil current is removed. In general, soon after this point, the coil current can be stopped, and the beam will continue to travel towards the bottom substrate, since the magnetic torque now acts in the opposite direction. As the device continues to move down, the magnetic element will magnetize further in the new direction, and the device latches against the bottom substrate.

According to Figure 4.7, the analysis just described does not apply to device 3, in

which the upper magnetic torque exceeds the elastic torque over the entire angular range of motion of interest. Therefore, in this case the coil must remain powered only until the magnetization in the device is sufficiently reversed so that when the coil field is removed, the magnetic torque will follow the bottom line. No portion of the upper magnetic torque line yields the bottom-latched position. Thus, for this device there is the added requirement that the magnetic torque must switch from the upper line to the lower line before the coil is turned off. However, the fact that the upper magnetic torque exceeds the elastic torque for all relevant φ introduces an asymmetry in the analysis for switching down and switching up. Since the upper magnetic torque line is stable at the lower substrate, simply moving from the lower line to the upper line is sufficient to produce switching of the device. Therefore, a short current pulse could be provided that will produce switching from the lower latched state to the upper latched state; and since no minimum amount of movement is required during the pulse to ensure stability, it is believed that this switching pulse may be made extremely short.

Table 4.2. Minimum external coil current for onset of switching and contact force for different configurations.

	Design 1	**Design 2**	**Design 3**
Minimum Operating Conditions			
$B_{external}$:	1.8 mT	13.0 mT	4.5 mT
B_{coil}:	0.3 mT (10 mT field)	1.2 mT (25 mT field)	0.4 mT (10 mT field)
Coil current:	40 mA	100 mA	35 mA
Latched Conditions			
Magnetization: Contact Force:	0.65 T (10 mT field) 14 μN (10 mT field)	0.22 T (25 mT field) 7.8 μN (25 mT field)	0.65 T (10 mT field) 4.2 μN (10 mT field)
Magnetization: Contact Force:	1.0 T (25 mT field) 53 μN (25 mT field)	0.43 T (50 mT field) 38 μN (50 mT field)	1.0 T (25 mT field) 18 μN (25 mT field)

Table 4.3. Modeled minimum switching times and energies for each design.

Design 1	Design 2	Design 3
Minimum energy: 85 μJ to switch 10 mT ext. field 1.2 ms pulse 0.6 mT – 40 mA thru coil	 1.0 mJ to switch 25 mT ext. field 2.1 ms pulse 1.5 mT – 140 mA thru coil	 (98+~0)/2=~50 μJ to switch 10 mT ext. field 1.4 ms pulse 0.5 mT from coil – 40 mA
Minimum Switch Time: 1.1 ms to switch @ 1.9 mT	 0.6 ms to switch @ 12 mT Higher current does not reduce switching time.	 1.3 ms to switch @ 1.9 mT

4.6.4 Contact Force

The contact force in the latched states for each device was determined through Equation 4.18 (Table 4.2). When the switching field is present, the magnetic torque is impacted, shown by reducing the upper magnetic torque line when switching from up to down (or increasing the lower magnetic torque line when switching from down to up). Once switching has been completed and the coil remains powered, it is apparent from Equation 4.19 that the presence of the switching field produces a greater magnetization, and thus a greater magnetic torque. The degree of excess torque over the minimum provided by the coil influences the speed of switching (greater driving force), and produces a greater contact force in the latched states if the coil remains powered. This

effect ceases to be enhanced once saturation of the magnetic material is realized during switching. The modeled contact forces (without coil current) for each device are shown in Table 4.2. The magnetization is greater when the coil current is supplied. The decrease in the degree of magnetization when the coil current is terminated produces a commensurate reduction in the contact force. As anticipated, design 1 is predicted to have the greatest calculated contact force, 14 μN. Both designs 1 and 3 retain 65 % magnetization once the current to the coil is terminated, but design 3 is calculated to experience a contact force of only 4.2 μN. The large decrease in the contact force between designs 1 and 3 is due mainly to the reduction in total permalloy volume as the degree of magnetization is calculated to be equal. Note that the reduction in contact force is greater than what would be predicted by ferromagnetic volume alone (3:1 ratio), since the hinges in both designs must overcome approximately 2 nN-m of elastic torque in order to make initial contact. Ruan et al. modeled contact forces for their magnetic actuators to be 10 μN in a 20 mT external magnetic field and 60 μN in a 50 mT external magnetic field [27]. These contact forces are significantly less than the type-1 devices presented here, in which 14 μN contact force is predicted in a 10 mT external magnetic field and 53 μN contact force predicted in an external magnetic field of only 25 mT. The type-2 and type-3 devices give contact forces closer to those of Ruan's device, owing to the reduced magnetic volume of design 3 and reduced shape anisotropy of design 2.

The greater contact forces predicted with design 1 show that the wider beam tip has an advantage, allowing for more patterned Ni/Fe strips to be present on a given device. Design 2 has a contact force (7.8 μN) bounded by designs 1 and 3, even though it has the

lowest shape anisotropy permalloy. The permalloy in design 2 does not exceed 22% magnetization in either latched state at the elevated 25 mT magnetic field; however, the fact that the device is shorter than design 3 and is in a larger external field results in an increased contact force. Design 2 could be modified to have a much larger contact force if further increases in shape anisotropy were to be incorporated into the design. A contact force in excess of 45 μN could be obtained if the permalloy were shaped in such a way as to achieve saturation at 25 mT; however, this increased contact force requires higher energy to switch the device in the greater background field of 25 mT. Furthermore, contact forces decrease with smaller switch sizes, as was shown in the Design section. Therefore, a larger benefit in contact force could be realized by raising the background magnetic field level from 10 mT to 25 mT in designs 1 or 3, but at the cost of increased energy to operate.

4.6.5 Minimum Latching Field

Table 4.2 shows that as the shape anisotropy is increased (going from design 2 to designs 1 and 3), the minimum external field necessary to achieve latched states decreases. This results from the increased magnetization due to the permalloy patterning. A greater external latching field, in turn, requires a greater switching magnetic field from the patterned coils, achieved by supplying increased current. This results in larger energy for a switching event.

4.6.6 Switching Speed and Energy

Figure 4.9 shows the impact of the switching field on the switching time. Increased switching fields, from the on-chip coil, act to increase the degree of magnetization of the ferromagnetic element, resulting in an increased driving torque and lower switch time. This effect continues to the point where the switching field results in complete magnetization of the beam. Further increase in the switching magnetic field does not reduce the switching speed.

This information was calculated to give Figure 4.10, where the energy to switch the 3 different devices is shown as a function of the switching field. Below some threshold value, the switching field does not totally eliminate the contact force and results in beam movement. Above this threshold value, small increases in the switching field result in large reductions in switching speed and energy; however, this effect quickly diminishes, and soon the switching energy again begins to rise, as shown in Figure 4.11. This means that the switching time does not decrease more than the square of the applied current to the coil that produces the switching field. The average energy to switch the device from one state to the other is plotted. These data are summarized in Table 3. Devices 1 and 3 are seen to require an order of magnitude less energy, and significantly less current due to their increased anisotropy and resultant ability to operate in lower magnetic fields. Furthermore, device 3 is predicted to require 40% less energy than device 1, owing to the SPS available from the downstate to the upstate. It should be noted that the long-pulse switching energy reported in Figure 4.10 is calculated assuming a current pulse is

supplied for the minimum duration that will produce a switching event. In most cases, the length of the current pulse was modeled to be approximately one-half the time for the beam to travel from φ_{top} to φ_{bottom}. However, the smaller device, design 2, has the potential for the shortest switching times, owing to its decreased mass and length. The lowest switching energy is expected to occur for design 3, in which one direction of switching is predicted to occur with very short current pulses and drastically reduced energy. An optimum design would have bi-directional SPS, patterned permalloy of designs 1 and 3, and the smaller beam size of design 2 to generate shorter beam travel times and larger contact forces sufficient for low resistance contact. For SPS, a larger current is required, but the contact forces and minimum external magnetic field for latching are unaffected.

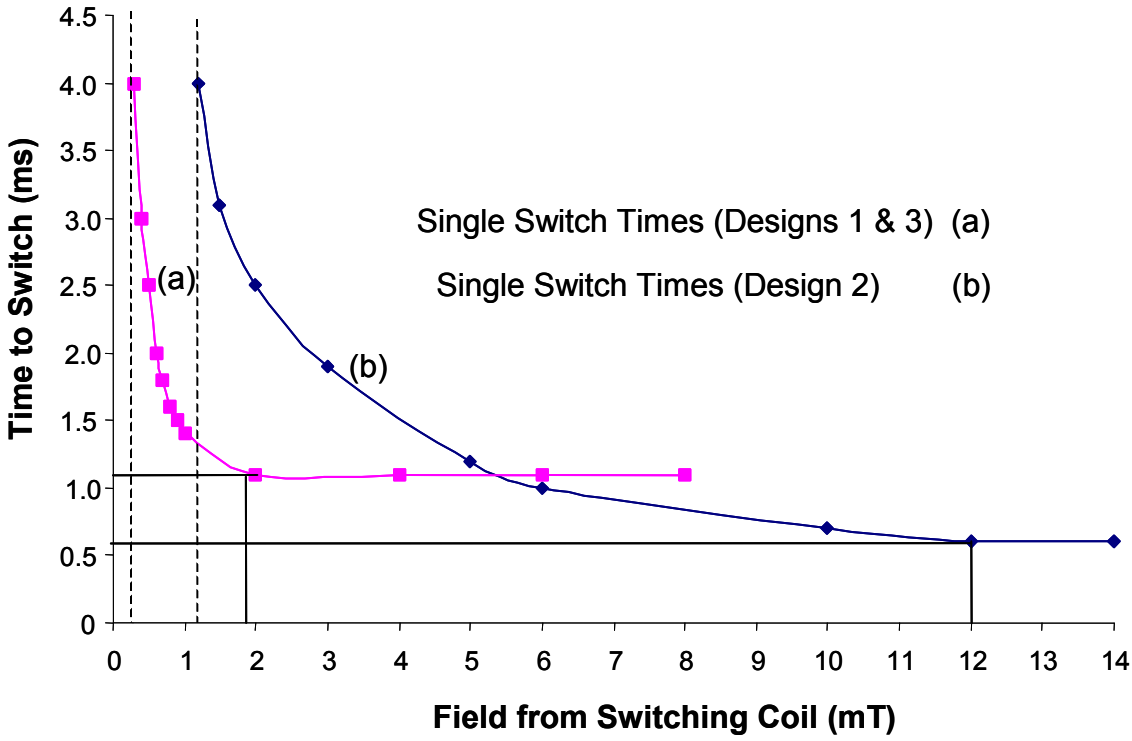

Figure 4.9. Modeled minimum pulse width required to switch the three device designs.

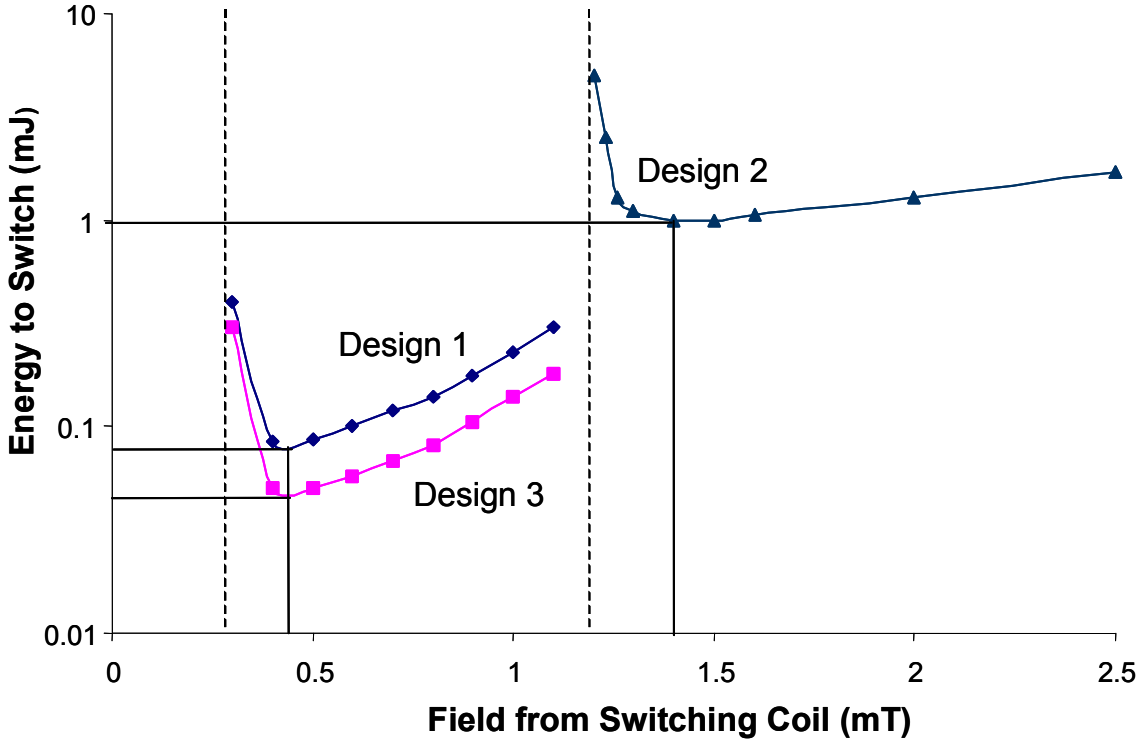

Figure 4.10. Modeled energy to switch the three device designs.

4.7 Summary

A bistable magnetic actuation mechanism has been modified and adapted for determining the design space for micro actuators with large actuation distance and low switching energy. This has led to a modeled regime where switching pulses may be exceedingly short with concomitant extremely low switching energy. The comprehensive modeling considers initial deflections of the cantilever and application angle of the external magnetic field to regain stability symmetry. Additionally, the very significant effects of the coercivity and shape anisotropy of the ferromagnetic material determine the separation of the two branches of the magnetic torque and permit modeling of switching speed, contact force, and minimum operating conditions. Designs differing in size, ferromagnetic volume, and shape anisotropy were chosen and highlight the difference between the long-pulse and SPS regimes. The designs vary in calculated values of contact force, with one design approximately of 14 μN at 10 mT, and larger contact forces possible with higher fields. They have switching speeds less than 3 ms, and suggest that switching energies could occur with as little as 84 μJ for the long-pulse regime and sub-μJ for SPS. SPS enables greater isolation to be achieved at greatly reduced switching energy, and minimal switching energy is achieved at the cost of reduced contact force. Compared to the previous data reported based on the long-pulse switching mechanism [27], the modeled relays in this study would actuate over much larger distances, 100 μm vs. 12 μm, with correspondingly slower switching speeds, 3 ms vs. 0.4 ms, and with similar energies, 84 μJ for long-pulse vs. 93 μJ, than previously reported [27].

CHAPTER 5

ASSEMBLY AND PERFORMANCE

A bistable magnetic MEMS actuator was fabricated using microelectronic processes including a two-substrate flip-chip assembly, multilevel metallization, and sublimation release to avoid stiction. The actuator was found to have excellent correspondence between observed and modeled behavior. The benefits of shape anisotropy are quantified. Lithographic patterning of the magnetic material into long narrow strips along the actuator's length resulted in much greater magnetic torques being developed at reduced external field levels. Low levels of anisotropy led to designs with low levels of magnetization and therefore required higher external magnetic fields, whereas high levels of anisotropy led to designs latching at 10 mT levels with contact forces greater than 14 μN with switching energies less than 100 μJ and a switching speed of less than 5 ms. More moderate levels of anisotropy resulted in a design space where < 1 μJ switching energies could be realized. Electrical performance has been demonstrated over 2 million cycles, and mechanical performance to 150 million cycles.

5.1 Theory

According to the analysis presented in chapter 4**,** the short-pulse switching (SPS) regime requires a much smaller overall actuation energy but requires a larger magnetic field (greater coil current) than the long pulse switching for a complete switching event to occur. That is, after the short-pulse is provided, some reversed magnetization, $M_{critical}$, must remain in the Ni/Fe in order to complete the switching event without any additional assistance from the coil. The minimum degree of magnetization that must be generated by the external coil to satisfy the SPS conditions must also satisfy the following, Equation 5.1, which follows from rearrangement of Equation 4.19.

$$B_{coil}\cos\varphi > B_{external}\sin\varphi + H_c + N_D M_{critical} \tag{5.1}$$

Where B_{coil} is the magnetic field produced by the coil, φ is the angle of inclination of the beam with respect to a given substrate, H_c is the coercivity of the permalloy, N_D is the demagnetization factor of the permalloy in the direction of M, $B_{external}$ is the background magnetic field, and θ is the angle the magnetization vector is rotated out-of-plane of the magnetic element. This required magnetic field for SPS exceeds the required magnetic field for long pulse switching (given by Equation 4.1) by the following quantity, Equation 5.2.

$$\Delta B_{coil}\cos\varphi > N_D\left(\frac{\Gamma_{elastic}}{VB_{external}} + M_{critical}\right) \tag{5.2}$$

Where V is the volume of the magnetic material, and $\Gamma_{elastic}$ is the elastic torque at the initial stable or latched position.

The minimum magnetization that must be realized in order for the SPS to succeed can be obtained through graphical analysis of the minor hysteresis loops of permalloy. Figure 5.1 depicts the major hysteresis loop of a ferromagnetic material in which the magnetization ranges from saturated in an initial direction to saturated in the opposite direction and back. Additionally, an example minor hysteresis loop is shown, which is followed whenever the magnetic field is diminished before achieving saturation. Assume the beam is initially in the downstate ($M < 0$) with magnetization given by point 1. A short current pulse is then supplied to the integrated coil, momentarily moving the magnetization along the bottom curve to point 2. Once the coil current is terminated, the magnetization will travel along a minor hysteresis loop to point 3, until reaching the same level of external field as initially in point 1. If the magnetization magnitude is sufficiently reduced so that the magnitude of the magnetic torque is now less than the elastic torque, the device will switch; and during switching, the magnetization will again increase due to the ever-increasing external field component along the permalloy beam. Once point 2 is passed, the magnetization will closely follow the major hysteresis loop (resulting in point 4). Through this figure, it can be seen that only a small value of the magnetization must be developed opposite the original direction in order for the remnant magnetization to closely follow the major hysteresis loop. In fact, if $M_{critical}$ is small compared to $\Gamma_{elastic}/(VB_{external})$, $M_{critical}$ may be neglected. This allows for an approximate value of

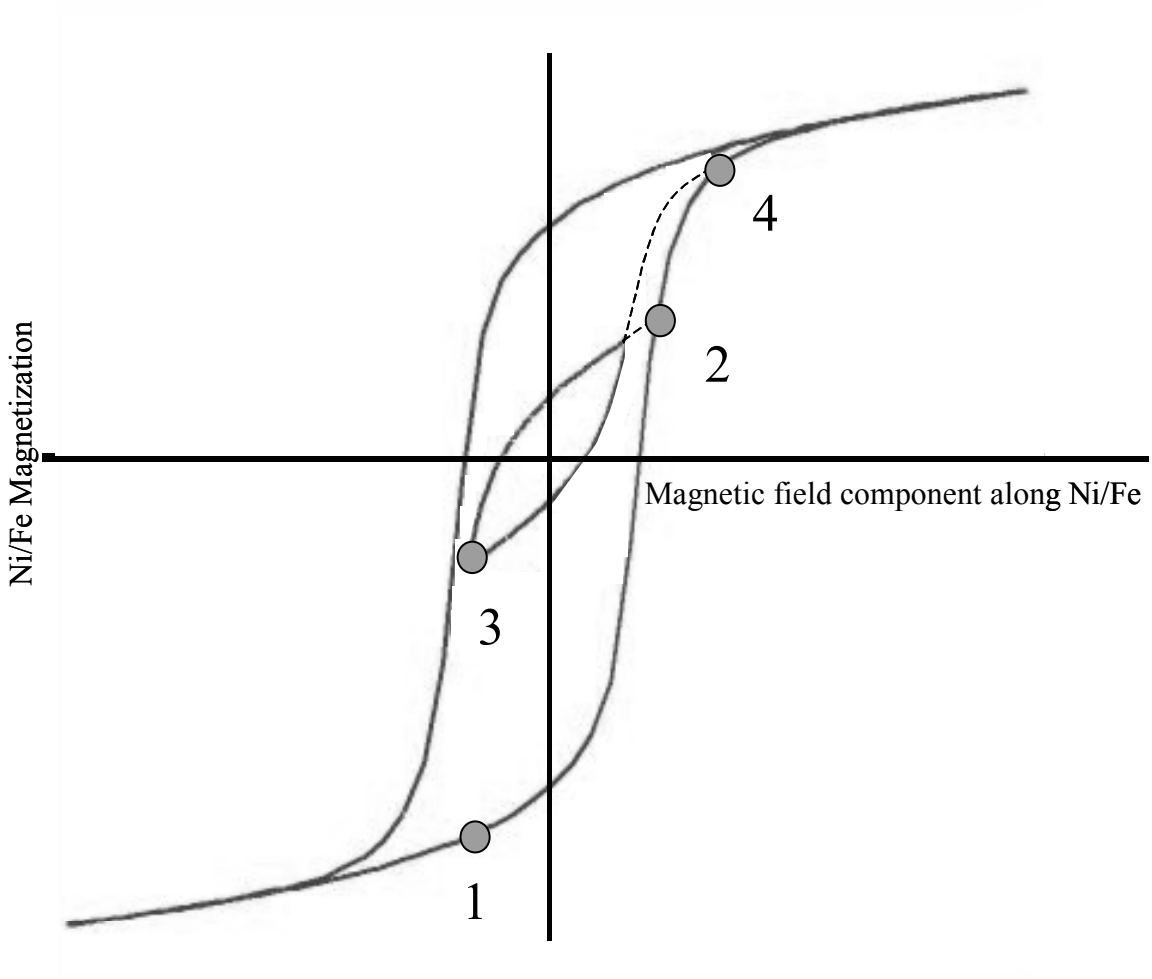

Figure 5.1. Hysteresis curves of a soft ferromagnetic material, depicting multiple path-dependent magnetization values at a given background magnetic field.

ΔB_{coil}, and therefore an increase in current, ΔI, to be calculated. Although a somewhat larger current must be applied, a great reduction in switching energy may be realized, as the time for magnetic realignment is much shorter than half the transient switching time.

In the remainder of this chapter it will shown that the minimum switching energy necessary to create a complete switching event can be anticipated and achieved by optimizing the demagnetization of the permalloy beam and the hinge stiffness. In order to test the validity of the optimization method, a two-substrate switch was fabricated using the optimized magnetic actuator to toggle between the microstrip transmission lines on opposing substrates. An exemplary fabrication process used to realize such a switch is provided. Before presentation of experimental analysis, typical fabricated devices are presented.

5.2 Magnetic Actuator Fabrication

The magnetic MEMS devices were fabricated on low-loss alumina substrates and flip-chip bonded together, according to the following processing steps.

5.2.1 Top Substrate Processing

The top alumina substrate is cleaned with a standard $5\%H_2SO_4+2\%H_2O_2$ / 1% ammonia / acetone / isopropanol sequence. The seed layer for the upper ground plane is DC sputtered with 200 Å of Ti, followed by 4 μm of Cu and 200 Å Ti (shown in Figure

5.2.1) which forms the ground plane. A 5 μm benzocyclobutene (BCB) film is then spun and cured as an isolation barrier between the ground plane and actuation coil. Next, 200 Å of Ti and 1800 Å Au is DC sputtered as seed layer above the BCB to form the actuation coil. 4 μm of soft gold is then electroplated at a current density of 5 mA/cm^2, a bath temperature of 50 °C, and a 600 RPM stir rate. AZ460 resist is spun on for 10 μm thickness, baked on a hot plate at 90 °C for 15 minutes, aligned to mask 1 to pattern the actuation coil, and exposed for 70 seconds for a total dose of 900 mJ/cm^2 (Figure 5.2.2). The resist is developed in AZ400K at a ratio of 1 part AZ400K to 4 parts DI water for approximately 3 minutes (5.2.3). The AZ resist is a positive tone resist, so the exposed regions are removed by the developer solution. Gold is etched for about 7 minutes in KI/I_2 solution to form the coils (5.2.4), and the photoresist is stripped in acetone. The exposed Ti seed layer is also stripped (5.2.5). The substrate is flipped over**.** The seed layer for the microstrip transmission line is deposited by DC sputtering 200 Å of Ti, followed by 2000 Å of Au. 4 μm of soft gold is electroplated to form the metal layer for the microstrip transmission line. AZ4620 resist is spun and exposed through mask 2, aligned to the previously patterned backside of the alumina substrate (5.2.6). After the photoresist has been patterned with the microstrips, Au and Ti are etched; and photoresist is stripped (5.2.7). The Au microstrips, along with the Au ground plane on the opposite side, will form the transmission lines. The next step is to plate up the tall posts which will act as standoffs to provide adequate substrate separation. 150 Å Ti is electron beam deposited, followed by 2000 Å Cu and 150 Å of Ti (5.2.8) to be used as an electrical bus for electroplating. A thick 30 μm layer of AZ4620 is spun onto the substrate and baked on a hot plate at 90 °C for 20 minutes. The substrate is aligned to mask 3, and the

photoresist is exposed for a total dose of 1550 mJ/cm^2 and developed to form the upper post vias. The Ti layer is removed with a 20 second dip in buffered oxide etch (BOE). The upper posts are formed by electroplating 30 μm of soft gold using the same conditions as before. This requires about 100 minutes electroplating time. Sn/Pb solder is used as a bonding medium and is electroplated above the 30 μm gold using a pulsed bath at a current density of 5 mA/cm^2 (5.2.9). The photoresist is stripped in acetone, and the top substrate is placed aside during the processing of the bottom substrate (5.2.10).

5.2.2 Bottom Substrate Processing:

The bottom alumina substrate is cleaned with a standard 5%H_2SO_4+2%H_2O_2 / 1% ammonia / acetone / ***i***sopropanol sequence. 200 Å of Ti and 1800 Å gold are DC sputtered as a seed layer for the lower layer transmission lines. The microstrip transmission line metal layer is formed with 4 μm of soft gold, which is electroplated at a current density of 5 mA/cm^2 at a bath temperature of 50 °C and 600 RPM stir rate. AZ460 resist is spun on for 10 μm thickness, baked on a hot plate at 90°C for 15 minutes, and aligned to mask 4. Gold is etched and photoresist is stripped, as shown in Figure 5.2.11, forming the transmission lines. Next the tall standoff posts and anchors are deposited. 150 Å Ti, followed by 2000 Å Cu and 150 Å Ti using electron beam evaporation. (Note, the Cu here is to act as a seed layer and electrical bus for the post and beam electroplating on the bottom substrate. A different metal is required so as to not lose the microstrips already patterned in Au.) A 30 μm thick layer of AZ4620 is spun

onto the substrate and baked on a hot plate at 90 °C for 20 minutes (5.2.12). Mask 5 is aligned, and the resist is exposed for a total dose of 1550 mJ/cm^2 and developed, forming the post vias. The Ti layer at the bottom of the vias is removed with a 20 second dip in buffered oxide etch (BOE) to provide adequate adhesion of the posts with the substrate. The lower posts are formed by depositing 30 μm of soft gold using the same electroplating conditions as before (5.2.13). This 30 μm photoresist is not removed and is instead used as a sacrificial layer for subsequent processing. 150 Å of titanium is electron beam deposited, followed by 1500 Å gold, as a seed layer for beam formation, and 2 μm of soft gold is electroplated using the same conditions as in top substrate processing. Note this thickness of soft gold will be the thickness of the cantilever hinges. AZ4620 is coated a second time (10 μm) and exposed through mask 6 at a dose of 900 mJ/cm^2 to form the permalloy mold. After the resist is developed, 12 μm of permalloy is selectively electroplated using a current density of 17 mA/cm^2 for 20 minutes (5.2.14). The permalloy bath composition was given by Ahn and Allen [18]. The top photoresist is then stripped with acetone. An additional layer of gold is then deposited over the lossy permalloy to improve the thermal and electrical properties of the device. The upper Au layer mold is then patterned with a 10 μm AZ4620 resist layer and exposed through mask 7 for 75 seconds, for a total dose of 1000 mJ/cm^2. After the resist is developed, the 2 μm soft gold upper layer is selectively electroplated over the permalloy, and then the photoresist is stripped (5.2.15). Next a layer of Sn/Pb covering the standoff posts is needed to form a low-temperature eutectic bond between the two substrates. To accomplish this, an AZ4620 resist layer is spun on for 10 μm, aligned and exposed through mask 8 and developed. 8 μm of Sn/Pb solder is electroplated using same bath and

conditions as found in top substrate solder electroplating (5.2.16). The final step is to pattern the multi-metal stack in the photoresist to form the RF switches. This is done by spinning 10 μm of AZ4620 and exposing through mask 9 for 70 seconds, for a total dose of 900 mJ/cm^2. The entire gold stack is then etched for about 7 minutes in KI/I_2 solution. Constant agitation is necessary. After the beam material has been etched, the Ti layer is removed with 15 second dip in buffered oxide etch (BOE), and the top photoresist is stripped in acetone. Last, a 100 Å Ti seed layer and a 4 μm ground plane layer are sputtered on the backside of the wafer to complete the lower substrate microstrip waveguide (5.2.17).

Both alumina substrates are then diced, and in order to avoid stiction in the release process the devices are released according to the following steps: the 30 μm thick photoresist layer is stripped with acetone; the Ti layer is removed with a 15 second BOE dip; the Cu seed layer is etched with 5% HAC / 2% H_2O_2 solution; the bottom Ti layer is removed with a 20 second BOE dip; devices are then soaked in acetone. Released beams are then transferred from acetone to clean cyclohexane. Dies are individually removed from cyclohexane, and after removing excess cyclohexane, are placed in a cool (0 °C) nitrogen-purged thermos directly above an external magnet. The devices are allowed to warm slowly, resulting in sublimation of the cyclohexane. Once the cyclohexane in contact with the cantilever beam has sublimed, the beam bends out of plane and stiction-free release of the devices is achieved. Mating pieces are then aligned and brought into contact using a Flip-Chip Bonder. The solder is heated and flows, bonding the pieces together (5.2.18).

The magnetic actuator forms a cantilever, which is doubly hinged to a post attached to the lower substrate. The post extends 30 μm above the lower substrate. The actuator provides a transmission path to switch between the two microstrip transmission lines on either substrate. With the exception of the thin layer of Sn/Pb solder bonding the connection-posts between the two substrates, the entire electrical signal path, including the posts, hinges, and contact pads were fabricated of gold. The ferromagnetic element of the beam is clad on both sides with 3 μm of gold to reduce thermal-induced bending and improve electrical performance. The offset of the two substrates is determined by the post height and solder thickness. An integrated electrical coil was patterned on the outside of the two-substrate assembly and is shielded by means of a ground plane to avoid any pick-up of the RF signal in the actuation coils.

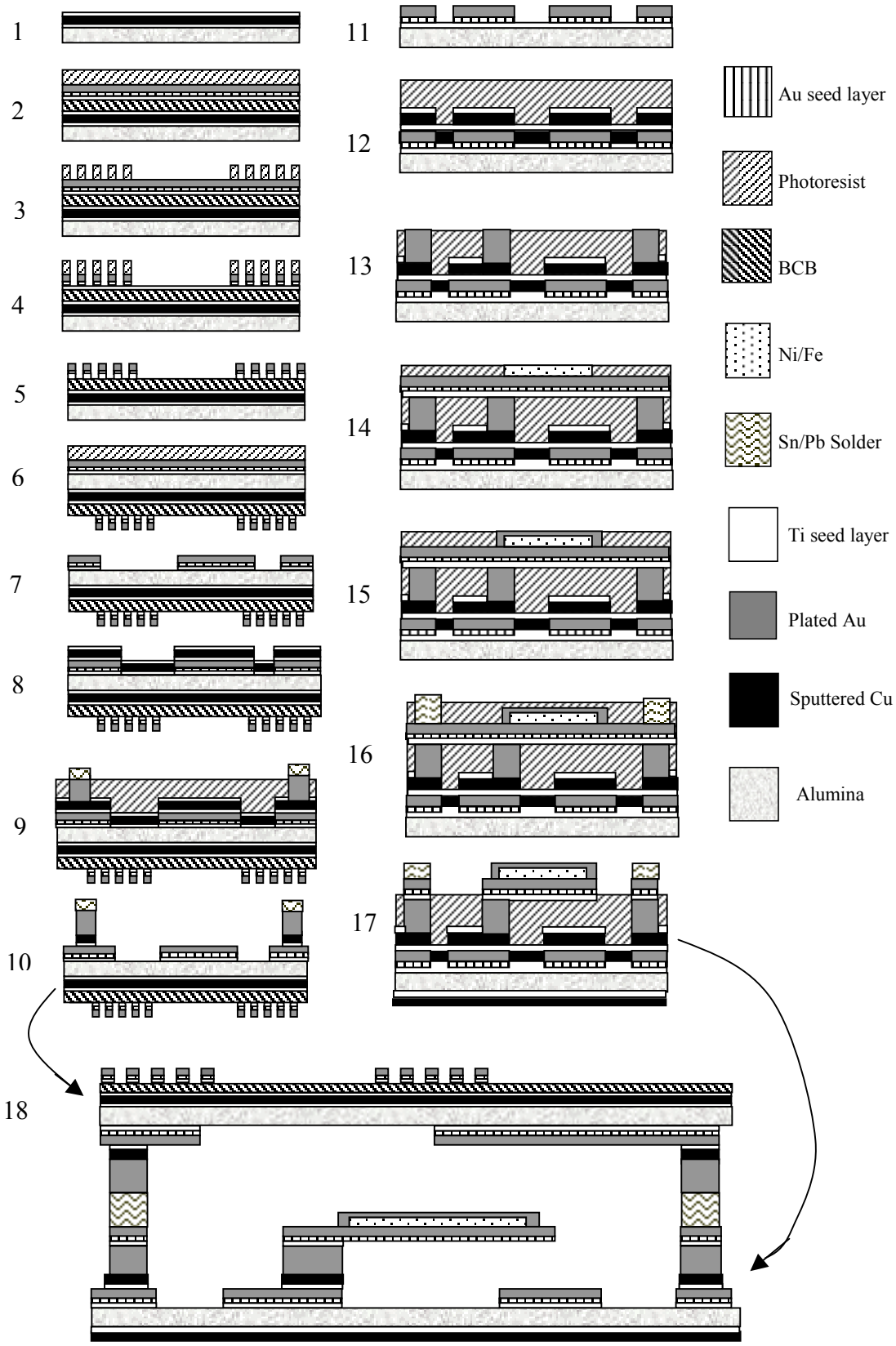

Figure 5.2. Selected processing steps for fabrication of magnetic actuator test device.

5.3 Results

Three different devices were built to match the three designs described previously [28]. The devices that were fabricated were summarized in Table 4.1. Designs 1 and 3 have longer beams with several patterned Ni/Fe strips, while Design 2 is a shorter device with a single Ni/Fe section. Previous work predicted Design 1 to have a 14 μN contact force at a background 10 mT magnetic field, whereas design 2 has a contact force about 8 μN in a 25 mT external magnetic field. Greater contact forces are achieved with larger background fields, with contact forces increasing as B^2 for designs with low anisotropy (design 2) and increasing with B for designs with high shape anisotropy (designs 1 and 3). Reduced field levels were used to facilitate low-energy switching. Design 2 was predicted to switch more quickly than the others, owing to reduced mass and greater driving torque during switching (proportional to $B_{external}$), but with a greater energy expenditure. Design 3 was designed to be a compromise between the first two designs.

Early fabricated type-2 devices depicting the actuator in the up and down positions are shown in Figures 5.3 and 5.4, respectively. Figure 5.3 shows an SEM micrograph of a sample magnetic actuator. The permalloy is patterned into a single continuous block which covers most of the gold cantilever. The gold microstrip transmission lines leading to the beam hinge, as well as the transmission line from the contact pad on the bottom substrate are both visible. In addition, other posts are present that determine the total separation of the two-substrate assembly. Figure 5.4 shows a closer view of the same device in the downstate, in contact with the bottom transmission line. The bilayer

permalloy/Au beam structure is evident.

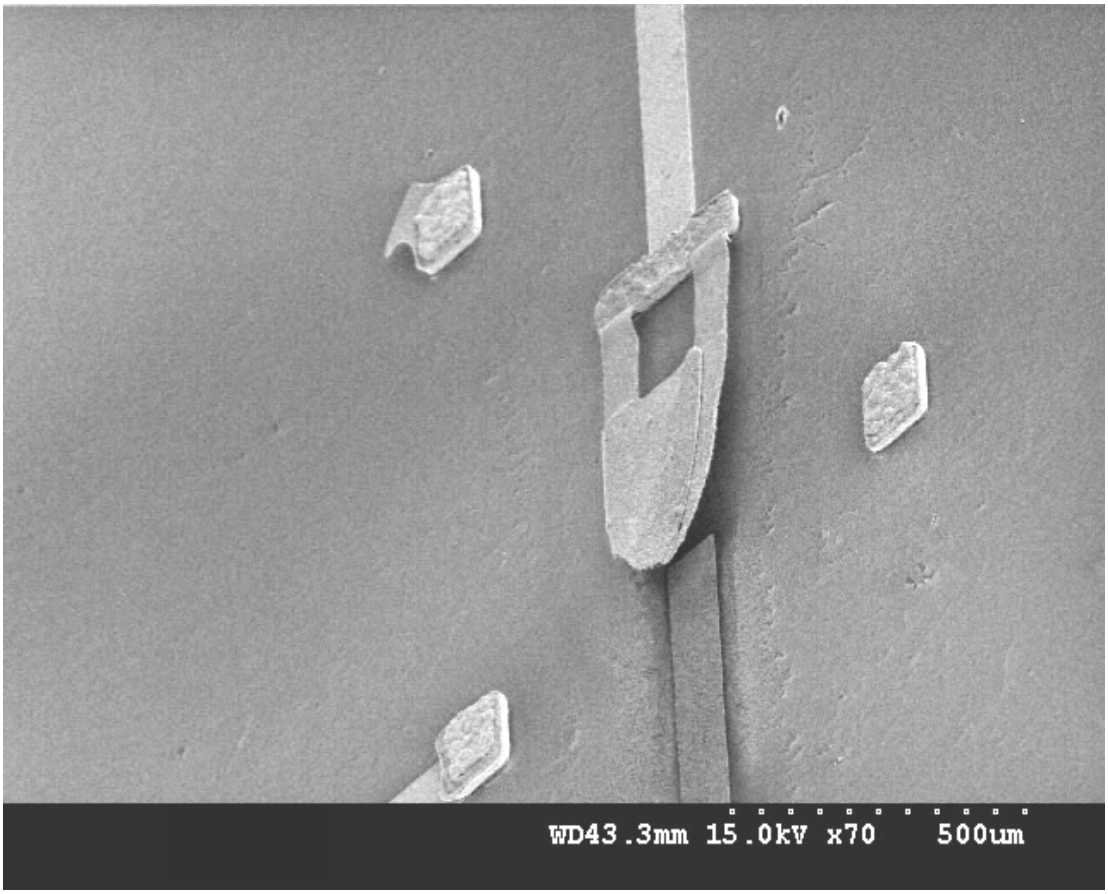

Figure 5.3. SEM of type-2 magnetic actuator above the contact pad in the up state.

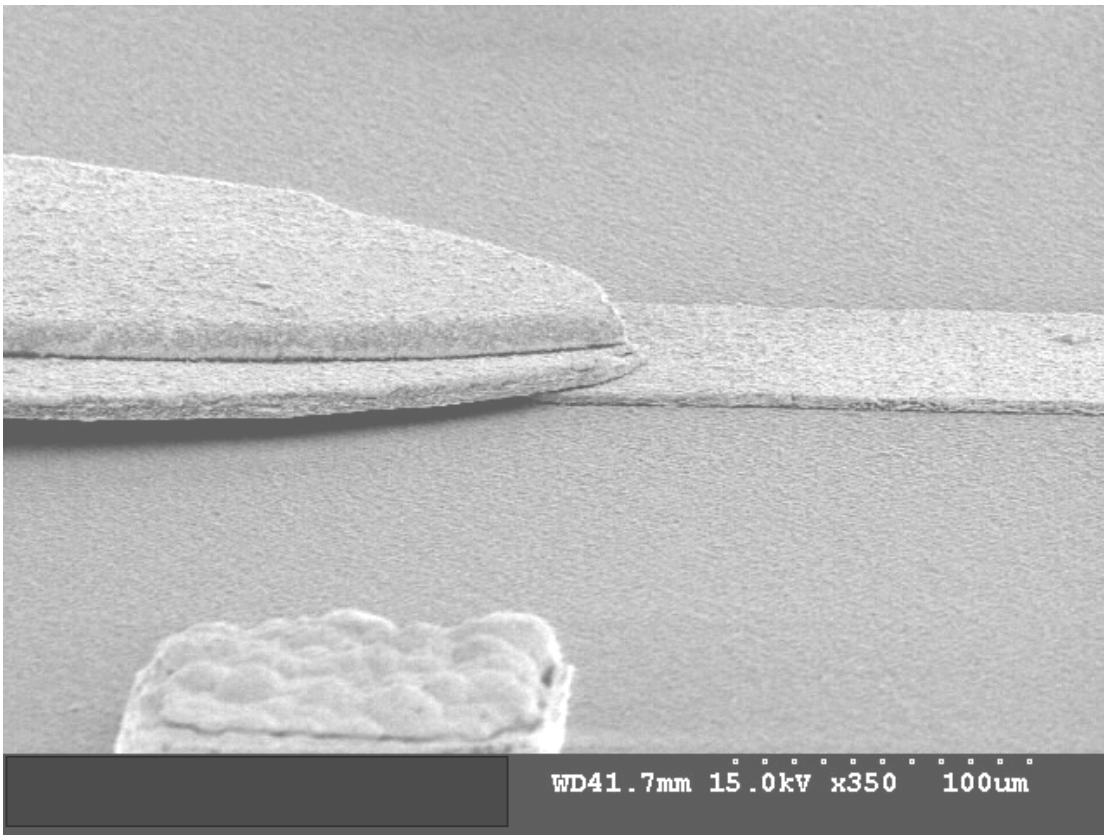

Figure 5.4. SEM of type-2 magnetic actuator making contact with the transmission line in the down state.

The attachment of the 2 μm thick cantilver hinge to the 30 μm elevated gold post is shown in Figure 5.5. In order for high device yield to be realized, it was necessary for the gold hinges to be at least 1 μm thick. Thinner hinges were often subject to inadequate contact to the elevated post, resulting in single-hinged devices. Also, weak hinges were also more easily damaged during the many solvent treatments during the release process.

In addition, thin gold hinges contribute to higher insertion loss since the number of available skin depths for transmission of the RF signal is reduced. For these reasons, the gold hinge thickness was fabricated to be at least 2 μm.

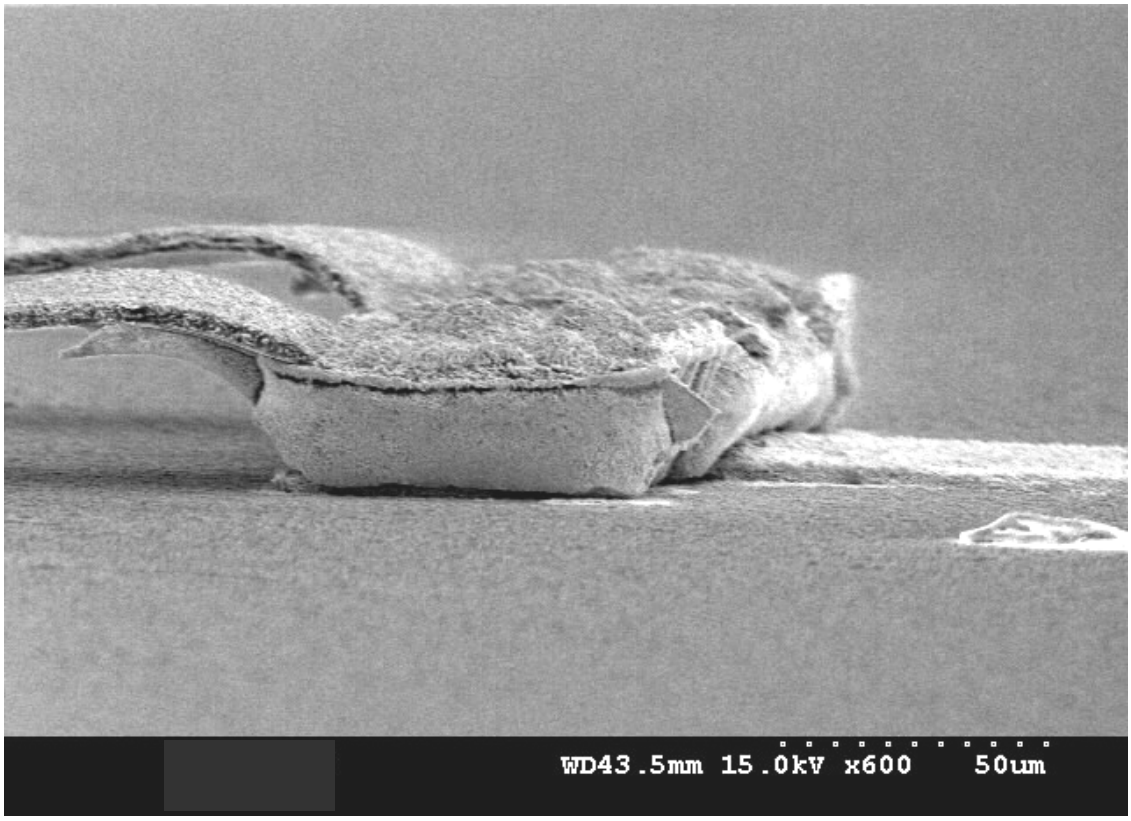

Figure 5.5. On left, the attachment of the gold hinge to the gold anchor of a fabricated type-2 magnetic actuator is shown. On right, the gold transmission line leads to the anchor.

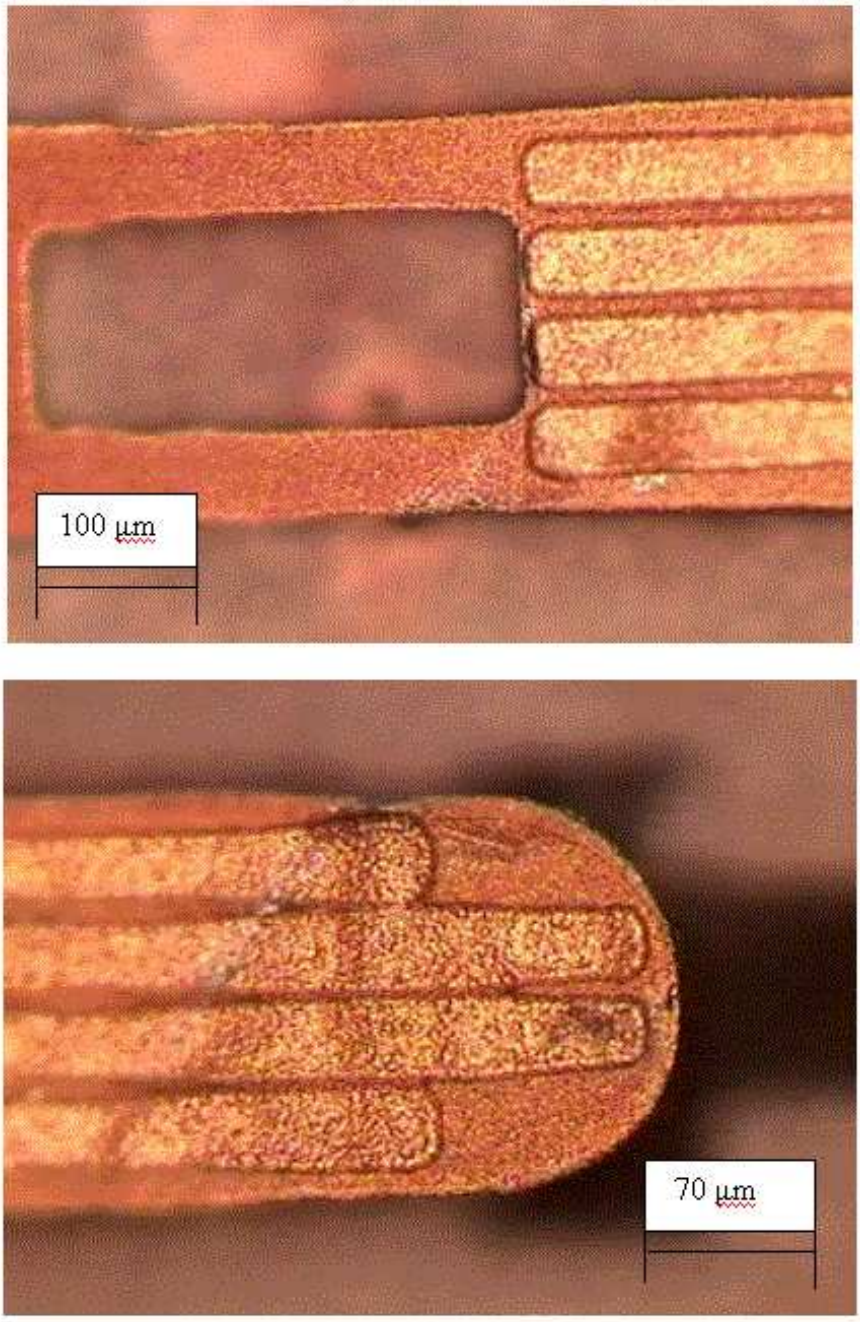

Figure 5.6. Cantilever end of type-3 design. a) shows the hinges, while b) shows the device tip.

The hinge and tip regions of a fabricated and released type-3 actuator are shown in Figures 5.6a and 5.6b, respectively. The actuator tip is approximately 50 μm above the substrate surface. The permalloy is patterned into four long, narrow strips for increased magnetization as described in chapter 4. In Figure 5.6b, the dark shadow on the right side of the image is the contact pad on the alumina substrate. In these images, gold has been electroplated over the permalloy strips. Figure 5.7 shows the tip region of a fabricated and released type-1 actuator. Note the eight gold plated permalloy strips. In these images, the copper seed layer protecting the gold microstrip transmission lines has not been removed and is responsible for the dark rough substrate surface.

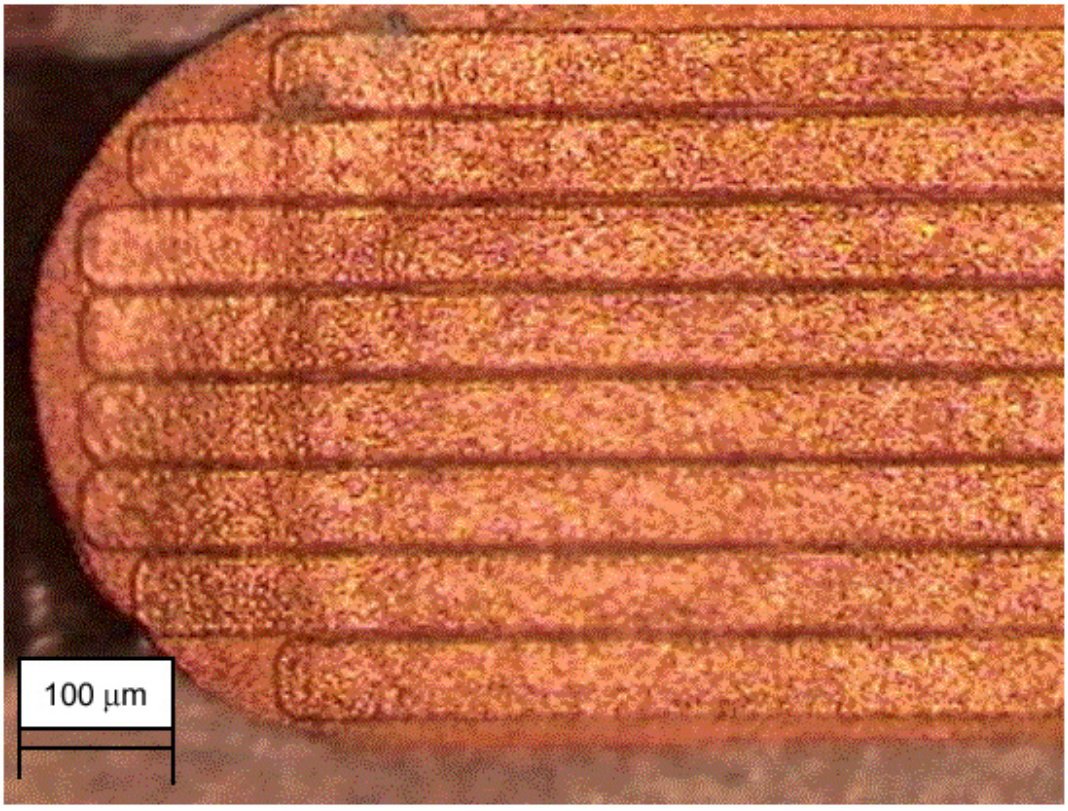

Figure 5.7. Cantilever end of type-1 design, showing the highly shape anisotropic 8 Ni/Fe strips.

The completed two-substrate assembly is shown in Figure 5.8. The upper substrate, with the printed coils exposed, is slightly smaller than the underlying bottom substrate. This is done so that wire bonding can easily be performed to the exposed contact pads on the perimeter of the bottom substrate. The completed chip shown measures 10 mm x 5 mm and contains two independent MEMS SPDT switches forming a transfer switch, each with its own switching coil.

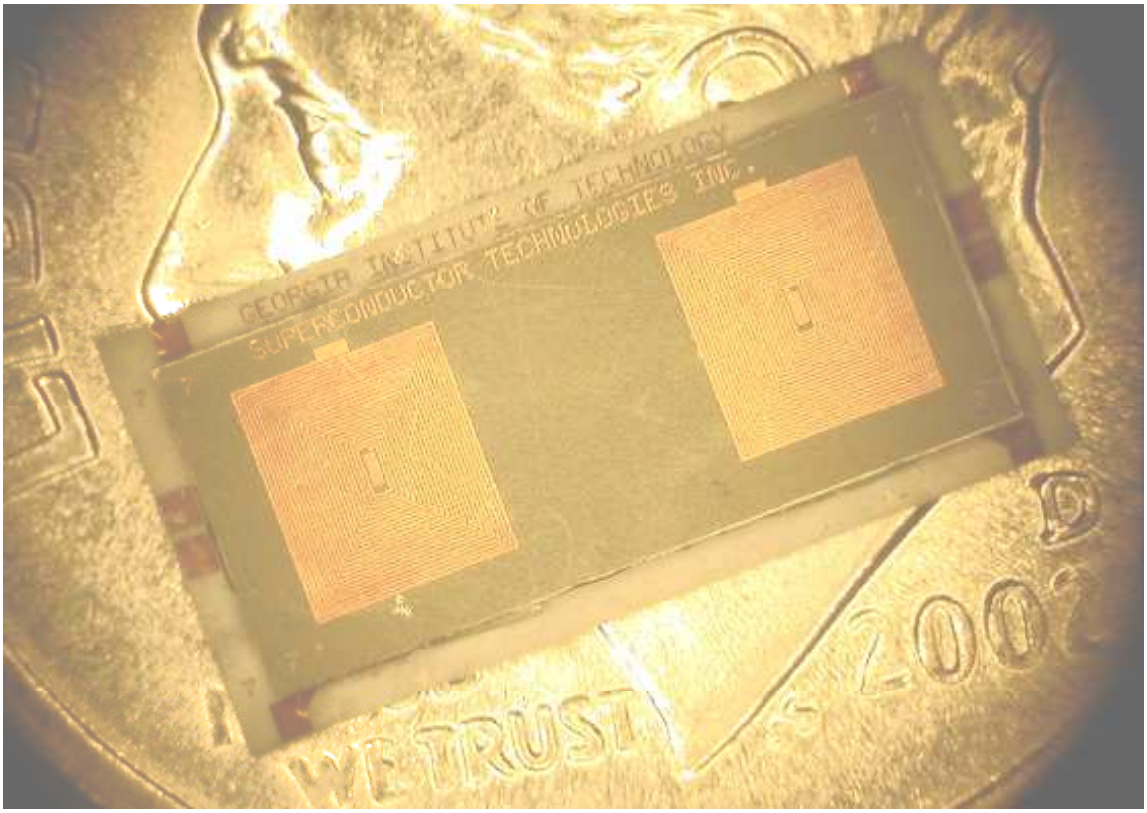

Figure 5.8. MEMS actuators assembled (size compared to U.S. dime (diameter 17.9 mm).

5.3.1 Modeling Comparison

Before comparing modeled and experimental dynamic operation, static response was examined to ensure accurate determination of magnetic volume, hinge stiffness, coercivity, and shape anisotropy. The response of the devices to external magnetic fields was tested above a calibrated electromagnet. Devices were tested in air at ambient conditions without an upper substrate. Field levels were confirmed with a handheld GMW, Inc. Hall Teslameter. In the presence of an external magnetic field, the magnetic beams rotate in order to increase their alignment with the field. This behavior is shown in Figure 5.9. In figure 5.9a, a sample device is shown from a side-view in a low background magnetic field. It can be seen that the beam makes an angle above the vertical. As the background magnetic field increases, the beam deflection increases as well (Figure 5.9b). The response of the three designs (presented in chapter 4 and detailed in Table 4.1) to external magnetic fields is presented in Figure 5.10. The initial inclination angle of each cantilever is the y- intercept value. A gradual increase in angular position of the beam is seen with application of low magnetic field. As the external field is raised, the beam moves more easily as a greater component of the external field lies along the beam length, producing a higher level of magnetization and therefore a greater magnetic torque. Eventually the magnetization of the beam becomes saturated, and experiences a slow asymptotic approach to $\pi/2$. For devices 1, 2, and 3, saturation appears to occur at 3 mT (point 1s), 22 mT (point 2s), and 6 mT (point 3s), respectively, as shown in Figure 5.10.

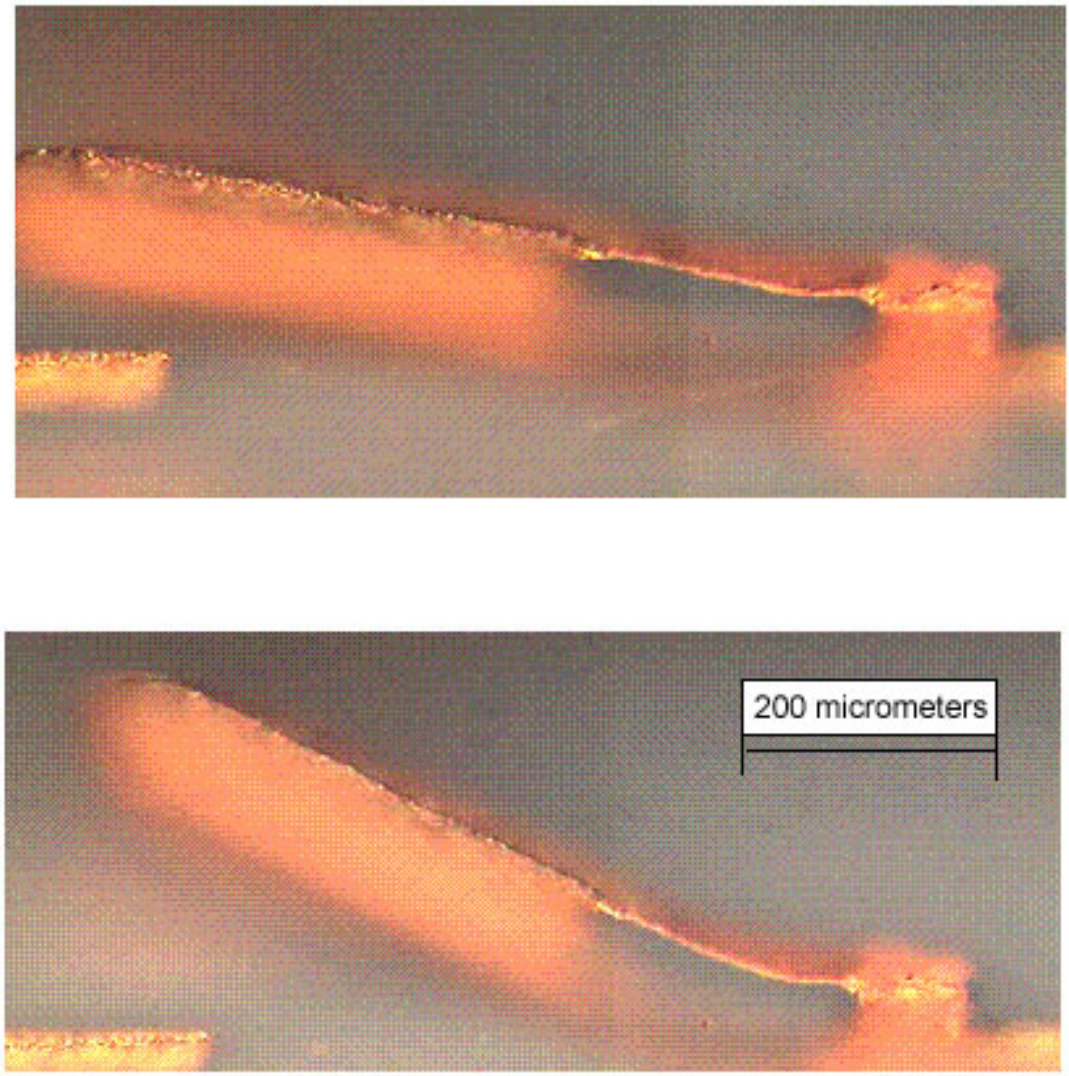

Figure 5.9. Magnetic beam under the application of a a) 10 mT external magnetic field, b) 30 mT external magnetic field.

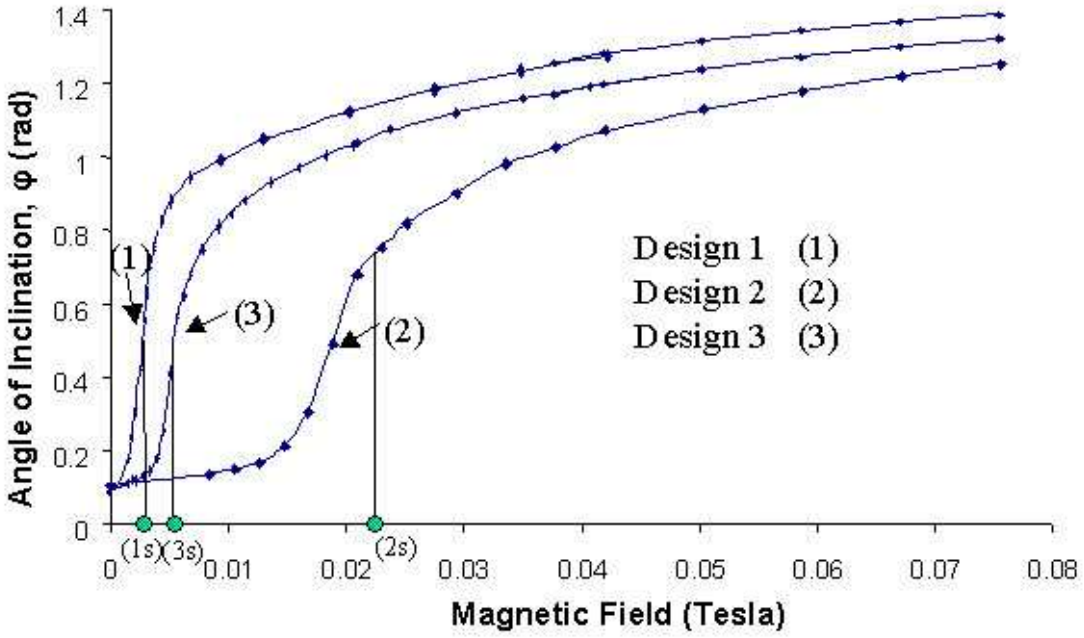

Figure 5.10. Observed characteristic deflection curves for three actuator designs, depicting behavior above and below saturation.

Note that these data follow the trends predicted by increased shape anisotropy and permalloy volume; that is, the designs with smaller length demagnetization factors and greater permalloy volume, resulting in a lower saturating external magnetic fields. Each area of these characteristic curves reflects a different combination of the above-mentioned factors. For instance, the onset of saturation is most strongly influenced by the combination of demagnetization, background magnetic field, and hinge stiffness. The behavior above saturation, however, is dominated by the relative magnitude of the hinge stiffness and magnetic volume; and low-field level behavior is influenced by the coercivity, demagnetization, and initial beam deflection. Excellent agreement between modeled and experimental behavior close to and above saturation permitted variation of the coercivity parameter until a best-fit value of 0.3 mT (250 A/m) was obtained for each device design. This value is in line with previously reported data [25]. It should be noted that the coercivity is a critical parameter for successful SPS. Low values of coercivity bring the $+H_c$ and $-H_c$ magnetic torque curves close together, virtually eliminating the possibility for SPS by reducing the range of hinge stiffness giving elastic torques bound by the magnetic torque and further diminishing the contact force available. Higher values of coercivity increase the potential for SPS and increased contact force, but due so by drastically increasing the magnitude of the current necessary for the short pulse, representing an increase in system cost.

The effect of reduced length demagnetization factor (the N_L value) on the characteristic curve shown in Figure 5.10 is quite large between device 2 and device 3, but the difference is less so between devices 3 and 1. This is explained by the increasing

impact of θ in the denominator of Equation 4.6. As the length demagnetization factor, N_L, decreases in going from device 2 to 3 and 1, θ is no longer dominated by N_L. In fact, while θ is negligible over the entire angular range of interest for the limited shape anisotropy in design 2, for both designs 1 and 3, θ plays an increasing role in determining the approach to saturation. This difference shown in Figure 5.10 between devices 1 and 3 is due to the larger permalloy volume of device 1 (producing a larger magnetic torque in a given magnetic field, resulting in a greater beam angular deflection for the same hinge stiffness, producing a larger permalloy magnetization, etc.), even though device 1 has a length shape demagnetization value smaller than in design 3.

Devices were modeled according to the static model used by Judy and Muller [25], and detailed in chapter 4. Deflection data for the devices were taken at a variety of magnetic field strengths, and these data were converted into inclination angles of the cantilevers. The magnetization data was calculated from the observed deflections using the known geometry of the permalloy and hinges, as well as the demagnetization factors calculated from the permalloy shape. The observed inclination angle and calculated magnetization data are compared to the modeled inclination angle and modeled magnetization data for the same device. As previously demonstrated by Judy and Muller, inclusion of the anisotropy torque in the static analysis greatly increases the correspondence between the model and observed behavior (particularly at low-field levels [25]), as shown in Figure 5.11, in which a type-2 device with 3 μm hinges is modeled. Thicker hinges were used so that the saturation of the permalloy occurred over a broader range in the external magnetic field. This permits determining how well the

model fits all regions of the device behavior.

It can be seen from Figures 5.10 and 5.11 that the incorporation of the anisotropy torque in the model delays the steep rise in magnetization and inclination angle in comparison to the analysis without it. This verifies that the values for θ over this range of magnetic field strength are on the same order of magnitude as the demagnetization factor for the permalloy segment. This also shows that while further reduction of the demagnetization factor may shift the steep portion of the magnetization curve to lower background magnetic field levels, this phenomenon will begin to diminish once the demagnetization factors become negligible in comparison to the values of θ. Accurate agreement in the non-saturated region of the characteristic curve is vital, since when substrates restrict the angular range of the device to ~+/- 0.1 rad incomplete magnetization will exist, and as the low field behavior requires more complex modeling. The data in Figure 5.9 confirm that the shape demagnetization factor does not limit the magnetic susceptibility of the permalloy beam; instead it is limited by θ, which is virtually independent of the shape anisotropy (provided N_L is known to be $<<1$). Therefore, a maximal degree of shape anisotropy exists such that further increase in the permalloy aspect ratio produces no gain in magnetization, and, in fact, only reduces the available volume for Ni/Fe patterning, reducing the magnetic torque.

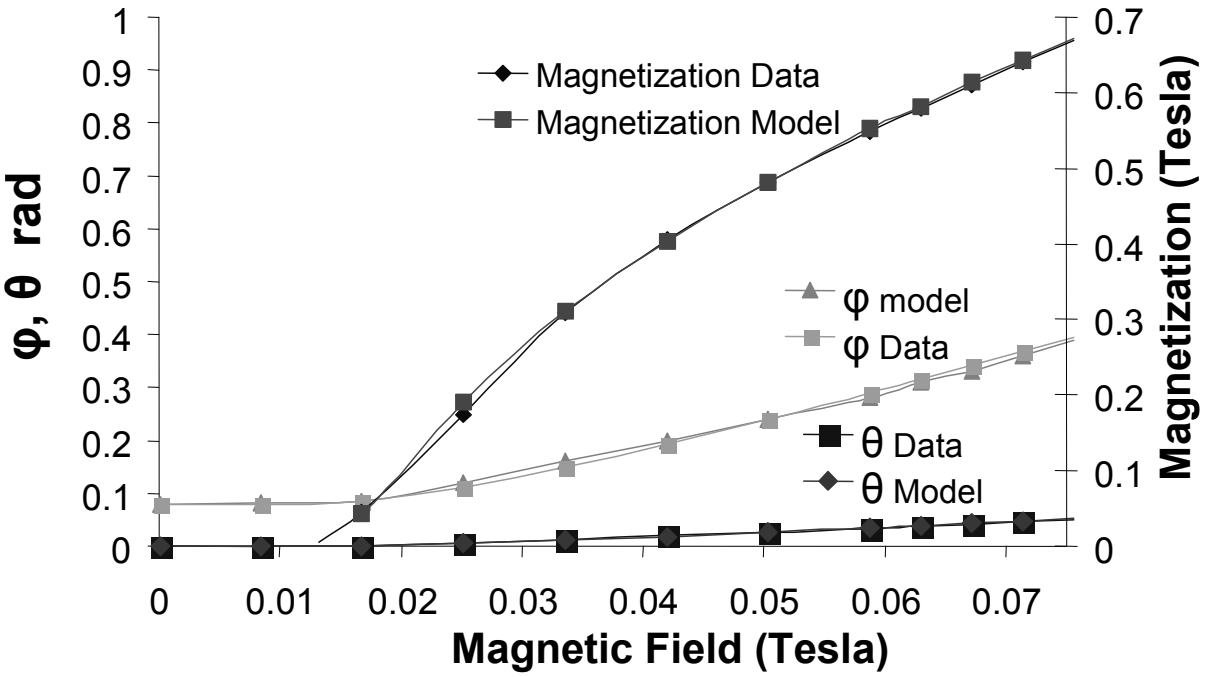

Figure 5.11. Comparison of modeled and experimental data for a type-2 device with 3 μm thick gold hinges. Best fit value of coercivity set to 250 A/m.

5.3.2 Measured Device Switching

Each of the three designs was also fabricated with optically transparent upper substrates so that appropriate testing could be performed while keeping the devices in view. Latching bistable behavior was observed for each of the three designs. The main point of interest is the minimum switching conditions required for operation of the devices, such as the minimum external field, B_{min}, that will produce latching, as well as the minimum current necessary to be supplied to the integrated coil in order to switch the state of the relay. These parameters were previously modeled and appear in Table 5.1, along with their experimentally determined values. For example, the modeling for design 1 predicted a minimum 40 mA must be supplied to the coil with a minimum background magnetic field of 1.8 mT in order to produce switching between two latched states. Experimentally, the lowest value of this parameter was found to be 30 mA supplied to the coil with a background magnetic field of 2.0 mT, in good agreement with the modeled values. Additionally, this value of 30 mA gives an estimate of the coercive field strength, since the elastic torque is diminished by the demagnetization factor, and $B_{external}$ sinφ is small for device 1 in a 10 mT magnetic field. Design 2 is found to require a much greater minimum external magnetic field to produce latching bistable states [28]. This is due to the much lower degree of shape anisotropy, and thus a much lower degree of magnetization at a given external magnetic field level. Therefore a larger background field is necessary to generate a magnetic torque large enough to suitably overcome the elastic torque due to the bending hinges.

Table 5.1. Comparison of modeled and experimental data for minimum conditions.

Minimum conditions	**Design 1**	**Design 2**	**Design 3**
Modeled			
$B_{external}$ minimum	1.8 mT ext field	13.0 mT ext field	4.5 mT ext field
B_{coil} minimum	0.35 mT from coil at 10 mT ext. field	1.2 mT from coil at 25 mT ext. field	0.40 mT from coil at 10 mT ext. field
I_{coil} minimum	40 mA to coil	100 mA to coil	35 mA to coil
Experimental			
$B_{external}$ minimum	2.0 mT ext field	17 mT ext field	7 mT ext field
B_{coil} minimum	0.30 mT from coil	1.0 mT from coil	0.35 mT from coil
I_{coil} minimum	30 mA to coil	100 mA to coil	35 mA to coil

The effect of the external magnetic field on the minimum pulse width needed for a 50 mA coil current to produce a switching event was measured for a type-3 device. Figure 5.12 shows that for external fields less than 12.7 mT (but greater than the minimum latching field) the minimum pulse length needed to switch a type-3 device with a 50 mA current is 1.15 ms (note, 1.15 ms is not the total time to switch, but rather the length of time the current pulse need be provided to the coil for switching to result and does not take into account and under damping (ringing) in the latched state). Ruan et al. reported a 0.2 ms minimum current pulse in order to result in switching of their MEMS magnetic relay [27]; however, the actuation distance for the Ruan design is much less, and therefore our actuator must travel over a larger angular range before the external field has sufficient component along the beam in the opposite direction. In fact, the ratio of distance moved by the Ruan device to these devices (50/10 = 5) is approximately the same as the ratio in minimum switch pulse time (1.15/.2 = 5.75). This 1.15 ms pulse of 50 mA corresponds to a switching energy of 80 μJ. However, as the background magnetic field is increased, longer pulse widths were required. For example, at 15.0 mT, a pulse of over 8 ms was required. Once the background field exceeded 15.7 mT, a 50 mA pulse of indefinite length could no longer switch the device (a larger current was required). At this external field, the condition presented as Equation 4.1 is no longer satisfied by the coil current.

During testing it was observed that device 3 could be switched in one direction with millisecond pulse widths, but could be switched the other direction with a pulse width shorter than 100 μs, confirming the SPS regime initially presented in chapter 4. This

asymmetry could not be explained by the testing method or equipment; however, an explanation was found after consulting the model of this design developed in chapter 4.

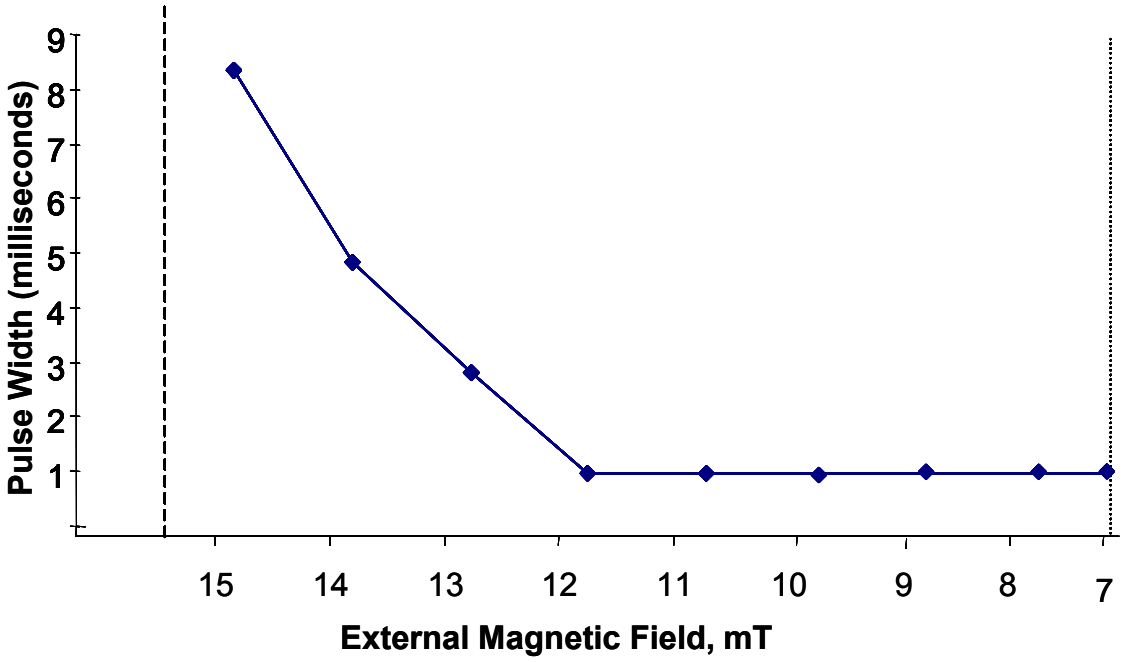

Figure 5.12. Minimum pulse width necessary to switch type-3 devices not operating in SPS mode, shown as a function of the background external magnetic field.

It was observed that a current of 50 mA was needed to switch the devices in the short-pulse regime, as opposed to 35 mA for the long-pulse switch. Figure 4.4 shows the magnetic field developed by the coil per unit of current supplied. For a type-3 device in a background field of 10 mT, the demagnetization is determined by the angle the magnetization vector, M, makes with the easy axis of the permalloy (θ) and the easy axis shape anisotropy factor, N_L. Figure 4.8 shows that the remaining elastic torque to be overcome is approximately 1 nN-m, predicting a ΔB_{coil} of 0.13 mT. A coil current of approximately 9 mA would account for this ΔB_{coil} necessary for short-pulse switching (shown in the Theory section). The observed increase of 15 mA for short-pulse switching is in close agreement with the calculated value and supports the conclusion that little only a small degree of reversed magnetization needs to be developed during the application of the coil current to dramatically affect the permalloy coercivity. Therefore, no large increase in current is required to realize short-pulse switching for type-3 devices.

5.3.3 Contact Resistance

The devices were placed in a background external field. The contact resistance across the devices was determined using a two-point measurement. A voltage generator supplied a square waveform to a potentiastat to produce the square current provided to the integrated coil. Typical values of the measured contact resistance were 0.5 Ω for new devices. Pulses varying in length from 1 ms to 10 ms were used to investigate the effect of switching speed on the switching of the various designs. Recorded contact resistance across the beam and microstrip also served to determine the effective switching speed of

the MEMS devices (< 5 ms).

5.3.4 Cycling and Lifetime Tests

Several devices of each design were cycled in order to test for the lifetime electrical and mechanical performance. The contact resistance across the device was measured at several intervals, and the device was observed for any signs of wear of mechanical fatigue or failure, such as metal delamination or cracking. Figure 5.13 shows the measured contact resistance of a transfer switch device of design 2 over 63 million cycles.

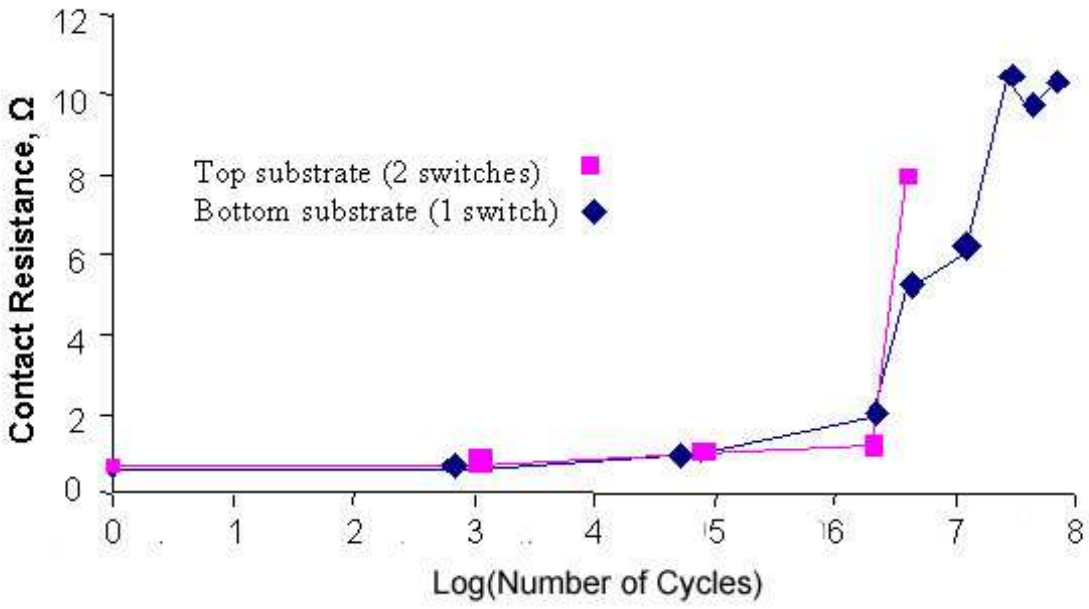

Figure 5.13. Device lifetime testing: measured change in contact resistance with cycling for a type-2 device.

Device cycling and testing occurred in an unpackaged state in ambient air. A DC current of 100 μA was applied in the latched states. The contact resistance was measured both in the upstate and the downstate. The upstate configuration connected two such switches across an RF transmission line on the upper substrate. The experimental resistance was divided by the number of switches in series, 2, to give a resistance per MEMS switching element. A cycling speed of 40 switching events per second (20 Hz) was observable with the aid of a video microscope, and this frequency was used for the bulk of cycling experiments. Over the first 2 million cycles, little to no change is observed in the contact resistance of the RF switch, and values of 0.5 - 0.7 Ω are measured. The actual contact resistance should be somewhat less than this value due to the error incurred in using a 2-point measurement. After 2 million cycles, the contact resistance in both states increased, rising to almost 10 Ω in the downstate after 27 million cycles (approximately 16 days of continuous testing). Reliable contact was not observed in the upstate at 12 million cycles. As the cycling continued no further increase in resistance was observed in the downstate. This abrupt increase in contact resistance could be due to particulate contamination (dust particles etc.) since no attempt was made at hermetic sealing or packaging the device. After 63 million cycles (approximately 40 days of continuous testing), the contact resistance was similar to that at 27 million cycles. At this point, testing was stopped. The results in Figure 5.13 are typical of what was observed with several samples.

Ruan at al. reported no permanent change in contact resistance over 4.8 million cycles, and stopped testing arbitrarily [27]. The results observed in this work support minimum lifetimes in this range, as significant change in contact resistance was not observed until

the 4-12 million cycle mark. It is believed that due to the faster switching speed of Ruan's device, cycling likely occurred at a quicker rate; therefore, much of the performance degradation observed over 2–12 million cycles may be in part due to environmental contamination over weeks of days of operation. Testing the unpackaged devices in ambient conditions represents a worst-case scenario in evaluating performance and device lifetime. It is therefore believed that these devices would operate over many more cycles before deterioration of contact resistance when properly packaged and operated in a clean, dry environment. Devices of each design were subjected to further cycling in order to ascertain the mechanical lifetime. Mechanical cycling continued to 150 million cycles. No observable wear of material delamination occurred, nor were the hinges found to experience a change in stiffness.

5.3.5 Contact Force

It is well known that the force applied at the point of contact influences the quality of the contact between MEMS devices and the contact pads. Holm's contact theory predicts a dependence of contact resistance on the –1/3 power of contact force, due to purely elastic deformation [42], and Schimkat showed agreement with this model for contact forces > 1mN. Hosaka has demonstrated that a contact force in the range of 50 μN is necessary to achieve contact resistances less than 100 mΩ [39]. Schimkat observed that ultra-clean metal to metal contacts where no organic residue is present could reduce contact resistance to 10 mΩ [40]. Hosaka observed and Hyman confirmed that the best contact was made by gold/gold interfaces; however, adhesion of the metal surfaces

results in bonding forces as high as 2 mN [39,41], much larger than those generated by this design; however, harder (stressed) gold reduced these adhesion forces by more than an order of magnitude [8].

In the devices presented here, the electroplated gold contact pads in contact with the sputtered gold underside of the contact pad offer a stress mismatch between the two layers. Experiments were performed on the magnetic actuators to determine the improvement in contact resistance achieved through increased contact force. A type-2 device was subjected to magnetic field levels in excess of the minimum required for latching, and the resistance across the device was measured using a two-point technique. After the beam makes initial contact with the pad at 18 mT, a high contact resistance (6.5 Ω) is observed, as shown in Figure 5.14. Increased background magnetic field levels, however, quickly reduce the measured contact resistance, dropping to 0.6 Ω with a 30 mT magnetic field. This field level is calculated to correspond to a contact force of 15 μN (see Appendix B). Further increase in background magnetic field level, and commensurate increase in contact force (up to 38 μN at 50 mT for design 2), was not observed to be of any further benefit in reducing contact resistance over this range in contact force. In this manner the operating field levels for the various device designs can be low enough to enable low switching energy, while high enough to benefit from greatly reduced contact resistance over the responsive 0 - 15 μN range. A calculated contact force of 102 μN gives a 275 mΩ contact resistance in the Oberhammer switch [4]. While the contact resistances measured with these switches are approximately twice that reported by Oberhammer, the contact force in our design is much less, owing to the great

increase in actuation force observed with electrostatic actuators in the latched state as a result of the inverse square dependence on the distance to the pull-in electrode. In addition, further increase in contact force past a 15 μN does not produce a noticeable or immediate reduction in contact resistance for these switches.

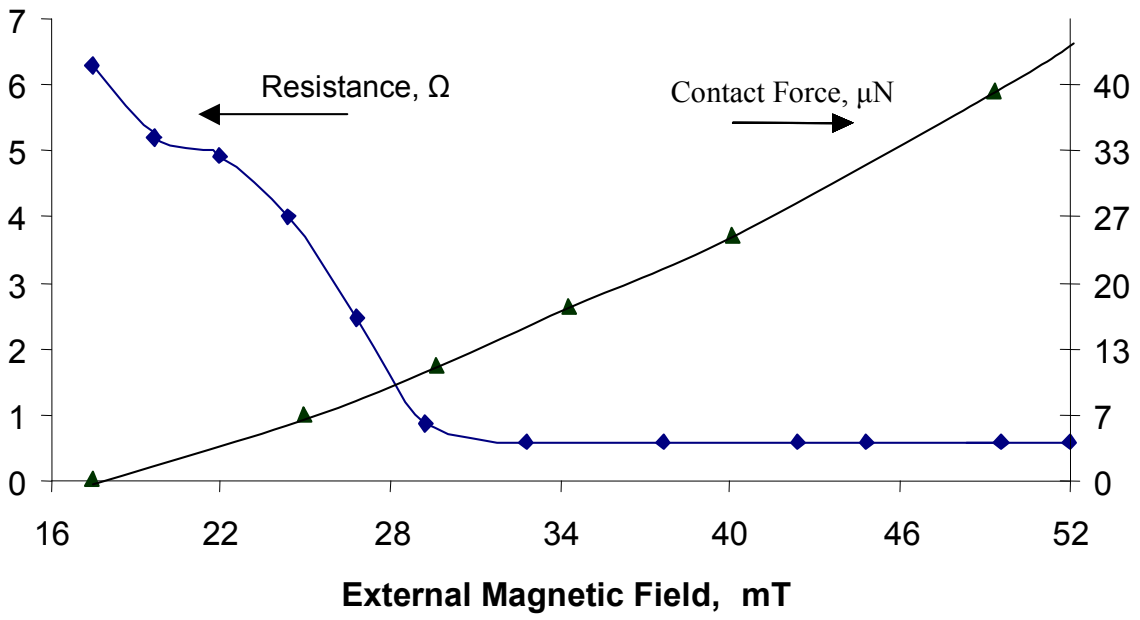

Figure 5.14. Measured change in contact resistance with background magnetic field and calculated contact force (given in μN) for a type-2 device.

5.3.6 Overdriving

When devices were operated in magnetic fields stronger than the minimum latching magnetic field, movement of the beam tip along the substrate was observed for devices 1 and 3. This behavior is desirable in many cases as it provides an additional degree of freedom for the design engineer. In the case of the RF switch, overdriving the actuation coil in a sinusoidal fashion creates a wiping action in either of the latched states that tends to clean the contact surface leading to higher quality electrical contacts. In the case of the microfluidic valve, the additional movement in the latched state could be used for regulating the amount of fluid passed through the device, or used in cytometry as a potential means of cell sorting. This capability was built-in to the design by nature of the long, flexible partial hinges. This effect was observed in devices 1 and 3 due to their enhanced magnetization, and therefore greater magnetic torque, in comparison to device 2 at similar background magnetic fields. Device 1 was observed to wipe a distance of approximately 50 μm in fields of 70 mT.

5.4 Discussion

The devices demonstrate these different modes of switching. All devices required at least a 1.2 ms pulse for switching in both directions with the exception of design 3. Design 3 required a 1.2 ms pulse of 50 mA for switching from the upstate to the downstate, but 100 μs at 50 mA was sufficient for switching from down to up. Below 40 mA, no pulse length produced switching from down to up. This supports the theory

that a minimal pulse magnitude is necessary to switch from the lower latched state to the upper latched state, but that there is no minimal pulse time. Pulses shorter than 100 μs were not investigated, but it is believed that shorter pulses could be used to activate the beam.

The SPS phenomenon was not observed with the higher anisotropic permalloy patterned on design 1 or the lower anisotropic permalloy patterned on design 2. The SPS was not observed with design 2 because the separation of the two magnetic torque lines is very small since it scales with N^{-1}, where N is the demagnetization factor of the permalloy geometry. Therefore, for design 2, there is only a very limited region of angles the beam can be rotated through, where the upper magnetic torque line lies above the elastic line while in the downstate; and conversely, there is a very limited region where the lower magnetic torque line lies below the elastic line while in the upstate. For design 3 the separation of the two magnetic torque lines is greatest, but the slope of the magnetic torque line is also proportional to N^{-1}. If the elastic torque line were perfectly flat ($k_\varphi = 0$), then this design would correspond to the same angular range where low energy switching may occur. For identically sloped elastic torque curves with the same initial inclination angle, the angular range for this effect is diminished. It can be seen that matching the stiffness of the hinge to the permalloy anisotropy could enhance the angular range over which low energy switching is observed. Increasing the stiffness of the hinge in design 1 would yield this effect for switching in both directions. The compromise for low energy switching is reduced contact force, as the increased hinge stiffness requires a greater fraction of the magnetic torque for bending. This technology could be used in RF relays,

as well as optical switches where contact force is less critical.

5.4.1 Applications

There are many applications for low energy, bistable magnetic actuators, including some that are complemented by the design and materials choices presented here. For cryogenic and/or higher-temperature applications, thermal stresses become significant. For MEMS devices to be used in extreme temperature environments, it is essential to choose materials that have similar coefficients of thermal expansion. In addition, thermal stresses may be further reduced by canceling thermally induced bending by cladding the magnetic material in gold.

In addition to maintaining an improved, clean electrical contact, the wiping observed may also be employed for other applications, including microfluidics. The wiping movement is well suited for use as a variable-flow rate valve. Devices which demonstrate this wiping behavior are presented in Chapter 6.

MEMS concepts can also be applied to RF, replacing traditional solid-state components such as PIN diodes and FETs that are inherently nonlinear, are poor at power handling, and consume larger amounts of DC power. This is especially evident in communications applications where, in some cases, a single MEMS component replaces and outperforms an entire solid-state circuit [6]. RF MEMS alternatives offer lower power consumption, excellent linearity, better isolation, lower insertion loss, and

increased functionality in applications where a high degree of frequency agility and sharp filtering is critical. A SPDT switching element could be used as a building block for a more complex switching network. For example, a tunable RF filter could be made by switching individual capacitative elements in and out with such a switch. SPDT switches can also be used in phase shifters to alter the phase length of a transmission line by switching sections of differing lengths in and out of the circuit. Figure 5.15 is a schematic of a SPDT switch built using the fabrication steps described in this paper. The design utilizes the magnetic bistability described by Ruan et al. [27]; however, this design makes use of the short-pulse switching, utilizes a post platform for reduced mechanical stress at the hinge, and minimizes thermal stresses by cladding the ferromagnetic material in gold, therefore reducing deformation in cryogenic environments.

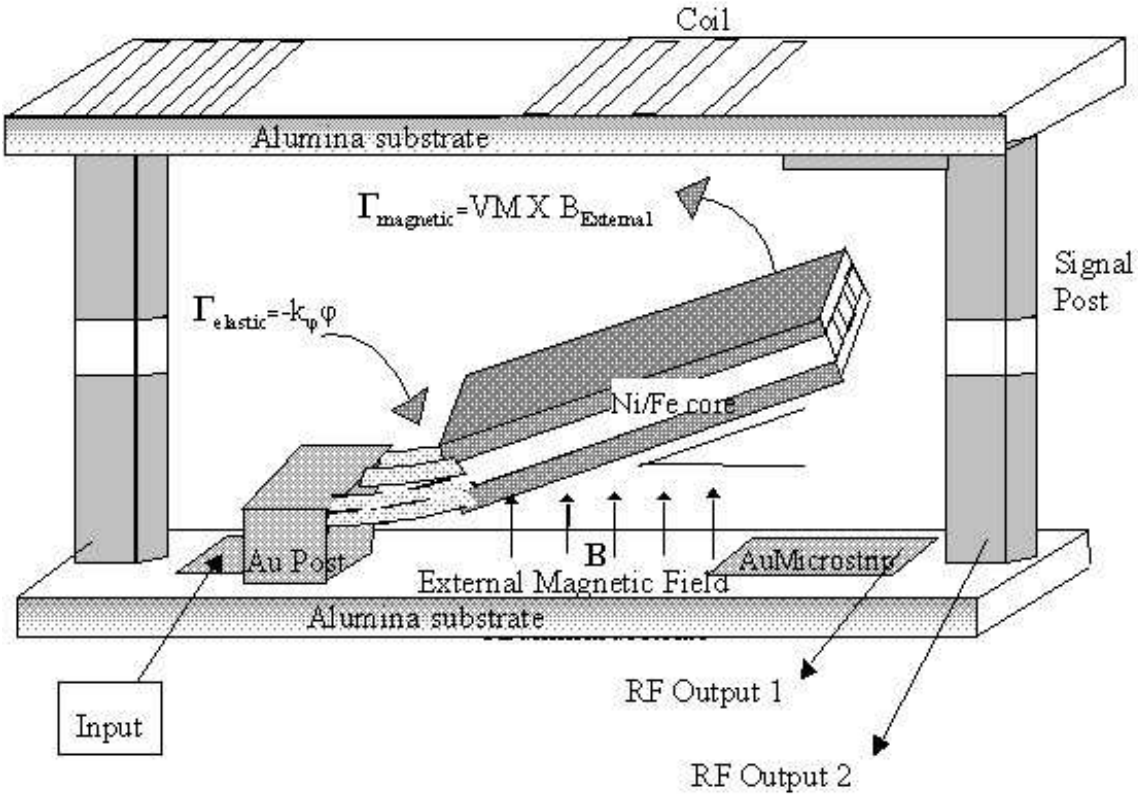

Figure 5.15. Geometric description of beam with flexible hinges and stiff permalloy magnetic element.

The SPDT design described in this study is well suited for these types of applications because there are no dead legs in the design. Device isolation is a critical measure of RF performance and is predominantly determined by the magnitude of the separation between the two RF outputs. Figure 5.16 shows a family of curves which demonstrate the modeled isolation achieved between two microstrip transmission lines on oposing substrates which are separated by various gap distances. The model suggests that in order to achieve isolation better than –50 dB over the range of 500-2000 MHz, a substrate separation of approximately 100 μm is necessary. Figure 5.17 shows the measured isolation across the transfer switch (2 switches in series). The isolation for the network is shown to be better than –50 dB across the entire band. The cantilever hinges were designed to be suitably flexible so that an external magnetic field of 100 Gauss could activate the switch, yet thick enough to be RF transmissive. The isolation of our device is comparable to the toggle switch presented in [11] in which –54 dB was measured at 1 GHz and the Oberhammer et al. switch with –45 dB at 2 GHz [4].

In order to verify the temperature dependence of the device, the insertion loss was monitored as the device was cooled from room temperature down to cryogenic temperature (77 K). Insertion loss (measured at 900 MHz) of -0.34 dB was observed at 300 K and improved to -0.17 dB at 77 K for the transfer switch. This compared well to the toggle switch from above (0.15 dB at 1 GHz, 0.21 dB at 3 GHz) [11]. Again, this insertion loss data is for two switches in series and approximately 10,000 μm of 5 μm thick gold transmission line leading to and from the two switches in the flip-chip assembly. With further design iterations, both isolation and insertion loss could be

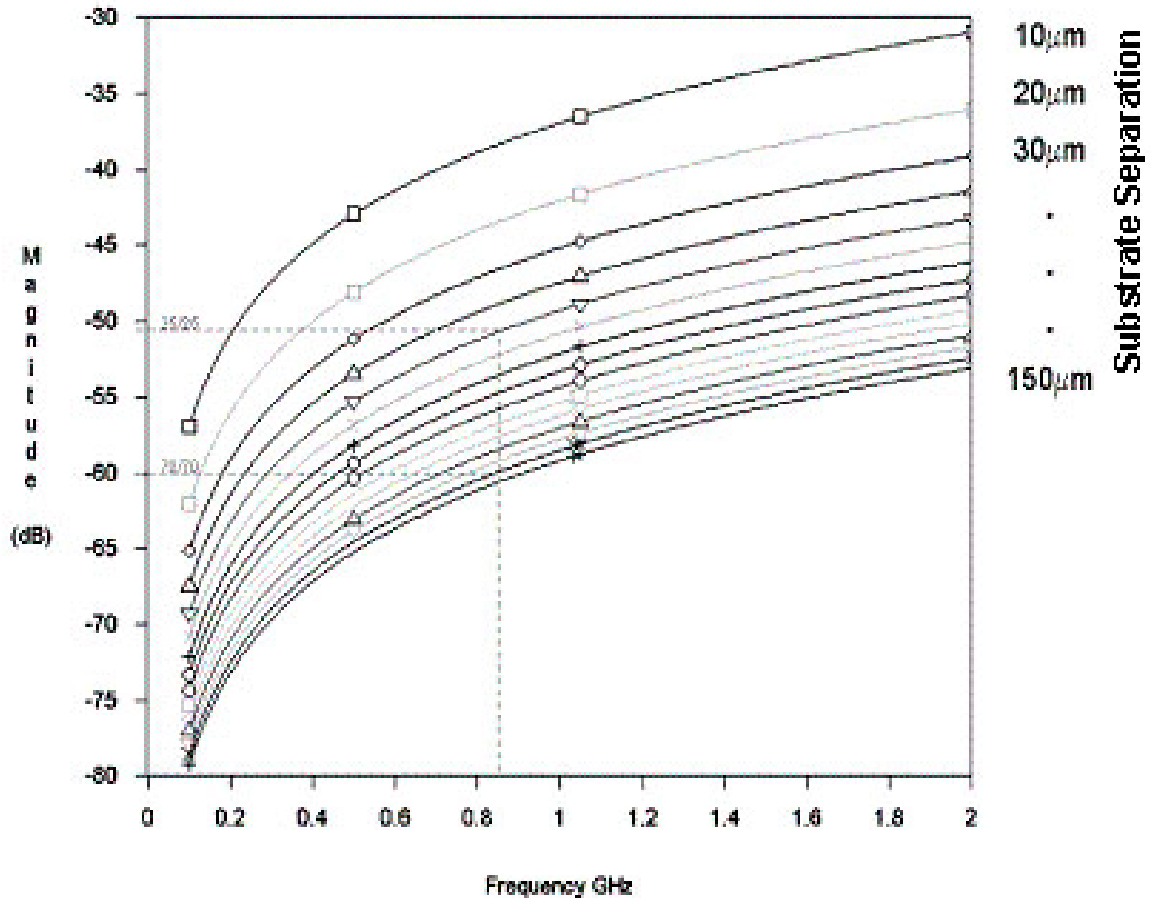

Figure 5.16. Modeled isolation achieved with two-substrate design as a function of the total substrate separation.

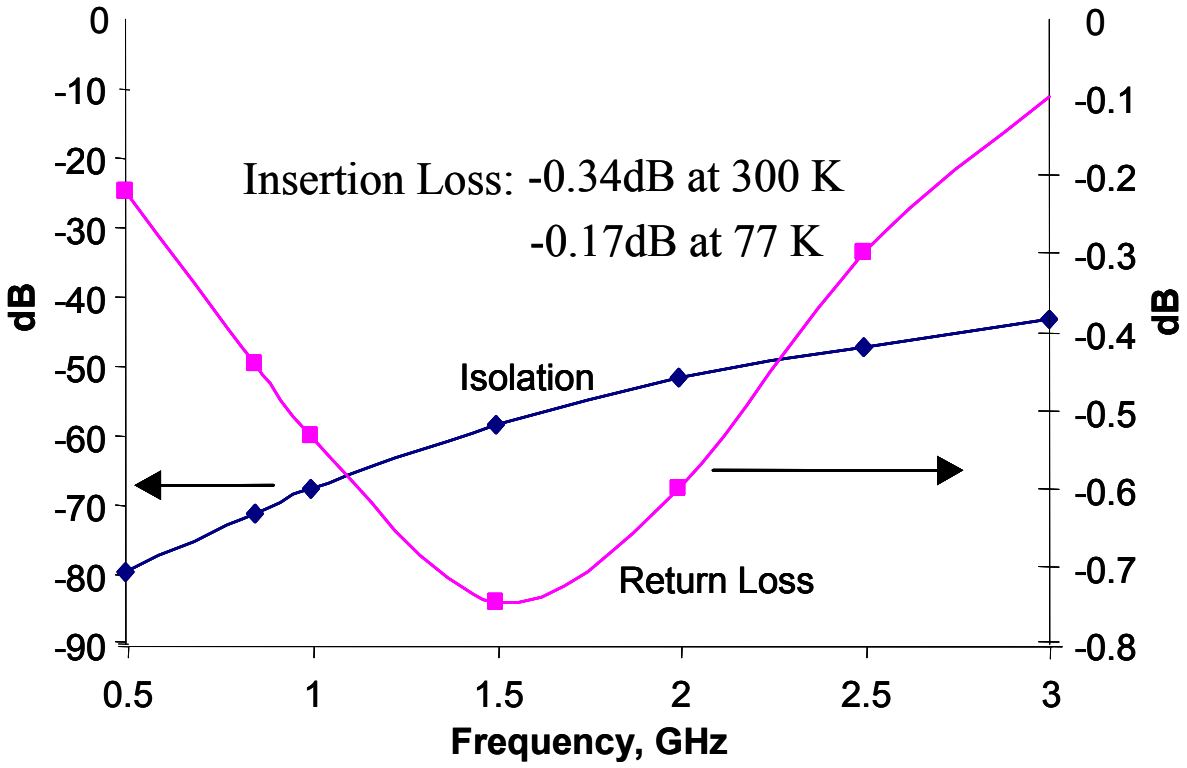

Figure 5.17. RF performance of fabricated MEMS transfer switch composed of two type-2 actuators: measured isolation, return loss, and insertion loss data for 2-switch in series device. Insertion loss data was taken at 900 MHz.

improved by impedance matching.

5.5 Summary

Three variations of SPDT MEMS RF switches were fabricated and tested for minimal switching energy, as well as electrical and mechanical reliability. Fabricated devices were found to have excellent correspondence between observed and modeled behavior. Isolation better than -50 dB was observed over the 500-2000 MHz range with insertion loss better than -0.2 dB. The design space for SPS was determined using the comprehensive model for this two-substrate doubly latching design. New designs were explored for minimum switching energy. It was found that magnetic torque curves that remain bounded by the elastic torque curve over the entire angular range of motion yield SPS. The coercivity of the magnetic material is critical in producing useful SPS behavior, even if the magnetic material is patterned in such a way as to maximize the magnetic susceptibility (through lithographic patterning of the Ni/Fe). Very low ferromagnet coercivity yields bistable actuation with minimal magnetization and very low contact forces. Hard magnetic materials with large coercivity produce a high degree of magnetization in the latched states, but require much larger currents be provided to enable switching, greatly increasing the energy expended. The coercivity of the ferromagnet is of great importance in generating a design satisfying the necessary contact forces and energy requirements. Actuator displacements of 100 μm were observed repeatedly with switching energies of 5 μJ from a 100 μs pulse of 50 mA. Further reduction in switching energy is anticipated, but shorter pulses were not investigated.

CHAPTER 6

MAGNETIC MEMS WIPING ACTUATOR

A MEMS magnetic actuator micro-switch has been fabricated which, in addition to the primary cantilever bending, exhibits a secondary wiping motion during overdrive. The wiping action occurs as lower the total energy of the actuator system decreases with increasing external magnetic field, H_o. The actuator is bath fabricated using standard microelectronic processing, and the ferromagnetic permalloy is patterned lithographically into long narrow strips on the actuator to maximize the magnetic torque generated for a given actuator size as described in chapters 4-5. The total wiping distance for a 1000 μm long switch was 50 μm with magnetic fields of 10 to 100 mT. A first-principles physical model has been derived for the equilibrium and dynamic behavior of the device, as well as discrete changes in position due to frictional effects.

6.1 Theory

A particularly useful method for determining both the static and dynamic solutions of a system composed of multiple members whose equilibrium is constrained by known relations makes use of the Lagrangian via the Euler-Lagrange Equation, Equation 6.1 [43].

$$\frac{\partial L}{\partial y_i} - \frac{\partial}{\partial t}\frac{\partial L}{\partial y_i'} + \sum_j \lambda_j(t)\frac{\partial g_j}{\partial y_i} = 0 \tag{6.1}$$

Where y_i are the chosen coordinates of the system, y_i` are the first derivatives of the y_i with respect to time, g_j are the system constraints, and λ_j are the undetermined multipliers used to calculate the forces of constraint. The Lagrangian, L, is defined as the difference between the kinetic energy, T, and potential energy, U, of the system, Equation 6.2.

$$L = T - U \tag{6.2}$$

The kinetic energy of the system, T, can be separated into terms related to the motion of the ferromagnetic beam and the attached hinges, $T = T_{beam} + T_{hinge}$. For the case where the mass of the beam greatly exceeds the mass of the hinge, the kinetic energy of the beam dominates the total kinetic energy, $T_{beam} >> T_{hinge}$. As the system wipes and moves to equilibrium, the beam tip translates across the substrate surface and rotates in the plane of the translation, as shown in Figure 6.1. As the beam rotates, it stands increasingly upright, $T = T_{beam} = T_{translational} + T_{rotational}$. Each term can be expressed in terms of the system mass, m, moment of inertia of the beam, I_{beam}, and the 2nd derivatives in time for both the translational coordinate, x, and the angular coordinate, φ, Equation 6.3.

$$T_{translational} = \frac{1}{2}m\left(\frac{\partial x}{\partial t}\right)^2 \tag{6.3a}$$

$$T_{rotational} = I\left(\frac{\partial \varphi}{\partial t}\right)^2 \tag{6.3b}$$

The total potential energy of the hinged beam system in an external magnetic field H_o is due to the magnetostatic energy of the ferromagnetic material and the potential energy stored in a stressed hinge, $U = U_{magnetostatic} + U_{hinge-potential}$. For an elastic spring with a vertical end displacement, Δz (as shown in Figure 1), the stored energy is expressed by Equation 6.4 [44].

$$U_{hinge-potential} = \frac{1}{2}k(\Delta z)^2, \quad where: k = \frac{12EI_{hinge}}{x^3} \tag{6.4}$$

Where k is the spring constant resisting this displacement, E is the elastic modulus of the hinge materials, I_{hinge} is the moment of inertia of the hinge, and x is the hinge length. The numerical factor 12 is required by the fixed/guided boundary conditions imposed by the support and beam, resulting in a 4x increase in stiffness over a free cantilever beam of same dimensions and material (as shown in Appendix B). It should be noted that the actual stiffness of this configuration should be slightly larger than that given here, owing to the variably sloped hinge end on the beam side, depending on the position of the device. However, if the angular range of the device is small, the error is treating the end as purely guided can be shown to be negligible.

The magnetostatic energy arises from the energy required for the external field to change the magnetization of the ferromagnetic material, as well as the energy associated with raising the magnetization in the presence of a demagnetizing field antiparallel to the magnetization vector M. Hence, the magnetostatic energy is expressed as in Equation 6.5

[37].

$$U_{magnetostatic} = V\int_0^M \vec{H}\cdot d\vec{M} \tag{6.5}$$

Where the total magnetic field H is due to the external magnetic field H_o, such as from an electrified coil, and the demagnetizing field H_D, Equation 6.6.

$$\vec{H} = H_o\vec{e}_Z + H_D\vec{e}_M = H_0\vec{e}_Z - |M|N_D\vec{e}_M \tag{6.6}$$

Where M is the magnetization of the ferromagnet, e_z is the unit vector in the direction of the external field, e_M is the unit vector in the direction of M, and N_D is the shape demagnetization factor in the direction of M (Figure 6.1c). The magnetization of the ferromagnetic material is expressed in terms of the external field (H_o), the coercivity (H_c), the shape anisotropy factor (N_D), and the total angle ($\theta+\varphi$), between the external field and M, yielding Equation 6.7 [45].

$$\vec{M} = \frac{H_c + H_0\sin(\varphi+\theta)}{N_D}\vec{e}_M \tag{6.7}$$

Where φ is the angle between the external magnetic field and the beam itself, and θ is the angle the magnetization vector is bent out of plane of the ferromagnet easy direction (Figure 6.1c). There is a maximal magnetization due to saturation, which cannot be exceeded, Equation 6.8.

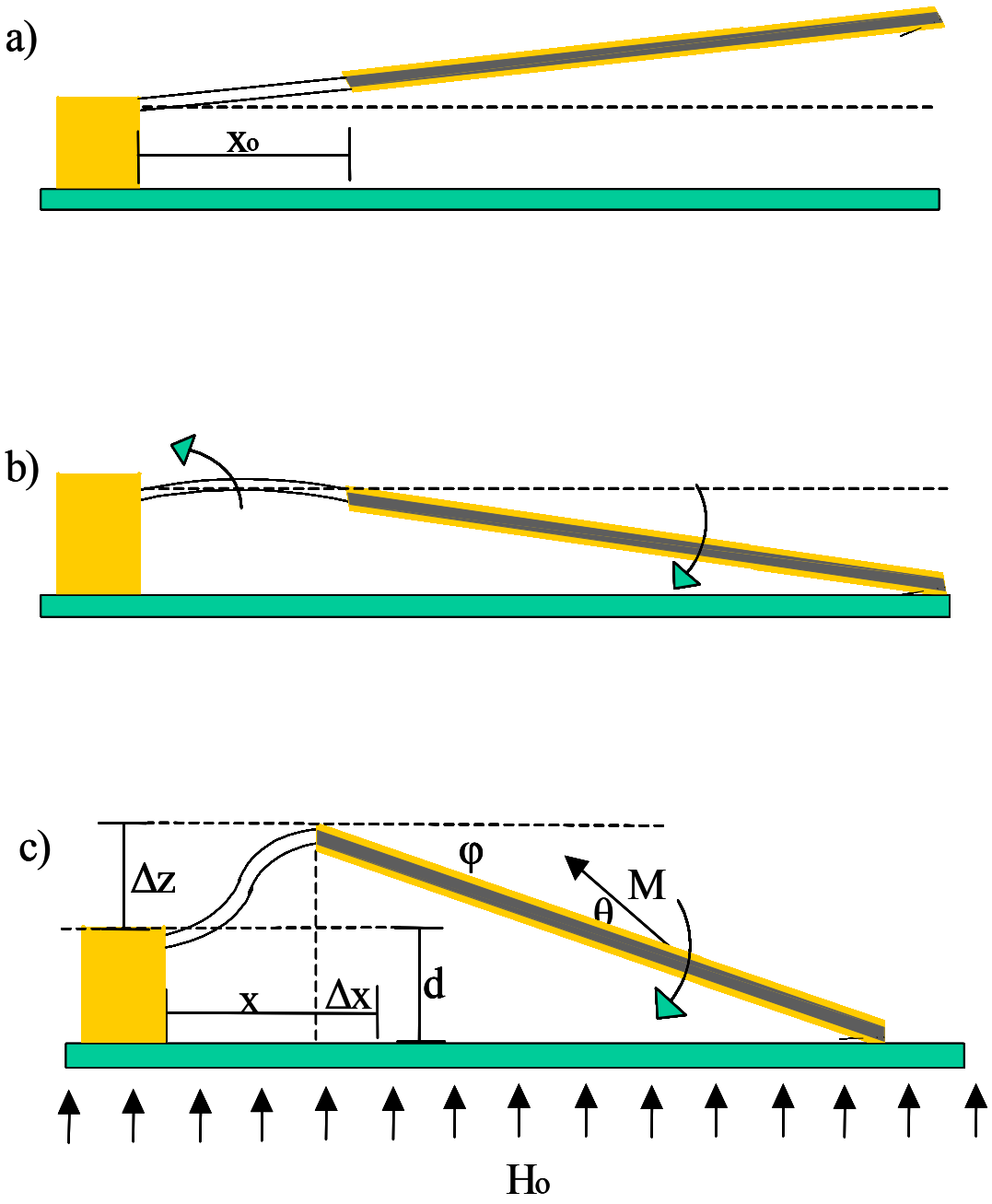

Figure 6.1. Schematic of magnetic actuator during a) off position, b) pull-in, and c) wiping.

$$M = Min\left\{M_s, \frac{H_c + H_0 \sin(\varphi + \theta)}{N_D}\right\} \tag{6.8}$$

The shape anisotropy factor is related to the length and thickness shape anisotropy factors, N_L and N_T respectively, and the angle θ (Equation 6.9) [46].

$$N_D = N_L \cos^2(\theta) + N_T \sin^2(\theta) \tag{6.9}$$

The magnetostatic energy may now be explicitly calculated, Equation 6.10.

$$\begin{aligned} U_{magnetostatic} &= V\int_0^M \left(H_0 \vec{e}_Z - |M| N_D \vec{e}_M\right) \cdot d\vec{M} \\ &= VH_0 M \sin(\theta + \varphi) - \frac{1}{2} VN_D M^2 \end{aligned} \tag{6.10}$$

Combining Equations 6.3a, 6.3b, 6.4, and 6.10, the Lagrangian may be expressed as Equation 6.11,

$$L = \frac{1}{2} m\left(\frac{\partial x}{\partial t}\right)^2 + I_{beam}\left(\frac{\partial \varphi}{\partial t}\right)^2 - VH_0 M \sin(\theta + \varphi) + \frac{1}{2} VN_D M^2 - 6EI_{hinge}\frac{(\Delta z)^2}{x^3} \tag{6.11}$$

where the system coordinates ($y_{i,}$) are given by Equation 6.12,

$$y_i = \{\Delta x_1, x, \varphi, \theta, \Delta z\} \tag{6.12}$$

where Δx_1 is the change in the projection of the hinge length along the substrate during the wiping motion. The magnetization, M, is not included in the system coordinates since Equation 6.7 defines M in terms of the system coordinates θ and φ. It is obvious

that pairs of the y_i are interrelated. For example, the hinge elevation Δz corresponds to a given hinge length projected onto the substrate, x, and a determined angular beam position, φ. Making use of the diagram presented in Figure 6.1c, the following two holonomic constraints can be written, Equations 6.13 a,b:

$$g_1 = \Delta z - X \sin\varphi + d = 0 \tag{6.13a}$$

$$g_2 = x - x_o + \Delta x_1 = 0 \tag{6.13b}$$

The last constraint is determined by the necessity for the arc length of the curved hinges to remain equal to x_o. Therefore, the decrease in the lateral component of the hinge, Δx, (due to wiping) is related to the elevation of the hinge end, Δz. In Appendix B this relationship is shown to be given by Equation 6.14.

$$g_3 = \Delta x_1 - \frac{\pi^2}{16}\frac{(\Delta z)^2}{x_0} = 0 \tag{6.14}$$

This gives five equations, one for each y_i, incorporating the three forces of constraint, (λ_1, λ_2 and λ_3). The constraining force for constraint g_1 is the force of contact of the cantilever tip on the bottom substrate (keeping the tip of the beam on the substrate)

The Euler-Lagrange equations may now be applied to L, giving one equation for each of the system coordinates, Equations 6.15 a-e.

$$\frac{\partial L}{\partial \varphi} \rightarrow MVH_0 \cos(\theta + \varphi) + \lambda_1\left(-X\cos\varphi\right) = 2I_{beam}\frac{\partial^2\varphi}{\partial t^2} \tag{6.15a}$$

$$\frac{\partial L}{\partial x} \rightarrow \lambda_2 + 18EI\frac{(\Delta z)^2}{x^4} = m\frac{\partial^2 x}{\partial t^2} \tag{6.15b}$$

$$\frac{\partial L}{\partial \Delta x_1} \rightarrow \lambda_2 + \lambda_3 = 0 \tag{6.15c}$$

$$\frac{\partial L}{\partial \theta} \rightarrow MVH_0\cos(\theta+\varphi) - \frac{V}{2}(N_T - N_L)M^2\sin(2\theta) = 0 \tag{6.15d}$$

$$\frac{\partial L}{\partial \Delta z} \rightarrow -12EI\frac{\Delta z}{x^3} + \lambda_1 - \lambda_3\left(\frac{\pi^2}{8}\frac{\Delta z}{x_0}\right) = 0 \tag{6.15e}$$

Therefore, using the five Euler-Lagrange equations (Equation 6.15) and three constraints (Equation 6.13 and 6.14), the system of five y_i and three λ_j is solvable for a given applied magnetic field, H_0.

6.2 Results and Discussion

The relevant geometrical description of the magnetic actuator is presented in Table 6.1. It was shown that increases in the magnetic field after substrate contact resulted in wiping of the beam tip along the substrate towards the hinges. Supplying current to the integrated coil on the substrate provided a variable magnetic field, which acted in addition to the external field. This behavior is depicted in Figure 6.1, which shows the movement of the actuator in response to increasing magnetic field. The actuator is shown at some initial position (6.1a). Application of the external field exerts a torque on the magnetic volume, bending the actuator towards the substrate (6.1b). The actuator is observed to move

gradually along the bottom substrate (6.1c) with further increases in the magnetic field. The actuator thus slides along the bottom contact providing a self-cleaning wiping action, which helps make low-resistance contact without fusion of the surfaces. This phenomenon was more prominent in the devices with longer hinges (i.e., lower spring constant) and higher degrees of ferromagnetic patterning.

Figure 6.2a shows an overhead view of the beam tip of an RF magnetic actuator, about to make contact with the gold contact pad on an alumina substrate below. The permalloy is lithographically patterned into long, narrow strips and electroplated with gold, as described elsewhere [12,13]. As the magnetic field is raised to 100 mT, the beam tip wipes along the contact pad (Figure 6.2b), moving a total lateral distance of 50 μm.

Table 6.1. Geometrical description of magnetically actuated MEMS device.

Beam Body (Au)	
Length	1000 μm
Width	400 μm
Thickness	8 μm
Permalloy (Ni/Fe)	
# of Strips	8
Strip Length	950 μm
Strip Width	40 μm
Strip Thickness	10 μm
Hinge (Au)	
# of Hinges	2
Hinge Length	300 μm
Hinge Width	35 μm
Hinge Thickness	2 μm

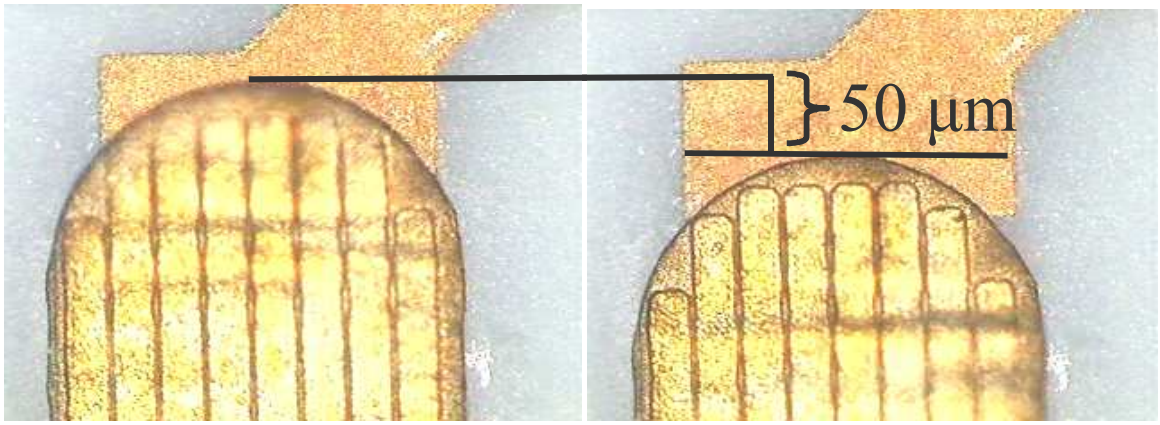

Figure 6.2. Overhead view of the type-1 magnetic actuator a) at first contact of the substrate contact pad and b) in a higher external magnetic field of 100 mT, corresponding to a 50 µm wiping distance. The 8 high aspect ratio Ni/Fe strips are visible.

The vertical elevation of the hinge of the devices were measured with the application of a variable external magnetic field as described in the Experimental section. Figure 6.3 shows the measured data for a device with a 1000 µm long beam and 300 µm long hinges. The data presented is typical of all devices fabricated with these dimensions. The hinge tip is observed to rise with increasing magnetic field, first at an increasing rate (as the magnetic torque increases from both the external field and increasing magnetization of the permalloy) at low field strengths. Figure 6.3 shows a transition from a quadratic increase in hinge elevation with external field to a linear response, indicative of saturation of the ferromagnetic material at approximately 20 mT. Eventually, there is a diminishing response as further increase in the hinge elevation requires much larger forces to induce additional bending of the cantilever. The wiping of the beam tip along the substrate was

observed using an optical microscope, and the distance moved was calculated by the position of the beam tip on a contact pad of known dimensions. This data is presented in Figure 6.4, shows a linear relationship between applied field and wiping distance above saturation.

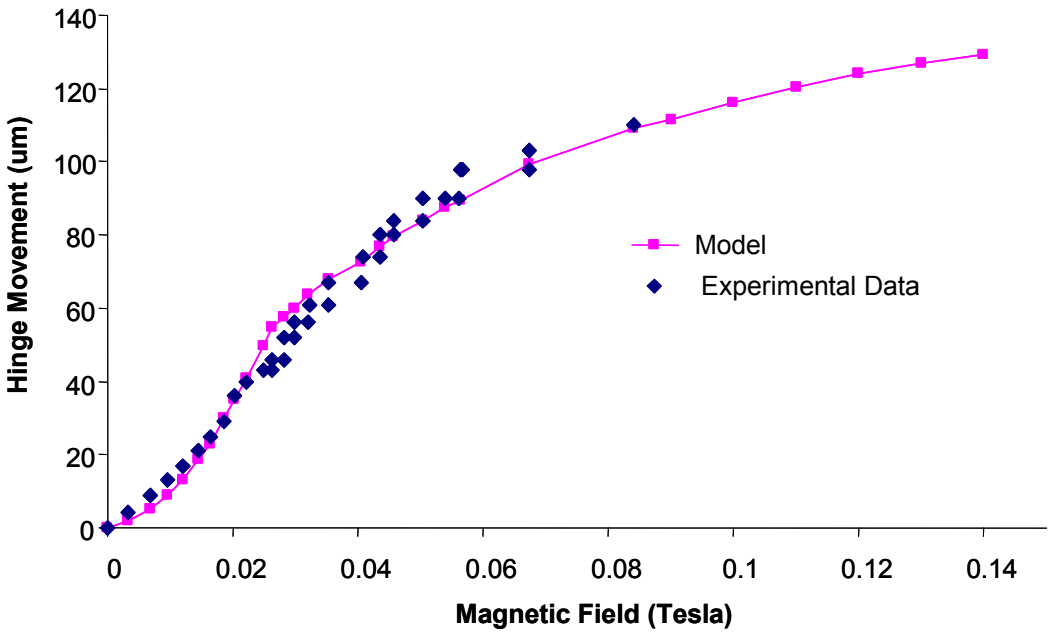

Figure 6.3. Comparison of model (a) and experimental data (b) for the maximal elevation of the hinge end as a function of the applied external magnetic field.

6.2.1 Dynamic Behavior

This system of equations may be solved for the dynamic behavior of both φ and x, which are related through the provided equations of constraint. The system of equations may be written explicitly in terms of derivatives of either coordinate by making use of the following form of constraint g_1, Equation 6.16.

$$\frac{\partial^2 \phi}{\partial t^2} = -\frac{\Delta z}{2X\Delta x_1}\left(\frac{\partial^2 x}{\partial t^2} + \frac{1}{2\Delta x_1}\left(\frac{\partial x}{\partial t}\right)^2\right) \tag{6.16}$$

Where $\Delta x_1 = x_0 - x$ (Equation 13b) and $\Delta z = \frac{4}{\pi}\sqrt{(\Delta x_1)(x_0)}$ (Equation 6.14). This simplifies the system to a differential equation in x, allowing calculation of an approximate switching speed of this device (Figure 6.5). Assuming the motion of the device is critically damped, the transient response is modeled to occur in approximately 1 ms. The time of this transient is expected to be shorter than the time required for the beam tip to move 100 μm vertically between two contact pads on separate substrates (2 - 5 ms) for high isolation switching in previous work [28-29].

6.2.2 Static Limit

The static case may be solved by eliminating the kinetic energy terms from the analysis and removing the time dependent parameters. In the static limit, the equilibrium

is dictated by the following conditions, Equation 6.17a, b.

$$m\frac{\partial^2 x}{\partial t^2} = 0 \tag{6.17a}$$

$$I_{beam}\frac{\partial^2 \varphi}{\partial t^2} = 0 \tag{6.17b}$$

Which results in $\lambda_2 = -\lambda_3$, with both approximately equal to zero. The remaining force of constraint λ_1, may now be isolated from both Equations 6.15a and 6.15e, yielding Equation 6.18.

$$\lambda_1 = F_{contact} = \frac{MVH_0\cos(\varphi+\theta)}{X\cos\varphi} = 12EI\frac{\Delta z}{x^3}\left(1+\frac{3\pi^2}{16}\frac{(\Delta z)^2}{x^2}\right) \tag{6.18}$$

Inspection of Equation 6.15a identifies λ_1 as the force of contact of the beam tip on the substrate, and correspondingly, $\lambda_1 X\cos\varphi$ as the constraining torque balancing the magnetic torque of the ferromagnetic material. Neglecting the second term in parenthesis on the RHS of Equation 6.18 introduces less than a 10% error provided $\Delta z < x/3$.

The magnetic torque on the magnetization vector M is balanced by the anisotropy torque, as shown in Equation 6.15d. This determines the angle of rotation, θ, of the magnetization away from the easy axis in terms of the inclination angle of the beam, φ.

For the case when the shape anisotropy factor through the ferromagnet thickness is approximately unity and a significant degree of magnetization exists. Theta is then small, and Equation 6.15d can be simplified to yield Equation 6.19.

$$MH_0 \cos(\theta + \varphi) = M^2 \sin\theta \tag{6.19}$$

Solving Equations 6.18 and 6.19 subject to Equation 6.8 and constraints g_1, g_2, and g_3 as functions of applied external field strength, H_o, the hinge elevation (Δz), hinge length (x) magnetization (M), and contact force ($F_{contact}$), may be determined and are presented as Figures 6.3, 6.4, 6.6, and 6.7, respectively. Saturation of the permalloy is calculated to occur with as little as 18 mT, and the contact force is generated at a rate of 2 μN/mT after saturation.

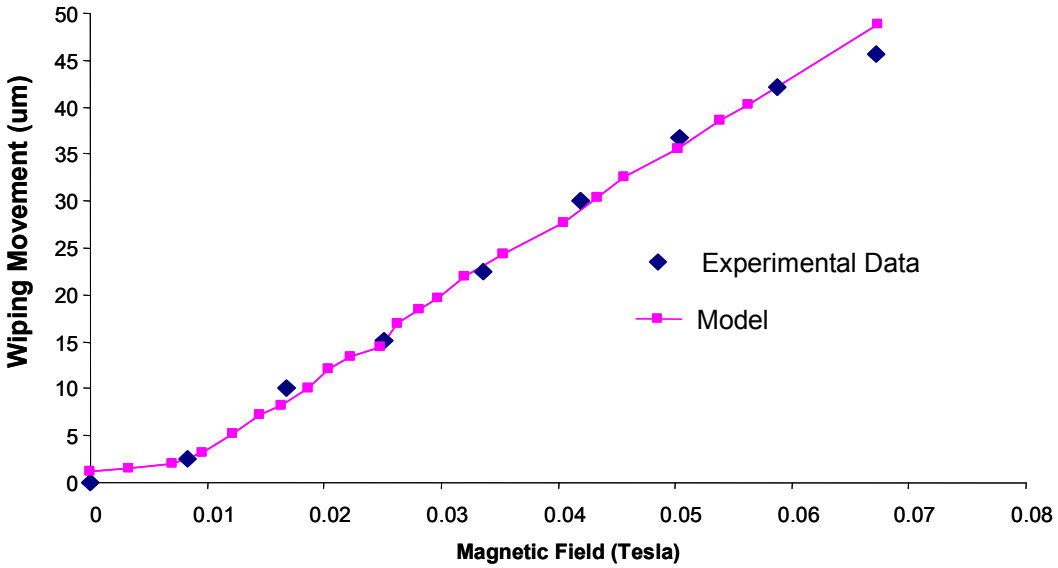

Figure 6.4. Comparison of the (a) model and (b) experimental data for the lateral wiping distance of the actuator tip as a function of the applied external magnetic field.

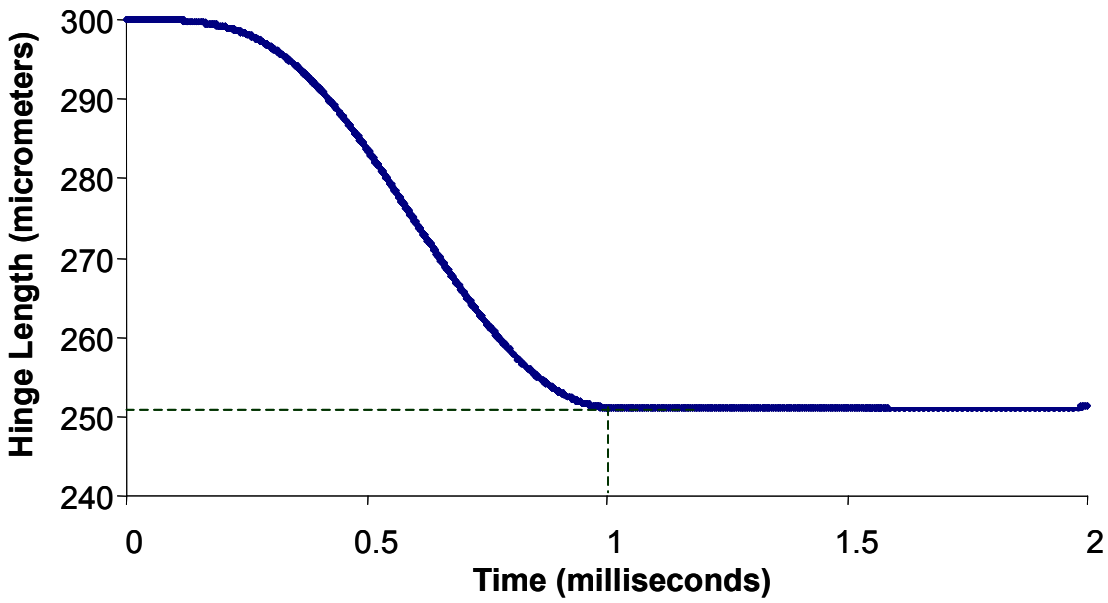

Figure 6.5. Dynamic behavior of the magnetic actuator in response to a 100 mT external magnetic field. The device is predicted to wipe 50 μm, calculated from the change in the x-component of the hinge length decreasing from 300 μm to 250 μm.

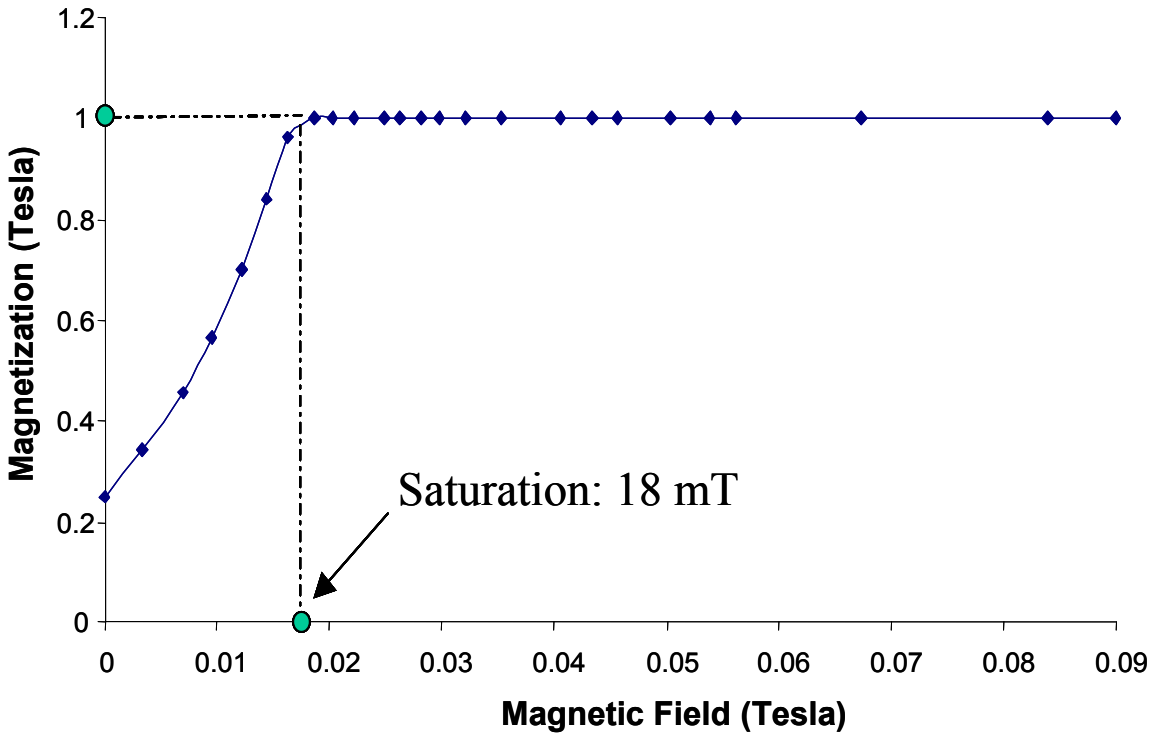

Figure 6.6. Modeled value of the permalloy magnetization with applied external magnetic field. Magnetization is seen to increase with a greater than linear dependence on external field, owing to the increased tilt of the actuator, which further acts to increase M. Saturation of the magnetic material is predicted to occur at 18 mT, assuming a saturation of 1.0 T.

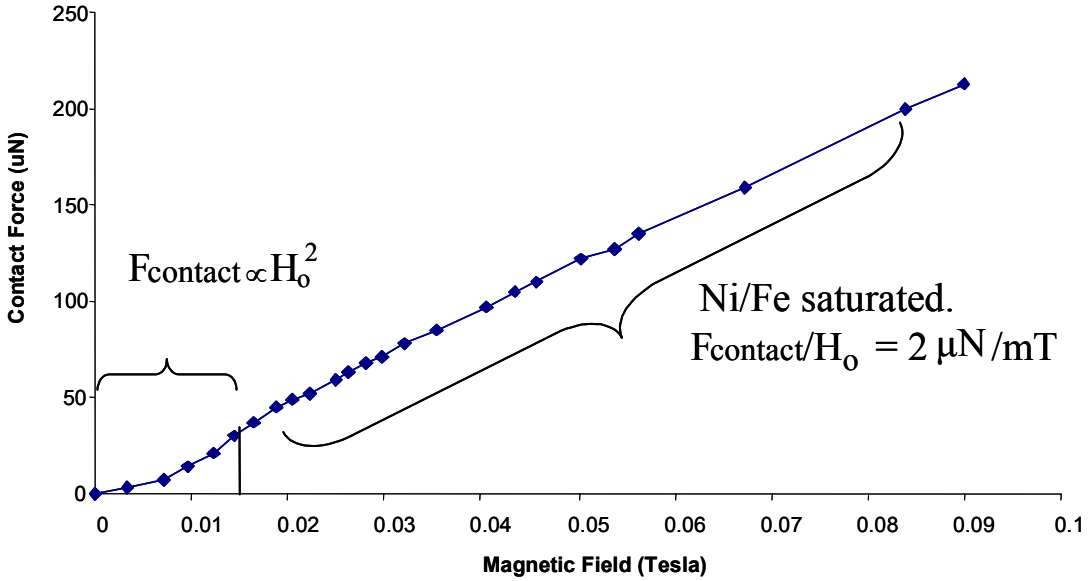

Figure 6.7. Calculated vertical contact force between the hinge tip and the bottom substrate.

6.2.3 Friction

In general a frictional force will exist, impeding the direction of wiping motion of the system (when the beam is in contact wiping with the substrate) and preventing minimization of the Hamiltonian. This force exerted by friction is related to the contact force between the beam tip and substrate by the coefficient of friction, μ. The frictional force is proportional to the contact force (the constraint λ_1 previously determined). Due to the small angle the beam makes with the horizontal, this frictional force contributes a much smaller torque about the beam center than the contact force. In fact the ratio of moments on the beam from the frictional force to the contact force can be shown to be μ

tan φ.

The presence of friction is necessary for appropriate contact force to be developed for achieving a low resistance electrical contact between the beam tip and substrate. However, if the friction is too great it will reduce the wiping phenomenon and result in a significant deviation in predicted performance. The frictional force acts as a lateral force on the hinge ends, extending the projection of the hinge length, x, by an amount Δx_2. This extension results in an additional potential energy term for the hinge, as two orthogonal forces determine the cantilever shape. The total hinge energy is modified by Equation 6.20.

$$U_{hinge-2} \propto EI \frac{(\Delta x_2)^2}{(\Delta z)^3} \tag{6.20}$$

The force produced by this potential for a displacement Δx_2 must equal the frictional force present on the beam, Equation 6.21. That is, the sign of Δx_2 must change depending on the direction of $F_{friction}$, and therefore depends on the direction of motion.

$$F_{hinge-2} \propto EI \frac{\Delta x_2}{(\Delta z)^3} \approx F_{Friction} \leq F_{contact} \propto EI \frac{\Delta z}{x^3} \tag{6.21a}$$

$$\therefore \Delta x_2 \approx \frac{(\Delta z)^4}{x^3} \tag{6.21b}$$

For a Δz of 100 μm over external fields ranging from 10-100 mT and an initial hinge length of 300 μm, the predicted extension, Δx_2, of the hinge projection due to the

frictional force is 4 μm.. At a Δz of 50 μm, Δx_2 is limited to 0.25 μm. During testing it was observed that after ramping the magnetic field to 100 mT, a lag in movement of the actuator occurred while reducing the field. Thus, the effect of friction results in a deviation from the model which becomes significant with larger external magnetic fields, i.e., >100 mT. Since the direction of this calculated deviation depends on the change in magnitude of the external field, a hysteresis is predicted.

However, after the onset of motion with an increase in the external field (as determined by the static friction value), the new equilibrium is determined by the value of the kinetic friction. Therefore, there should be some discretization to the device position. Assuming a kinetic friction value 50% lower than the static value, jumps in position of up to 3 μm are predicted. This phenomenon partially obscures the anticipated hysteresis. Figure 6.3 shows both the experimental and modeled data for the hinge elevation, Δz, for an increasing external magnetic field. The experimental data shows good agreement with the model, reproducing the large vertical change of 100 μm in the hinge elevation over a 50-mT range in background field, followed by a range of reduced response as the hinges become further compressed. Furthermore, discontinuities in hinge elevation of 2-4 μm were measured, in agreement with the predicted values.

6.3 Summary

The wiping movement of a MEMS magnetic actuator has been observed and measured, and the factors identified which determine the ease of such motion. A first principles model has been created that predicts the equilibrium and dynamic behavior of such devices, and anticipates the 50 μm lateral wiping measured. Additionally, the existence of a hysteresis dependent upon the external field magnitude and position "stepping" due to friction are predicted and observed. Excellent agreement was observed between experimental data and the model for the device equilibrium. Measurement of the transient response was not investigated. The wiping movement is believed to prolong the lifetime of semi-permanent electrical contacts. Precise control over beam position in this manner could find applications in fluidic valve technology and in optical switches.

CHAPTER 7

CONCLUSIONS

7.1 Summary of Work

The concepts of electrostatic and magnetic actuation were investigated, and significant scientific contributions were made on each front. In particular, biaxial stress gradients formed by lithographically patterning a bimetallic structure composed of gold in two differently stressed states were used to increase the tuning range of MEMS variable capacitors. An ever-decreasing radius of curvature from hinge to tip described the shape of the released cantilevers. For certain hinge and tip combinations, the biaxial stress profile has enabled a doubling of the capacitance range for the MEMS cantilever. Applications of this technology include cryogenic RF MEMS tuners, in which oxidation resistance of gold, absence of thermal mismatch of the bimetallic gold cantilever, and excellent RF properties of gold are all essential. The gradual uncurling of the gold actuator drastically reduced the hysteresis of the MEMS cantilever in comparison to previous designs with uniaxial stress gradients.

Bistable actuation mechanisms were also investigated with the attempt of identifying means of reducing the energy expenditure of an RF MEMS relay. Magnetic actuation was chosen to be superior for this endeavor, and cryogenically compatible, high isolation, low insertion loss RF switches were designed, modeled, fabricated and tested. Large throw

(100 μm) MEMS relays with better than 50 dB isolation from DC to 2.0 GHz and with less than 0.1 dB insertion loss per MEMS switch were realized. A current of 40 mA applied through the in-plane integrated coil was found to be suitable for actuation of this switch design, and external magnetic fields of 10 mT were appropriate for holding the latched state of the actuator. Typical switching times were 2-5 ms, and switching energies were typically in the 100 μJ range.

Several factors were investigated, including the relationship between contact force and contact resistance. The greatest reduction in contact resistance was found to occur within the first 10 μN of contact force, with very little further benefit observed with modest increase in contact force. Also, electrical lifetime was determined to be 2-4 million cycles during testing in an unpackaged state in ambient air. Mechanical lifetime was found to be much longer (>150 million cycles).

Further analysis of the design space of these magnetic actuators led to a significant advancement. Optimization of the actuator geometry (hinge stiffness), permalloy patterning (aspect ratio of strips), and intrinsic properties of the magnetic material (coercivity, saturation) led to a design where very short current pulses through the integrated coil were sufficient to switch the state of the device. In particular, shortening of the coil current pulses to 100 μs (shorter pulses could not be tested, but are believed to be viable) reduced switching energies to the 5 μJ range. This is of great value in cyogenic systems, potentially reducing the heat load of arrays of these MEMS relays by > 95%.

During overdriving of magnetic actuators with high magnetic volume (>2 million μm^3) and low hinge stiffness (< 1 10^{-8} Nm/rad), the tips of these devices were observed to wipe along the substrate towards the hinged end. This additional mode of operation is potentially valuable in maintaining a clean electrical contact between the actuator tip and contact pad during normal operation. A fundamental physical model of this phenomenon has been developed and agrees with the experimental data.

7.2 Comparison of Electrostatic and Magnetic Actuation

In order to meet the isolation requirements of a high performance RF MEMS switch, the actuation distance must be increased. The dependence of isolation on the separation distance between the two bonded substrates was shown in Figure 5.16 as a function of the frequency of the RF signal. This information is presented in Figure 7.1 in a different format, showing the linear dependence of isolation on the logarithm of the actuation distance. Data is shown for both 0.9 GHz and 2.0 GHz. This model predicted a 90 μm substrate separation and actuation distance was necessary to yield an isolation of 50 dB.

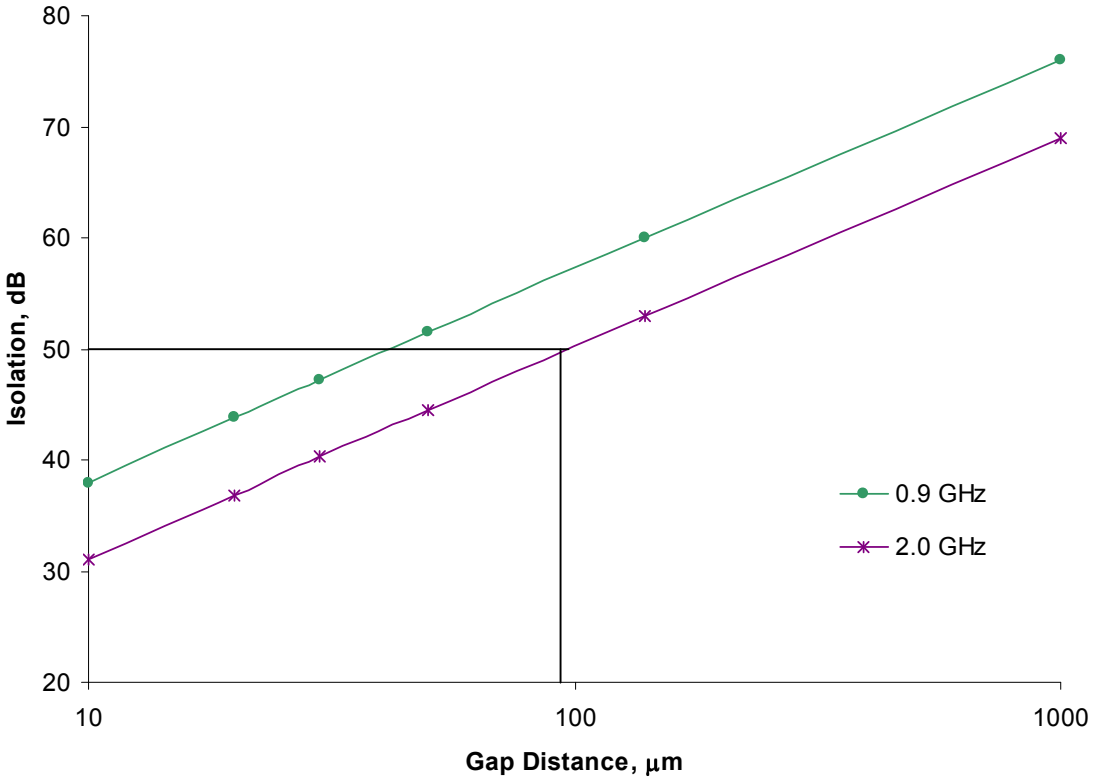

Figure 7.1. RF isolation as a function of gap distance.

For a given gap distance, g, the electrostatic torque, $\Gamma_{electrostatic}$, generated on a conductive cantilever is given by Equation 7.1.

$$\Gamma_{electrostatic} = \int_0^L \frac{F_{electrostatic}}{L} x \cdot dx = \frac{\varepsilon A V^2 L}{4g^2} \tag{7.1}$$

Where L is the length of the cantilever, A is the area of the pull-in electrode (assumed to

be equal to the area of the cantilever), V is the applied voltage difference between the cantilever and pull-in electrode, and ε is the permittivity of the gap between the cantilever and electrode.

The torque experienced by a cantilever composed of magnetic material is given by Equation 7.2.

$$\Gamma_{electrostatic} = -MV_F B\cos(\theta) \tag{7.2}$$

where M is the magnetization of the magnetic material, V_F is the volume of the ferromagnetic material, B is the external magnetic field, and θ is the angle between the magnetization and external field vectors.

The ratio of these two torques is given by Equation 7.3.

$$\frac{\Gamma_{magnetic}}{\Gamma_{electrostatic}} = -\frac{MVB\cos(\theta)}{\frac{\varepsilon A V^2 L}{4g^2}} \tag{7.3}$$

Assume the following: the angle θ is approximately equal to 0, the ferromagnetic material is saturated ($M = M_{sat}$), the actuator length is 1000 μm, the ferromagnetic footprint is equal to the area of the pull-in electrode, a ferromagnetic thickness of 10 μm, and epsilon given as the permittivity of free space. Now, the ratio presented in Equation 7.3 is investigated for three different cases, as described in Table 7.1.

Table 7.1. Three cases for comparison of electrostatic and magnetic actuation.

	V, volts	**B, Tesla**	**Critical Gap, μm**
1	10	0.01	1.7
2	100	0.01	17
3	10	0.1	0.5

The logarithm of the ratio of the magnetic and elastic torques for each of these 3 cases is plotted versus gap distance, and is shown as Figure 7.2. For case 1, a magnetic torque advantage exists above 1.7 μm; for case 2, a magnetic torque advantage exists above 17 μm; and for case 3, a magnetic torque advantage exists above 0.5 μm. A magnetic torque greater than the electrostatic torque at a given gap distance implies a shorter switching speed for the magnetically actuated device, a critical feature in relay design. This ratio of torques also gives information on the contact force achieved in the latched state for each mechanism. For example, assuming a 1 μm dielectric layer separating the pull-in electrode at a relative potential of 100 V (case 2) gives a contact force advantage of over 2 orders of magnitude for the elelectrostatically actuated MEMS switch; however, for a potential difference of 10 V supplied by the pull-in electrode (case 3), the contact force advantage switches to the magnetic actuation scheme.

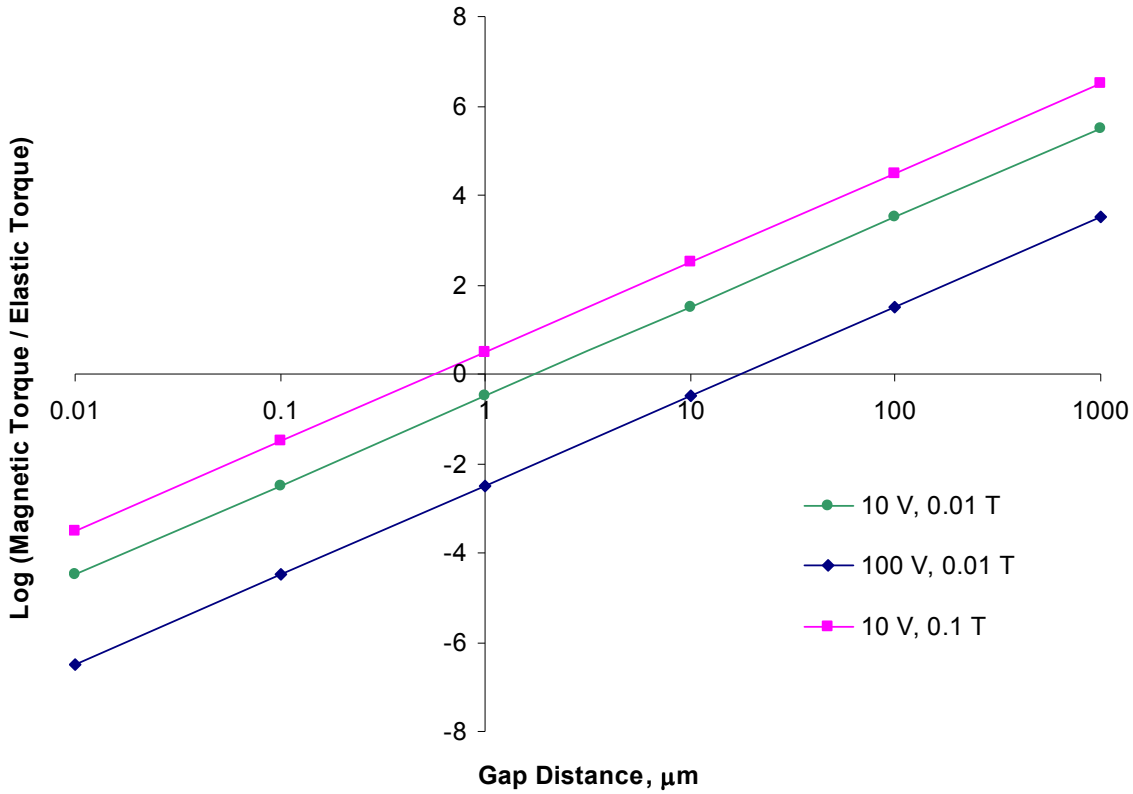

Figure 7.2. Magnetic to Elastic torque ratio as a function of gap distance.

For type-1 and type-3 magnetic actuators (chapters 4-5) in a 10 mT external magnetic field, the smallest current through the 30 Ω integrated coil that produced reliable switching was found to be 30 mA and 40 mA, respectively. This results in an average on power to the coil of approximately 40 mW. Using the value for the continuous power for electrostatically controlled relays of 0.1 mW (from Table 1.1), this suggests to a 400 times increase in operating power for the magnetically actuated devices presented in this work.

However, since the magnetic actuators were designed to be bistable (chapter 4), they only consume power during switching, and therefore their average power consumption is linearly related to both the switching time and the switching frequency, as shown in Equation 7.4.

$$\left(\frac{P_{\text{magnetic}}}{P_{\text{electrostatic}}}\right)_{\text{average}} = 400 \cdot \text{t}_{\text{switch}} \cdot f_{switch} \tag{7.4}$$

where $P_{magnetic}$ is the average magnetic actuation power, $P_{electrostatic}$ is the average electrostatic control power, f_{switch} is the switching frequency, and the switching speed, t_{switch}, is given by:

$$d = \frac{1}{2} \cdot a \cdot \text{t}_{\text{switch}}^2 \tag{7.5}$$

where a is the average acceleration of the actuator during switching, and d is the actuation distance. The instantaneous acceleration is give by:

$$\Gamma_{magnetic} = \text{MV}_{\text{F}}\text{B}\cos(\theta) = \frac{1}{2} m \cdot L^2 \cdot a \tag{7.6}$$

where M is the magnetization of the magnetic material, assumed here to be saturated during switching. Finally, the ratio of average powers can be written as follows:

$$\left(\frac{P_{\text{magnetic}}}{P_{\text{electrostatic}}}\right)_{\text{average}} \propto \sqrt{\frac{\text{d}}{\text{B}}} \cdot f_{switch} \tag{7.7}$$

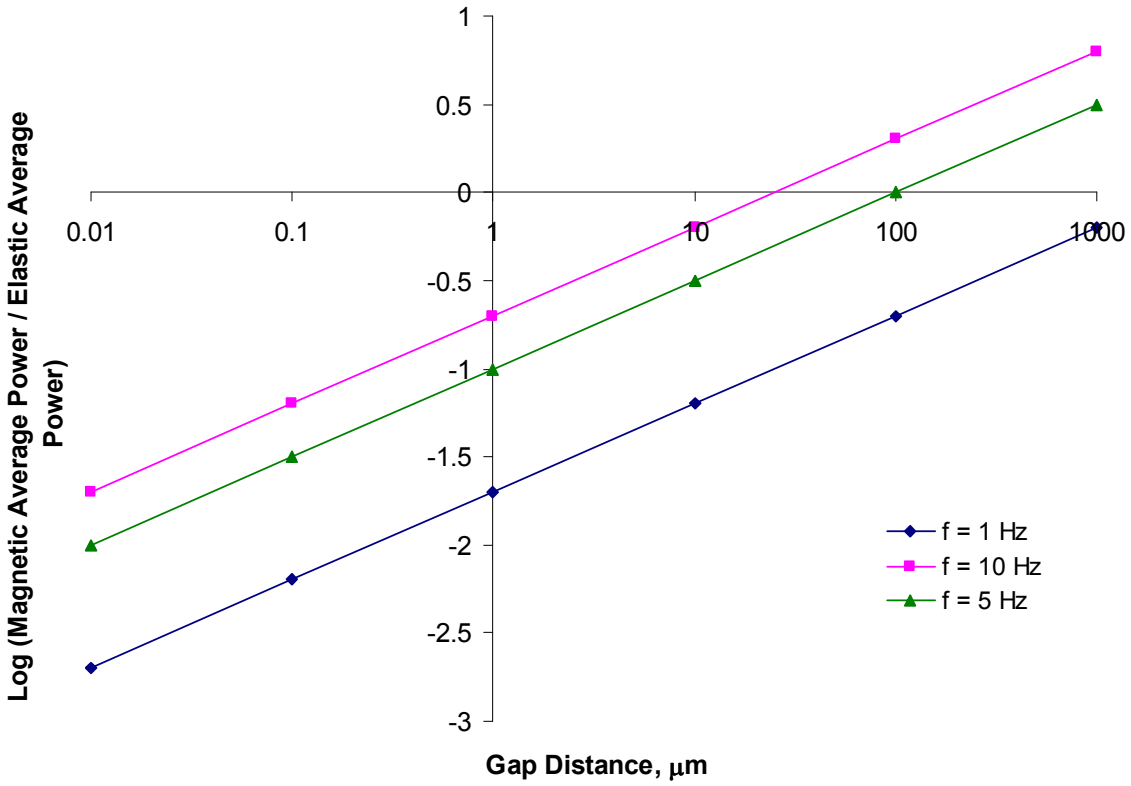

Figure 7.3. Average power ratio for magnetic and elastic actuation mechanisms as a function of gap distance.

The dependence of this average power ratio on the switching frequency of the relay is shown in Figure 7.3 for a device operating in a 10 mT external magnetic field. It is predicted that the RF MEMS relay presented in this work, switching at an operating frequency of 5 Hz, consumes the same energy as electrostatically actuated RF MEMS

switch described in Table 1.1. The energy required to operate the actual magnetic relay in a cryogenic environment would be considerably less than this, due to the increased conductivity of the gold microfabricated coil. In addition, further design of this coil in the form of additional layers of turns would produce the same switching magnetic field at much lower operating currents, again reducing the energy expenditure. Therefore, due to these considerations, this large throw MEMS magnetic relay would consume less power than its electrostatic competition, even operating at 40 switching events per second.

CHAPTER 8

RECOMMENDATIONS

While it is the belief of the author that this work has been a significant contribution to the literature on MEMS magnetic actuators, there exist several opportunities to further the work presented. The following are possible future contributions.

1) Investigation of the value of the wiping action presented in chapter 6 when used as a regular cleaning cycle during the operation of the magnetic relay.
2) Determination of technical merit in adding mechanically harder conductive material to the contact area of the relay, with the goal of reduction in wear of the actuator tip during longer lifetimes.
3) Fabrication of magnetically bistable MEMS actuators experiencing the SPS event in both directions by optimization of the intrinsic magnetic properties of the magnetic material (specifically coercivity).
4) Development of magnetically actuated, mechanically bistable relay by use of more flexible bridge materials (for example, polymeric material) and lithographically patterned hard magnetic cylinders on the bridge. See next section for premise of this idea.
5) Investigation of additional geometrical arrangements of the bistable magnetic actuators. For example, multiple actuators off a single post for more complex signal routing, etc.

8.1 Mechanical Bistability

Another design that may exploit the idea of bistability is the idea of using magnetic actuation to switch between mechanically stable equilibrium positions. A second design was investigated that utilizes mechanically stable configurations instead of magnetically stable configurations. Consider a bowed metal bridge above two anchors as shown below in Figure 8.1. Such geometry can be achieved through release of a sacrificial material beneath the metal, leaving the curved surface shown. This beam configuration is stable to small displacements. For example, if the beam were to be deflected downward slightly and then released, the beam would return to its original position. However, if the beam were to be deflected much further (for example by a force applied downwards at the bridge 8.1.

8.1.1 Principle of Operation

To calculate the force present on such a magnetic object, it is necessary to express the force through the gradient of the potential as shown in Equation 8.1,

$$\begin{aligned}\vec{F}_{magnetic} &= -\nabla U = \nabla(\vec{m}\cdot\vec{B}) \\ &= \vec{m}\times(\nabla\times\vec{B}) + (\vec{m}\cdot\nabla)\vec{B} = (\vec{m}\cdot\nabla)\vec{B} = m_z\frac{\partial B_z}{\partial z}\hat{k}\end{aligned} \tag{8.1}$$

where $\hat{k}$ is the unit vector along the z-axis. Using this analysis, the total force acting on a

series of magnetic dots can be expressed by Equation 8.2.

$$\vec{F}_{magnetic} = (N_{dots} V_{dot} \vec{M}) \nabla_z B_z \tag{8.2}$$

If the magnetic force is greater than the force required to change the mechanical configuration by effectively buckling the beam bridge, then a bistable switch can be designed. Thus the key to the design is expressed in Equation 8.3.

$$\vec{F}_{magnetic} \cdot \hat{k} > \vec{F}_{buckling} \cdot \hat{k} \tag{8.3}$$

A schematic of a device using this concept is shown in Figure 8.1. Two beam members with several magnetic disks take advantage of the gradient of the magnetic field. When this device is flexed and moved from the upstate to the downstate, the longer signal contact reed moves a greater distance. This large throw generates a high isolation for the device and allows the RF signal to travel directly from input to output.

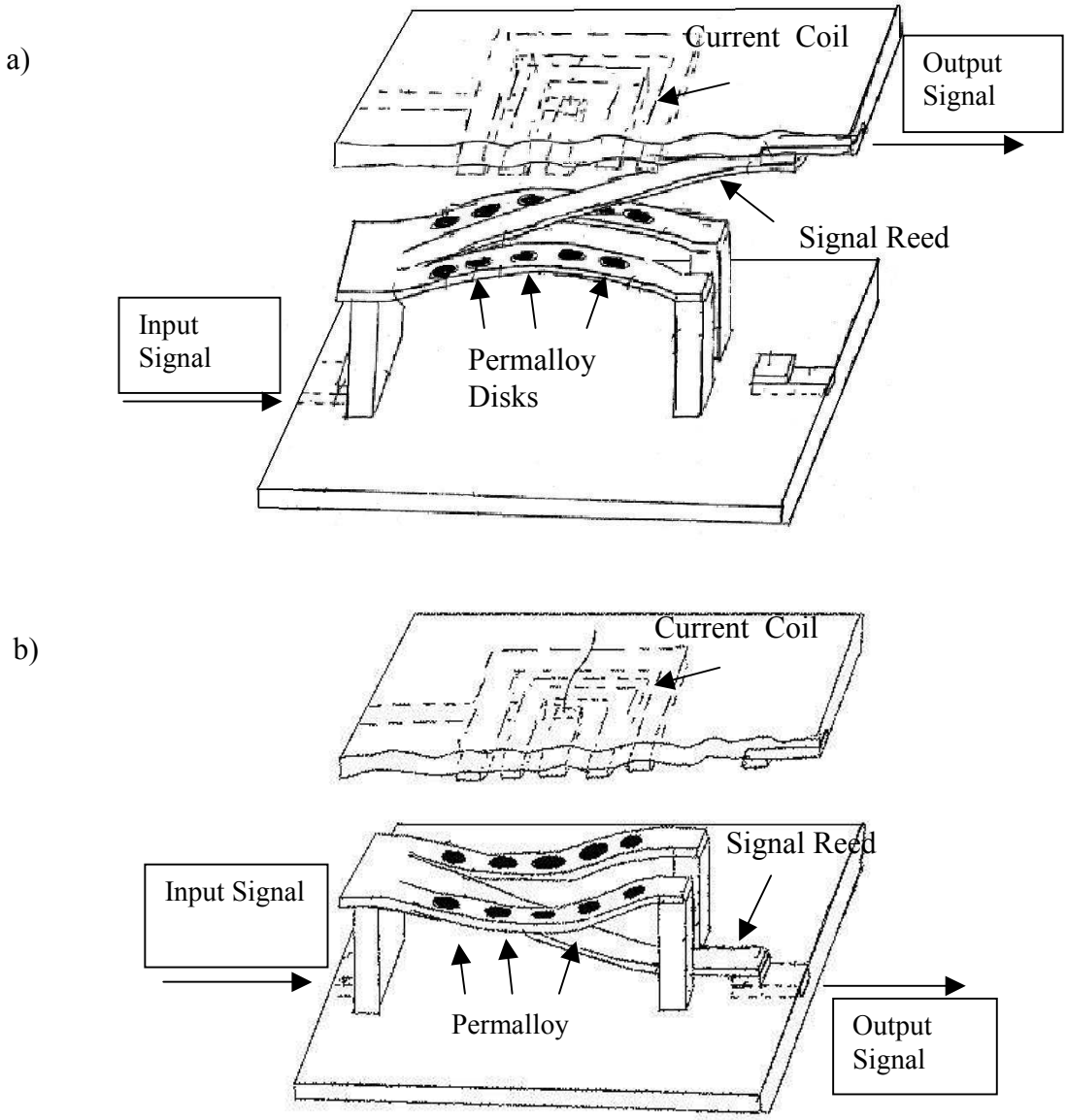

Figure 8.1. Schematic of mechanically bistable device in both equilibrium positions: a) upstate and b) downstate.

8.1.2 Gold Bridges

One approach for fabrication consisted of patterning lines of polypropylene carbonate (PPC) 100 μm in width and 20 μm thick. A 1.5 μm film of gold was then evaporated above the PPC, and was then patterned orthogonal to the PPC lines using the same mask. Sacrificing the PPC then left bridges of gold arced over the silicon wafer below. Figures 8.2 and 8.3 show the resultant metal bridges.

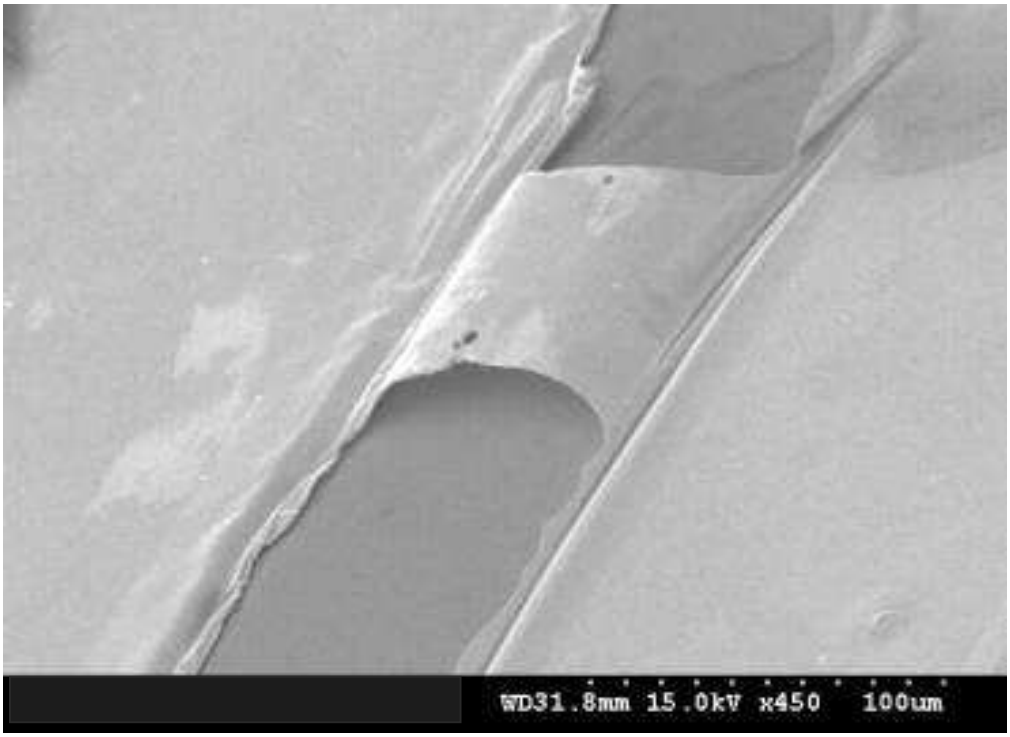

Figure 8.2. 100 μm x 100 μm gold bridge.

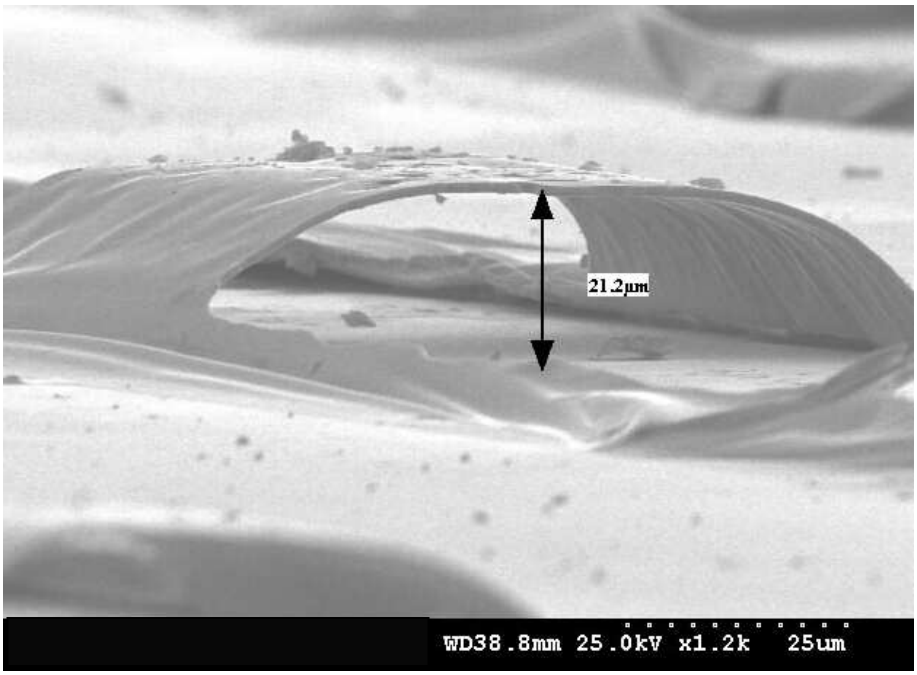

Figure 8.3. Same gold bridge showing 21µm height (of sacrificed PPC).

8.1.3 Processing

The processing steps for fabrication of the gold bridges are as follows:

1. Spin PPC (polypropylene carbonate) on an oxidized wafer to achieve a thickness of 20-25 µm and a width of 100 µm. Soft bake the polymer at 110 ^{o}C for 10 minutes. Measure the thickness of the polymer with the profilometer.
2. Expose the polymer on the MA6 mask aligner at a wavelength of 365 nm. Use the mask with the polymer lines. The dose should be 1000 mJ/cm^2. The time for exposure should be approximately 70 seconds. After exposing, place the wafer on

a hotplate to decompose the exposed polymer. Set the hotplate at 110 ^{o}C, and place the wafer on the hotplate for 10 minutes.

3. Place the wafer in Unity 200 P developer for 10 seconds, agitating the solution. After rinsing the wafer with DI water and drying, measure the peak height and the peak width with the profilometer.
4. Evaporate 400 Å of titanium and 15,000 Å of gold onto the patterned polymer lines.
5. Spin on Shipley 1827 photoresist. Spin the resist at 2000 RPM at a ramp rate of 500 RPM/second for 30 seconds. Soft bake the resist at 90 ^{o}C for 2-3 minutes. Pattern bridges with the polymer line mask orthogonal to the polymer lines covered with titanium and gold. Expose the resist with a dose of 105 mJ/cm^2. The time for exposure should be approximately 10-15 seconds at a wavelength of 365 nm on the MA6 mask aligner. Develop the resist with Shipley 354 developer base. The developer should be agitated while the resist dissolves away. Developing time is 2-5 minutes. Post bake the resist at 100 ^{o}C for 1 minute on a hotplate.
6. Etch the exposed gold with a standard gold etchant (1:2:10 I_2:KI:H_2O). The etch time will be 30-60 minutes. This gives an etch rate of 1.5-3.0 μm per hour. The etch rate will vary with different concentrations of etchant. After removing the gold, rinse the wafer with DI water and dry.
7. Etch the titanium layer with BOE. Leave the wafer in the BOE for no more than 5 seconds. Rinse the wafer with DI water and dry.
8. Strip the Shipley 1827 resist with Shipley 1112A photoresist stripper. Heat the

stripper to 50 ^{o}C, helping the resist to dissolve more quickly. Rinse the wafer with DI water and dry.

9. Place the wafer in the furnace to decompose the polymer beneath the patterned gold bridges. The wafer should be placed in a furnace at 170 ^{o}C for 2 hours.

8.1.4 Nanoindentation

In order to evaluate the stiffness of the resultant metal bridges and the possibility of bistability, use of a nanoindenter was required. The nanoindenter consists of a small movable tip that measures the magnitude of the small forces necessary to move such a device over small deflections. The indenter can be operated in one of two modes. In displacement mode the user defines a displacement ramp, where the indenter tip makes contact with the bridge sample and moves it over the input range. The software measures the force applied to the tip at each position, and produces a graph of force versus displacement. In load control, the user inputs a range of force to apply, and the software plots the corresponding change in sample position.

For the gold bridge sample, it was found that 2000 μN was more than sufficient to move the bridge over the 20 μm range available. Therefore, a load control ramp was setup that slowly increased the force applied by the indenter tip on the sample to the maximum. Then the load was lowly decreased back to 0 μN. The results are typical of those shown in Figure 8.4.

In Figure 8.4, over the first 15 μm of deflection the bridge moves with a relatively constant stiffness of 50 μN/μm. At this point, the bridge experiences a large change in deflection with no further increase in force. To the contrary, the bridge actually begins to require less force for further deflections. This phenomenon represents instability in the gold bridge. The sudden increase in force present at 22 μm is the effect of the nanoindenter tip coming into contact with the wafer surface. The silicon beneath the beam was etched with KOH before indentation, allowing the bridge to buckle down and extend beneath the original plane of the wafer. However, the nanoindenter tip used for this measurement was not able to maintain contact with the bridge due to the large relative size of the nanoindenter tip. The radius of curvature of the tip used for this measurement is approximately 200 μm, whereas the entire length of the metal bridge is only 100 μm.

Another point of interest is the return of the applied force on the beam from the maximum value at 2000 μN to 0 μN. As seen in Figure 8.4, the bridge moves only very slightly back towards its original position and remains 22 μm down from the original position of the bridge. This is evidence that the bridge has buckled down and is in a new stable configuration. This was confirmed through inspection of the bridges before and after nanoindentation. Before nanoindentation the bridge surface is smooth, like the bridge shown in Figure 8.3. After indention, there are three relative maxima and minima along the bridge length, as expected in the buckled mode.

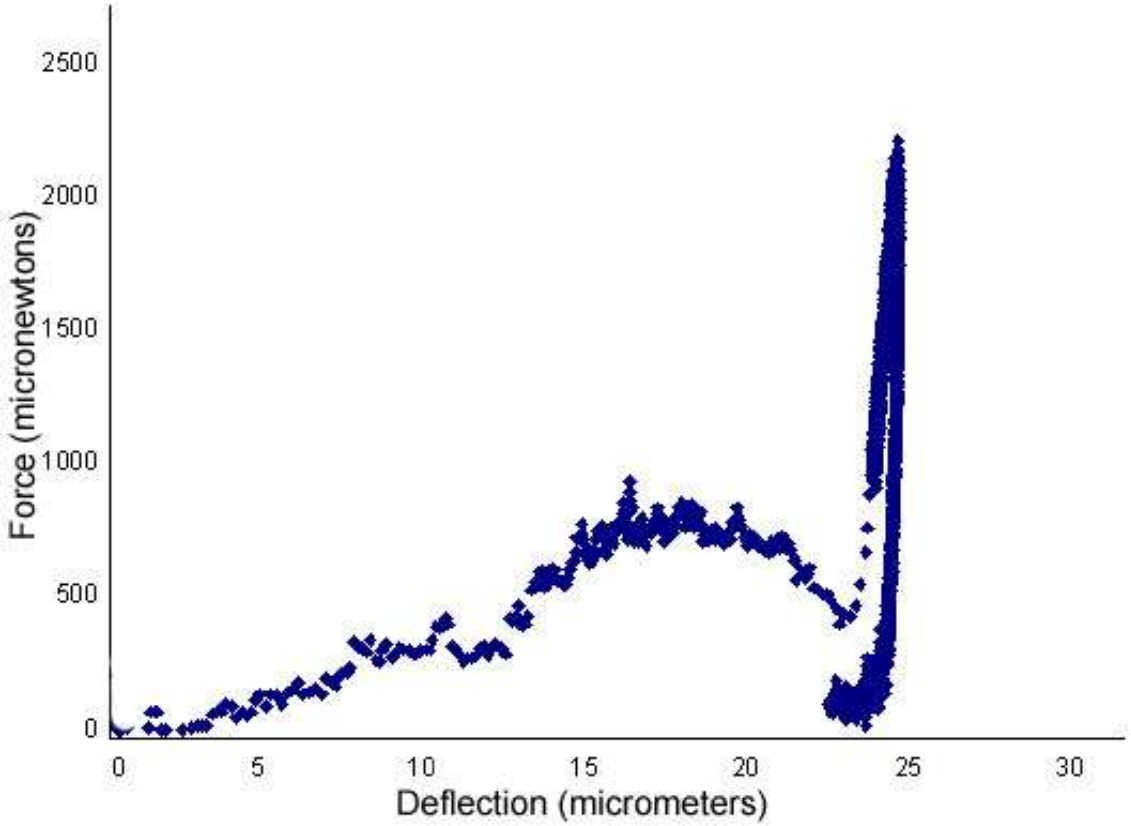

Figure 8.4. Nanoindentation data of sample gold bridge.

From these tests, success in fabricating mechanically bistable gold bridges was evidenced. Furthermore, it is believed that incorporation of these elements into the design shown in Figure 8.3 would not introduce much difficulty; however, the 800 μN force required to change the state of the single mechanically bistable beam from up to down is too large for practical MEMS design, as an extremely large gradient field would be necessary to produce a force capable of buckling two such gold bridges.

However, advances could be made in materials and design that could make such an approach feasible. If the switch were to be used in cryogenic environments, such as the magnetic actuator presented in chapters 4 and 5, then use of HTS to pass large currents through a series of integrated coils could generate a much larger gradient field. Also, the bridge could be fabricated from polymeric material, greatly reducing the force necessary to switch between equilibrium positions.

APPENDIX A

MAGNETICS

A.1 Forces and Torques on Magnetic Dipoles

A material with magnetic moment, m, in a magnetic field, B, has a potential energy expressed by Equation A.1. The magnetic moment, m, may be expressed as the product of the volume of the sample with the magnetization value of the material [47].

$$U = -\vec{m} \cdot \vec{B} = -\vec{M}\, V \cdot \vec{B} \tag{A.1}$$

Therefore, when the magnetic field and magnetization are completely aligned ($\theta = 0$), the energy of the interaction is minimized. Similarly, when the magnetic field and magnetization are antiparallel, the most unfavorable energetic state is realized. This is demonstrated in Figure A.1.

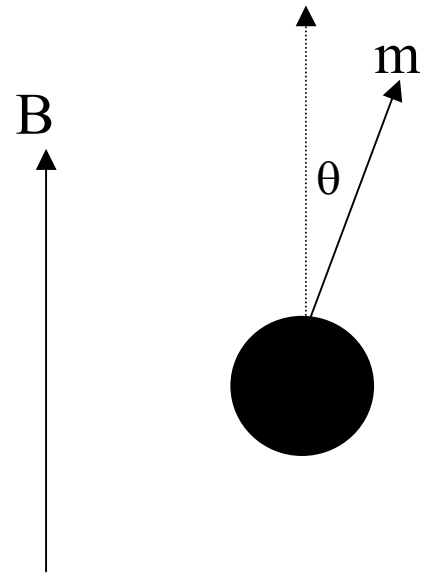

Figure A.1. Alignment of the magnetic moment, m, of a magnetic material with the external magnetic field, B. The potential energy of the configuration is related to the magnitude of the B field and the magnetic moment, as well as the angle between these vector quantities.

Recalling that the force may be expressed through the gradient of the potential field leads to Equation 2.2 [37].

$$\vec{F}_{magnetic} = -\nabla U = V\nabla(M \cdot B) \tag{A.2}$$

If the field is uniform, there will be no net force on the magnetic material. However, if the magnetization and field are not aligned there will be a moment present acting on the magnetic material, given by Equation A.3 [48].

$$\vec{M}_{mag} = -\frac{\partial U}{\partial \theta} = V\,\vec{M} \times \vec{B} \tag{A.3}$$

A.2 Magnetic Materials

The total magnetic field, $\vec{B}$, is related to both the field intensity, $\vec{H}$, and the magnetization of the sample, $\vec{M}$, through Equation A.4.

$$B = \mu_0 H + M \tag{A.4}$$

Here, μ_o is the permeability of free space, equal to $4\pi\ 10^{-7}$ T/(A/m). $\vec{M}$ is related to the field intensity, $\vec{H}$, through the dimensionsless quantity, the magnetic susceptibility, χ.

$$M = \mu_0 \chi H \tag{A.5}$$

Thus, $\vec{B}$ may be rewritten as a function of $\vec{H}$ only through Equation A.6:

$$B = \mu_0 H + \mu_0 \chi H = \mu_0 H(\chi + 1) \tag{A.6}$$

The magnetic susceptibility is a real quantity that may be either positive or negative. The sign and field dependence of χ, readily indentify the class of magnetic material to which the sample belongs. The three main classes of magnetic materials are as diamagnetic, paramagnetic, and ferromagnetic. Some materials display more exotic magnetic properties and are characterized as ferrimagnetic, antiferromagnetic, and superparamagnetic.

A.2.1 Diamagnetism

Diamagnetic materials weakly oppose an applied magnetic field. This interaction is

induced as predicted by Lenz's law. It is the result of electron orbital rotation For these materials $\chi < 0$, although the interaction is typically on the order of -10^{-5}. Some common examples of diamagnetic materials are gold, silver, copper, and water. It was first thought that all materials should experience diamagnetism, as electrons would generally tend to oppose the applied field [46**].**

A.2.2 Paramagnetism

Materials experiencing paramagnetism have enhanced internal fields. For these materials $\chi > 0$, although the interaction is typically on the order of 10^{-3} to 10^{-5}. Common materials that experience paramagnetism are oxygen, aluminum, and sodium. This is often the result of an impurity of ferromagnetic atoms or the presence of conduction electrons. Therefore this is a relatively weak interaction, and in most cases can be neglected. However, the Langevin theory of paramagnetism naturally leads to an analysis of ferromagnetism [46]. The potential energy of n electrons spinning with magnetic moment M_b at an angle θ to the applied external magnetic field is given as Equation A.7.

$$U = -nM_B H\cos(\theta) \tag{A.7}$$

Owing to statistical mechanics, the probability for a given spin to be present at an angle theta is proportional to the Boltzman factor exp(-U/kT). Taking the component of M in the direction of H, and integrating over the entire solid angle results in an expression for the technical magnetization M (Equation A.8):

$$M = NnM_B L(\gamma)$$
$$\gamma = \left(\coth(\alpha) - \frac{1}{\alpha} \right) \tag{A.8}$$
$$\alpha = \frac{nM_b H}{kT}$$

where L(γ) is the Langevin function, which goes to 1 for large γ and can be approximated by γ/3 for small γ; n is the number density of spins, M_b is the magnetic moment of an electron spin, T is the temperature, and k is Boltzman's constant. A detailed derivation can be found in many elementary magnetism texts [45-48]. This allows computation of the magnetic susceptibility, χ.

$$\chi = \frac{M}{\mu_0 H} = \frac{N(nM_B)^2}{3kT} \tag{A.9}$$

A.2.3 Ferromagnetism

This is the strongest of the magnetic material enhancements. If the total energy of the magnetic moment is given by Equation A.7, at room temperature the energy of thermal motion, kT, is approximately 1000 times larger than the potential energy of the magnetic moment in a 1 Tesla field [47]. This supports random alignment of magnetic moments. In order to account for ferromagnetism, an additional energy must be present due to interactions of the individual magnetic moments with the neighboring atoms. The Weiss theory of ferromagnetism can describe this phenomenon through the following potential (Equation A.10):

$$U = -nM_B\left(H + wM\right)\cos\left(\theta\right) \tag{A.10}$$

Here, w is a parameter termed the interaction energy and is related to the quantum mechanical exchange integral. This model implies that a ferromagnet "sees" an additional and dominant field wM produced by the surrounding material. Use of the same technique for analysis as in the case of the Langevin theory of paramagnetism, leads to the following form for the magnetization.

$$M = NnM_B L\left(\gamma\right) \tag{A.11}$$

$$\gamma = nM_B\left(\frac{H + wM}{kT}\right) \Rightarrow M = \frac{\gamma kT}{nM_b w} - \frac{H}{w} \tag{A.12}$$

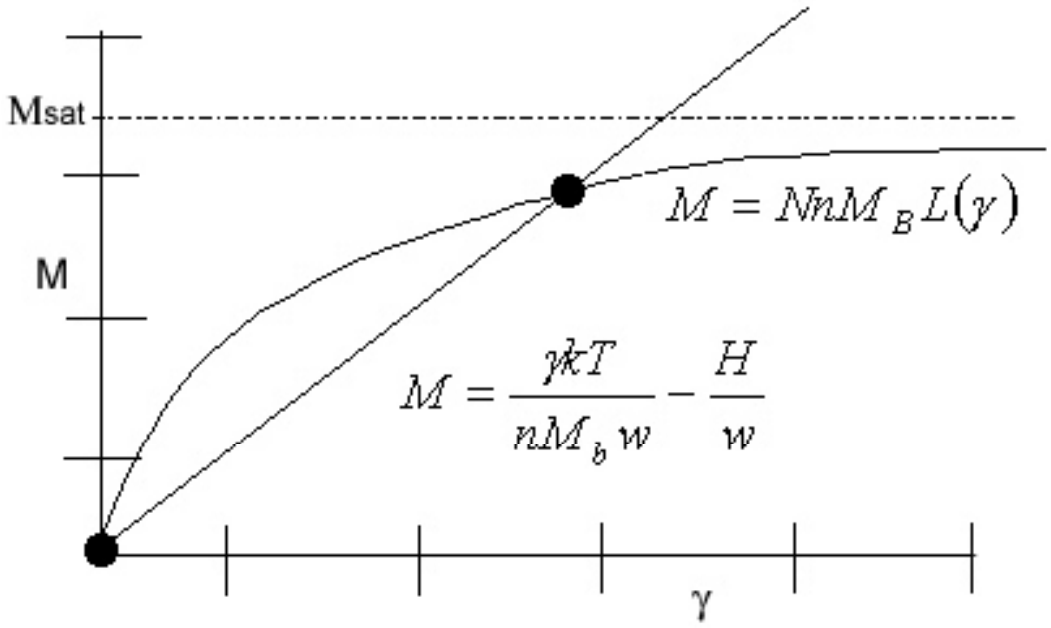

Figure A.2. Graphical solution for magnetization of ferromagnetic material. A maximum magnetization (saturation) is shown by the horizontal dashed line. The magnetic field and temperature dependence of M are shown by the graphed equations.

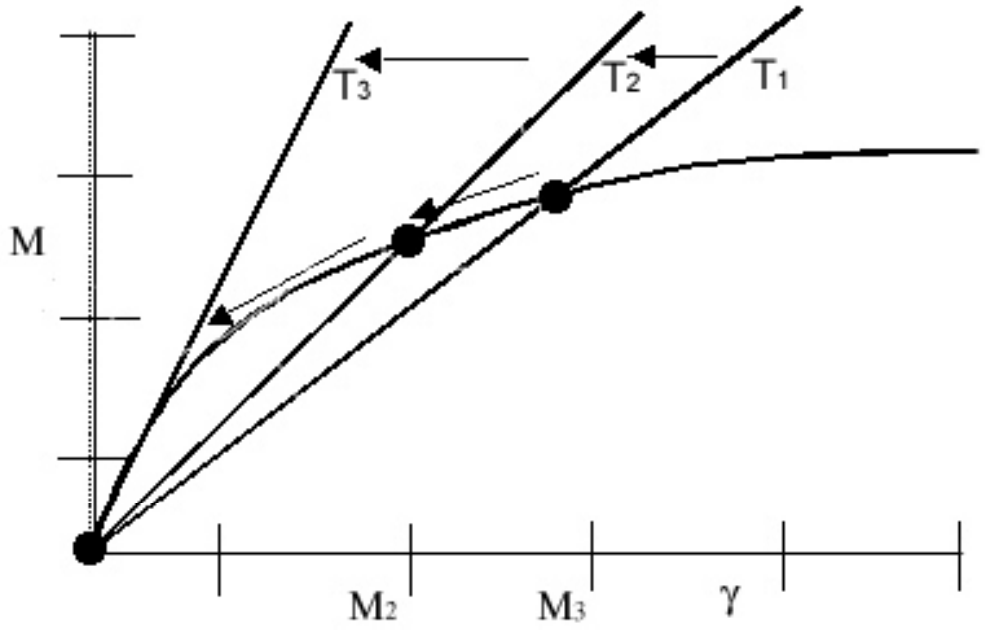

Figure A.3. Depiction of the impact of increasing temperature on the magnetization of a ferromagnetic material. For $T < T_3$, the curie temperature, nontrivial solutions exist for the magnetization.

In the case shown there are two intersections for the two equations for the magnetization, M. The trivial solution at γ equals zero is ignored, and the solution for positive γ is taken to be the solution. If the external magnetic field were to be increased, the M_1 curve would shift down, intersecting curve M_2 at a higher value of γ and giving an increased magnetization. If the temperature were to be increased, the slope of M_1 would be increased and the solution to the system would move to the left, as shown in Figure A.3. For a great enough temperature, there exists no nontrivial solution to the system. At this point the only solution to the above system is zero magnetization. This temperature may be solved for by using the small γ approximation for L(γ). This leads to:

$$T_{critical} = \theta = \frac{N(\mathrm{nM_b})^2 w}{3k} \tag{A.12}$$

This temperature is named the Curie temperature and is the maximum temperature for which magnetization exists for a ferromagnetic material [46]. Since the response of a ferromagnetic material is not linear with applied field, the magnetic susceptibility is not a constant. It has large values at low applied fields that decrease as the external field is increased. The most ordering is obtained with the first amount of external field. This is due to the large magnitude of the quantity w identified earlier. The interactions between neighboring domains is very small, and the energy cost to align opposed to the external field is very great. When no field is applied, the material either has zero net magnetization (as though it were heated above the Curie Temperature and then slowly cooled) or has a remament magnetization. If the remanent magnetization is low, this

corresponds to a relatively weak value of w since a low value of w moves the line to the left, decreasing the intersection for the magnetization. However, for a very large value of w, the slope of curve M_2 will be very small, and the intersection with M_1 will occur at a greater value of M.

The magnetic susceptibility, χ, is typically on the order of 1000 for materials such as iron, and even greater for materials such as permalloy and others. In this case, $\chi+1$ is large in comparison to 1, so the relative permeability is defined as follows:

$$M = \mu_0 H(\mu_r - 1) \tag{A.13}$$

Defining $\mu_r = \chi + 1$, the magnetization can be related to the field intensity and the relative permeability, μ_r.

$$B = \mu_0 H(\chi + 1) = \mu_0 \mu_r H \tag{A.14}$$

A.3 H-M Curve

For a paramagnetic or diamagnetic sample, analysis of the interaction is straightforward. An external field is applied, and a slight magnetic field is developed within the material as determined from the value of the magnetic susceptibility. For ferromagnetic materials, however, the response of the material to an applied field requires additional explanation.

A ferromagnetic material consists of many substructures named domains. Domains are regions where all spins are aligned. In the absence of an external applied magnetic field, these domains may become randomly aligned, producing no net magnetization over the bulk of the material (state O in Figure A.4).

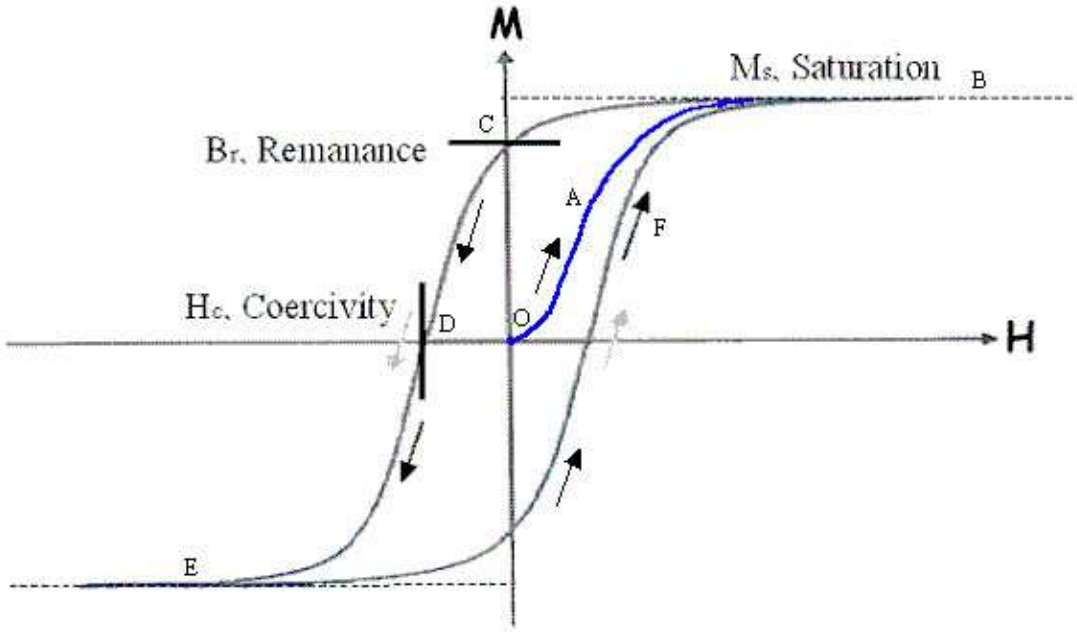

Figure A.4. M-H curve of a typical ferromagnetic material.

At this state, suppose an external field were applied. This external field would cause rotation of the spins of the individual domains in order to reduce the magnetic potential energy presented before. The external field increases the energy of the individual domains to oppose the field. As the external field is increased, the individual magnetization vectors of the domains are brought ever more into alignment with the external field, thus creating a larger net technical magnetization of the sample (point A). Once the spins are brought into complete alignment, the resultant magnetization has reached a maximal value (point B), termed the saturation magnetization, M_{sat}. Further application of external fields higher than that required to reach saturation have no impact on the magnetization of the material. Now, the external field is reduced to zero (point C). Some of the domains may relax in the absence of the external field, but the net magnetization will not reduce completely to zero since the internal field still imposes ordering on the substructure. The magnetization that remains with no external field present is called the remanance, B_r. If the field were now applied in the direction in opposition to the remaining magnetization, the net magnetization would be reduced further. At some point, the applied external magnetic field would cancel the internal magnetization, resulting in zero magnetization (point D). This external field required for this is called the coercive field, given by $-H_c$. Further application of this field results in saturation of the material in the opposite direction at the same value M_{sat} (point E). The shape swept out by the M-H curve is called the hysteresis loop. The area enclosed by this curve represents the net heat generated in the sample during one complete cycle.

A.4 Hard and Soft Magnetic Materials

The simplest classification of ferromagnetic materials is based on the width of the H-M curve discussed earlier. Ferromagnetic materials with coercivity values greater than that of iron (therefore having wide H-M loops) are termed “hard” materials, while those ferromagnetic materials with coercivity values smaller than iron (therefore having narrow H-M loops) are called “soft” materials (Figure A.5) [48]. Soft magnetic materials are used in applications when little permanent magnetization was desired. Hard magnetic materials, on the other hand, could be used in applications where permanent magnetization is useful, such as in a permanent magnetic source [48]. In this work, soft magnetic materials such as permalloy were used since the low coercivity of this material permits a small external magnetic field to greatly influence its magnetization. Similarly, the magnetization is not “frozen in” and can easily be reversed by relatively low external fields.

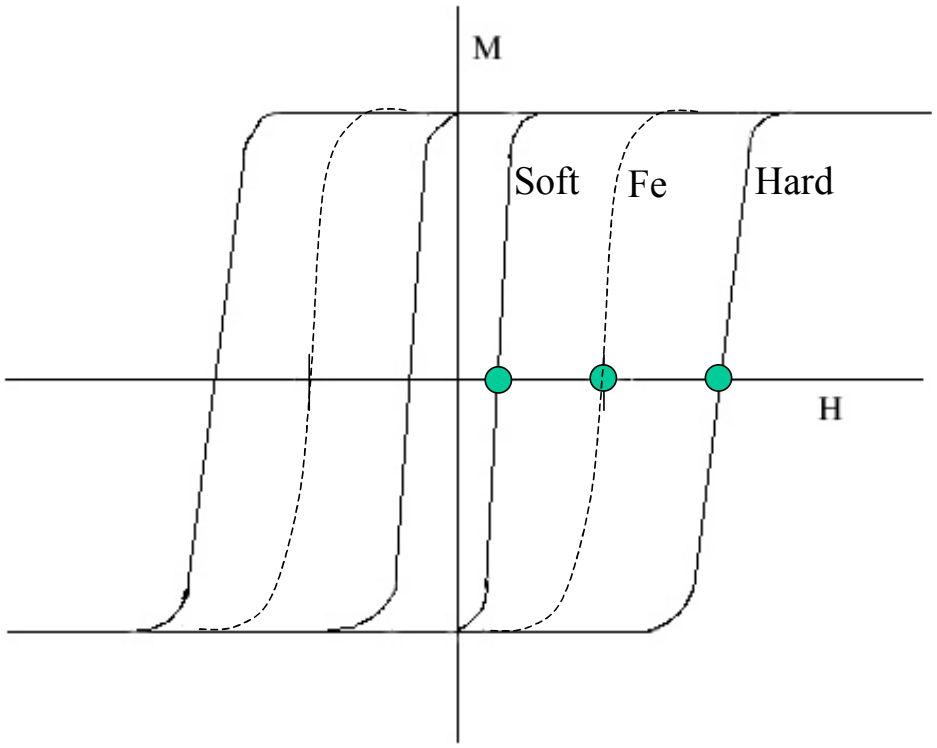

Figure A.5. Hard and soft magnetic materials.

A.5 Effect of Demagnetization on M-H Loop

When the H-M loop was introduced before in A.3, the H field present in the sample was plotted on the abscissa. It should be noted that the internal H field present within the sample is not identical to the applied external H field. In general, the internal H field will be less that the external H field [46]. Therefore, in switching the x-axis to the internal field, an apparent horizontal shearing of the B-H curve occurs. This is can be understood as follows: a certain value of magnetization corresponds to a specific internal H field, as described by Equation A.5. For a sample with a given demagnetization factor N, the internal H field is related to a greater external H field. The internal H field is equal to the external H field reduced by the quantity N M, where M is the magnetization. Therefore, each value of magnetization corresponds to a greater external magnetic field than internal magnetic field. This effect is demonstrated by the following Figure, A.6 [46]. In this figure, an external H field AC produces a magnetization OC in the magnetic sample. However, the demagnetizing field due to the sample geometry reduces the external field AC by the quantity AB, leaving an internal H field equal to BC. This results in a lower effective permeability, since the magnetic response of the magnetic material is now limited by both the material permeability and sample geometry. Thus, a larger external magnetic field is necessary to reach a specified value of magnetization.

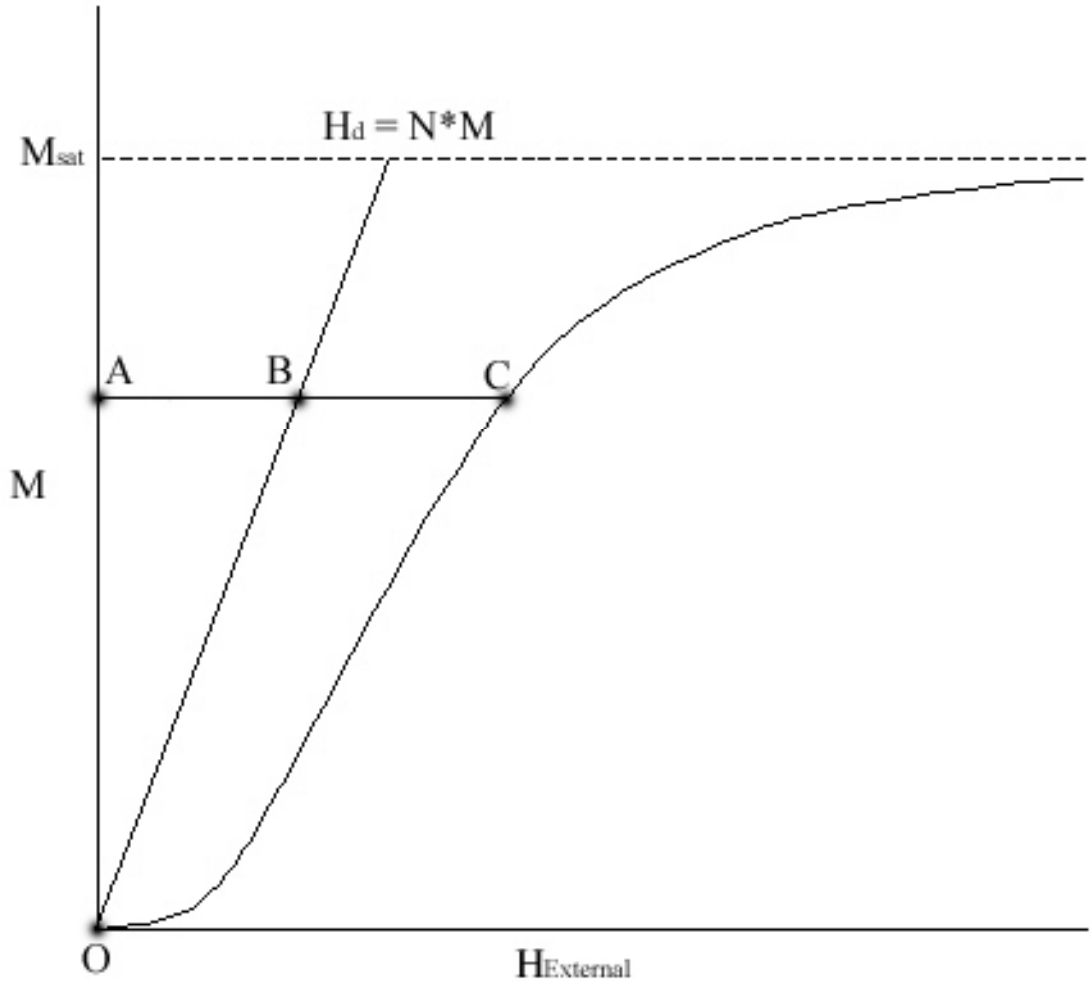

Figure A.6. Stretching of the M-H curve due to demagnetization.

APPENDIX B

CALCULATIONS

B.1 Demagnetization Field and Demagnetization Factors

Magnetic anisotropy may result from many causes, including temperature treatments of the magnetic material and deposition in the presence of external magnetic fields. The greatest cause of magnetic anisotropy is most easily controlled and results from the sample geometry. The application of an external magnetic field results in magnetic charges on the surface of any magnetic sample, resulting in the creation of a magnetic field in opposition to the applied external field. This opposing field is named the demagnetization field, and the internal field is related to the external field and the demagnetization field through Equation B.1.

$$\mathrm{H}_{\mathrm{internal}} = \mathrm{H}_{\mathrm{external}} + \mathrm{H}_{\mathrm{demag}} \tag{B.1}$$

The demagnetizaion field is given as follows,

$$H_{demag} = -\frac{MN_{beam}}{\mu_0} \tag{B.2}$$

where N_{beam} is the demagnetization factor in the direction of the applied magnetic field. The size of the demagnetization factor depends on the geometry of the sample. The demagnetization field is largest in the smallest dimension of the sample. Similarly, the demagnetization field is smallest in the largest dimension of the sample. The reason is due to the separation of the magnetic poles: the further apart between these magnetic surface charges, the weaker the interaction and the smaller the demagnetizing field. For short separations the demagnetization factor may be large. Demagnetization factors are subject to the normalization condition shown in Equation B.3.

$$N_a + N_b + N_c = 1 \tag{B.3}$$

Substituting Equation B.1 into B.2 and solving for M,

$$H_{beam} - \frac{MN_{beam}}{\mu_0} = \frac{M}{\mu_0(\mu_r - 1)} \tag{B.4a}$$

$$M = \frac{\mu_0 H_{beam}}{N_{beam} + \frac{1}{\mu_r - 1}} \tag{B.4b}$$

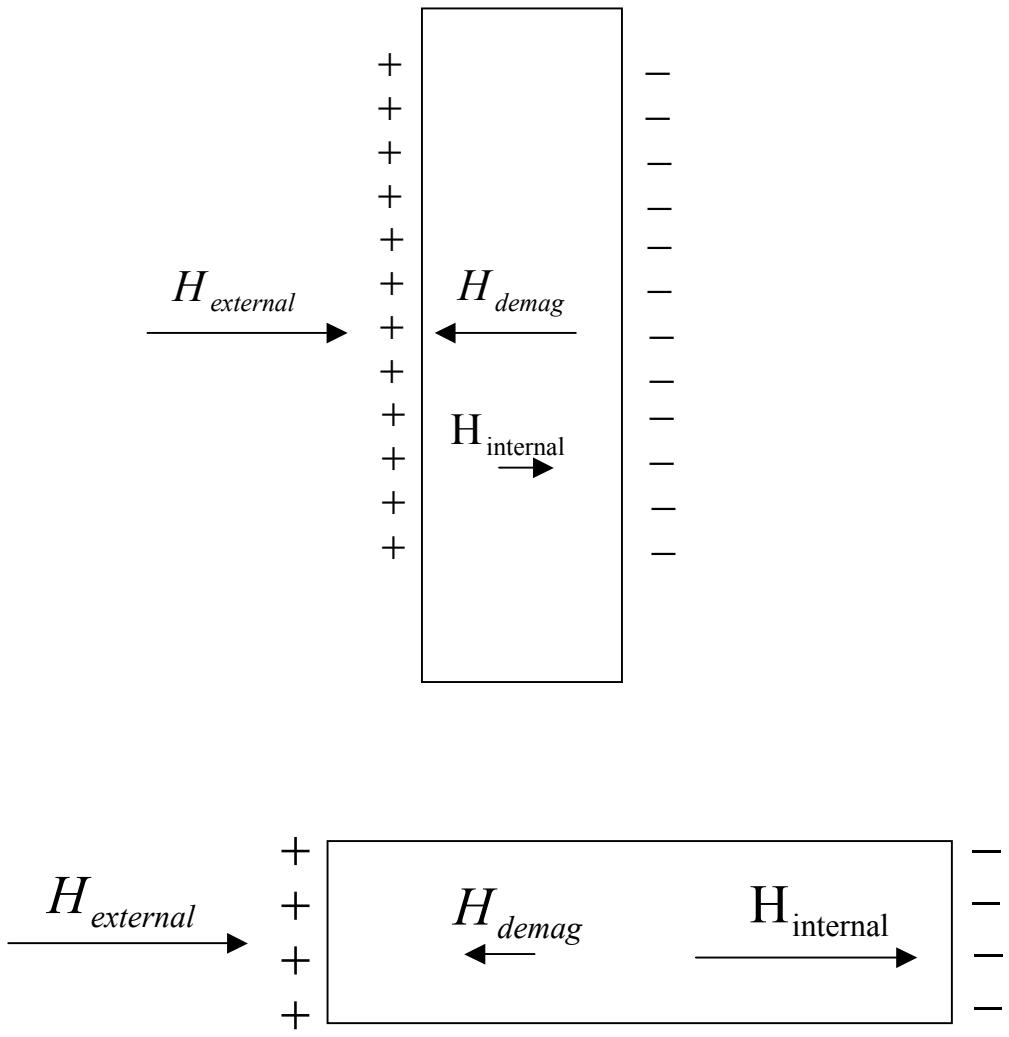

Figure B.1. Proximity of magnetic charges determines strength of demagnetizing field.

Table B.1. Demagnetization factors for common geometries.

Dimensional Ratio	Prolate	Oblate	Cylindrical Rod
0	1	1	1
1	0.3333	0.3333	0.27
10	0.0203	0.0696	0.0172
100	0.000430	0.00776	0.00036
1000	0.0000066	0.000784	0.0000036

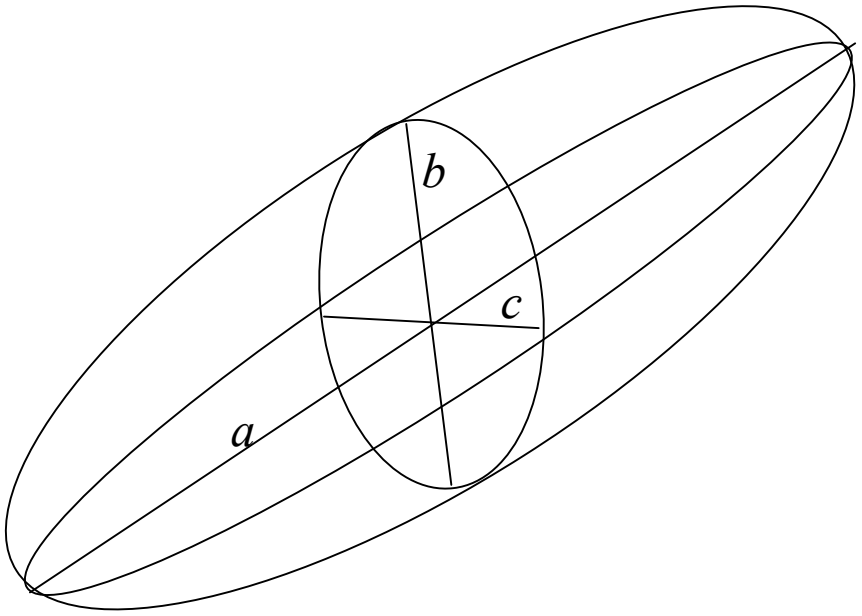

Figure B.2. General ellipsoid with axes a > b > c.

The actual magnetization of the sample is the minimum of the following two quantities:

$$M = \min(M_s, M) \tag{B.5}$$

In the case where a > b >> c and a and b do not greatly differ, the demagnetization factors N_a and N_b can be approximated as [48]:

$$N_a = \frac{\pi}{4}\frac{c}{a}\left(1 - \frac{1}{4}\left(\frac{a-b}{a}\right) - \frac{3}{16}\left(\frac{a-b}{a}\right)^2\right) \tag{B.6}$$

$$N_b = \frac{\pi}{4}\frac{c}{a}\left(1 + \frac{5}{4}\left(\frac{a-b}{a}\right) + \frac{21}{16}\left(\frac{a-b}{a}\right)^2\right) \tag{B.7}$$

For a permalloy segment with width = 200 μm, length = 500 μm, and thickness = 10 μm (such as the design-2 magnetic actuators presented in chapters 4-5), the demagnetization factors are calculated as follows:

$$N_a = \frac{\pi}{4}\frac{10}{500}\left(1 - \frac{3}{20} - \frac{27}{400}\right) = 0.012 \tag{B.8}$$

$$N_b = \frac{\pi}{4}\frac{12}{500}\left(1 + \frac{3}{5} + \frac{189}{400}\right) = 0.039 \tag{B.9}$$

$$N_c = 1.000 - 0.039 - 0.0014 = 0.947 \tag{B.10}$$

This method was used to calculate the demagnetization factors for the design-2 permalloy geometry considered in this work; however, for the permalloy patterns used for designs 1 and 3, a >> b > c, and Equations B.6 and B.7 do not apply. If used, they overpredict the value of N_a and underpredict the value of N_b. The shape anisotropy coefficients for an

ellipsoid were originally solved by Osborn in 1945 in terms of elliptical integrals [49]. Judy later constructed a series of charts for quick determination of N_a, N_b, and N_c as functions of the ratios c/a and b/a [25]. The solution for N_a, N_b, and N_c is as follows [25]:

$$N_A = \frac{\cos\vartheta\cos\varphi}{\sin^3\vartheta\sin^2\alpha}\left(F(k,\vartheta) - E(k,\vartheta)\right) \tag{B.11}$$

$$N_B = \frac{\cos\vartheta\cos\varphi}{\sin^3\vartheta\sin^2\alpha\cos^2\alpha}\left(E(k,\vartheta) - F(k,\vartheta)\cos^2\alpha - \frac{\sin^2\alpha\cos\vartheta\sin\vartheta}{\cos\varphi}\right) \tag{B.12}$$

$$N_C = \frac{\cos\vartheta\cos\varphi}{\sin^3\vartheta\cos^2\alpha}\left(\frac{\cos\vartheta\sin\vartheta}{\cos\varphi} - E(k,\vartheta)\right) \tag{B.13}$$

$$\cos\vartheta = \frac{c}{a} \tag{B.14}$$

$$\cos\varphi = \frac{b}{a} \tag{B.15}$$

$$\sin\alpha = \frac{\sin\varphi}{\sin\vartheta} \tag{B.16}$$

$$0 \le \alpha, \vartheta, \varphi \le \frac{\pi}{2} \tag{B.17}$$

where F(k, υ) is an elliptical integral of the first kind, E(k, υ) is an elliptical integral of the second kind, k is the modulus, and υ is the elliptical integral amplitude. This method was used to calculate the shape demagnetization factors for the 940 μm x 30 μm x 12 μm design 1 permalloy patterns and the 800 μm x 30 μm x 10 μm device 3 permalloy patterns. For these two designs, the shape demagnetization factors were approximately equal and were found to be: $N_a = 0.0010$, $N_b = 0.25$, $N_c = 0.75$. Use of Equation B.6

results in an erroneous value of N_a almost 5x larger. Therefore, the patterning of the magnetic material into strips has reduced the shape demagnetization factor along the direction of the major axis by a factor of 10, which has a direct impact on the magnetization response of the permalloy to a given external magnetic field.

B.2 Equilibrium Solution

Now that demagnetization factors are calculated, we can calculate the magnetization, magnetic torque, and contact force present for a given magnetic actuator in a known external magnetic field. Equations B.18-B.21 describe the equilibrium conditions for the magnetic actuator. For the condition of contact,

$$\Gamma_{\text{magnetic}} = \Gamma_{\text{anisotropy}}, \neq \Gamma_{\text{elastic}} \tag{B.18}$$

where the magnetic, anisotropic, and elastic torques are given by:

$$\Gamma_{\text{magnetic}} = M\text{VB}\cos\gamma \tag{B.19}$$

$$\Gamma_{\text{anisotropy}} = \frac{N_L - N_T}{2} \text{V}M_{sat}^2 \sin 2\theta \tag{B.20}$$

$$\Gamma_{\text{elastic}} = k_\varphi \left(\varphi - \varphi^o\right) \tag{B.21}$$

where

$$M = \mathrm{Min}\left\{\frac{B\sin\gamma \pm H_c}{N_D}, M_{sat}\right\} \tag{B.22}$$

$$N_D = N_l \cos^2\theta + N_t \sin^2\theta \tag{B.23}$$

$$\gamma = \varphi + \theta - \alpha \tag{B.24}$$

B.2.1 Type-3 Actuator in 10-mT Field

As an example, we consider a type-3 actuator ($N_T = 0.95$, $N_L = 0.0010$) in a 10 mT external magnetic field with no initial beam deflection (and consequently, $\alpha = 0$). Setting the anisotropy torque and the magnetic torque equal results in:

$$M^2\theta = MB\cos\gamma \tag{B.25}$$

Since at the condition of contact, φ is determined by position of the upper and lower substrates. These positions are approximately +/- 0.045 radians. Considering the case of the upper latched position, $\cos\gamma$ can be shown to be approximated by unity. In chapters 4-5 this assumption was not made since unbounded beams were modeled and measured in order to determine magnetic properties of the permalloy; and in those cases, γ (φ in this case-for the assuming θ much smaller than φ) could not be assumed to be a small angle. In this case, we consider the upper latched state with $\varphi = 0.045$ radians. Using this, and the form of the magnetization given by Equation B.22 (assuming the unsaturated

condition),

$$\theta\,(B\,(\varphi+\theta)+H_c)/N_D = B \tag{B.26}$$

And given the following known variables: B = 10 mT, M_{sat} = 1.0 T, H_c = 0.2 mT, φ = 0.045 rad.

The variable θ may be solved for as follows:

$$10\text{ mT} = (.45\text{ mT} + 10(\theta)\text{ mT} + 0.2\text{ mT})(\theta / (N_L+\theta^2)) \tag{B.27}$$

$$10\,(N_L+\theta^2) = (.65 + 10\,(\theta))\,\theta \tag{B.28}$$

$$N_L = 0.065\,\theta \tag{B.29}$$

$$\theta = 0.016\text{ rad} \tag{B.30}$$

Using Equation B.23, the total demagnetization factor may now be calculated.

$$N_D = N_L + \theta^2 = 0.00125 \tag{B.31}$$

From which calculation of M follows:

$$M = (10\ mT\ (0.045 + 0.016) + 0.2\ mT) / 0.00125 = 0.65\ T \quad (B.32)$$

The magnetic torque and elastic torques are now calculated.

$$\Gamma_{magnetic} = MVB \cos\gamma = (0.65\ T)(10\ mT)(10^{7}/4\pi)(10^{-12})(.96) = 5.2 * 10^{-9}\ N\text{-}m \quad (B.33)$$

$$\Gamma_{elastic} = 0.045\ rad * 2.0\ (10^{-8})\ N\text{-}m/rad = 10^{-9}\ N\text{-}m \quad (B.34)$$

The difference between these two torques is used to determine the contact force.

$$\Delta\Gamma = 4.2\ (10^{-9})\ N\text{-}m \quad (B.35)$$

Finally, using Equation 4.18, the contact force is calculated.

$$F_{contact} = \Delta\Gamma / \text{beam length} = 4.2\ (10^{-9})/(10^{-3}) = 4.2\ \mu N \quad (B.36)$$

The minimum latching external magnetic field is that such that elastic torque is balanced by magnetic torque at latched position. This occurs when

$$\Gamma_{magnetic} = MVB = 10^{7}/(4\pi)\ B\ (9.6*10^{-13}\ m^{3})(B * 0.045\ rad + 0.2\ mT) / 0.00125 \quad (B.37)$$

$$= 9.6 * 10^{-6} / 4\pi * B\ (0.045B + 0.2\ mT) / 0.00125 = 10^{-9}\ N\text{-}m = \Gamma_{elastic}$$

Simplifying, B_{min} is calculated.

$$B\,(0.045 * B + 0.2\ mT) = 1.7\,(10^{-6})\ T^2 \quad \text{(B.38)}$$

$$B_{min} = 4.5\ mT \quad \text{(B.39)}$$

This value is lower than the experimental value of 7.0 mT. However, the value of θ must be confirmed at this new external field value.

$$4.5\ mT = (0.20\ mT + 4.5\,(\theta)\ mT + 0.2\ mT)(\theta / (N_L + \theta^2)) \quad \text{(B.40)}$$

$$4.5\,(N_L + \theta^2) = (.40 + 4.5\,(\theta))\,\theta \quad \text{(B.41)}$$

$$N_L = 0.088\,\theta \quad \text{(B.42)}$$

$$\theta = 0.011\ rad \quad \text{(B.43)}$$

$$N_L + \theta^2 = 0.0011 \quad \text{(B.44)}$$

B.2.2 Type-1 Actuator in 10-mT Field

For a type-1 device, which has approximately 3 times the ferromagnetic volume of type-3,

$$B\,((0.045 + 0.011)\,B + 0.2\ mT) = 0.56\,(10^{-6})\ T^2 \quad \text{(B.45)}$$

From this, the minimum external latching field is calculated to be $B_{min} = 1.8$ mT, slightly

larger than the 1.5 mT observed in experiment.

At 10 mT, this type-1 device generates a magnetic torque of 15.0 nN-m, giving a difference between the magnetic and elastic torques of $\Delta\Gamma$ = 14.0 nN-m, resulting in a calculated $F_{contact}$ of 14.0 μN.

B.2.2.1 Type-1 and Type-3 Actuators in 25-mT Field

These calculations are repeated at an elevated external magnetic field of 25 mT. Using again the equilibrium condition, Equation B.26, and the known constants: B = 25 mT, M_{sat} = 1.0 T, H_c = 0.2 mT, φ = 0.045 rad, we solve for θ:

$$\theta ((1.125 \text{ mT} + 25\ \theta \text{ mT} + 0.2 \text{ mT}) = 25 \text{ mT} (N_L + \theta^2) \quad \text{(B.46)}$$

$$\theta (1.325) = 25 (N_L) \quad \text{(B.47)}$$

$$\theta = 25 (0.001) / (1.325) = 0.019 \text{ rad} \quad \text{(B.48)}$$

Calculating N_D:

$$N_D = N_L + \theta^2 = 0.0013 \quad \text{(B.49)}$$

Calculating M:

$$(25\ \text{mT}\ (0.045 + 0.019) + 0.2\ \text{mT}) / 0.0013 > M_{sat}, \text{ therefore } M = M_{sat} \quad \text{(B.50)}$$

For the type-3 device,

Calculating magnetic torque:

$$\Gamma_{magnetic} = MVB \cos\gamma = (1.0\ \text{T})(25\ \text{mT})(10^7 / 4\pi)(.96\ 10^{-12}) = 19.1\ \text{nN-m} \quad \text{(B.51)}$$

Calculating elastic torque:

$$\Gamma_{elastic} = k\,\varphi = 0.045\ \text{rad} * 2.0\ (10^{-8})\ \text{N-m/rad} = 10^{-9}\ \text{N-m} \quad \text{(B.52)}$$

Torque difference:

$$\Delta\Gamma = 18.1\ \text{nN-m} \quad \text{(B.53)}$$

Contact Force

$$F_{contact} = \Delta\Gamma / \text{beam length} = 18.1\ (10^{-9})/(10^{-3}) = 18.1\ \mu\text{N} \quad \text{(B.54)}$$

Following similar calculations, for the type-1 device,

$$\Gamma_{magnetic} = 56.0\ \text{nN-m} \quad \text{(B.55)}$$

$$\Delta\Gamma = 55.0 \text{ nN-m} \quad \text{(B.56)}$$

$$F_{contact} = 55.0 \ \mu N \quad \text{(B.57)}$$

B.2.3 Type-2 Actuator in 25-mT Field

For the type-2 magnetic actuators, the same quantities may be calculated using the same equilibrium condition. However, the external magnetic field, latched angle, and shape demagnetization factor are changed. Using the known variables: B = 25 mT, M_{sat} = 1.0 T, H_c = 0.2 mT, φ = 0.08 rad , the calculations proceed as follows:

$$25 \text{ mT } (N_L + \theta^2) = \theta \ ((2 \text{ mT} + 25 \ \theta \text{ mT} + 0.2 \text{ mT}) \quad \text{(B.58)}$$

$$25 \ (N_L) = \theta \ (2.2) \quad \text{(B.59)}$$

$$\theta = 0.11 \text{ rad} \quad \text{(B.60)}$$

$$N_D = N_L + \theta^2 = 0.023 \quad \text{(B.61)}$$

$$M = (25 \text{ mT} \ (0.08 + 0.11) + 0.2 \text{ mT}) / 0.023 = 0.22 \text{ T} \quad \text{(B.62)}$$

$$\Gamma_{magnetic} = MVB \cos\gamma = (0.22 \text{ T})(25 \text{ mT})(10^7/4\pi)(1.2 \ 10^{-12} \text{ m}^3) = 5.3 \ (10^{-9}) \text{ N-m} \quad \text{(B.63)}$$

$$\Gamma_{elastic} = k\,\varphi = 0.08 \text{ rad} * 1.6\,(10^{-8}) \text{ N-m/rad} = 1.4\,(10^{-9}) \text{ N-m} \quad \text{(B.64)}$$

$$\Delta\Gamma = 3.9\,(10^{-9}) \text{ N-m} \quad \text{(B.65)}$$

$$F_{contact} = 7.8\ \mu\text{N} \quad \text{(B.66)}$$

B.2.3.1 Type-2 Actuator in 50-mT Field

$$\theta = 0.12 \text{ rad} \quad \text{(B.67)}$$

$$N_D = N_L + \theta^2 = 0.024 \quad \text{(B.68)}$$

$$M = (50 \text{ mT } (\ 0.08 + 0.12) + 0.2 \text{ mT}) / 0.024 = 0.43 \text{ T} \quad \text{(B.69)}$$

$$\Gamma_{magnetic} = 5.3\ (.43 \text{ T}/\ 0.22 \text{ T})(50 \text{ mT} / 25 \text{ mT}) = 20.7\ (10^{-9}) \text{ N-m} \quad \text{(B.70)}$$

$$\Gamma_{magnetic} - \Gamma_{elastic} = 19.1 \text{ nN-m} \quad \text{(B.71)}$$

$$F_{contact} = 38.2\ \mu\text{N} \quad \text{(B.72)}$$

Minimum latching field is that such that elastic torque is balanced by magnetic torque at latched position. This occurs when

$\Gamma_{magnetic} = MVB = (10^7 / (4\pi))\ B * 1.2 * 10^{-12}\ (B\ (0.08 + 0.12) + 0.2\ mT) / 0.02 =$

$$1.2*10^{-5} / 4\pi * B\ (0.2\ B + 0.2\ mT) / 0.02 = 1.6\ (10^{-9})\ N\text{-}m \quad (B.73)$$

$$B\ (\ 0.2B + 0.2\ mT) = 3.35\ (10^{-5})\ T^2 \quad (B.74)$$

$$B_{min} = 13\ mT \quad (B.75)$$

This value is slightly lower than the 17 mT experimental value.

B.3 Change in Hinge Projection onto X-Axis

If the shape of the hinge is given by some y(x), then the total arc length of the hinge, assuming the hinge is bounded by x = 0 and x = x_o is given by:

$$x^* = \int_0^{x_0} \sqrt{1 + \left(\frac{dy(x)}{dx} \right)^2}\, dx \quad (B.76)$$

This calculation obviously returns a value x' greater than x_o. However, the amount which x' exceeds x_o gives a first order correction to the upper bound in the integral, yielding an approximate value of the hinge projection along the x axis. Under the assumptions of zero slope at both x = 0 and x = x_o and a z-axis displacement of the hinge end Δz,

Equation B.77 gives the form of the hinge profile,

$$y(x) = \frac{\Delta d}{2}\left(1 - \cos\left(\frac{\pi x}{x_0}\right)\right) \tag{B.77}$$

with first derivative given by:

$$\frac{dy(x)}{dx} = \frac{\Delta d}{2}\frac{\pi}{x_0}\left(\sin\left(\frac{\pi x}{x_0}\right)\right) \tag{B.78}$$

Substitution of Equation B.10 into Equation B.8 gives Equation B.79.

$$\begin{aligned} x^* &= \int_0^{x_0}\sqrt{1+\left(\frac{\Delta d}{2}\frac{\pi}{x_0}\left(\sin\left(\frac{\pi x}{x_0}\right)\right)\right)^2}\,dx \\ &\approx \int_0^{x_0}\left(1+\frac{1}{2}\left(\frac{\Delta d}{2}\frac{\pi}{x_0}\sin\left(\frac{\pi x}{x_0}\right)\right)^2\right)dx \\ &= x_0 + \frac{1}{2}\left(\frac{\Delta d}{2}\frac{\pi}{x_0}\right)^2\int_0^{x_0}\left(\sin\left(\frac{\pi x}{x_0}\right)\right)^2 dx, \mathit{forsmall}\left(\frac{\Delta d}{2}\frac{\pi}{x_0}\right)^2 \end{aligned} \tag{B.79}$$

Here, the square root has been approximated by its 2-term Taylor expansion. The remaining integral may be calculated by change of variables, as shown in Equation B.80.

$$\int_0^{x_0}\left(\sin\left(\frac{\pi x}{x_0}\right)\right)^2 dx = \frac{1}{\alpha}\int_0^{\pi}(\sin(y))^2 dy \tag{B.80}$$

letting $y = \alpha x$, and where $\alpha = \frac{\pi}{x_0}$. Since over a single period the square of both the sine and cosine functions bound equivalent areas above the y-axis, the following substitution may be made. Identification of the trigonometric sum as unity yields Equation B.81.

$$\frac{1}{\alpha}\int_0^{\pi}(\sin(y))^2 dy = \frac{1}{\alpha}\int_0^{\pi}\frac{1}{2}\left(\sin^2(y)+\cos^2(y)\right)dy = \frac{1}{2\alpha}\pi = \frac{x_0}{2} \tag{B.81}$$

Substitution into Equation B.79

$$x^* = x_0 + \frac{1}{x_0}\left(\frac{\pi\Delta d}{4}\right)^2 \tag{B.82}$$

Defining Δx_1 as $x`-x_o$ gives the equation of constraint g_3.

$$g_3 = \Delta x_1 - \frac{\pi^2}{16}\frac{(\Delta z)^2}{x_0} = 0 \tag{B.83}$$

B.4 2nd Derivative of Equation of Constraint

The following two equations of constraint are provided

$$g_1 = \Delta z - X \sin\varphi + d = 0 \tag{B.84}$$

$$g_3 = \Delta x_1 - \frac{\pi^2}{16}\frac{(\Delta z)^2}{x_0} = 0 \tag{B.85}$$

Solving both g_1 and g_3 for Δz gives the following

$$\Delta z = \frac{4}{\pi}\sqrt{\Delta x_1 x_0} = X \sin\varphi - d \tag{B.86}$$

Since the beam is known to rotate only a small amount, we make the following simplification:

$$\sin\varphi \approx \varphi \tag{B.87}$$

Solving Equation B.86 for φ gives:

$$\varphi = \frac{d + \frac{4}{\pi}\sqrt{\Delta x_1 x_0}}{X} \tag{B.88}$$

The first derivative with respect to time may be calculated

$$\frac{\partial\varphi}{\partial t} = -\frac{2}{\pi X}\sqrt{\frac{x_0}{\Delta x_1}}\frac{\partial x}{\partial t} \tag{B.89}$$

The second derivative is also calculated:

$$\begin{aligned}\frac{\partial^2\phi}{\partial t^2} &= -\frac{2}{\pi X}\sqrt{\frac{x_0}{\Delta x_1}}\frac{\partial^2 x}{\partial t^2} - \frac{1}{\pi X}\sqrt{\frac{x_0}{(\Delta x_1)^3}}\left(\frac{\partial x}{\partial t}\right)^2 \\ &= -\frac{2}{\pi X}\sqrt{\frac{x_0}{\Delta x_1}}\left(\frac{\partial^2 x}{\partial t^2} + \frac{1}{2\Delta x_1}\left(\frac{\partial x}{\partial t}\right)^2\right) \\ &= -\frac{\Delta z}{2X\Delta x_1}\left(\frac{\partial^2 x}{\partial t^2} + \frac{1}{2\Delta x_1}\left(\frac{\partial x}{\partial t}\right)^2\right)\end{aligned} \tag{B.90}$$

where in the final step substitution for Δz was made as shown in Equation B.86. This relation is necessary to solve the system of equations generated from the Euler-Lagrange technique, as the system may now be expressed as a differential equation in terms of the coordinate x.

$$\frac{\partial^2\phi}{\partial t^2} = -\frac{\Delta z}{2X\Delta x_1}\left(\frac{\partial^2 x}{\partial t^2} + \frac{1}{2\Delta x_1}\left(\frac{\partial x}{\partial t}\right)^2\right) \tag{B.91}$$

B.5 2/3rd Rule for Electrostatic Actuation

Consider the schematic shown in Figure B.3, where the electrostatic actuator is modeled as two rectangular plates of area A, separated by an initial gap distance d. The top plate is attached to a linear spring with spring constant, k, while the bottom plate is fixed in place. A voltage V is applied to one of the plates, wile the other is grounded, resulting in an attraction of the plates and movement of the upper plate by an amount x.

Therefore, the force on the upper plate resisting motion due to the spring may be expressed as:

$$F_{spring} = kx \tag{B.92}$$

while the force of attraction between the two plates is:

$$F_{electrostatic} = -\frac{1}{2}\varepsilon A\frac{V^2}{(d-x)^2} \tag{B.93}$$

The value x may be solved for by noting the sum of these two forces must be zero for static equilibrium.

$$F_{spring} + F_{electrostatic} = kx - \frac{1}{2}\varepsilon A\frac{V^2}{(d-x)^2} = 0 \tag{B.94}$$

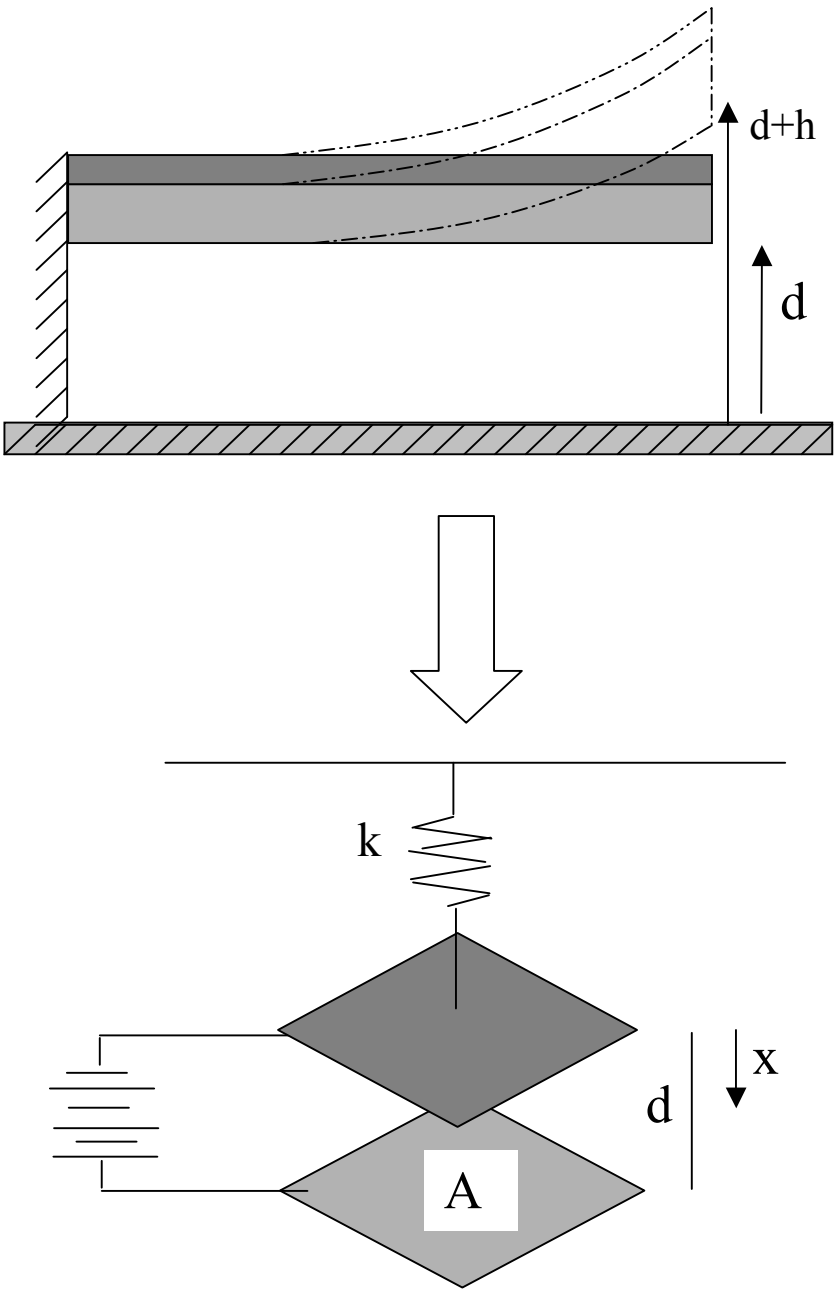

Figure B.3. Diagram of electrostatic actuator modeled as parallel plate capacitor.

However, in order for the equilibrium of the system to be stable, the second partial derivative of the potential energy with respect to x must be positive. This requires that:

$$\frac{\partial F_{total}}{\partial x} < 0 \tag{B.95}$$

The equilibrium becomes unstable with equality of Equation B.29.

$$k - \varepsilon A \frac{V^2}{(d-x)^3} = 0 \tag{B.96}$$

$$\varepsilon A \frac{V^2}{(d-x)^3} = k(d-x) \tag{B.97}$$

Substitution of Equation B.97 into Equation B.94 gives the critical value of x for which stable solutions of the system no longer exist.

$$F_{spring} + F_{electrostatic} = -kx + \frac{1}{2}k(d-x) = 0 \Rightarrow x = \frac{d}{3} \tag{B.98}$$

Using this value for x, the pull-in voltage is calculated [12,13].

$$V_{pull-in} = \sqrt{\frac{8kd^3}{27\varepsilon A}} \tag{B.99}$$

Once the spring has been displaced 1/3rd of its initial displacement, the upper rectangular

plate is pulled down to the bottom plate. In general, a dielectric material will coat the bottom electrode and prevent shorting of the capacitor plates during pull-in. Once the pull-in occurs, the electrostatic force holding the plates together has increased greatly, while the elastic force in the spring has increased by less than a factor of 3. The new forces may be expressed by Equations B.100 and B.101.

$$F_{spring} = k(d - t_D) \tag{B.100}$$

$$F_{electrostatic} = \frac{-\varepsilon A V^2}{2t_D{}^2} \tag{B.101}$$

Where t_d is the thickness of the dielectric covering the bottom plate. At this point, equilibrium between these two forces no longer exists. The amount by which the electrostatic force exceeds the restoring force exists as a force of contact between the upper plate and the dielectric. In order to release the upper plate from the fixed lower plate, the potential applied across the capacitor must be reduced so that equilibrium may be reestablished between the electrostatic and elastic restoring forces. This occurs at:

$$V_{release} = \sqrt{\frac{2k(d - t_D)t_D{}^2}{\varepsilon A}} \tag{B.102}$$

The ratio of the release voltage to the initial pull-in voltage is

$$\frac{V_{release}}{V_{pull-in}} = \sqrt{\frac{27(d - t_D){t_D}^2}{4d^3}} \approx \frac{3\sqrt{2}}{2}\frac{t_D}{d} \tag{B.103}$$

Therefore, the amount of hysteresis that results in strongly related to the proximity of the two electrodes at pull-in. For thicker dielectric layers, the hysteresis is reduced. In addition, this concept can be extended to predict that instabilities that result in a large increase in the electrostatic attractive force result in much larger hysteresis than pull-in behaviors characterized by short instabilities.

B.6 Calculation of Coil Resistance

Resistance of a regular conductor with resistivity p length L cross sectional area A is expressible through the following equation

$$\mathrm{R} = \frac{\mathrm{p\,L}}{A} \tag{B.104}$$

The cross-sectional area is equal to the product of the height h and width w of the coil windings, Equation B.105.

$$\mathrm{A} = \mathrm{w} \cdot \mathrm{h} \tag{B.105}$$

The length of the coil conductor can be written as:

L = number of turns (number of sides per turn)(average length of coil side) (B.106)

For a 25 turn gold coil 4 μm thick and 20 μm wide with average side length 1000 μm, the resistance is calculated to be:

$R = 2.4\ (10^{-6})\ \Omega\text{-cm}\ [25\ \text{turns}\ (4\ \text{sides/turn})(1000\ \mu\text{m})] / [(20\ \mu\text{m})(4\ \mu\text{m})] = 30\ \Omega$ (B.107)

B.7 Time to Electroplate

The required time to electrochemically deposit a desired thickness may be calculated by performing a charge balance. If a current density I_p (mA/cm^2) is supplied to an electroplating area A (cm^2) for a time t (seconds), the charge required is:

$$Q = \frac{I_p\ A\ t}{1000}\ \text{Coulombs} \qquad \text{(B.108)}$$

For a desired thickness, h (cm), the electroplated volume is:

$$V = A \cdot h \qquad \text{(B.109)}$$

The number of moles of material is given by:

$$\text{Number moles metal} = \frac{V\,p}{M_w} \tag{B.110}$$

Where p (g/cm^3) is the metal density, and M_w is its molecular weight (g/mol). Assuming n electrons are transferred for each atom of metal electrodeposited, the number of moles of electrons required is:

$$\text{N moles electrons} = \text{N moles metal} * n \tag{B.111}$$

The charge necessary equivalent to the transfer of this quantity of electrons is given through Faradays constant, F:

$$Q = \text{N moles electrons } (F) \tag{B.112}$$

Where F is equal to 96,500 C/mol electrons

As an example, for the electrodeposition of soft gold, in which 1 electron is transferred for each atom of gold, the electroplating time is:

$$\frac{I_p\,A\,t}{1000} = \frac{A\,h\,p}{M_w}\,n\,(96500) \tag{B.113}$$

$$t = \frac{h\ p\, n\, (9.65 \cdot 10^7)}{M_w\ I_p} \tag{B.114}$$

n = 1 mol e / mol Au, p =19.3 g/cm^3, M_w = 197 g/mol

$$t = h\ (9.65*19.3/197)10^7 / I_p \tag{B.115}$$

For a current density of 5 mA/cm^2,

$$\frac{t}{h} = 2 \cdot 10^6\ \frac{s}{cm} \tag{B.116}$$

Therefore, in order to electroplate 1 μm of gold, the time required is 2 (10^2) s. This gives the expected time of approximately 100 minutes to electroplate 30 μm of soft gold as described in chapters 4-5.

B.8 Coil Operating Power

The power P (W) consumed in supply of current I (Amps) to a coil of resistance R (Ohms) is calculated through Equation B.117:

$$P = I^2\ R \tag{B.117}$$

For a coil of resistance 30 Ohms, the 40 mA required to switch magnetic actuator type-3

in a 10 mT external magnetic field is calculated to be

$$P = (40^2\ 10^{-6}\ A^2)\ (30\ \Omega) = 48\ mW \tag{B.118}$$

B.9 Calculation of Switching Field from Coil

$$\Gamma_{magnetic} = VB\left(sgn\gamma \cdot Min\left\{ \frac{B_{coil,x} + Bsin|\gamma| \pm H_c}{N_D}, M_{sat} \right\} \right) \cdot cos\gamma \tag{B.119}$$

For a type-1 device in a 10 mT external magnetic field, with latched state given by φ = 0.045 radians, coercivity 250 A/m, demagnetization factor 0.0010, ferromagnetic volume 2.7 (10^6) μm^3, and residual elastic torque 1 nN-m, the magnetic field required to be generated by the coil is calculated:

$$B_{coil} = 10\ mT * 0.045 + 0.2\ mT - (10^{-9}\ N\text{-}m)(0.0010)(4\ \pi * 10^{-7}\ T^2/J/m^3)/(3 * 10^{-12}\ m^3)/(10\ mT) = 0.61\ mT \tag{B.120}$$

For a type-2 device, the calculation is adjusted to account for the 25 mT external magnetic field, φ = 0.08 radians upstate, ferromagnetic volume 1.2 (10^6) μm^3, demagnetization factor 0.010, and residual elastic torque 1.6 nN-m:

$$B_{coil} = 25\ mT * 0.08 + 0.2\ mT - (1.6 * 10^{-9}\ N\text{-}m)(0.01)(4\ \pi * 10^{-7}\ T^2/J/m^3) / (1.2 * 10^{-12}$$

m^3) / (25 mT) = 1.5 mT (B.121)

For a type-3 device, the calculation proceeds as for the type-1 device, with the exception of ferromagnetic volume 0.96 (10^6) μm^3

B_{coil} = 10 mT * 0.045 + 0.2 mT – (10^{-9} N-m)(0.0010)(4 π * 10^{-7} $T^2/J/m^3$)/(0.96 * 10^{-12} m^3) / (10 mT) = 0.53 mT (B.122)

Using the 10 mT/A magnetic field generation from the microfabricated coil, the anticipated current to switch each the three actuator designs are 61 mA, 150 mA, and 53 mA for designs 1, 2, and 3, respectively.

B.10 Euler Lagrange Calculations

The Lagrangian for the wiping magnetic actuator was derived in chapter 6 and is given here as Equation B.123.

$$L = \frac{1}{2}m\left(\frac{\partial x}{\partial t}\right)^2 + I_{beam}\left(\frac{\partial \varphi}{\partial t}\right)^2 - VH_0M\sin(\theta+\varphi) + \frac{1}{2}VN_DM^2 - 6EI_{hinge}\frac{(\Delta z)^2}{x^3} \quad \text{(B.123)}$$

The equations of motion for x, Δx_1, and Δz are straightforward; however, the Lagrange

equations of motion for θ and φ are much more complex.

φ:

$$dL/d\varphi = -VH_o [M\cos(\varphi + \theta) + \sin(\varphi + \theta)H_o \cos(\varphi + \theta)/N] + V(M H_o \cos(\theta + \varphi))$$

$$= VM\cos(\theta + \varphi)\,(M N / \sin(\theta + \varphi) - 2 H_o)$$

$$= M V H_o \cos(\theta + \varphi) \qquad \text{(B.124)}$$

And if $M = M_{sat}$ = constant, the same value is obtained, with M replaced by M_{sat} in the final answer of B.124.

θ:

$$dL/d\theta = -VH_o[M\cos(\theta + \varphi) - \sin(\theta + \varphi)H_o\{\cos(\theta + \varphi)/N$$

$$- 2\sin(\theta + \varphi)/N^2 \sin(\theta)\cos(\theta)(N_T - N_L)\}] + V\,(N M\,(H_o/N \cos(\theta + \varphi)$$

$$-H_o \sin(\theta + \varphi)/N^2\,((\sin\theta)\cos(\theta)(N_T - N_L) - \tfrac{1}{2}\, H_0 \sin(\theta - \varphi)/N^2 \sin\theta\cos\theta)$$

$$+ V M^2 \sin\theta\cos\theta$$

$$= VH_oM\cos(\theta + \varphi) - \tfrac{1}{2}\, M^2 \sin(\theta)\cos(\theta)\,(N_T - N_L) \qquad \text{(B.125)}$$

Again, if $M = M_{sat}$ = constant, the same value is obtained, with M replaced by M_{sat} in the final answer of B.125.

B.11 Stiffness of Beams

B.11.1 Fixed/Free Beam

For a cantilever beam of length L with a fixed end at x = 0 and a free end at x = L, the curved shape the beam makes under application of an external load may be calculated by the Euler-Bernoulli beam equation, Equation B.126.

$$EI\frac{d^4y}{dx^4} = p(x) \tag{B.126}$$

where E is the elastic modulus of the beam material, I is the moment of inertia of the hinge, and p(x) is the pressure distribution applied downward on the beam surface. The boundary conditions for the fixed/free beam in which a single load is applied to the end at x = L are: 1) zero deflection at x = 0, 2) zero beam slope at x = 0, 3) zero moment at x = L. Since the only load provided to the beam is at x = L, integration of Equation B.126 yields

$$EI\frac{d^3y}{dx^3} = C_1 \tag{B.127}$$

where the constant C_1 is identified as –F, where F is the magnitude of the downward force present at the beam end. Integrating a second time gives:

$$EI\frac{d^2y}{dx^2} = -Fx + C_2 \tag{B.128}$$

where the constant C_2 is solved by utilization of boundary condition 3. Integrating a third time gives:

$$EI\frac{dy}{dx} = -\frac{1}{2}Fx^2 + FLx + C_3 \tag{B.129}$$

where the constant C_3 is determined by the condition of zero slope at the fixed end (boundary condition 2). One last integration, and satisfaction of zero deflection at x = 0 gives the following for the beam profile.

$$y(x) = \frac{Fx^2(3L - x)}{6EI} \tag{B.130}$$

The final end-beam deflection may be calculated by evaluating Equation B.39 at the condition x = L:

$$y(L) = \frac{FL^3}{3EI} \tag{B.131}$$

This expression for force and end displacement determines the spring constant of the fixed/free cantilever beam.

$$F = k \cdot y_{x=L} \Rightarrow k = \frac{3EI}{L^3} \tag{B.132}$$

B.11.2 Fixed/Guided Beam

For a beam of length L with a fixed end at x = 0 and a guided end at x = L, the curved shape the beam makes under application of an external load may be calculated by the Euler-Bernoulli beam equation, Equation B.126. The boundary conditions for the fixed/guided beam in which a single load is applied to the end at x = L are: 1) zero deflection at x = 0, 2) zero beam slope at x = 0, 3) zero slope at x = L. Since the only load provided to the beam is at x = L, integration of Equation B.126 yields

$$EI\frac{d^3y}{dx^3} = C_1 \tag{B.133}$$

where the constant C_1 is identified as –F, where F is the magnitude of the downward force present at the beam end. Integrating a second time gives:

$$EI\frac{d^2y}{dx^2} = -Fx + C_2 \tag{B.134}$$

Integrating a third time gives:

$$EI\frac{dy}{dx} = -\frac{1}{2}Fx^2 + C_2x + C_3 \tag{B.135}$$

The constant C_3 is determined by the condition of zero slope at the fixed end (boundary condition 2), whereas the constant C_2 is determined by the condition of zero slope at the guided end, x = L (condition 3).

$$EI\frac{dy}{dx} = -\frac{1}{2}Fx^2 + \frac{1}{2}FLx = \frac{1}{2}Fx(L-x) \tag{B.136}$$

One last integration, and satisfaction of zero deflection at x = 0 (boundary condition 1) gives the following for the beam profile.

$$y(x) = \frac{Fx^2(3L-2x)}{12EI} \tag{B.137}$$

The final end-beam deflection may be calculated by evaluating Equation B.45 at the condition x = L:

$$y(L) = \frac{FL^3}{12EI} \tag{B.138}$$

This expression for force and end displacement determines the spring constant of the fixed/guided cantilever beam.

$$F = k \cdot y_{x=L} \Rightarrow k = \frac{12EI}{L^3} \tag{B.139}$$

Therefore, the spring constant for the fixed/guided beam is 4 times larger than of the fixed/free cantilever beam.

B.12 Calculation of ΔB_{coil}

From 5.2, the necessary condition for an incremental increase in the magnetic field generated by the integrated coil to produce a SPS event is:

$$\Delta B_{coil} \cos\varphi > N_D \left(\frac{\Gamma_{elastic}}{VB_{external}} + M_{critical} \right) \tag{B.140}$$

A minimum value for ΔB_{coil} may be calculated by assuming $M_{critical}$ equal to 0. Then, for a type-3 magnetic actuator in a 10 mT external magnetic field with magnetic volume $8.6 * 10^5$ μm^3 and elastic restoring torque of 1 nN-m, ΔB_{coil} is calculated to be:

$$\Delta B_{coil} > \frac{N_D \cdot 10^{-9} J}{10^{-12} m^3 \cdot 10^{-2} T} \left(\frac{4\pi T^2}{10^7 J/m^3} \right) = \frac{4\pi}{100} N_D T \approx 0.13\, mT \tag{B.141}$$

This increase in magnetic field can be converted to an increase in current necessary to be supplied to the integrated coil by the analysis used to create Figure 4.4. According to Figure 4.4, the maximum in-plane field component for the given integrated coil is 15 mT/A. Instead of averaging this component over the 1000 μm long permalloy strip to yield a mean value of 10 mT/A, it is believed that the maximum value influences the magnetization state of the entire beam along the direction of greatest length. The out-of-plane component from the microfabricated coil, however, acts along the direction of greatest demagnetization, and approximately averages to zero (examining the change in

sign of the z-component of the magnetic field) given suitable placement of the permalloy strip.

$$0.13\,mT \rightarrow \frac{1000\,mA}{15\,mT} \rightarrow 9\text{ mA} \tag{B.142}$$

This gives a required increase of 9 mA to the coil in order to produce an SPS event.

REFERENCES

1. G. Rebeiz, *RF MEMS: Theory, Design, and Technology*, *1st ed*. Hoboken, NJ. Wiley, 2003.

2. E. Camargo, *Design of FET Frequency Multipliers and Harmonic Oscillators*. Artech House, Boston. 1998.

3. G. Rebeiz and J Muldavin. "RF MEMS Switches and Switch Circuits," IEEE Microwave Mag., Vol. 2, pp. 59-71, (2001).

4. J. Oberhammer and G. Stemme, "Design and Fabrication Aspects of an S-Shaped Film Actuator Based DC to RF MEMS Switch." Journal of Microelectromechanical Systems, 13, 421-428. (2004).

5. K. Peterson, "Micromechanical Switches on Silicon," IBM J. Res. Develop., Vol. 23, No. 4, 376-385, July 1979.

6. J. Yao. "RF MEMS from a device perspective," J. Micromech. Microeng. 10. R9-R38. (2000).

7. L. Larson, R. Hackett, et al. "Microactuators for GaAs-based Microwave Integrated Circuits," in Proc. Transducers 1991, San Francisco, CA. June 24-27. pp. 743-746. (1991).

8. H. Schlaak, "Potentials and Limits of Micro-Electromechanical Systems for Relays and Swiches," 21st International Conference on Electrical Contacts, 9-12 Sep. Zurich. (2002).

9. V. Milanovic, M. Maharbiz, et al. "Microrelays for Batch Transfer Integration in RF Systems." Journal of microelectromechanical Systems, 9, pp. 787-792. (2000).

10. H. Nguyen, D. Hah, et al., "Angular Vertical Comb-Driven Tunable Capacitor With High-Tuning Capabilities." Journal of Microelectromechanical Systems, 13, 406-413. (2004).

11. B. Schauwecker, K. Strohm, et al., "A New Type of High Bandwidth RF MEMS Switch-Toggle Switch." Journal of Semiconductor Technology and Science, 2. 237-245. (2002).

12. A. Chinthakindi, D. Bhusari, B. Dusch, J. Musolf, B. Willemsen, E. Prophet, M. Roberson, and P. Kohl. "Electrostatic Actuators with Intrinsic Stress Gradient.

Part-I. Materials and Structures" Journal of the Electrochemical Society, 149, H139-H145 (2002).

13. A. Chinthakindi and P. Kohl. "Electrostatic Actuators with Intrinsic Stress Gradient. Part-II" Journal of the Electrochemical Society, 149, H146-H152 (2002).

14. S. McClure, L. Edmonds, et al. "Radiation Effects in MicroElectroMechanical Systems (MEMS): RF Relays." T. Trends in Optocoupler Radiation. 2002.

15. H. Espinosa, M. Fischer, "Identification of Residual Stress State in an RF-MEMS Device." white paper in MTS Systems Corporation, 2001.

16. J. Park, G. Kim, et al. "Electroplated RF MEMS Capacitive Switches." Journal of Microelectromechanical Systems, 9, 639-644. (2000).

17. G. Gray, M. Morgan, and P. Kohl. "Electrostatic Actuators with Expanded Tuning Range Due to Biaxial Intrinsic Stress Gradients." Journal of Microelectromechanical Systems. 13, (2004).

18. C. Ahn and M. Allen, "A Fully Integrated Surface Micromachined Magnetic Microactuator with a Multilever Meander Magnetic Core." Journal of Microelectromechanical Systems, 2, 15-22, (1993).

19. W. Taylor and M. Allen, "Fully Integrated Magnetically Actuated Micromachined Relays." Journal of Microelectromechanical Systems, 7, 181-191 (1998).

20. X. Yang, A. Holke, et al., "An Electrostatic, On/Off Microvalve Designed for Gas Fuel Delivery for the MIT Microengine." Journal of Microelectromechanical Systems, 13, 660-668. (2004).

21. M. Campanu, J. Boyd, and P. Hesketh, "Design, Fabrication, and Testing of a Bistable Electromagnetically Actuated Microvalve." Journal of Microelectromechanical Systems, 9, 181-189, (2000).

22. E. Hung and S. Senturia. "Extending the Travel Range of Analog-Tuned Electrostatic Actuators." Journal of Microelectromechanical Systems, Vol. 8, No. 4, December 1999, pp 497-505.

23. A. Dec and K. Suyama, "Micromachined Elctro-mechanically Tunable Capacitors and their Applications to RF IC's," IEEE Trans. Microwave Theory Techn., Vol. 46, no. 12, pp. 2587-2596, (1998).

24. P. Kohl, "Electrodeposition of Gold," Modern Electroplating, M.Schlesinger and M. Paniov, Wiley 2002.

25. J. Judy and R. Muller, "Magnetically Actuated, Addressable Microstructures." Journal of Microelectromechanical Systems, 6, 249-256, (1997).
26.
26. J. Wright, Y. Tai, and S. Chang, "A Large-Force Fully-Integrated MEMS Magnetic Actuator." Technical Digest: 1997 International Conference on Solid-State Sensors and Actuators: Transducers '97, 2, 793-796, (1997).

27. M. Ruan, J. Shen, and C. Wheeler. "Latching Electromagnetic Relays." Journal of Microelectromechanical Systems, 10, 511-517, (2001).

28. G. Gray and P. Kohl, "Magnetically Bistable Actuator. Part I: Low Switching Energy Regime." Sensors and Actuators (2004).

29. G. Gray, L. Zhu, and P. Kohl, "Magnetically Bistable Actuator. Part II: Low Switching Energy Regime." Sensors and Actuators (2004).

30. Cronos, JDS Uniphase, Thermomechanical DC Microrelay, http://www.memsrus.com/prodrelay.html

31. G.Gray and P. Kohl, "Modeling and Performance of a Magnetic MEMS Wiping Actuator," In Review, 2004.

32. Y. Okinaka and C. Wolowodiuk, Journal of the Electrochemical Society, 128, (1981).

33. C. Klein, "How Accurate are Stoney's Equation and Recent Modifications." Journal of Applied Physics, Vol. 88, pp. 5487-5489. (2000).

34. H. Tanimoto, S. Sakai, Y. Koda, K. Otsuka, E. Kita, and H. Mizubayashi. Mechanical properties of nanocrystalline gold after low-temperature irradiation.

35. J. Bernstein, W. Taylor, et al., "Electromagnetically Acuated Mirror Arrays for use in 3-D Optical Switching Applications." Journal of Microelectromechanical Systems, 13, 660-668. (2004). 526-534. (2004).

36. C. Liu, "Micromachined Magnetic Actuators Using Electroplated Permalloy," IEEE Transactions on Magnetics, 35, 1976-1985, (1999).

37. J. Jackson, *Classical Electrodynamics, 3rd ed*. New York, NY: John Wiley & Sons, Inc., 1999.

38. E. Fullin, J.Gobet, et al., "A New Basic Technology For Magnetic Micro-Actuators." MEMS 1998 Workshop. Heidelberg. Jan 25-29, (1998).

39. H. Hosaka, "Micro Electro Mechanical Systems", 7-10 Feb. 1993, Fort Lauderdale, Florida, IEEE, (1993).

40. Schimkat, "Contact Materials For Microrelays," in Proc. IEEE Micro Electro Mechanical Systems 1998, Heidelberg, Germany, Jan. 25-29, 1998, pp.190-194.

41. D. Hyman and M. Mehregany, "Contact Physics of Gold Microstructures for MEMS Switches." IEEE Trans. Compon. Packaging Technology, vol 22, 357-364. (1999).

42. R. Holm, *Electrical Contacts*, Springer-Verlag. (1967).

43. J. Marion and S. Thornton, *Classical Dynamics of Particles and Systems, 4th ed*. Fort Worth: Harcourt Brace & Company, 1995.

44. S. Senturia, *Microsystem Design*. Kluwer Academic Publishers, 2001.

45. B. Cullity, *Introduction to Magnetic Materials*. Reading, MA: Addison-Wesley, 1972.

46. L. Bates, *Modern Magnetism, 3rd ed.* London: Cambridge University Press, 1951.

47. R. Bozorth, *Ferromagnetism.* New York: D. Van Nostrand Company, Inc., 1951.

48. S. Chikazumi, *Physics of Magnetism*. New York: John Wiley & Sons, Inc., 1964.

49. J. Osborn, "Demagnetizing Factors of the General Ellipsoid," Phys. Rev., vol. 67, nos. 11 & 12, pp 351-357, 1945.

50. L. Yao, J. Zhang, et al., "Nonlinear Dynamic Characteristics of Piezoelectric Bending Actuators Under Strong Applied Electric Field." Journal of Microelectromechanical Systems, 13. 645-652. (2004).

51. B. Charlot, F. Parrain, et al., "A Sweeping Mode Integrated Fingerprint Sensor With 256 Tactile Microbeams." Journal of Microelectromechanical Systems, 13. 636-643. (2004).

52. R. Roark, *Roark's Formulas for Stress and Strain*, W. Young, Ed., 6th ed. New York: McGraw-Hill, 1989.

53. L. Katehi, G.Rebeiz, et al. "MEMS and Si-Micromachined Components for Low-Power, High-Frequency Communications Systems." 1998 IEEE MTT-S International Microwave Symposium Digest, Vol. 4. pp. 331-333, June (1998).